Modeling and Analysis of Microtubule-Mediated Chromosome Transport During Mitosis

A DISSERTATION
SUBMITTED TO THE FACULTY OF THE GRADUATE SCHOOL
OF THE UNIVERSITY OF MINNESOTA
BY

Melissa Klein Gardner

IN PARTIAL FULFILLMENT OF THE REQUIREMENTS
FOR THE DEGREE OF
DOCTOR OF PHILOSOPHY

Advisor: David J. Odde

August, 2008

Acknowledgements

In making the transition from industry to academia, I have been overwhelmed with the number of intelligent and supportive people who have guided and assisted me along the way.

First, I would like to thank my advisor, David Odde, whose patience, humor, and understanding at even the most difficult moments rescued me during times of self-doubt and discouragement. I am confident that the training I have received from Dave is unmatched, and I will sorely miss our scientific discussions, which have been a weekly highpoint for me over the past few years. I am confident that taking on an opinionated older student would be difficult for any mentor, but Dave has risen to this challenge with grace and optimism. Dave taught the first class that I took in returning to school. He was my inspiration then, and will continue to be my chief inspiration now as I move ahead in science.

Our collaborators at the University of North Carolina – Chapel Hill have been unmatched in their support and encouragement. I am especially grateful to Kerry Bloom, who, in addition to teaching me biology and guiding me into meaningful research areas, can always think of just the right thing to say to make things better when life seems dark. Kerry provides a constant stream of new ideas to think about, and his motivation to continue learning as well as his courage to move into "uncharted territories" has given me the courage to pursue my dreams.

I would like to thank Ted Salmon for his unfailing enthusiasm for my work, and for his unending support for me personally. My discussions with Ted have been critical to guiding my thinking.

Chad Pearson, Le Paliulis, David Bouck, and Jeff Molk are great scientists and good friends. It requires patience to teach biology to an engineer who is only familiar with "in-silico" experiments, and I am forever grateful to Chad, Le, David, and Jeff for their time and help.

I am very grateful to Julian Haase. Julian's help in making strains, taking images, and in growing up cells to prepare for my visits has been invaluable.

Although we have never met in person, I am thankful to Brian Sprague for his help with the yeast mitosis model-convolution code. In addition, Vince VanBuren provided helpful advice with the microtubule dynamics code.

Alan Hunt and Henry Schek have been great collaborators. Their experiments with nanoscale microtubule dynamics are amazing, and it has been an honor to test our microtubule dynamics simulations against their data. Alan is a fun and intelligent scientist, and our discussions with Alan are among the highlights of my graduate career.

I thank Mark Winey, Janet Meehl, and Eileen O'Toole for helpful discussions and for first-rate electron tomography work.

I am grateful to current and former members of the Odde lab, especially Dominique Seetapun, Clarence Chan, Andy Bicek, and Mauris Desilva, for technical help, interesting discussions, and for moral support.

My committee members - Victor Barocas, Tom Hays, and Jonathan Sachs - have been helpful and encouraging. I appreciate their time and effort in providing advice and in guiding my research.

I would like to thank my children - Kaitlin, David, and Noah - for their patience and love during this long endeavor. My parents, Joan and Frank Klein, have been wonderful sounding boards, and never wavered in their support and encouragement for me. Finally, I would especially like to thank my husband Keith, who not only shouldered double duty in household responsibilities on many occasions while I was working full-time and attending school part-time, but is also my resident programming expert.

Dedication

This dissertation is dedicated to my husband Keith.

His confidence in me never faltered.

His support for me never failed.

His ability to bail me out of impossible programming jams was unbelievable.

My gratitude to him is without words.

Abstract

During mitosis, dynamic arrays of kinetochore-associated microtubules (kMTs) and molecular motors are organized into a mitotic spindle that serves to accurately segregate chromosomes into daughter cells. Understanding the dynamics and organization of mitotic spindle components could ultimately apply to clinical applications, such as in cancer treatment, because of the centrality of the mitotic spindle in mediating cell mitosis.

Computer simulation can provide a bridge between mitotic spindle phenotypes and the individual dynamic spindle components that produce these phenotypes. I have found that by simulating the dynamics of kMTs mediating chromosome segregation during mitosis, it is possible to build a model for their regulation which results in specific predictions for molecular functions within the mitotic spindle. Specifically, by simulating the dynamics of molecular motors and chromosomes relative to kMT dynamics, and by comparing these simulations to experiments using fluorescent proteins and cryo-electron tomography, major mechanisms regulating proper chromosome congression in yeast have been uncovered. I have shown (1) that tension generated via the stretch of chromosomes between sister kinetochores is important in regulating the proper separation of sister kinetochores during metaphase, and (2) that a molecular motor, specifically the Kinesin-5 molecular motor Cin8p, is responsible for mediating a gradient in kMT catastrophe frequency that is required for proper chromosome congression.

Dynamic microtubule plus-ends are responsible for the proper segregation of chromosomes during mitosis, as well as for other critical cellular functions. By performing molecular-level Monte Carlo simulations of microtubule assembly and comparing these simulations to *in vitro* measurements of microtubule assembly, I have found that microtubule assembly at the nanoscale is highly variable. This result supports a model for microtubule dynamic instability in which there is exists a substantial and dynamic GTP-cap during microtubule assembly that is critical for microtubule growth.

TABLE OF CONTENTS

LIST OF TABLES

LIST OF FIGURES

LIST OF ABBREVIATIONS

aMT	Astral Microtubule
ANOVA	Analysis of Variance
CEN	Centromere
CFP	Cyan Fluorescent Protein
DIC	Differential Interference Contrast
DNA	Deoxyribonucleic Acid
EM	Electron Micrograph
FRAP	Fluorescence Recovery After Photobleaching
GAL	Galactose
GDP	Guanosine diphosphate
GFP	Green Fluorescence Protein
GMP-CPP	Guanylyl-(alpha, beta)-methylene-diphosphonate
GTP	Guanosine triphosphate
HU	Hydroxyurea
ipMT	Interpolar Microtubule
kMT	Kinetochore Microtubule
LacI	Lactose Repressor
LacO	Lactose Operator
MAP	Microtubule-Associated Protein
MT	Microtubule
NA	Numerical Aperature
NLS	Nuclear Localization Signal
PSF	Point Spread Function
p-value	Probability of Fit
RFP	Red Fluorescent Protein
SPB	Spindle Pole Body
SSE	Sum of Squares Error
Tub	Tubulin
WT	Wild-type

CHAPTER ONE

GENERAL INTRODUCTION

(Portions of the introduction have been reproduced with permission from *Current Opinion in Cell Biology*: [1] and [2])

Microtubules in Mitosis

During mitosis, dynamic microtubules mediate the proper segregation of the replicated genome into each of two daughter cells. These dynamic microtubules are the major actors within the mitotic spindle, which is additionally composed of spindle poles, kinetochores, and the replicated chromosomes themselves (reviewed in [3-5]).

Microtubules have an inherent polarity, and are generally attached at their minus-end to the poles of the mitotic spindle [6, 7]. Microtubule plus-ends are often associated with a kinetochore, a complex protein-based structure that serves as the essential mechanical linkage between dynamic microtubules and chromatin (reviewed in [8, 9]). The structure and molecular composition of the kinetochore is now emerging, with the finding that multiple distinct protein complexes cooperate to achieve and maintain chromosome-microtubule coupling and regulate kinetochore-attached microtubule (kMT) plus-end assembly (reviewed in [9, 10]).

Microtubules are most dynamic at their plus-ends, with extended periods of polymerization (growing) and depolymerization (shortening) [11]. Changes between these two states are stochastic, characterized by "catastrophe" events (a switch from growing to shortening state) and "rescue" events (a switch from shortening to growing). This process is termed dynamic instability [12]. During metaphase, the dynamic instability of kMTs can contribute to the oscillations of chromosomes, a behavior called "directional instability" [13] . Although microtubule plus-ends are dynamic in a wide range of mitotic spindles, the magnitude of observed chromosome oscillations due to directional instability varies between organisms [14-19], (reviewed in [20]). In general, the dynamic instability behavior of microtubules is thought to be responsible for

kinetochore attachment during prophase and prometaphase and for aligning kinetochores during metaphase, such that sister chromatids are ultimately segregated into each of two nascent daughter cells during anaphase (reviewed in [21-23]). The congression of sister chromatids to a metaphase plate midway between the two spindle poles is a characteristic hallmark of metaphase, after which correction of segregation errors is relatively limited [24-26]. Therefore, prometaphase, metaphase, and anaphase represent key phases in the accurate segregation of chromosomes.

Modeling in Mitosis

The inherent complexity of the mitotic process, or even a single phase of mitosis such as metaphase, has made it challenging to infer the underlying mechanisms of chromosome motility directly from experimental observation. To manage this complexity, mathematical and computational models have recently been developed to integrate experimental results and provide a physical framework for further investigation of mitotic chromosome motility, in particular its control at the kinetochore [27-29]. Key common elements of theoretical models for kinetochore motility include (1) the critical role of kMT dynamic instability, and (2) the importance of forces exerted at the kinetochore in either directly or indirectly regulating kMT dynamic instability.

As presented in chapter 2, we have now developed a systematic method for simulating the regulation of chromosome motility during mitosis and then comparing the simulation results to experiments. This method, which we term "model-convolution", involves creating theoretical models for the localization and dynamics of fluorescent proteins, and then comparing these models to experiment by generating simulated images that can be quantitatively compared to experimental images.

Mitosis in *Saccharomyces cerevisiae*

The mitotic process is especially amenable to computational modeling in the budding yeast *Saccharomyces cerevisiae*, as the number of mitotic spindle components are limited, and the interaction between kinetochores at microtubule tips is direct. Specifically, there are a total of 32 kinetochores in budding yeast, with only one

kinetochore microtubule associated with each kinetochore [30]. Because of this direct interaction, simulations as described in chapter 3 can be used to explore the role of forces exerted at the kinetochore in directly regulating kMT dynamic instability. Here we find that tension at the kinetochore originating from the stretch of chromosomes between sister kinetochores regulates kMT plus-end dynamic instability. Specifically, tension due to the stretch of chromosomes between sister kinetochores promotes rescue of depolymerizing kMT plus-ends, while low tension suppresses rescue to increase the fidelity of kinetochores to the correct half-spindle.

In chapter 4, the model for kMT dynamic instability in yeast is further tested via a newly described assay. Here, GFP-tubulin fluorescence recovery after photobleaching (FRAP) experiments are spatially resolved within the mitotic spindle at ~60 nm intervals. In this way, kMT dynamics in yeast are quantified to show that metaphase chromosome congression is specifically the result of spatial "attractor points" that result from the spatial regulation of kMT plus-end dynamic instability. It is hypothesized that, although kMT plus-end rescue frequency is likely regulated by tension, a gradient in catastrophe frequency, together with a tension-mediated rescue frequency gradient, could spatially regulate kMT dynamic instability to mediate chromosome congression.

Finally, in chapter 5, the origin of the theoretical gradient in kMT plus-end catastrophe frequency is investigated. By performing simulations to predict the knock-out phenotypes of a potential catastrophe gradient mediator, we find experimentally that the Kinesin-5 molecular motor Cin8p promotes length-dependent disassembly of kMTs. By modeling Cin8p motors explicitly and by comparing their simulated dynamics to experiments, we find that their length-dependent concentration at kMT plus-ends follows naturally both from their plus-end directed motoring properties and from their microtubule cross-linking properties. Thus, we identify a new property for the highly-studied Kinesin-5 molecular motor Cin8p as a major mediator in mitotic chromosome congression.

Microtubule Dynamics at the Nanoscale

As described above, microtubules (MTs) are dynamic, growing and shortening at their ends via αβ-tubulin dimer addition and loss. These dynamics are important for rapid cellular restructuring of the cytoskeleton, as well as for mediating the delivery of cellular cargos. Numerous studies using light microscopy have quantitatively characterized this behavior both *in vitro* and *in vivo* [11, 31, 32].

Although dynamic instability has been well characterized at the spatial resolution of light microscopy (~200 nm), dynamic characterization at single molecule resolution is just now emerging. Until recently, our understanding of MTs at single molecule resolution has rested largely on electron microscopy studies. These studies have shown that MTs are typically composed of 13 individual protofilaments consisting of αβ tubulin heterodimers lined up end to end. The electron microscopy images of growing and shortening MT tips reveal that shortening MT ends can have outwardly curling individual protofilaments, while growing ends are relatively straight [33-36]. Tubulin heterodimers that are added to MT tips are GTP-bound. Because the GTP nucleotide is subsequently hydrolyzed to GDP after incorporation into the MT lattice, the difference in structure between growing and shortening MT tips has been attributed to a difference in preferred orientation of GTP versus GDP nucleotide-containing αβ tubulin heterodimers [37, 38]. Specifically, the GDP-bound tubulin heterodimer is believed to curl outwardly when exposed at MT ends, resulting in destabilization of the lateral bonds between the tubulin subunits. This destabilization then leads to depolymerization of the MT lattice. Conversely, a "cap" of GTP-bound tubulin heterodimers at the MT tip leads to relatively straight growing ends that stabilize the MT from rapid depolymerization. However, the size and structure of the stabilizing GTP-tubulin cap remains unclear.

While the electron microscopy data has provided important nanoscale information, it has not supplied direct information about MT dynamics because samples are fixed prior to imaging. In chapter 6, data is presented in which molecular-scale Monte Carlo simulations are run and compared with new *in vitro* data on MT dynamics at the nanoscale. Here, MT dynamics are characterized at nanometer scale resolution using

high-resolution tracking of MT-attached beads. These studies have led to new insights into (1) the mechanisms of dynamic instability behavior at the single molecule level, and (2) the effect of compressive loading on these behaviors. These studies, combined with computational modeling, provide a new framework for understanding MT assembly dynamics.

Microtubules and the Mitotic Spindle: Structure

In the work described above, microtubule dynamics were studied either *in vitro*, in which the environment surrounding the microtubule was carefully constructed with beads and laser traps, or in the *in vivo* mitotic spindle, in which nature has carefully constructed the microtubule-based mitotic spindle environment. Future research will involve integrating forces that originate from molecular motors, chromatin, and microtubule-associated proteins to understand how the microtubule-based mitotic spindle structure is established and maintained. The data in chapter 7 present a first step in this direction. Here, additional spindle stresses are imposed using a dicentric chromosome mutation that prevents sister chromosome segregation during anaphase. Through this assay, the microtubule-associated proteins that are important in maintenance of structural spindle integrity are identified. Future work will involve dissecting the roles of each of these proteins in organizing and supporting the mitotic spindle structure itself.

CHAPTER TWO

HYPOTHESIS TESTING VIA INTEGRATED COMPUTER MODELING AND DIGITAL FLUORESCENCE MICROSCOPY

(Contributing Authors: Melissa K. Gardner, David J. Odde, and Kerry Bloom)
(Reprinted with permission from *METHODS* (2007))

Abstract

Computational modeling has the potential to add an entirely new approach to hypothesis testing in yeast cell biology. Here we present a method for seamless integration of computational modeling with quantitative digital fluorescence microscopy. This integration is accomplished by developing computational models based on hypotheses for underlying cellular processes that may give rise to experimentally observed fluorescent protein localization patterns. Simulated fluorescence images are generated from the computational models of underlying cellular processes via a "model-convolution" process. These simulated images can then be directly compared to experimental fluorescence images in order to test the model. This method provides a framework for rigorous hypothesis testing in yeast cell biology via integrated mathematical modeling and digital fluorescence microscopy.

Introduction

As high-speed computing has become widely accessible to all disciplines, a unique opportunity now exists to integrate sophisticated digital light microscopy with mathematical modeling of cellular processes. Historically, integration of theoretical modeling with cell biology has been limited. Each field has developed independently with distinct fundamental tools and separate languages for communication. Here we review an alternate approach to computational modeling in which experiments and theory are integrated to combine the sophistication of digital fluorescence microscopy with computer modeling of underlying cellular processes.

Quantitative modeling can contribute to experimental hypothesis testing in yeast cell biology both by providing for quantitative analysis of results and predictions, as well

as constraining hypotheses to be physically plausible. Often, hypothesis testing via computer modeling will generate new or restructured models to explain experimental results. After building a computational model to better understand one set of experimental results, this model can then be used to design future experiments and predict results from these experiments. In this way, computational modeling can be used to assess the utility of proposed experiments, allowing for targeting of future experiments to those that may be most productive in producing meaningful conclusions.

Specifically, quantitative modeling can be used in combination with fluorescence microscopy in yeast to better understand protein dynamics (Box 1). The development of fluorescent protein fusions now allows sophisticated analysis of cellular components in living cells via digital fluorescence microscopy. The ability to quantitatively visualize fluorescent protein localization and dynamics provides strong clues to underlying cellular processes, and hypotheses are generally built on developing models for these processes. In using computational modeling to simulate an underlying cellular process, quantitative and qualitative predictions of the hypothesized model can be developed subject to a known set of model assumptions. Comparison of simulated predictions for fluorescent protein spatiotemporal dynamics to experimental images gathered via digital fluorescence microscopy then provides for quantitative model evaluation and the subsequent evolution and development of hypotheses.

Materials and Methods

Modeling of Green Fluorescent Protein (GFP) Dynamics

In order to begin modeling any cellular process, the sub-system to be modeled must be carefully defined. A complex cellular process (e.g., mitosis), can generally be broken down into more manageable sub-systems for detailed quantitative modeling (e.g., the yeast mitotic spindle). This sub-system can then be defined by its structural and molecular components (e.g., chromosomes, kinetochores, etc.). The definition and scope of the sub-system require careful thought. An extremely complex and elaborate sub-system could result in a very computationally intensive model that is difficult to comprehend, even when it correctly predicts sub-system behavior. In contrast, a very

narrow or simplified sub-system may ignore processes or components that may be critical to the experimentally observed fluorescent protein dynamics.

Once a sub-system is defined, a straightforward procedure can be followed for systematic development of a computational model.

1) The particular process to be modeled should be selected based on the desire to answer a specific question. For example, modeling of the yeast mitotic spindle through the entire cell cycle may result in a highly complex model with a correspondingly long and tedious development time, whereas limiting the modeling effort to the specific stage being studied (e.g. metaphase) reduces the complexity, thus allowing for a more focused and potentially more fruitful modeling effort. Such restricted models can then serve to provide the framework for understanding preceding and subsequent processes.

2) The physical structure of the sub-system to be modeled must be defined, and the sizes and relative physical locations of sub-system components should be scaled correctly. For example, in the case of the yeast mitotic spindle, high resolution structural data gathered via electron microscopy [30] can be used to define the spindle pole body sizes, as well as the relative locations of microtubule attachment to these structures. These sizes and locations are then integrated into the computer model [29].

3) Explicit rules for the positioning of fluorophores in the cell during the cellular process need to be defined. For example, the localization of fluorescent kinetochore proteins in the mitotic spindle relies at least in part on the dynamics of individual microtubules attached to each kinetochore. Therefore, kinetochore-attached microtubule dynamics will govern the positions of simulated fluorescent kinetochore proteins. Thus, hypothesis testing via a computational model requires explicit rules and assumptions for how fluorophore positions are established in the underlying cellular process.

4) Time scales and motion constraints must be established for the components of the underlying cellular process that establish fluorophore positions. For example, microtubule plus ends attached to fluorescent kinetochore markers grow and shorten over time. Rules for the rates of microtubule growth and shortening, as well as the frequency of changing states, will then govern the simulated fluorescent protein dynamics associated with the kinetochore.

5) Assumptions inherent in the proposed model should be defined as explicitly as possible and critically reviewed. These assumptions define the limitations and scope of the model, and should thus be clearly articulated and examined. If modeling predictions are inconsistent with experimental results, then it is necessary to review and reassess the model assumptions. For example, by modeling kinetochore protein dynamics based on the growth and shortening of microtubules, an assumption inherent to this model is that the kinetochore remains attached to the plus-end of the microtubule throughout the entire simulation. Therefore, events or mutations that may result in detachment of the kinetochore from its microtubule may not produce modeling results that match experimental observations.

Modeling methods and guidelines

Deterministic vs Stochastic Modeling Methods

There are two basic classes of models that are commonly used to simulate cellular processes. The first type of model is a deterministic model, in which a system of mathematical differential equations is developed to completely characterize the underlying cellular process. Deterministic modeling can be used for characterization of biochemical cellular processes and networks [39-41]. There is a software modeling environment called "Virtual Cell" available on-line that is useful for modeling of biochemical interactions via numerical solutions to reaction-diffusion equations [42-44]. This software allows the user to build a biological model for a system based on its quantitative physical and chemical details. An advantage of deterministic modeling is that in developing mathematical equations to describe a cellular process, interactions and dependencies of system components can be explicitly understood.

The second commonly used method for simulation of cellular processes is stochastic modeling [45, 46]. This method takes advantage of probabilities and computer random number generators in order to capture the stochastic aspects of a living system. For example, key aspects of a given cellular process may fluctuate due to normal variations in protein expression levels, such that fluorescent protein localization and dynamics would vary from cell to cell, and over time within a given cell. Stochastic

modeling attempts to capture the range of results that may be expected from a given experiment simply due to the normal variation present in any living system [47]. There are many commonly used methods for stochastic modeling, including "Monte Carlo" simulations [45, 46]. Stochastic models can be helpful in understanding how normal cell-to-cell variation in experimental results could affect the ability to detect subtle differences in cellular behavior. A disadvantage of stochastic modeling is that simulations need to be repeated many times in order to adequately sample the range of system fluctuations. Also, the quantitative relationships between system behavior and parameter values is often more obscure than it is when closed-form mathematical solutions are obtained.

Fundamental physical principles and observed physical phenomena

Once a sub-system is defined and a modeling method selected, a specific mathematical model can be built. Ideally, the model is based on fundamental physical laws and principles, such as conservation of mass, momentum, and energy. Rates of cellular processes should be constrained by fundamental physical processes as well, such as the known rates of molecular diffusion.

Experimentally observed phenomena may also be included in a model. For example, the dynamic instability behavior of microtubules is a phenomenon that, while not completely understood at the molecular level, has been widely observed in living cells and thus may be an important aspect of a given cellular process. Observed phenomena that are included in a model (i.e. "descriptive modeling") should be listed as model assumptions, since a detailed explanation for the behavior based on fundamental physical laws and principles may not be practical or even necessary.

Model Parameters

Finally, once a model has been developed, there are often many model parameter values and constants, such as rate and diffusion constants, that must be defined and constrained in order to generate results. Where possible, parameter values should be experimentally measured or estimated from the existing literature in order to establish

physically plausible ranges. In addition, all parameter value assignments should be carefully reviewed and listed as model assumptions. Often, model results will be more sensitive to some parameters than to others. It is important to understand which parameters have most influence on the modeling results, and to test the physically plausible ranges of these parameters to ensure that modeling results and conclusions are not unduly dependent on the value of one particular parameter. Constraining a parameter to very narrow range provides an excellent opportunity with which to more stringently test the model.

Simulation of Digital Fluorescence Images (Model-Convolution)

Once a computational model for a particular cellular sub-system has been developed, a critical step in seamlessly integrating computer modeling with experimental cell biology is to develop an output for the simulation that can be conveniently compared to experimental results. In some cases, quantitative experimental data, such as relative sizes or time scales required to complete cellular activities, can be directly compared to simulation results. In a recent example of integrated modeling and experimental work, the time required for simulated kinetochore "capture" by microtubules was directly compared to experimentally observed prometaphase duration times [48, 49].

In order to conveniently compare experimental fluorescent protein dynamics and localization data from living cells to simulation results, we have developed a method for simulating fluorescence images which we call "model-convolution" [29, 50, 51]. Using model-convolution, simulation results can be evaluated against experimental results by direct comparison of simulated fluorescence images to experimental fluorescence images.

The model-convolution method takes advantage of the fact that experimental noise and the spreading of light inherent in the microscope imaging system (as characterized by the point spread function) can be quantified experimentally. By simulating fluorescent protein dynamics and localization, high resolution fluorescence images can be generated (Figure 2.1A). Then, the high resolution simulated image is convolved with the experimentally measured microscope point spread function. Finally, after adding experimental background fluorescence and noise, the resulting simulated

fluorescence image can be quantitatively compared to experimental images (Figure 2.1B). In this way, model-convolution can provide an exact comparison of theoretical fluorescent protein distributions against experimental results, validating models within a known degree of statistical certainty [29]. The development of quantitative animations as an additional simulation output can increase the utility of the simulation by providing clear illustrations that are useful for visualizing and assimilating the emergent behaviors of the underlying model (Figure 2.1C). In particular, very complicated models become increasingly difficult to "deconstruct," meaning that it is difficult to understand, and explain in words, why the model explains a given set of observations. As computing power increases and model construction becomes even more facile, it is expected that model deconstruction will become limiting to further progress. In this regard, we have found that animations aid in model deconstruction (for an example of the yeast spindle simulation animation, see http://www.tc.umn.edu/~oddex002/). In addition, creating simulated images and movies via the model-convolution method creates a model output that ideally "looks" like the real thing. This allows the experimenter to inspect simulated images and movies in the same way that the experimental images and movies are inspected.

Quantitative observation of experimental GFP dynamics

The appropriate collection of experimental images for comparison to simulation is critical to the success of integrated modeling and experimentation. In the yeast mitotic spindle example, image acquisition was carried out as described previously [52] on a Nikon TE2000 microscope with a 1.4 NA, 100x DIC oil immersion lens [53]. Images were acquired with an ORCA II ER cooled CCD camera. Cells were pipetted onto slabs of 25% gelatin containing minimal media +/- 2% glucose as described by Yeh *et al*. (1995)[54]. The microscope was modified for automated switching between fluorescence and differential interference contrast (DIC) by replacement of the camera mount with a filter wheel (BioPoint 99B100; Ludl Electronic Products Ltd.) containing the analyzer component of the DIC optics. The computer-controlled (MetaMorph 4.6 software) microscope executed an acquisition protocol taking fluorescence images at 1-u*m* axial

steps and a single DIC image corresponding to the central fluorescence image. Fluorescence excitation through a 490/10-nm filter was normally attenuated to 1–10% of the available light from a 100 W mercury arc lamp. Fluorescence emission was collected through a 530/15-nm band pass filter. DIC images were made by rotating the analyzer into the light path and taking a 0.6-s exposure. The images corresponding to a single time-lapse point were projected to a single image by using only the brightest pixel at any one location. Registration of DIC and fluorescence images was verified by imaging of 1-um fluorescent beads in DIC and fluorescence modes.

As simulated images generated via model-convolution account for the experimental microscope point spread function and noise, image processing techniques such as experimental deconvolution are not required. Specific experimental considerations for quantitative comparison of fluorescent images to modeling results are as follows.

(1) Signal linearity: It is important that the fluorescent signal remains at sub-saturation levels in order to properly quantify fluorescent protein localization.

(2) Frame of reference: In order to properly assess the orientation of the cell within the focal plane of the microscope, frame of reference points must be established. If possible, these points should be spaced appropriately to assess whether the region of interest remained in focus during the entire experiment. For example, in the yeast mitotic spindle example, spindle pole body markers provided a frame of reference for the length and orientation of the mitotic spindle. Image stacks at multiple planes of focus can be used to evaluate the orientation of the cell.

(3) Noise: As experimental noise will be incorporated into simulated images, it is necessary to quantify experimental noise levels on each image. The measurement method and location for evaluation of noise levels should be carefully considered to accurately reflect noise in the region of interest. For example, in the yeast mitotic spindle analysis, it was necessary that experimental noise be evaluated within the nuclear envelope just outside of the spindle area for the best approximation of noise levels in the spindle.

(4) Sample numbers: For quantitative comparison to simulation results, it is preferred that experimental sample sizes be as large as possible. In addition, images from control cells are required, so that controls can be simulated in parallel with experimental runs. Small sample size does not preclude hypothesis testing, but does make hypothesis rejection less likely.

Quantitative data analysis: Comparison of experimental and simulated data

Close integration of experimental cell biology and computational modeling requires quantitative data analysis for the comparison of experimental data to simulated image data. Thus, the method for fluorescence image data analysis requires careful consideration. The fluorescence signal should be quantified as a function of spatial position, such that localized fluorescence signal is normalized over the total signal for the area of interest in each image. In order to account for small variations in yeast mitotic spindle length , we have developed a method for "binning" of fluorescence signal into a standard number of bins with a constant relative axial location for each bin [29, 50]. For example, fluorescence intensity is analyzed by pixel for each spindle regardless of length. These "pixel" fluorescence intensity values are then recombined into a standard number of "bins" for each spindle. Thus, although absolute bin sizes will vary over different spindle lengths, the relative location of each bin should remain constant so that normalized signal by bin location can be averaged over many images and cells. The localization of various fluorescent protein positions can then quantified and compared relative to a standard "spindle bin number." Using this method, experimental normalized fluorescence signal for each bin can be quantitatively compared to simulation results.

We then calculate a probability of fit (p-value) to quantify the overall fit of the experimental data to the simulation data for a given set of parameter values. The p-value is an estimate of the probability that the deviations between the model and the experiment could have arisen by chance alone.

The p-value is calculated as follows:

(1) Multiple trials are simulated, and then normalized fluorescence signal is calculated by bin for each trial. A "grand average" is calculated for each bin by averaging values for a given bin over all trials.

(2) In order to assess the variation in fluorescence signal localization of each simulated trial against the "grand average" value over all simulated trials, the difference in mean signal (error) is calculated for each bin location against the "grand average" value for that bin over all trials. The error values for a given trial are then squared and summed over all bins to calculate the "sum-of-squares" error (SSE) for each trial as compared to the "grand average" over all simulated trials.

(3) The SSEs for each simulated trial are then ranked from smallest to largest.

(4) The SSE for the experimental data is then calculated against the "grand average" value over all simulated trials, as described in step (2).

(5) The ranking of the experimental SSE in the list of simulated SSE values determines the likelihood that the model could have given rise to the experimental data (e.g., if the experimental SSE is less than 50 of 100 simulated trial SSEs, $p=0.50$). If the SSE value for the experimental data is larger than all of the simulated trial SSE values, the experimental data does not lie within the range of simulation data, but rather falls outside of the range of variation between successive simulation runs (e.g., for 100 simulated trials the p-value would be less than 0.01). Thus the p-value would fall outside of the acceptable range, indicating that the simulation does not accurately predict the experimental results [29]. In comparing simulation data to experimental data, high p-values ($p>0.05$) indicate that simulation results are not statistically different from experimental results.

In this way, a statistical comparison is made between the simulation and the experimental fluorescence image data. If the simulation does not accurately reproduce experimental results within the expected range of variability, then either the model hypothesis is incorrect or assigned model parameter values need adjustment. For this reason, a

thorough search of potential parameter values is required prior to rejecting a model altogether.

Conclusions

Computational modeling is an iterative process which incorporates rigorous hypothesis testing and parameter value estimation. Ideally, models will be continuously challenged with new experiments and ideas. For example, a model that successfully reproduces an experiment that tests only fluorescent protein localization in static images may be significantly challenged by subsequently simulating an experiment that accounts for the temporal dynamics of fluorescent protein localization within a given cell [50]. To simulate the new experiment, one is constrained to use only the parameter values found to be valid for the first experiment. Subsequent experiments further constrain parameter space, and eventually may invalidate the model altogether. The budding yeast is a particularly appropriate organism in which to use this method because the experimental molecular tools are relatively advanced and the number of molecular components is relatively limited compared to other eukaryotes. The failure of a given model to reproduce experimental results generally leads to questions about the hypothesis used to develop the simulation. For example, simplifying assumptions should be reviewed, as well as processes or cellular components that were not considered in developing the original hypothesis. The process of developing a model that can successfully reproduce multiple experiments, each experiment testing a different aspect of a cellular process [50], is a journey requiring a close linkage between experiment and theory, resulting in a sharing of knowledge and technology that will facilitate our ability to achieve a more complete understanding of the cell.

Acknowledgements

This work was supported by the Whitaker Foundation, the National Science Foundation, and the National Institutes of Health.

Tables and Figures

BOX 2.1: A process for integrating computational modeling with digital fluorescence microscopy to better understand the underlying processes that regulate fluorescent protein localization and dynamics in yeast. Modeling provides a framework for iterative hypothesis testing and guiding of new experiments. A key to this process is the quantitative comparison of simulation results to experimental results, allowing for rigorous model evaluation.

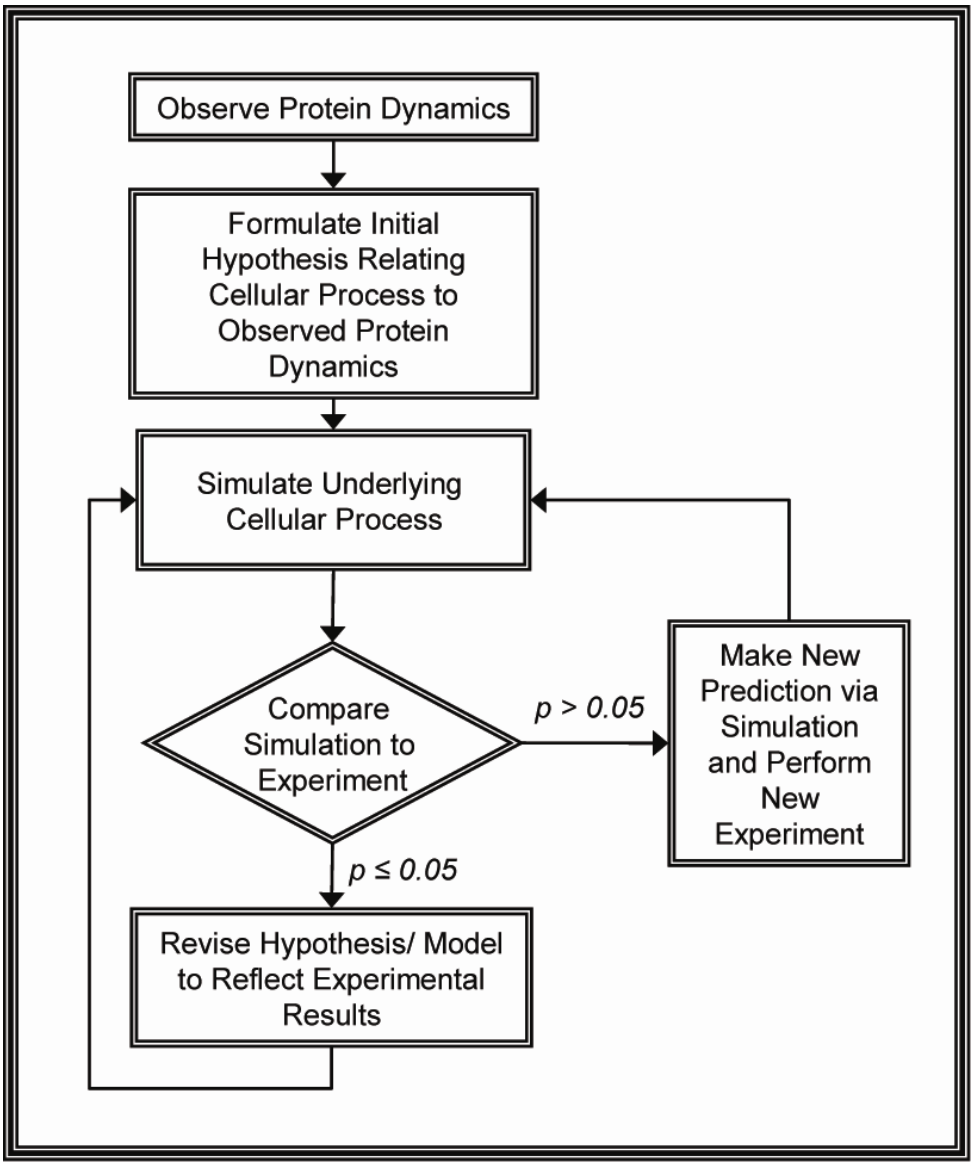

FIGURE 2.1: The model-convolution process is used for rigorous model evaluation against experimental results [29, 50]. (A) Simulated "sharp" images of fluorophore localization in the yeast mitotic spindle are convolved with the experimentally measured microscope point spread function and background in (B), scale bar 1000 nm. (red, spindle pole body markers, green, kinetochore-associated markers) (C) Quantitative animations provide for visualization of model components and predicted behaviors of underlying cellular processes.

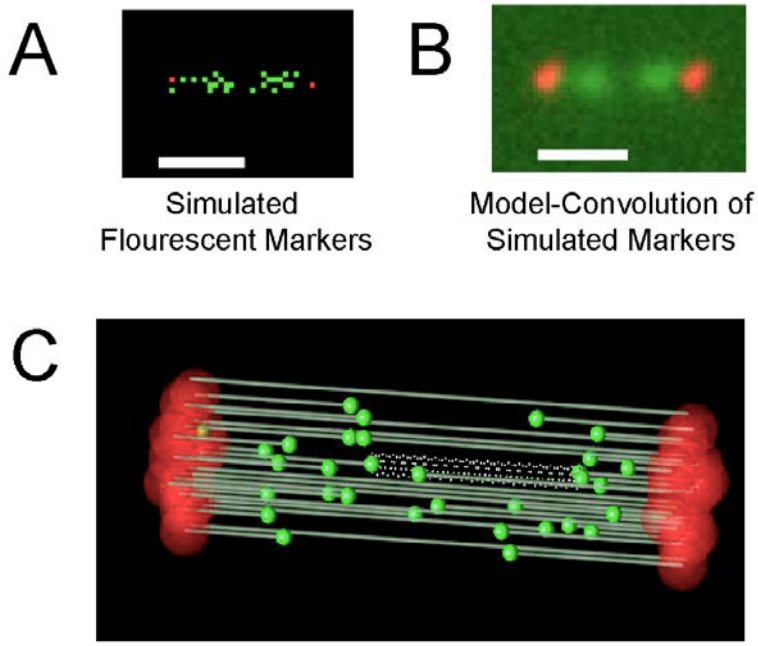

CHAPTER THREE

TENSION-DEPENDENT REGULATION OF MICROTUBULE DYNAMICS AT KINETOCHORES CAN EXPLAIN METAPHASE CONGRESSION IN YEAST

(Contributing Authors: Melissa K. Gardner, Chad Pearson, Brian Sprague, Kerry Bloom, E.D. Salmon, and David J. Odde: *MKG performed simulations and completed all image/data analysis, CGP performed experiments, BS provided coding advice*)
(Reprinted with permission from *Molecular Biology of the Cell* 16(8) (2005))

Abstract

During metaphase in budding yeast mitosis, sister kinetochores are tethered to opposite poles and separated, stretching their intervening chromatin, by singly attached kinetochore microtubules (kMTs). Kinetochore movements are coupled to single microtubule plus-end polymerization/depolymerization at kinetochore attachment sites. Here we use computer modeling to test possible mechanisms controlling chromosome alignment during yeast metaphase by simulating experiments that determine: 1) mean positions of kinetochore Cse4-GFP, 2) the extent of oscillation of kinetochores during metaphase as measured by fluorescence recovery after photobleaching (FRAP) of kinetochore Cse4-GFP, 3) the dynamics of kMTs as measured by FRAP of GFP-tubulin, and 4) mean positions of unreplicated-chromosome kinetochores that lack pulling forces from a sister kinetochore. We rule out a number of possible models and find the best fit between theory and experiment when it is assumed that kinetochores sense both a spatial gradient that suppresses kMT catastrophe near the poles, and attachment site tension that promotes kMT rescue at higher amounts of chromatin stretch.

Introduction

During mitosis a dynamic array of kMTs serves to accurately segregate a duplicated genome into two complete sets of chromosomes [4, 11, 23, 55, 56]. Budding yeast offers an attractive system for answering fundamental questions about the regulation of kMT dynamics, as each kinetochore is believed to be attached to only one kMT plus end [30, 57, 58]. The relative simplicity of the yeast spindle, with

approximately 16 kMT minus ends anchored at each pole, makes this an excellent system for computational modeling. Although the dynamics of individual kMTs have not been directly observed *in vivo*, kMT plus ends appear to exhibit dynamic instability, switching stochastically between extended periods of polymerization and depolymerization [19, 59]. In general, regulation of microtubule (MT) dynamic instability involves control of four parameters – the rates of polymerization and depolymerization, and the frequencies of catastrophe (transition from growing to shortening), and rescue (transition from shortening to growing) events. In budding yeast, kinetochore movement during metaphase is coupled to individual kMT growth and shortening, which likely occurs solely by polymerization and depolymerization at the kinetochore attached kMT plus-ends [59, 60].

Labeling of single centromere proximal markers in yeast indicates that sister centromeres separate towards opposite sides of the spindle during metaphase, and exhibit abrupt transitions in their direction of movement, as would be expected for dynamic instability of kMTs [18, 19, 61, 62]. Fluorescently labeled kinetochores persist in clusters midway between each spindle pole body and the spindle equator during yeast metaphase, and therefore the oscillations of fluorescent probes on chromosome arms suggest that dynamic kMT plus-ends coordinate congression of kinetochores to a steady-state bilobed metaphase configuration in yeast [19, 63].

Green fluorescent protein (GFP) kinetochore fusions, such as Cse4-GFP, allow for live-cell imaging of kinetochores in yeast spindles [19, 64, 65]. In our previous work, a stochastic model of kMT plus-end dynamics in the budding yeast metaphase spindle was developed and then evaluated by simulating images of kinetochore-associated fluorescent probes (Sprague et al., 2003). Although individual kMT dynamics cannot be resolved, computer simulations of kMT dynamics combined with statistical measures of how well the simulation data predicts experimental fluorescence kinetochore distributions recorded by live cell imaging can be used to build an understanding of budding yeast mitotic spindle kMT dynamics [29]. Through this analysis, it was demonstrated that a model based on any set of constant dynamic instability parameters was insufficient to explain how kinetochores tend to cluster midway between the poles and the equator in

yeast metaphase spindles [29]. However, reasonable agreement between simulated and experimental data for the distribution of kinetochores was found using a model with a temporally stable spatial gradient between the spindle poles in either catastrophe or rescue frequency combined with constant values for the other frequency [29]. For example, in the spatial gradient models, higher frequencies of catastrophe in the middle of the spindle relative to the poles promoted kinetochore movement poleward, or higher frequencies of rescue near the poles relative to the middle of the spindle promoted kinetochore movement away from the poles.

It has been proposed for higher eukaryotes that mechanical tension on the kinetochore could modulate MT stability, acting as a key regulator of kMT dynamics [13, 16, 17, 23, 55, 66, 67]. Recent evidence in *Xenopus* extract spindles indicated that mechanical stress regulates MT dynamics locally at the kinetochore-MT attachment site, such that tension between sister kinetochores may promote MT polymerization [15, 68] . In addition, tension between sister kinetochores is important for the stability of kMT attachments and for turning off the spindle checkpoint that regulates anaphase onset in yeast [69]. Due to the significant spacing between sister kinetochores in yeast metaphase (~700 nm), communication between sister kinetochores is likely facilitated via mechnanical tension through the intervening chromatin, as chemical signaling over such a distance would be improbable.

Here we have used computer simulation to explore how mechanical tension at the kinetochore might contribute to metaphase chromosome alignment in budding yeast. First, we established that spatial gradient models similar to those described by Sprague et al. (2003) do not predict the low incidence of kinetochores crossing the equator, as observed experimentally by measurements of fluorescence recovery after photobleaching (FRAP) of the kinetochore-associated protein Cse4-GFP (Pearson et al., 2004). We then tested four various ways that kinetochore tension alone or in combination with catastrophe or rescue gradients between the poles would predict the extent of kinetochore movements as measured by the Cse4-GFP FRAP data. The best fit to the experimental data was achieved by kinetochores sensing a stable gradient between the poles to spatially control kMT plus-end catastrophe frequency, and sensing tension generated via

chromatin stretching between sister kinetochores to control kMT plus-end rescue frequency. This model also quantitatively reproduces metaphase kinetochore distributions and kMT dynamics as measured by GFP-Tubulin FRAP experiments without parameter value adjustment between different experimental data sets. In addition, by eliminating simulated tension between sister kinetochores, the model quantitatively reproduces the kinetochore distribution in yeast mutants (*cdc6*) that enter mitosis with unreplicated chromosomes. In these cells, chromosomes in mitosis have single kinetochores and thus lack the tension generated via chromatin stretching from a sister kinetochore. Kinetochores in *cdc6* mutant spindles achieve average positions up close to the poles, positions not predicted by the rescue gradient model.

All of the simulations were based on the explicit assumptions that: 1) kMT dynamics are at steady-state during metaphase (see Figure A.1 and Supplemental Material), 2) there is one kinetochore attached per MT, 3) MT assembly dynamics occur only at the kinetochore, 4) kinetochores do not detach from MTs during steady-state metaphase, and 5) the kinetochore marker Cse4-GFP closely tracks the plus-end dynamics of kMTs (see Figure A.2 and Supplemental Material). In addition, spindle length was held constant during each simulation, although the exact distribution of experimentally observed spindle lengths was reproduced in both wild-type and *cdc6* simulations, such that spindle length was allowed to vary between each simulation. A number of alternate models were considered and failed to reproduce one or more of the four different experimental results (Table A.1, Supplemental Material). In this way, we show that a model in which the kinetochore regulates kMT dynamics by sensing both distance from its sister kinetochore (via tension) and spindle position relative to the middle of the spindle (via a catastrophe gradient) is able to reproduce experimentally observed kinetochore dynamics and congression in yeast metaphase.

Materials and Methods

Yeast strains and media

The yeast strains used for this study were KBY2125 (MATa *cdc6GAL-CDC6:URA cdc15-2 PDS1 myc:LEU2* pKK1 *cse4::HB SPC29CFPKAN*), KBY2010

(MATa *trp1-63, leu2-1, ura3-52, his3-200, lys2-801 cse4::HYG* pKK1) and KBY2012 (MATa *trp1-63, leu2-1, ura3-52, his3-200, lys2-801 cse4::HYG SPC29-CFP-KAN* pKK1). Fluorescent constructs to generate GFP labeled kinetochores (Cse4-GFP) and CFP labeled centromeres (Spc29-CFP) were previously described [19].

Cell growth techniques and conditions were previously described [29]. However, KBY2125 was grown in galactose media for expression of Cdc6p. Unreplicated chromosomes were generated by arresting an asynchronous culture in S-phase with 200 mM hydroxyurea (HU) for two hours. Cells were then washed into glucose media to repress Cdc6p expression with HU for one hour, released from HU into glucose media, and allowed to complete replication and progress through mitosis. Cells were then allowed to progress into a second mitosis with unreplicated chromosomes. Control cells were created by repeating the S-phase arrest protocol in galactose only to maintain Cdc6p expression.

Fluorescence Microscopy

All cell imaging was performed as previously reported [19, 29].

Simulation of MT dynamics

A Monte Carlo technique was used to simulate individual kMTs undergoing dynamic instability using MATLAB (Version 6.0, The MathWorks, Natick, MA) as previously described [29]. Additional details provided in Supplemental Materials.

Simulation of image formation by fluorescence microscopy

Simulated kinetochore positions were compared to experimentally obtained images of kinetochore-bound fluorescence by simulation of the image formation process in fluorescence microscopy [29]. Briefly, it was assumed that each kinetochore remained attached to the tip of its kMT for the duration of the simulated experiments. At specified time points in each simulated experiment, a simulated fluorescence image of the spindle was generated by convolving the three-dimensional point spread function of the microscope with the kinetochore and spindle pole body position matrices [29].

Simulation of Cse4-GFP and GFP-tubulin FRAP experiments

FRAP experiments were simulated by modeling experimental fluorescence bleaching events and quantifying recovery over time. Detailed simulation methods are described in supplemental materials**.**

Simulation of kinetochore distribution in cdc6 (replication deficient) spindles

As in the simulation of wild-type spindles, the spindle length and relative background noise for each *cdc6* replication deficient experimental image were matched to create a simulated fluorescence image of each mutant spindle. All remaining aspects of the MT dynamics simulations were identical to wild-type cells, with the exception that 8 kMTs were modeled per spindle pole rather than 16 for replicated chromosomes. It was assumed that, on average, the 16 single kinetochores were distributed in equal numbers to each pole.

Results

Model Assumptions

As in previous work [29], we have utilized a simplified model of the yeast metaphase spindle to test mechanisms for the congression of kinetochores to a metaphase configuration. All models considered assumed that kMTs exhibit dynamic instability, as observed in yeast cytoplasmic MTs [70-74] (see Supplemental Material for further review).

In terms of spindle structure, the model was constructed to be consistent with electron micrographs of the yeast spindle [30], where kMT tips were only allowed to grow straight from the spindle pole (i.e. no microtubule curving or splaying was allowed). In addition, any kMT that grew the entire length of the spindle to the opposite pole immediately switched to a shortening state, whereas any kMT that completely shortened to its spindle pole immediately switched to a growth state.

In the simulation, all growth and shortening was assumed to take place at the kMT plus-ends. Minus-end depolymerization (i.e. poleward flux) was not required to

reproduce results in any of the simulations. Rates of kMT polymerization and depolymerization were assumed to be constant over the length of the spindle, and unaffected by force, as suggested by recent measurements in *Xenopus* extract spindles [75].

In all cases, kinetochores were assumed to remain attached to the plus-end tip of the kMT throughout the simulation, an assumption supported by lack of recovery in Cse4-GFP FRAP experiments [51]. In addition, possible lateral interactions between chromosomes and kMTs are ignored in the simple Hookean spring model for tension between sister kinetochores. For example, chromosomes could become transiently associated with interpolar MTs so that the forces on the two kinetochores would not be equal and opposite, as we assumed. In the interest of parsimony, we opted for the simplest possible model that explains all of the data analyzed.

Models without tension-dependent dynamic instability parameters allow equator crossing

To determine the extent of kinetochore equator crossing in yeast metaphase spindles, kinetochore-associated Cse4-GFP fluorescence in one half-spindle was photobleached and spindles observed for 10 minutes. A mean Cse4-GFP recovery percentage of 4.5+/-7.3% (n=9, Figure 3.1D) was observed in 10 minute recovery time experiments [51]. This low level of fluorescence recovery indicates that kinetochores are highly constrained to their respective half-spindle [51]. As cells proceed normally into anaphase following photobleaching of Cse4-GFP, it is not likely that photodamage has affected normal kinetochore dynamics. In addition, FRAP experiments performed using centromere proximal GFP-lacI/lacO markers indicated that these markers were stably oriented to their respective bud or mother cell, supporting a low incidence of kinetochores switching attachment to their respective poles in yeast metaphase spindles (Pearson et al., 2004). Sister centromeres rarely reassociate after separation during metaphase, such that switching from one spindle-half to another would be unlikely [18, 19].

A limitation of this experiment and of yeast spindles in general is that individual kinetochores cannot be directly tracked. For this reason, simulation is extremely helpful

in understanding how the dynamics of individual kinetochores could be regulated to reproduce the low level of fluorescence recovery as observed in the Cse4-GFP FRAP experiments.

KMT dynamics were simulated using models with spatial gradients in catastrophe and rescue frequency for plus-ends as a function of position along the spindle axis [29] (Figure 3.1A). Cse4-GFP FRAP simulations were run for each model using parameter values that were optimized to best reproduce the experimentally observed kinetochore distributions for wild-type metaphase spindles (a constraint not imposed in previous work (Pearson et al, 2004)). Position-dependent models for regulation of kMT plus-end catastrophe frequency (Figure 3.1A) or rescue frequency performed poorly in the Cse4-GFP FRAP simulations (see Table 3.1 and Figure 3.1B,C,D), meaning that these models do not effectively constrain kinetochores to the correct half-spindle (Figure 3.1E). Here, we calculate a "probability of fit" (p-value) to evaluate statistically how well the mean experimental Cse4-GFP fluorescence recovery percentage would fit into a set of fifty mean simulated recovery percentages (n=13, each simulation, see Supplemental Material for detail). Models with calculated p-values less than 0.05 on any single test were considered to be unacceptable, whereas models with $p>.05$ could not be statistically ruled out. In general, both the catastrophe gradient model and the rescue gradient model predict clustering of kinetochores into a bilobed metaphase configuration (peak kinetochore clustering at gold arrows, Figure 3.1A). However, the symmetry of each of these two models does not provide sufficient a directional cue at the kMT plus-end to ensure that kinetochores remain confined to the half-spindle to which they are directly attached. This results in equator-crossing events, as kinetochores tend to cluster on either side of the equator, without regard to their spindle pole body attachment side and without regard to the behavior of their sister kinetochore (Figure 3.1E).

Models including tension-dependent dynamic instability parameters limit equator crossing and reproduce kinetochore Cse4-GFP FRAP experiments

Because both the catastrophe and rescue gradient models failed, we then considered models in which the parameters of kMT plus-end dynamic instability

depended not only on position, but also on tension generated by the stretch of chromatin between sister kinetochores. In this model, sister kinetochores are assigned such that the position of each kinetochore in the spindle has a direct impact on the dynamics of its sister kinetochore in the opposite half-spindle based on the amount of centromere stretch. High tension is proposed to promote rescue and thus kinetochore movement away from the kMT-attached pole, or alternatively low tension is proposed to promote catastrophe and therefore kinetochore movement towards the pole.

Two models which included position-dependent gradients and tension to control catastrophe or rescue frequencies at kMT plus-ends successfully reproduced the lack of Cse4-GFP FRAP observed experimentally (Table 3.1 and Figure 3.2 A-E). Therefore, both of these models effectively control kinetochore dynamics by keeping centromeres in their respective half-spindle (Fig 3.2F), and thus act to minimize fluorescence recovery in the simulated Cse4-FRAP experiment. The reason these models succeed is because as a simulated kinetochore enters the opposite half-spindle during plus-end assembly, it tends to approach its sister kinetochore. This reduces tension, destabilizing the kMT plus-end, so that the kinetochore rapidly returns to its own half-spindle (Figure 3.2F).

Ranges of acceptable parameter values across all wild-type kMT models and experiments are listed in Table 3.2. The ranges of values for growth and shrinking velocities are similar to those measured for cytoplasmic MTs during metaphase, and catastrophe and rescue frequency model values are somewhat higher than values reported for cytoplasmic MTs (see Table 3.2). The "spring constant" determines the magnitude of the tension effect. Although a lower tension effect can be somewhat offset by increasing the gradient in catastrophe frequency, a minimum value for the spring constant (0.8 μm^{-1}) is required in order to impart directionality to the model, thus maintaining kinetochores in the correct half-spindle throughout the simulation. In order to reject a given model, parameter sets were tested and optimized over a wide range of parameters, similar to previous work [29].

Experimental metaphase kinetochore distributions are correctly predicted by models including tension-dependent dynamic instability parameters

To further assess models combining stable spatial gradients in catastrophe or rescue frequency with tension-dependent parameters, simulations of kMT dynamics were run and the plus-end positions recorded at the conclusion of each simulation. These positions were used to generate simulated fluorescence images of kinetochore-bound Cse4-GFP (as in Figure 3.3B,C). Statistical comparison of simulated Cse4-GFP images to the experimentally observed steady-state metaphase kinetochore fluorescence distribution was then used as a computational screen for selection of valid models (See Figure A.1 and Supplemental Material for analysis of steady-state metaphase). The two models where catastrophe and rescue frequency depend on both a spatial gradient and kinetochore tension were successful in predicting the average distribution of kinetochores between the poles at metaphase (Figure 3.3A-D, Table A.1). Spatial gradient models with no tension-dependent parameters qualitatively reproduced experimentally observed metaphase kinetochore clustering, but resulted in low calculated p-values (Table A.1). By quantitatively analyzing experimental spindle images to include steady-state metaphase spindles only (see Supplemental Material), models for regulation of kMT dynamics are more tightly constrained as compared to our previous work (Sprague et al, 2003).

Kinetochore distributions in metaphase spindles lacking tension are correctly predicted by the catastrophe gradient with tension-dependent rescue model

To test the hypothesis that tension between sister kinetochores regulates kMT dynamics in yeast, we performed experiments using a replication deficient *cdc6* mutant that is incapable of developing tension between sister kinetochores (Stern and Murray, 2001). Here, chromosomes in mitosis have single kinetochores and lack the tension generated via chromatin stretching from a sister kinetochore.

Kinetochore positions at metaphase in *cdc6* mutants were quantified using the Cse4-GFP fluorescence distribution (n=27 cells, 54 spindle halves). The *cdc6* mutant cells generally had spindles with kinetochore clusters very near to each spindle pole body, as shown in Figure 3.5B. The peak in mean kinetochore-associated fluorescence relative to the pole was ~ 0.21 μm in *cdc6* mutants, as compared to ~0.39 μm in control

metaphase cells, a ~46% reduction in mean kMT length. These experimental results indicate that kMT dynamics are altered in spindles lacking tension between sister kinetochores, resulting in net shortening of average kMT lengths.

Prior to simulation of the *cdc6* mutant data, parameter value sets for each model to be tested were adjusted to reproduce the Cse4-GFP fluorescence distribution for *GALCDC6* control cells grown in galactose media (with replication) and arrested in HU ($p>0.10$). Specifically, V_g and V_s were reduced by ~15% in all models as compared to previous yeast strain simulations, although values remained well within the range of values given in Table 3.1. Tension-dependent catastrophe and tension-dependent rescue models were then used to simulate kinetochore movements in the *cdc6* mutants by reducing the spring constant in each model to zero (Figure 3.4A,B). This reduction effectively eliminated any tension effect on kMT dynamics. A catastrophe frequency gradient together with a tension-dependent rescue frequency model modified such that the chromatin "spring constant" was reduced to zero was successful in quantitatively reproducing the kinetochore distribution in tension deficient spindles ($p=0.11$, Figure 3.4A,D,F). In contrast, a model based on a position-dependent rescue gradient with the spring constant for a tension-based catastrophe frequency model reduced to zero performed very poorly in predicting kinetochore positions in *cdc6* mutants ($p<<0.01$, Figure 3.4B,E.F). The position-dependent rescue gradient model relies on a high rescue frequency at the poles, which decreases towards the spindle equator. This tends to push kinetochore clusters towards the equator, such that rescue gradient models are ineffective in reproducing kinetochore clusters very near to the poles, as was experimentally observed in the *cdc6* mutant phenotype. These results argue against a spatial rescue gradient model for regulation of budding yeast kMT dynamics during metaphase.

Thus, a model where the kinetochore senses spindle position to regulate kMT plus-end catastrophe frequency, and senses tension generated from the stretch of chromatin between sister kinetochores to regulate kMT plus-end rescue frequency was the single model that was able to reproduce all experimental results (see Table A.1 and Supplemental Material for further details).

GFP-Tub1 FRAP experiments are correctly predicted by simulated kMT dynamics

The final step in our analysis was to ask how well simulated kinetochore dynamics predict metaphase kMT dynamics. GFP-Tub1 FRAP experiments were simulated using the parameter value sets as defined above (Table 3.1) and then compared to published results [59]. Interpolar MTs were assumed to be stable and non-dynamic in the simulation, such that all recovery was the result of kMT plus-end dynamics, as in Figure 3.2F. GFP-Tub1 recovery profiles for simulated kMT dynamics qualitatively and quantitatively reproduced experimental results (Figure 3.5) for the parameter values of dynamic instability listed in Table 3.1. The average experimental time to half-maximal recovery was 52±24 seconds (n=6, [59]), as compared to a simulated half-maximal recovery time of 53±15 seconds (n=6). Growth and shortening velocities were highly constrained in simulations of the GFP-Tub1 FRAP data. Rapid velocities (>2 μm/min) generally resulted in faster MT turnover than is experimentally observed.

Discussion

The extent of kinetochore oscillation is limited in models with kMT plus-end dynamic instability regulated by tension, thus reproducing Cse4-GFP FRAP results

Regulation of kMT dynamics in a local tension-dependent manner results in a "self-correcting" system, in which the range of chromatin stretching, and therefore the mean sister kinetochore separation distances, are tightly controlled. In a model where catastrophe is regulated by a spatial gradient and rescue is regulated by tension between sister kinetochores, kMT lengths will tend to be most stable at moderate tension values (Figure 3.6A and Figure 3.2A, gold arrows), away from the high catastrophe zone at the spindle equator. In this way, congression of kinetochores to a metaphase configuration can be accurately reproduced regardless of the initial positions of the MT attached kinetochores, as shown in Figure 3.6B.

Tension-based control of kMT dynamics is particularly efficient in limiting excursions of kMTs across the spindle equator. As Cse4-GFP protein is stably bound to the kinetochore during metaphase [51], recovery of bleached Cse4-GFP in FRAP experiments results exclusively from unbleached kinetochores shifting from the

unbleached half-spindle to the bleached half-spindle after the bleach event. Lack of any significant recovery in Cse4-GFP FRAP experiments implies that kinetochores in metaphase spindles remain constrained to the half-spindle in which their kMT is anchored. This half-spindle fidelity is reproduced effectively in models where the kinetochore senses tension developed from chromatin stretch to regulate kMT plus-end dynamics (Figure 3.2). As a kMT grows across the spindle equator, its attached kinetochore moves closer to its sister, reducing tension (Fig 3.6A(1)). After a catastrophe event near the spindle equator, low tension ensures that the kMT will undergo steady depolymerization to return the kinetochore to its correct half-spindle. This tension-dependent rescue effect is consistent with studies on animal cell kinetochores [16, 67] and with experimental fluorescence speckle microscopy experiments by Maddox et al. (2003), in which *Xenopus* extract MTs switched from polymerization to depolymerization when there was loss of tension at the kinetochore. Modeling of the Cse4-GFP FRAP experiment indicates that recovery is highly sensitive to even a small percentage of MT plus-ends growing across the spindle equator, as significant recoveries (~14%) were predicted in simulations using a position-dependent catastrophe gradient model (no tension-based regulation), in which ~3 kMTs (out of 32 total) were present in the wrong half-spindle at any given time during the simulation. Accurate replication of GFP-Tub1 FRAP experiments indicates that simulated kMT dynamics approximate the kMT turnover in yeast metaphase spindles, such that although kinetochores rarely cross the equator, they remain dynamic, oscillating back and forth between the spindle equator and their attached pole (Figure 3.2E).

Lack of tension at the kinetochore in cdc6 mutants results in net kMT depolymerization, both experimentally and in simulation

The model with a spatial gradient in kMT plus-end catastrophe frequency and with kMT plus-end rescue frequency dependent on tension at the kinetochore provided an excellent fit to the *cdc6* mutant experimental data, where lack of tension results in clustering of kinetochore-associated fluorescence very near to each spindle pole body (Figure 3.6C). In this model, loss of tension at the kinetochore significantly reduces

overall kMT rescue frequency, allowing kinetochores to move on average closer to the spindle pole bodies (Figure 3.4). Peak catastrophe frequencies increase at the equator as a natural consequence of increasing spindle length in the spatial catastrophe gradient model.

A model based on a spatial rescue gradient with catastrophe frequency at the kMT plus-end dependent on the stretch on chromatin between sister kinetochores performed very poorly in reproducing tension-deficient *cdc6* mutants (Figure 3.4E,F). In this model, rescue frequencies are high at the poles, and decrease with distance from each pole, similar to polar ejection forces in vertebrate spindles. A high rescue frequency at the spindle pole moves simulated kinetochore clusters in tension-deficient spindles towards the equator, thus failing to reproduce the experimentally observed average kinetochore positions for *cdc6* mutants. In the above assays, we have identified a model where kinetochores sense both a stable gradient between the poles to control kMT plus-end catastrophe frequency, and tension developed from chromatin stretch to control kMT plus-end rescue frequency. This is the best model, as it successfully reproduces all four simulated experiments with an overall probability of $p>0.10$.

Implications of tension-dependent kMT plus-end dynamic instability for budding yeast mitosis

Tension-based regulation of kMT dynamics provides a mechanism for kinetochores under high tension to relieve this tension by switching from poleward movement (which builds tension) to an away from pole movement (which relieves tension)(Figure 3.6A(3)) [15]. Without a means to relieve tension, kinetochores could possibly detach from kMTs due to high mechanical stress on the MT-kinetochore attachment [15, 16, 67]. If not resolved before anaphase, such detachments would lead to aneuploidy.

Low tension at the kinetochore may have critical consequences for the fidelity of chromosome segregation as well. Spindle assembly checkpoint signaling requires tension between sister kinetochores [76-81] , and low tension could act to destabilize attachment of MTs to kinetochores [69, 80, 82].

Thus a model where the kinetochore senses both spindle position to regulate kMT plus-end catastrophe frequency and tension generated via chromatin stretch to regulate kMT plus-end rescue frequency has the overall effect of limiting the range of tensions experienced at the kinetochore as compared to a model with position-dependent switching frequencies only. Limiting the range of tensions to intermediate levels (as in Figure 3.6A(2)) may help the spindle avoid MT detachment by reducing high forces on the kinetochore, and allow the checkpoint to be turned off by limiting low tension. The net result is that both high and low tension on kinetochores are unfavorable, resulting in a congressed state of approximately uniform separation distance between sister kinetochores.

In contrast to Cdc6p-depleted spindles, in which kinetochore localization near the poles suggests that lack of tension results in net depolymerization of kMTs, loss of tension and kMT attachment in *ndc10* kinetochore mutants does not result in significant MT depolymerization [60]. Therefore, it may be that the kinetochore itself acts to depolymerize kMTs via a catastrophe gradient, an effect which could be antagonized by tension. Loss of attachment could thus allow for net polymerization of MTs, as is observed for interpolar MTs.

A mechanism for tension-dependent regulation of kMT dynamics

Our analysis shows that tension promotes kMT assembly by increasing rescue. What could be a mechanism by which tension promotes rescue? One possibility for tension dependent regulation of kMT dynamics is a purely physical effect mediated by the kinetochore. For example, recent work with the purified components of the Dam1p/DASH complex shows that the complex forms rings around microtubules *in vitro* [83, 84]. This type of structure could form a sleeve that surrounds the kMT tip and links to other kinetochore components (reviewed by [85]), although the existence of rings *in vivo* remains an open question [86]. As shown schematically in Figure 3.7A, the kinetochore-associated sleeve could move towards the kMT minus end during depolymerization via protofilament splaying and peeling. As a kinetochore moves away from its sister, tension will build in the intervening chromatin (green spring), and in the

kinetochore itself (blue spring), advancing the sleeve toward the kMT plus end. This would in turn force kMT protofilaments to straighten (Figure 3.7B). The straightening of protofilaments could suppress tubulin departures from the kMT tip, and thereby promote rescue (Figure 3.7C).

What would be the force required to promote rescue? The answer hinges on how much energy is required to straighten a curled GDP-tubulin dimer. Previous analyses estimate the mechanical energy stored in the lattice upon GTP hydrolysis to be about 2.1-2.5 k_BT [87, 88]. This amount of energy is equal to ~10 pN-nm, so that the force required to straighten one GDP dimer of length 8 nm would be F=10 pN-nm/8 nm=1.25 pN. Since there are 13 protofilaments, there would a requirement of F_{total}=13 X 1.25 pN = 16 pN. Is this characteristic force plausible? Previous analysis of chromatin stretching in budding yeast metaphase showed that the centromere proximal chromatin is highly stretched, to the point where individual nucleosomes are almost certainly forced off the chromatin [19]. Studies with laser tweezers in vitro show that ~15-20 pN is required to force nucleosomes off of double-stranded DNA [89]. Thus the typical tension generated via chromatin stretch during yeast metaphase is approximately equal to that estimated as necessary for kMT protofilament straightening.

Models lacking a spatial gradient in catastrophe frequency result in loss of sister kinetochore separation at metaphase

The catastrophe frequency gradient shown in Figure 3.2A is an essential model element. In a model that includes a spatial gradient in catastrophe frequency, kMT plus-ends experience a peak in catastrophe frequency at the spindle equator. This has the effect of destabilizing kMT plus-ends located at the spindle equator, such that kinetochores tend to cluster on either side of the equator in a bilobed metaphase configuration.

A model in which kinetochores sense both a spatial gradient in catastrophe frequency and attachment site tension to promote rescue results in specific predictions for spindles with a reduced catastrophe gradient, as might be observed in mutants depleted of a theoretical catastrophe gradient mediator molecule (Figure 3.6D). In simulations with

the catastrophe gradient modified such that the peak catastrophe frequency at the equator is 3-fold less than in wild-type simulations while catastrophe frequency at the poles remains unchanged, metaphase kinetochore clusters collapse into a single focused cluster that stochastically moves between spindle halves and transiently separates into closely spaced separated clusters (representative simulated image, Figure 3.6D).

What could be the origin of a position-dependent catastrophe gradient? A spatially segregated antagonistic kinase/phosphatase pair could establish a stable gradient in phospho-state of a regulatory substrate [29, 90]. If the substrate is capable of promoting kMT catastrophe in a manner dependent on its phosphorylation state, then there will be a position-dependent castastrophe gradient over the length of the spindle. In yeast, Stu2p acts at kMT plus-ends to promote dynamics [60, 72, 91], and may be required to promote transient sister chromatid separation [92]. Given that Stu2p is known to affect kMT dynamics, it seems to be a likely candidate for the gradient, although it is not clear how phosphorylation might be involved. Another possibility is Gsp1 (Ran), which could modulate kMT dynamics via a gradient of Ran-GTP, an MT stabilizer [93]. Other microtubule-associated proteins implicated in regulating MT dynamics, such as Kip3p (an MT depolymerase), Kar3p, Cin8p, or Dam1p could mediate a gradient in kMT plus-end catastrophe as well.

In conclusion, by using computer simulations that account for both presumed kMT dynamics and the imaging of those dynamics, a method we call "model-convolution", we have identified a model for kMT dynamics in the yeast metaphase spindle. Certainly the mitotic spindle is complex, but our analysis shows that a number of simple models, and even some relatively sophisticated models, ultimately fail to describe the observed behavior. Through a process of continual model scrutiny via integrated modeling and experiment we expect that alternative plausible scenarios of similar complexity can be tested and key experimental predictions made (e.g. as with Cse4-GFP distribution in the cdc6 mutant). As individual kMT dynamics have not been resolved in live cells, the ability to simulate kinetochore dynamics in wild-type and genetically manipulated spindles will provide a useful tool for future studies aimed at understanding the complex mechanisms underlying mitosis.

Acknowledgements

I would like to thank Bodo Stern and Andrew Murray for providing the *cdc6* strain. Thanks also to Mark Winey for providing yeast microscopy data and for helpful suggestions on the manuscript. Funding provided by National Science Foundation Career Award to DJO (BES 9984955), National Institutes of Health grant (GM24364) to EDS, and National Institutes of Health grant (GM32238) to KSB.

Tables and Figures

TABLE 3.1. Cse4-GFP FRAP Simulation Results

Model Description	Simulated Mean Cse4-GFP Recovery Percentage[a]	Probability of Fit to Experimental Results (p-value)[b]
(Experimental Results)	4.5±7.3 % [c]	---
Position-dependent regulation of kMT Catastrophe Frequency[a]	13.8 ±2.5 %	p<0.02
Position-dependent regulation of kMT Rescue Frequency[a]	19.2 ± 10.1%	p<<0.02
Position-dependent Catastrophe + Tension-dependent Rescue[a]	6.5 ±1.7 %	p=0.24
Position-dependent Rescue + Tension-dependent Catastrophe[a]	8.3 ±2.0 %	p=0.05

[a]All mean recovery percentages are reported for model parameter sets that are optimized to qualitatively reproduce steady-state Cse4-GFP kinetochore clustering in yeast metaphase spindles

[b]The probability of fit (p-value) was calculated through comparison of experimental mean recovery values to the range of simulated recovery values over 50 experiments (see Supplemental Material for calculation detail). The 10 minute time point data was used for comparison to simulation, as the simulation was allowed to run for a simulated recovery time of 10 minutes prior to evaluation of simulated recovery.

[c]Experimental results reported for 10 minute recovery times (n=9) (Pearson et al., 2004).

TABLE 3.2. Wild-type model parameter value ranges and constraints

Parameter Description	Symbol	Range of Acceptable Values (All Wild-type Models)
Growth Velocity	V_g	1.0 - 2.0 μm/min[a]
Shortening Velocity	V_s	1.0 – 2.0 μm/min[b]
Spring Constant[c]	ρ^*	0.8 – 1.5 μm^{-1}
Catastrophe Frequency	k_c	0.25-35 min^{-1}[d]
Rescue Frequency	k_r	2.0-25 min^{-1}[e]

[a]Cytoplasmic MT measurements, V_g =0.5μm/min [70]
[b]Cytoplasmic MT measurements, V_s =1.35μm/min [70]
[c]Applies to models with tension-dependent switching frequencies only.
[d]Longer *cdc6* mutant spindles result in a higher calculated catastrophe frequency at the spindle
equator, as shown in Fig. 3.6A. Cytoplasmic MT measurements, k_c=0.12 min^{-1}; [70]
[e]Cytoplasmic MT measurements, k_r=0.36 min^{-1} [70]

FIGURE 3.1. Position-dependent gradient models for the regulation of kMT dynamics fail to reproduce Cse4-GFP FRAP experimental results. (A) The catastrophe gradient model: kMT plus-end catastrophe frequency peaks at the spindle equator, while plus-end rescue frequency remains constant. (B) Representative simulated image prior to the bleach event using the catastrophe gradient model (kinetochore-associated Cse4-GFP, green; Spindle pole body-associated Spc29-CFP, red). (C) Significant fluorescence recovery of kinetochore-associated Cse4-GFP fluorescence using the spatial catastrophe gradient model does not reproduce experimental results. (D) Representative Cse4-GFP FRAP experimental and simulated time series of fluorescence recovery. Kinetochore-associated markers in one half-spindle were bleached and then observed over time in order to quantify fluorescence recovery. As Cse4-GFP is stably bound at the kinetochore, fluorescence recovery results exclusively from redistribution of kinetochores between spindle halves. The lack of recovery observed experimentally indicates that kinetochores remain constrained to their own half-spindle throughout the experiment. Models with position-dependent catastrophe frequencies only (i.e. no tension dependence) do not limit spindle-equator crossing sufficiently to reproduce experimental results. (E) Typical simulated plus-end kMT positions at steady-state using the spatial catastrophe gradient model for regulation of MT dynamics. The representative trace shows a pair of sister kMT plus ends and their movements relative to the spindle poles and the equator. Although individual kinetochores separate and oscillate on either side of the spindle equator, kinetochores frequently move into the opposite half-spindle for extended periods of time.

Figure 3.1

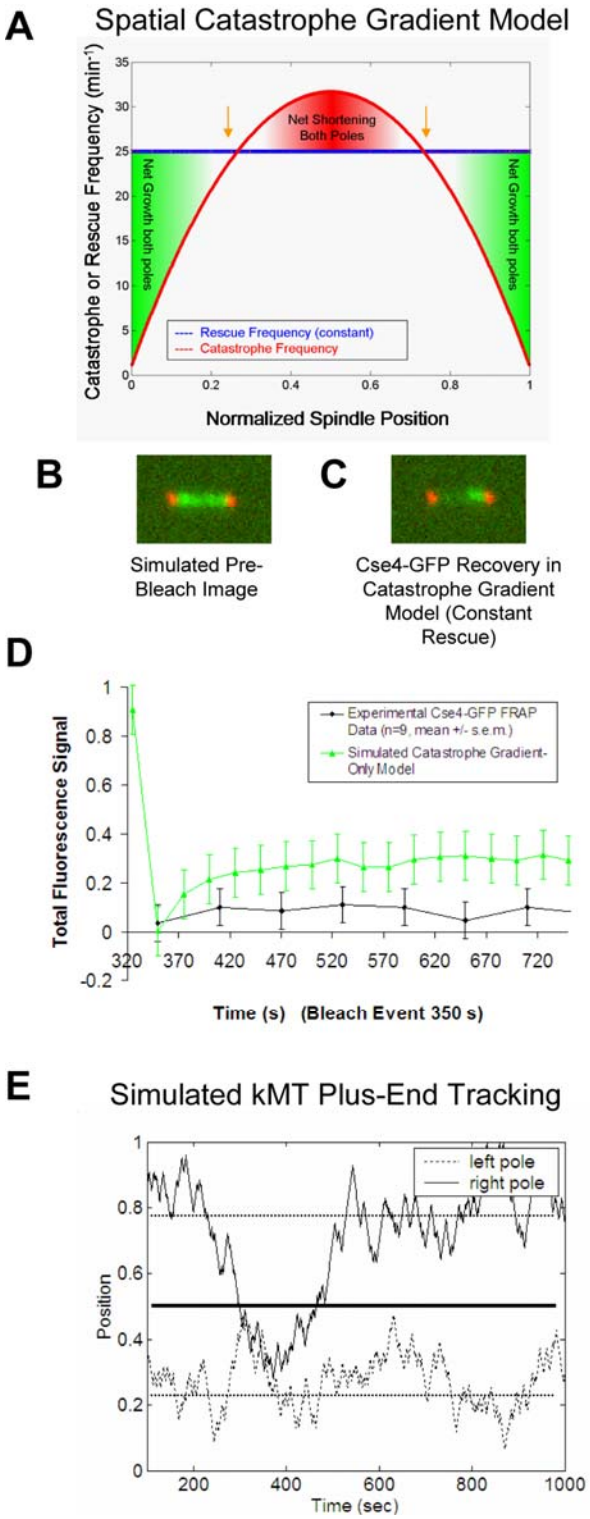
A
Spatial Catastrophe Gradient Model
Catastrophe or Rescue Frequency (min-1)
Net Shortening Both Poles
Net Growth both poles
Net Growth both poles
Rescue Frequency (constant)
Catastrophe Frequency
Normalized Spindle Position
B
Simulated Pre-Bleach Image
C
Cse4-GFP Recovery in Catastrophe Gradient Model (Constant Rescue)
D
Total Fluorescence Signal
Experimental Cse4-GFP FRAP Data (n=9, mean +/- s.e.m.)
Simulated Catastrophe Gradient-Only Model
Time (s) (Bleach Event 350 s)
E
Simulated kMT Plus-End Tracking
left pole
right pole
Position
Time (sec)

FIGURE 3.2. Models where kinetochores sense both spindle position and tension due to chromatin stretch successfully reproduce Cse4-GFP FRAP experimental results. Excursions of kMT plus-ends into the opposite spindle half are limited, and therefore these models quantitatively reproduce Cse4-GFP FRAP experimental results. (A) The spatial model for regulation of kMT plus-end catastrophe frequency with kMT rescue frequency regulated by tension generated via chromatin stretch between separated sister kinetochores: rescue frequencies shown are mean values calculated for a given spindle position during the simulation, as rescue frequency is directly dependent on the sister kinetochore separation distance. Dependence of kMT plus-end rescue frequency on tension between sister kinetochores is directional, such that mean rescue frequencies tend to decrease as kMTs lengthen, due to decreased separation between sister kinetochores. For this distribution, Vg=Vs=2.0 μm/min, and the spring constant ρ^{*}=0.9 μm^{-1}. Gold arrows correspond to the spindle locations of predicted peaks in kinetochore-associated Cse4-GFP fluorescence. (B) The spatial model for regulation of kMT plus-end rescue frequency with kMT catastrophe frequency regulated by tension between sister kinetochores. (C) Representative simulated images for the Cse4-GFP FRAP experiment using a model where the kinetochore senses spindle position to regulate kMT plus-end catastrophe frequency, and senses tension generated via chromatin stretch to regulate kMT plus-end rescue frequency. For the model shown in (A), there is negligible visible recovery in Cse4-FRAP experiment simulations, reproducing experimental results. (D) Simulated Cse4-GFP FRAP images for the model shown in (B). (E) Representative Cse4-GFP FRAP experimental and simulated time series of fluorescence recovery. Models that include regulation of kMT plus-end switching frequencies based on tension between sister kinetochores reproduce experimental results (F) Typical simulated plus-end kMT positions at steady-state for the models shown in (A) and (B). Here, equator crossing is limited, as kMT plus-ends are less likely to experience rescue events as kinetochores move closer to their sisters. Kinetochores rarely cross the equator, but remain dynamic, moving towards the spindle equator and back to the poles.

Figure 3.2

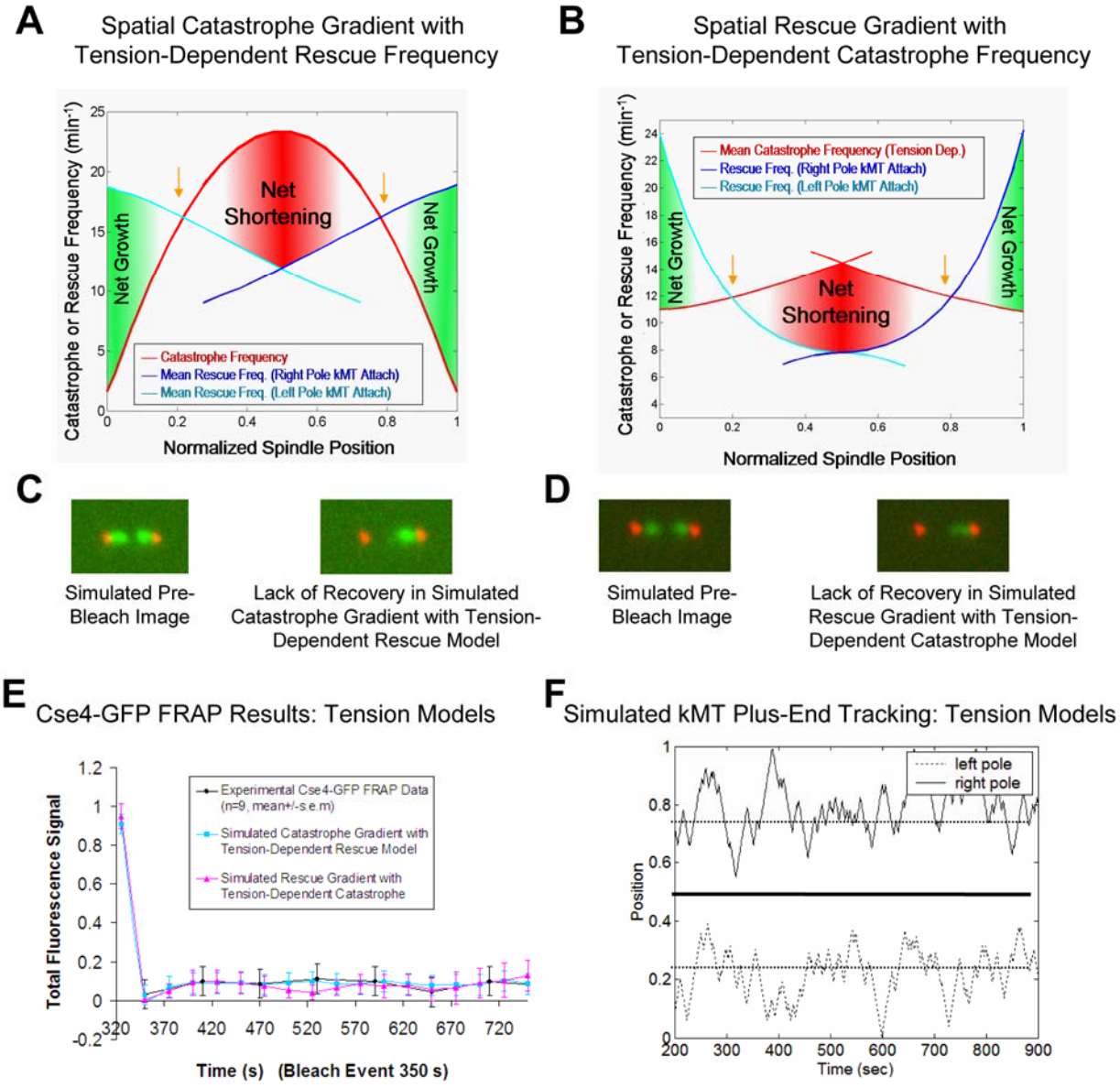
A
Spatial Catastrophe Gradient with Tension-Dependent Rescue Frequency
Net Growth
Net Shortening
Net Growth
Catastrophe Frequency
Mean Rescue Freq. (Right Pole kMT Attach)
Mean Rescue Freq. (Left Pole kMT Attach)
Catastrophe or Rescue Frequency (min-1)
Normalized Spindle Position
B
Spatial Rescue Gradient with Tension-Dependent Catastrophe Frequency
Mean Catastrophe Frequency (Tension Dep.)
Rescue Freq. (Right Pole kMT Attach)
Rescue Freq. (Left Pole kMT Attach)
Net Growth
Net Shortening
Net Growth
Catastrophe or Rescue Frequency (min-1)
Normalized Spindle Position
C
Simulated Pre-Bleach Image
Lack of Recovery in Simulated Catastrophe Gradient with Tension-Dependent Rescue Model
D
Simulated Pre-Bleach Image
Lack of Recovery in Simulated Rescue Gradient with Tension-Dependent Catastrophe Model
E
Cse4-GFP FRAP Results: Tension Models
Experimental Cse4-GFP FRAP Data (n=9, mean+/-s.e.m)
Simulated Catastrophe Gradient with Tension-Dependent Rescue Model
Simulated Rescue Gradient with Tension-Dependent Catastrophe
Total Fluorescence Signal
Time (s) (Bleach Event 350 s)
F
Simulated kMT Plus-End Tracking: Tension Models
left pole
right pole
Position
Time (sec)

FIGURE 3.3. The models reproduce experimental metaphase kinetochore clustering. (A) Experimental metaphase spindle image of Cse4-GFP labeled kinetochores (green) relative to Spc29-CFP labeled spindle poles (red). (B) A representative simulated image using the model as shown in 2A. Tight kinetochore-associated fluorescence clusters are comparable to the experimental image. Scale bar, 1000 nm. (C) A representative simulated image using the model as shown in 2B. (C) Quantitative analysis of average simulated kinetochore clustering observed via Cse4-GFP with comparison to mean experimental results. Simulation results reproduce experimental results for both the model shown in 2A and in 2B.

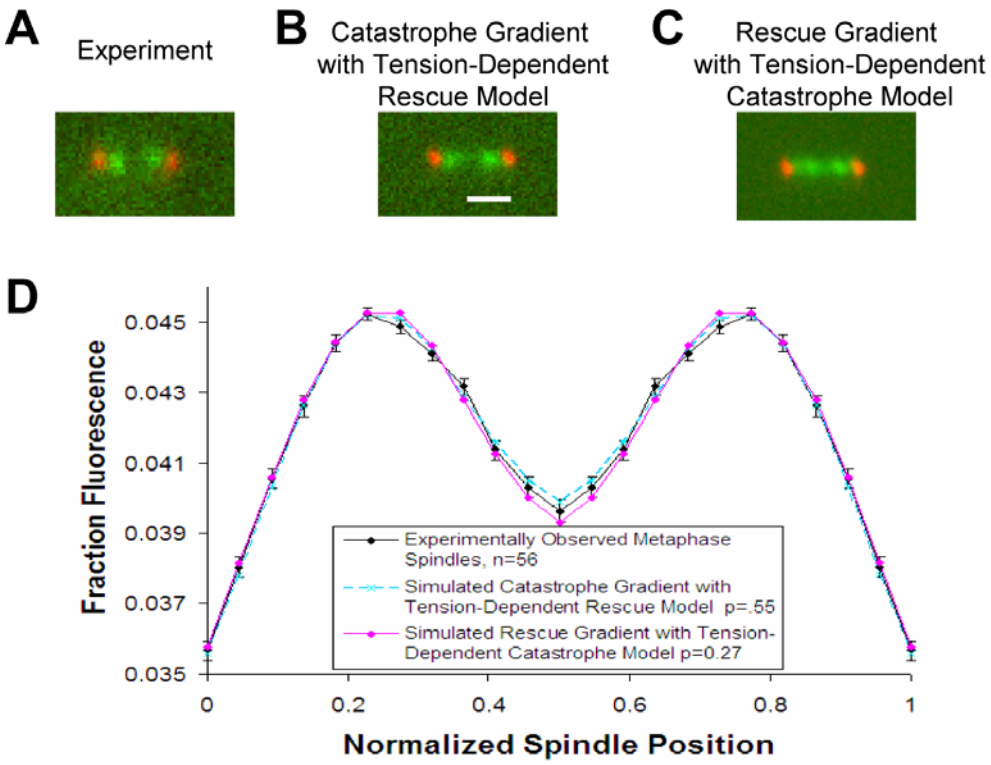

FIGURE 3.4. Experimental measurement and simulation of kinetochore-associated fluorescence in cdc6 mutant cells. (A) In a model where kinetochores regulate kMT plus-end rescue frequency by sensing tension generated through the stretch of chromatin between sister kinetochores, *cdc6* mutant cells with single-kinetochore chromatin can be modeled by reducing the tension "spring constant" to zero and increasing simulated spindle lengths to match experimentally observed values. Gold arrows indicate the locations of predicted peaks in kinetochore-associated fluorescence. For this distribution, Vg=Vs=1.7 μm/min, and the spring constant ρ^{*}=0 μm^{-1}. (B) The tension "spring constant" is reduced to zero in a model where the kinetochores regulate kMT plus-end catastrophe frequency by sensing tension generated via the stretch of chromatin between sister kinetochores. (C) The experimental effect of loss of tension in Cdc6p depleted cells. Kinetochores (Cse4-GFP, green) are clustered near the poles (Spc29-CFP, red), indicating that the net kMT length is shorter in the mutant spindles as compared to wild-type cells. (D) Simulated effect of loss of tension between sister kinetochores using a model where rescue frequency is regulated by tension. Kinetochores are clustered very near to the poles, qualitatively and quantitatively reproducing experimental observations of *cdc6* mutant cells. Scale bar, 1000 nm. (E) Simulated effect of loss of tension using a model where catastrophe frequency is regulated by tension at the kinetochore. (F) Quantitative analysis of simulated kinetochore clustering with comparison to experimental fluorescence distribution in tension-deficient spindles. Models with increased spindle length but without tension loss do not reproduce experimental results ($p<.01$). In addition, the rescue gradient model with tension dependent catastrophe frequency fails to reproduce experimental results ($p<.01$).

Figure 3.4

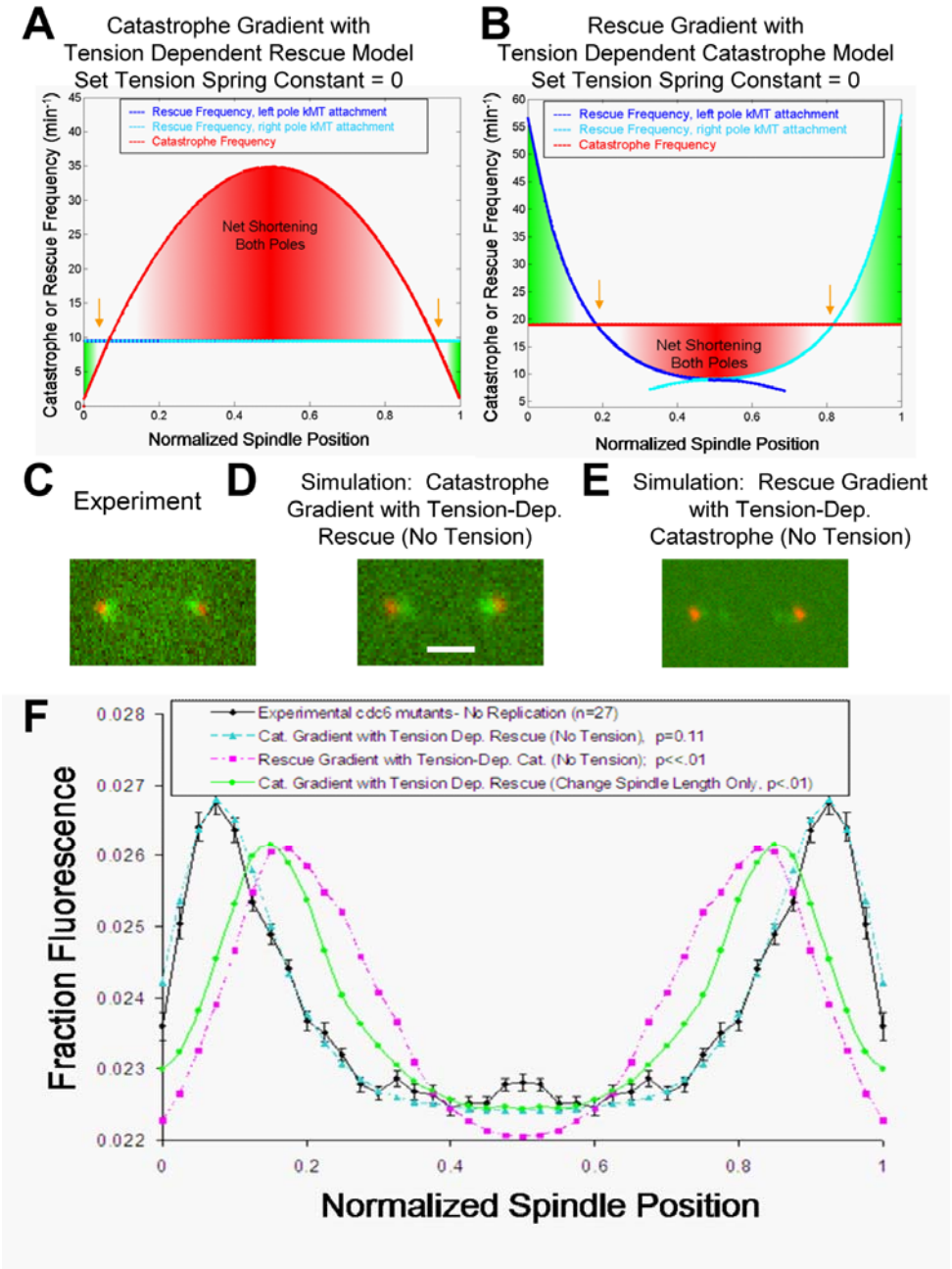
A
Catastrophe Gradient with Tension Dependent Rescue Model Set Tension Spring Constant = 0
Rescue Frequency, left pole kMT attachment
Rescue Frequency, right pole kMT attachment
Catastrophe Frequency
Net Shortening Both Poles
Catastrophe or Rescue Frequency (min-1)
Normalized Spindle Position
B
Rescue Gradient with Tension Dependent Catastrophe Model Set Tension Spring Constant = 0
Rescue Frequency, left pole kMT attachment
Rescue Frequency, right pole kMT attachment
Catastrophe Frequency
Net Shortening Both Poles
Catastrophe or Rescue Frequency (min-1)
Normalized Spindle Position
C
Experiment
D
Simulation: Catastrophe Gradient with Tension-Dep. Rescue (No Tension)
E
Simulation: Rescue Gradient with Tension-Dep. Catastrophe (No Tension)
F
Experimental cdc6 mutants- No Replication (n=27)
Cat. Gradient with Tension Dep. Rescue (No Tension), p=0.11
Rescue Gradient with Tension-Dep. Cat. (No Tension); p<<.01
Cat. Gradient with Tension Dep. Rescue (Change Spindle Length Only, p<.01)
Fraction Fluorescence
Normalized Spindle Position

FIGURE 3.5. Simulation of GFP-Tub1 FRAP experiments. Experimentally, GFP-Tub1 labeled spindles are imaged, and half-spindles are photobleached at time t=0 [59]. FRAP of the bleached half-spindle and loss-of-fluorescence in the unbleached half-spindle are quantified experimentally and in simulations. Simulated results are compared to live cell experimental data from Maddox et al. (2000). For the simulation results shown, Vg=Vs=2.0 μm/min, and the spring constant ρ^{*}=0.9 μm^{-1}. Catastrophe and rescue frequency are modeled as shown in Figure 2A. GFP-Tub1 recovery profiles for simulated kMT dynamics qualitatively and quantitatively reproduce experimental results (p=0.96). The average experimental time to half-maximal recovery was 52±24 seconds (n=6, [59]), as compared to a simulated half-maximal recovery time of 53±15 seconds (n=6).

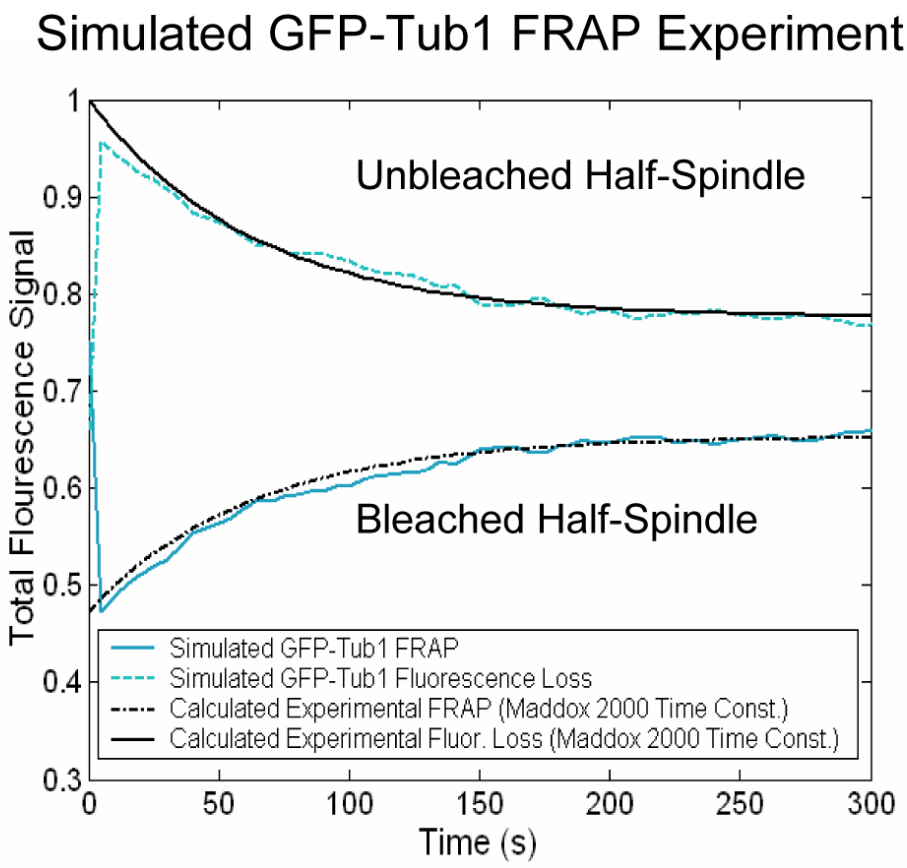

FIGURE 3.6. Model for metaphase congression in budding yeast. For clarity, the right kinetochore is fixed at its mean position, while the left kinetochore moves, although both kinetochores are dynamic in simulation, each affecting the relative tension experienced by its assigned sister. Kinetochores are green, spindle pole bodies red, kMTs blue, and the cohesin/chromatin "spring" is gray. Gold arrows indicate spindle locations of predicted peaks in kinetochore-associated fluorescence. (A1) The left kinetochore is near to the spindle equator, under low tension, resulting in a high catastrophe and low rescue frequency for the kMT plus-end originating from the left pole. This biases the left kMT plus-end towards net depolymerization. (A2) The left kinetochore in the quarter spindle area with "proper" sister separation and moderate tension has equal probabilities of catastrophe and rescue at the left kMT plus-end. Therefore, the left kMT is not biased towards either growing or shrinking. (A3) The left kinetochore is near the left kMT spindle pole body and under high tension, resulting in a low catastrophe and high rescue frequency at the kMT plus-end. This biases the left kMT plus-end towards net polymerization. (B) Simulation of congression: from an initially random distribution of kinetochore localization at the initiation of the simulation (t=0), the simulation results in alignment of kinetochores into a metaphase configuration within a few minutes. (C) Simulation of anaphase via loss of tension: after normal metaphase alignment, a sudden loss of tension results in simulated kinetochore movement to average positions close to the spindle poles. This is observed experimentally for Cdc6p depleted cells, and during anaphase A [19, 94, 95]. Simulated spindle lengths were increased to match experimentally observed Cdc6p depleted spindles. (D) A representative simulated image in which a theoretical catastrophe gradient mediator molecule is depleted (Scale bar, 1000 nm). A 3-fold decrease in peak catastrophe frequency at the equator results in one focused cluster of kinetochore-associated fluorescence which stochastically moves from one spindle half to another, and transiently separates into two closely spaced clusters. Thus, a gradient in catastrophe frequency drives the separation of sister kinetochores to generate chromatin stretch.

Figure 3.6

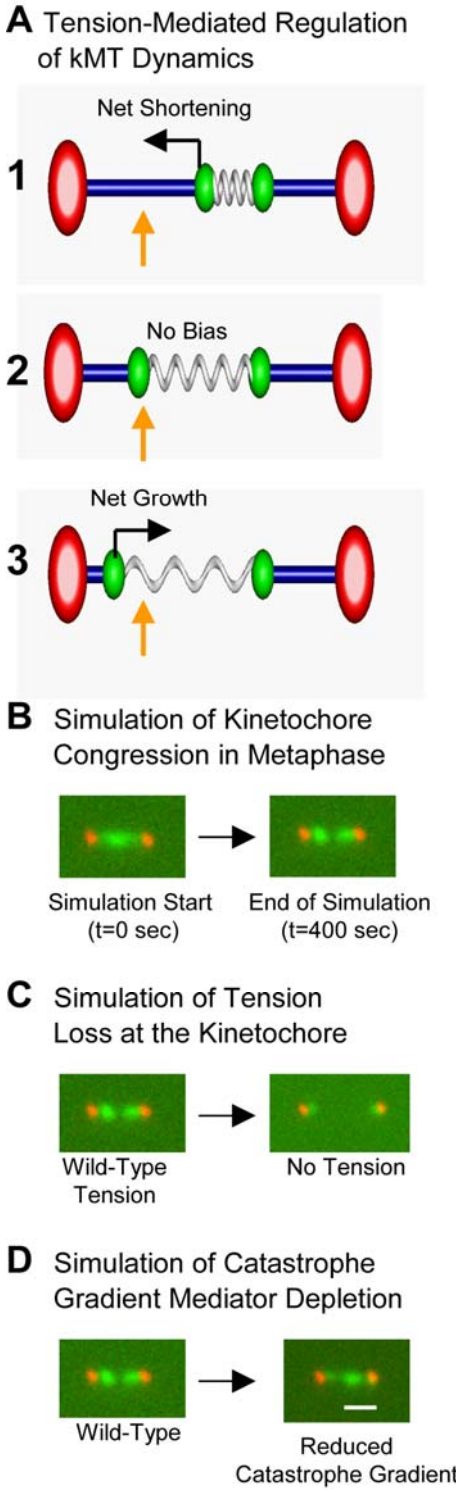
A Tension-Mediated Regulation of kMT Dynamics
Net Shortening
1
No Bias
2
Net Growth
3
B Simulation of Kinetochore Congression in Metaphase
Simulation Start (t=0 sec)
End of Simulation (t=400 sec)
C Simulation of Tension Loss at the Kinetochore
Wild-Type Tension
No Tension
D Simulation of Catastrophe Gradient Mediator Depletion
Wild-Type
Reduced Catastrophe Gradient

FIGURE 3.7. A speculative mechanism for tension-dependent rescue. (A) In this hypothetical mechanism, the kinetochore sleeve (possibly formed via the Dam1/DASH complex) is pushed toward the kMT minus end via protofilament splaying during depolymerization. Simultaneous depolymerization at the sister kMT plus end (not shown) tends to build tension, stretching the kinetochore (blue spring) and the chromatin (green spring). (B) As tension builds, the sleeve is pulled toward the kMT plus end to limit protofilament splay. (C) Protofilament straightening stabilizes the tip against further depolymerization, and so promotes rescue. The stabilized tip rescues and starts to polymerize.

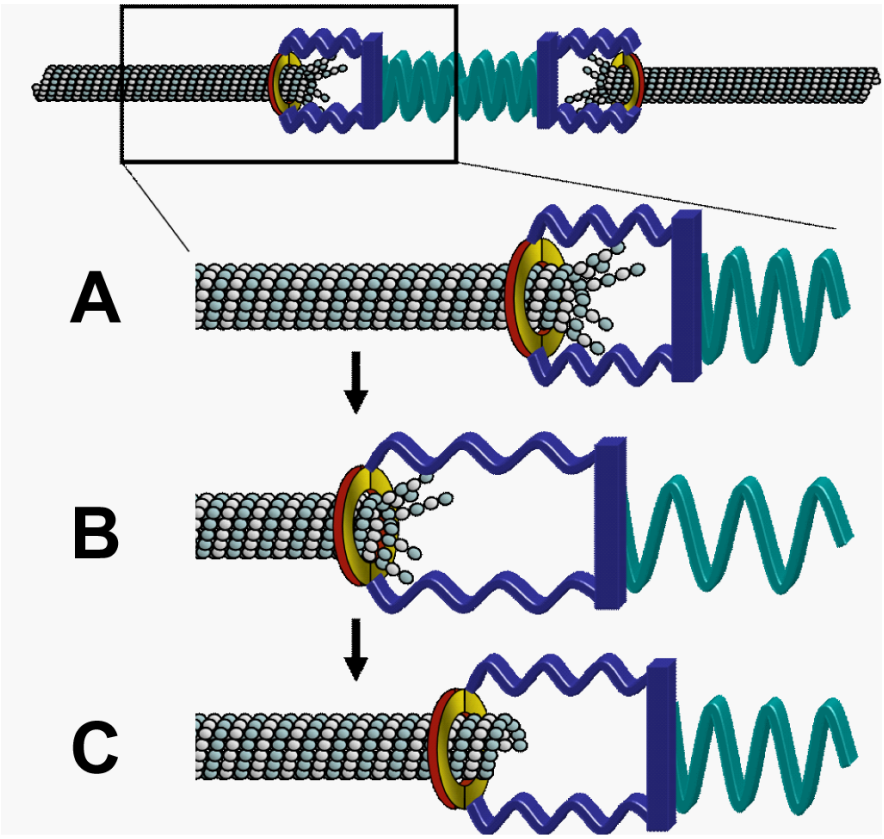

CHAPTER FOUR

MEASURING NANOMETER SCALE GRADIENTS IN SPINDLE MICROTUBULE DYNAMICS USING MODEL CONVOLUTION MICROSCOPY

(Contributing Authors: Melissa K. Gardner*, Chad Pearson*, Leocadia Paliulis, E.D. Salmon, David J. Odde, and Kerry Bloom)
*Co-first authors: *MKG performed simulations and completed all image/data analysis, CGP and LVP performed FRAP experiments*)
(Reprinted with permission from *Molecular Biology of the Cell* 17(9) (2006))

Abstract

A computational model for the budding yeast mitotic spindle predicts a spatial gradient in tubulin turnover that is produced by kinetochore-attached microtubule (kMT) plus-end polymerization and depolymerization dynamics. However, kMTs in yeast are often much shorter than the resolution limit of the light microscope, making visualization of this gradient difficult. To overcome this limitation, we combined digital imaging of fluorescence redistribution after photobleaching (FRAP) with model convolution methods to compare computer simulations at nanometer scale resolution to microscopic data. We measured a gradient in microtubule dynamics in yeast spindles at ~65 nm spatial intervals. Tubulin turnover is greatest near kinetochores and lowest near the spindle poles. A β-tubulin mutant with decreased plus-end dynamics preserves the spatial gradient in tubulin turnover at a slower time scale, increases average kinetochore microtubule length ~14% percent, and decreases tension at kinetochores. The β-tubulin mutant cells have an increased frequency of chromosome loss, suggesting that the accuracy of chromosome segregation is linked to robust kMT plus-end dynamics.

Introduction

Budding yeast is an important genetic model system for studying the mechanisms of accurate mitotic chromosome segregation. In metaphase, chromosomes become aligned with one sister kinetochore attached to the microtubule plus-end from one spindle pole and the other sister attached to the plus-end from the opposite spindle pole prior to

chromosome segregation in anaphase. This amphitelic kinetochore attachment and chromosome biorientation allows sister kinetochores to pull and stretch their intervening centromeric chromatin, thereby generating tension at kinetochores that promotes stability of kMT plus-end attachment [25, 55]. Force generation for stretching centromeres, aligning chromosomes, and segregating sister chromatids is coupled to changes in kMT length ([19, 59, 96]). With kMT plus-end depolymerization, kinetochores pull chromosomes poleward. Conversely, kinetochores move away from the poles with kMT plus-end polymerization, thereby reducing kinetochore tension. Kinetochores could also be pulled poleward by flux, which is coupled to depolymerization at pole-anchored kMT minus ends [21, 97]. Poleward flux occurs by the net addition of tubulin subunits at the microtubule plus-end and subtraction of subunits at the minus-end while kinetochores remain attached to spindle-pole anchored kMTs. This generates poleward forces on kinetochores during mitosis. However, in budding yeast, evidence so far indicates that kMT minus-ends are capped (indicating no microtubule minus-end disassembly), that flux does not occur, and that kinetochore movements depend only on kMT plus-end dynamics [58, 59, 98-101].

Unlike tissue cells, budding yeast kinetochores gain attachment to a single kMT nucleated from the spindle pole [30, 57, 58]. Because microtubules are singly attached to kinetochores, kMT plus-end dynamics can be directly linked to centromere stretching and thus tension generated at the kinetochore [19, 61, 62, 102]. Dynamic kMTs mediate kinetochore position, and thus kinetochores become clustered to average metaphase positions on either side of the spindle equator. Kinetochore congression to the equatorial metaphase plate requires spatial cues along the spindle length so that kinetochores can detect the spindle equator. One possible model for this is a spatial gradient in the regulation of microtubule dynamics predicted by our earlier modeling studies [29, 96].

Previously, we used simulations of kMT microtubule dynamics to study how kMTs could facilitate chromosome congression in yeast [29, 96, 103]. In our model, kinetochore microtubule dynamics are regulated by (1) a spatial gradient between the spindle poles and (2) tension generated from centromere stretch. The spatial gradient promotes catastrophe of kMT plus-ends at the center of the spindle and suppresses

catastrophe near the spindle poles. This gradient is sufficient to establish basic spindle bipolarity so that kinetochores are usually clustered midway between the pole and the equator. In addition, tension promotes microtubule plus-end rescue and lack of tension suppresses rescue, which acts to correct most of the residual equator crossing events. Together, these mechanisms lead to clustering of sister kinetochores on either side of the spindle equator, with high fidelity of kinetochores to their respective half-spindle [96].

A new prediction of this model is that a spatial gradient in kMT turnover should be established over the length of the spindle, such that tubulin turnover is highest near the kinetochores and lowest near the spindle pole. Clustering of sister kinetochores on either side of the spindle equator is predicted to result in rapid tubulin turnover specifically where kinetochore-attached microtubule plus-ends are clustered on either side of the spindle equator. This is achieved by spatial variation of kMT catastrophe and rescue frequencies over the length of the spindle, even though the rates of kMT polymerization and depolymerization remain constant. Thus, spatial variation in the parameters of kMT dynamic instability, specifically in catastrophe and rescue frequency, predict a spatial gradient in tubulin turnover over the spindle length. Previous GFP-tubulin FRAP studies measured the average half-life of tubulin within kMTs to be approximately 50 sec [59], but no attempt was made to detect a gradient in FRAP half-times because the average length of kinetochore microtubules at metaphase (~390 nm [30]) was approximately equal to the extent of microscope blur, as quantified by the point-spread function (PSF). Since the length of the proposed tubulin turnover gradient in yeast is close to or even less than the theoretical resolution limit of the light microscope (~220 nm at 510 nm wavelength (GFP) by the Rayleigh criterion), detection of such a gradient presents a technical challenge [104].

To overcome this potential limitation, we have combined a technically improved GFP-tubulin FRAP assay with model convolution microscopy methods to quantify tubulin turnover in spindle MTs. This improved FRAP technique provided (1) increased temporal resolution, and (2) a collection of microtubule turnover data at ~65 nm spatial sampling intervals along the length of the mitotic spindle. The positions of fluorescent microtubules in computer simulations of dynamic kMTs were convolved with the three-

dimensional microscope PSF (model convolution microscopy) to reproduce the spatially resolved FRAP experiment. The statistically-defined agreement between the experimental microscopic data and the simulated images in turn defined the valid parameter values for the spatial gradient in kMT plus-end dynamics.

A prediction of the model was that reduced kMT plus-end dynamics should preserve the FRAP gradient at a slower time scale and produce a tighter clustering of sister kinetochores on either side of the spindle equator. The optimal positioning of kinetochores and attached kMT plus-ends was defined by the spatial regulation of kMT catastrophe and rescue frequencies [96]. The length of plus-end excursions away from this optimal position on either side of the spindle equator depended directly on the growth and shortening velocities of the plus-ends. With rapid growth and shortening velocities, longer kMT growth and shortening excursions away from the most stable (mean) position were possible. This resulted in weak clustering of kMT plus-ends. Alternatively, slower kMT plus-end growth and shortening velocities lead to tighter clustering of kinetochores in the model, as kMT plus-ends are less likely to make longer excursions away from their most stable position. We tested this prediction using a β-tubulin mutant (*tub2C354S*) that suppresses microtubule plus-end dynamics [74]. The gradient in tubulin turnover was preserved and kinetochores were more tightly clustered in β-tubulin mutant metaphase spindles. This indicated that the regulation of kMT dynamics required to produce kinetochore clustering on either side of the spindle equator was maintained. Surprisingly, we also discovered that centromere stretch was reduced, and chromosome loss increased in the β-tubulin mutant. The higher chromosome loss rate suggested there is a link between average kinetochore tension, as dictated by microtubule dynamics, and the accuracy of chromosome segregation.

Materials and Methods

Yeast strains and cell culture

The strains used in this study were KBY2129 (*MAT***a,** *LEU2::GFP-TUB1::leu2Δ1, SPC29RFPKAN, trp1-63 leu2-1 ura3-52 his3-200 lys2-801*), KBY2012 (*MAT***a,**, *SPC29CFPKAN, cse4::HB,* pKK1, *trp1-63 leu2-1 ura3-52 his3-200 lys2-801*),

KBY2700GT (*MAT*a, *LEU2::GFP-TUB1::leu2Δ1, SPC29RFPKAN, trp1 Δ 63, his4-917, ura3-52, TUB1*, *TUB2*), KBY2701GT (*MAT*a, *LEU2::GFP-TUB1::leu2Δ1, SPC29RFPKAN, trp1Δ63, his4-917, URA3/ura3-52, TUB1*, *tub2-C354S*), KBY2702 (*MAT*a, *SPC29CFPKAN, cse4::HYG,* pKK1*, trp1 Δ 63, his4-917, ura3-52, TUB1*, *TUB2*), KBY2703 (*MAT*a, *SPC29CFPKAN, cse4::HYG,* pKK1*, SPC29RFPKAN, trp1Δ63, his4-917, URA3/ura3-52, TUB1*, *tub2*-C354S), KBY2700RS (*MAT*a, *SPC29RFPKAN, leu2Δ1, trp1Δ63, his4-917, URA3/ura3-52, TUB1*, *tub2-C354S*, pRS315) and KBY2701RS (*MAT*a, *SPC29RFPKAN, leu2Δ1, trp1Δ63, his4-917, URA3/ura3-52, TUB1*, *tub2-C354S,* pRS315). The strains listed above are adapted from those described by Gupta et al. [74]. pKK1 is a pRS314-based plasmid containing the centromere specific histone-H3 variant, *CSE4*, fused to *GFP* [19, 64].

Cell growth techniques and conditions were performed as previously described [60, 96, 103].

Fluorescence imaging and photobleaching

Imaging techniques were performed as previously described [19, 60, 103]. The general FRAP techniques performed were previously described [59, 60]. In this study, the microscope used for FRAP was a Nikon Eclipse TE2000E stand with 100X PlanApo NA 1.4 objective with a Hamamatsu Orca ER camera. The microscope back port was fitted with a Point Source (Southampton, UK) beam expander fiber optically coupled to a SpectraPhysics (Mountain View, CA, USA) 50 mW Argon ion laser to bring the photobleaching light into the back aperture of the objective. The laser exposure was 25 msec with light attenuated by neutral density. Fluorescent images were acquired at intervals between 2 sec and 2 min, depending on the experiment.

To ensure the spindle was in focus, we included Spc29RFP labeled SPBs to mark the spatial position of GFP-Tub1 fluorescence redistribution relative to the SPB. For increased temporal resolution, only single image planes were acquired.

Data analysis

Analysis of FRAP experiments to determine fluorescence redistribution half-times ($t_{1/2}$) was performed as previously reported [59], except that raw fluorescence data was collected for every unbinned camera pixel (~65 nm). In order to collect accurate fluorescence recovery data by position along the length of the spindle, poles markers were included in the assay, and were used to provide a frame of reference for image analysis. Spindles in which one or both pole markers moved out of focus during the experiment were rejected. Fluorescence was collected over the length of the spindle and then integrated over 15 pixels perpendicular to the centerline of the spindle at each spindle position using MATLAB (Version 6.0, The MathWorks, Natick, MA) as previously described [29, 96]. To account for variations in spindle length, integrated data at each spindle position were then averaged into 24 bins per spindle, such that each bin contained data from 1-2 pixels (typically 1 pixel), depending on spindle length. Data for each of the 24 bins along the length of the spindle were averaged over all of the experiments. Fluorescence recovery half-times ($t_{1/2}$) were calculated based on the recovery profile of each bin as previously described [59].

Kinetochore localization, as measured by Cse4-GFP fluorescence, was measured as described previously [29, 96].

Simulation methods

Simulation of the GFP-tubulin FRAP experiment was performed as previously described [96], with the exception that fluorescence was calculated for every pixel during recovery to provide a comparison with experimental results. kMT dynamics were simulated via MATLAB, with simulated images generated at specified time points to correspond to experimental values. The bleach status of every incorporated and free-pool GFP-tubulin dimer was recorded at every time point in the simulation. FRAP was then realized as unbleached GFP-tubulin dimers were incorporated into bleached MTs via plus-end polymerization. Simulated fluorescence values by pixel were then normalized into 24 bins, as described above.

In the current simulation, interpolar microtubules (ipMTs; of which we assumed there were eight, versus 32 kMTs) were considered to be non-dynamic [59] and to run the

length of the spindle [30, 57]. We tested the effect of dynamic ipMTs on the GFP-tubulin FRAP simulation, and assuming similar growth and shortening rates between kMTs and ipMTs, dynamic ipMTs had little effect on FRAP half-times where kMT fibers were relatively abundant (Supplemental Figure B.1).

Plasmid loss assays

For plasmid loss experiments, KBY2700RS and KBY2701RS were grown in SD-Leu media to mid-logarithmic growth before dilution into SD-complete (non-selective) media and grown for 17 hours at 24ºC. Cells were then plated onto SD-complete plates before replica plating to SD-complete and SD-Leu. Three separate experiments were performed. The plasmid loss percentage was then calculated by determining the ratio of colonies found on the selective versus non-selective media.

Results

Simulations predict rapid tubulin turnover at sites of kMT plus-end clustering

To understand how the regulation of microtubule dynamics could facilitate kinetochore clustering and metaphase alignment, GFP-tubulin FRAP experiments were simulated for yeast metaphase spindles (Materials and Methods). In the simulation, kMT growth and shortening was assumed to take place at the kMT plus-ends, and the polymerization and depolymerization rates of kMT plus-ends were assumed to be constant over the spindle length. This assumption is made for simplicity in parameter evaluation, and is supported by previous measurements of cytoplasmic microtubule dynamics, in which growth and shortening rates were similar (Table 4.2, [74]). However, the simulated catastrophe and rescue frequency were not constant over the length of the spindle. A spatial gradient in catastrophe and rescue frequency results in kinetochore (and thus kMT plus-end) clustering on either side of the spindle equator as is experimentally observed during yeast metaphase. The GFP-tubulin FRAP simulation predicted that clustering of kMT plus-ends in the mitotic spindle results in a spatial variation of tubulin turnover rate over the length of the spindle, such that turnover will be most rapid in the location of plus-end clustering, with a decreased rate of turnover

elsewhere (Figure 4.1A; Supplemental Movie 1). Alternatively, simulations with constant catastrophe and rescue frequency over the length of the spindle do not predict kinetochore and kMT plus-end clustering on either side of the spindle equator (Figure 4.1B). In simulations where catastrophe and rescue frequency are constant, the distribution of kMT plus-ends was even over the length of the spindle, and thus no gradient in tubulin turnover was predicted (Figure 4.1B; Supplemental Movie 2).

GFP-tubulin turnover varies as a function of position within the mitotic spindle

To test whether kMT turnover rates vary as a function of spindle position, as predicted by the spatial catastrophe and rescue frequency gradients in the model (Figure 4.1A), we used laser photobleaching to selectively bleach one-half of a yeast metaphase spindle labeled with GFP-tubulin. Photobleaching was performed using a diffraction-limited spot from the 488 nm line of an Argon-ion laser and recovery was followed by high resolution digital imaging, initially acquiring images at ~2 sec intervals and then increasing the time interval. Fluorescence was collected at each pixel cross section for the CCD camera along the length of the spindle and then integrated over 15 pixels perpendicular to the centerline of the spindle at each spindle position or "bin" (Figure 4.2A, B; Materials and Methods). This allowed for monitoring of fluorescence recovery separately in each camera pixel (~ 65 nm width) along the length of the yeast metaphase spindle. We found that GFP-tubulin FRAP was indeed fastest where plus-ends were clustered, midway between the spindle equator and each SPB (Figure 4.2C).

The time to half-maximal recovery was then calculated for the entire bleached half-spindle at sub-diffraction limited sampling (~65 nm) intervals along the length of the spindle (Figure 4.2C). The mean half-time ($t_{1/2}$) for GFP-tubulin FRAP was approximately 110 sec near the SPB and approximately 40 sec midway between the SPB and the spindle equator. The average $t_{1/2}$ of 65±31 sec is in agreement with previously reported values of 52±23 sec for wild-type spindles ([59], $p=0.33$). In some cases, adjacent sampling intervals were statistically different ($p<0.05$, by t-test, Supplementary Table B.1). A slight upturn in GFP-tubulin half-times was observed near the equator, as

predicted by the model (Fig. 4.1A). The experimentally observed upturn was slightly larger, however, not significantly different from that predicted by the model.

The experimental results are quantitatively consistent with the plus-end clustering model predictions ($p=0.42$, parameter values Table 4.1, Figure 4.1A), and inconsistent with a model that does not exhibit plus-end clustering, regardless of parameter value ($p<0.01$, Figure 4.1B). In addition, this demonstrates that the spatially resolved FRAP analysis yields information on gradients in behavior over distances as small as ~65 nm, well below the theoretical resolution of the microscope (~220 nm for 510 nm wavelength light).

Kinetochores are clustered at positions of most rapid GFP-tubulin exchange

In our computational simulations, the location of kinetochore clustering was predicted to be the site of the most rapid GFP-tubulin FRAP (Figure 4.3A, white box). To test this prediction in live cells, we quantified the average location of the kinetochores (labeled with Cse4-GFP) relative to the site of the most rapid GFP-tubulin turnover or FRAP. For reference, Spc29-CFP and RFP was used to mark the spindle poles for cells with Cse4-GFP labeled kinetochores and GFP-tubulin labeled microtubules, respectively. Representative experimental fluorescence images are shown in Figure 4.3B. The Cse4-GFP fluorescence intensity or rate of GFP-tubulin recovery was plotted as a function of relative spindle position and the two data sets were quantitatively compared. As shown in Figure 4.3C (green arrow), the average kinetochore position on either side of the equator in the yeast metaphase spindle corresponded to the location of most rapid GFP-tubulin FRAP (Figure 4.3C, orange arrow). Thus, kMT plus-end dynamics were greatest at the approximate site of kinetochore clustering.

kMT minus-ends are ~50 nm from Spc29-RFP at the spindle poles

The mean distance between the centroid of the Cse4-GFP labeled kinetochore cluster and Spc29-CFP at the poles was 430 nm (Table 4.2). This would be an accurate measure of the mean length of kMTs if the kMT minus ends were located at the site within the SPB where Spc29-CFP is located. To determine the distance from Spc29 to the

kMT minus ends, we quantitatively evaluated the distribution of GFP-tubulin fluorescence near the Spc29-RFP pole marker (kMT minus-end). By using two color fluorescence imaging, we are not constrained by the diffraction limit of resolution with a single wavelength. As shown in Figure 4.4A, the microscope "point spread function" (PSF) spreads out the fluorescence via diffraction of light through the microscope lens. This blurring effect prevented detection of the offset distance between the Spc29-RFP spindle pole marker and GFP-tubulin at the kMT minus ends by the naked eye. Although this separation distance was not readily apparent by eye, we reasoned that the relative amount of GFP-tubulin associated fluorescence at the pole would be more intense if kMT minus-ends were in close proximity to the Spc29 SPB marker (Figure 4.4A(1)), and less intense if kMT minus-ends were further from the Spc29 SPB marker (Figure 4.4A(2)). Thus, the intensity of GFP-Tub1 flourescence near to the SPB marker was predicted to vary according to the magnitude of the offset between GFP-tubulin at the kMT minus-ends and the Spc29-RFP SPB marker (Figure 4.4A, B). By simulating experimental yeast spindles and then convolving these simulations with the experimentally measured microscope PSF (model-convolution), quantitative predictions can be made for the relative amount of GFP-tubulin associated fluorescence in the "bin" at the spindle pole, as well as the bins nearby, using different values of the MT minus-end/Spc29 SPB marker offset (Figure 4.4B, C). Using this approach, we estimated the kMT minus-end position to be ~50 nm from the centroid of the Spc29-RFP fluorescence. Subtracting this distance from the length between Cse4-GFP and Spc29-CFP gives a mean length for kinetochore microtubules at metaphase of ~380 nm, similar to that measured by EM studies (~390 nm; [30]). Thus, the model-convolution method extracts spatial information below the resolution limit of the light microscope and enables an accurate measurement of average kMT lengths.

The spatial gradient in tubulin turnover persists even when kMT dynamicity is reduced by a β-tubulin mutant

We next asked how the experimentally observed spatial gradient in tubulin turnover rate would be affected by a mutation that resulted in reduced dynamics at kMT

plus-ends. In this case, reduced microtubule dynamicity, or the number of tubulin subunits exchanged over time, may increase the time required for kinetochore alignment in prometaphase, but not necessarily affect kinetochore position or distribution. The parameters of dynamics have been measured for the plus-ends of cytoplasmic microtubules in the β-tubulin mutant (*tub2C354S*) [74](Table 4.1). With this mutation, microtubule dynamicity is reduced throughout the cell cycle, resulting in reduced rates of spindle elongation and slower cellular growth. As was previously observed, GFP-tubulin FRAP rates were also significantly slowed in this mutant strain [74] (Figure 4.5A, Table 4.2). Using high resolution FRAP to analyze mutant spindle dynamics, a gradient in recovery half-times was observed (Figure 4.5B). This gradient is similar to wild-type spindles, but recoveries proceed on a slower time scale at both kinetochores and spindle poles. FRAP half-times near the SPBs were approximately 200 sec, with the most rapid half-times approximately 90 sec near the spindle equator (Figure 4.5A, B). Thus, plus-end clustering during metaphase is likely maintained in the β-tubulin mutant spindles, despite reduced microtubule plus-end dynamics.

Computer modeling predicts single kinetochore dynamics in the β-tubulin mutation

By reproducing the experimentally observed high resolution FRAP results in both wild-type and β-tubulin mutant spindles, we can simulate the microtubule plus-end dynamics at single kinetochores in yeast (Table 4.1, Simulation Parameter Values, Supplemental Movies 1 and 2). In these simulations, kMT growth and shortening rates are assumed to be constant and equal to each other over the length of the spindle. Simulation of the high-resolution FRAP experiment in the β-tubulin mutant spindles required a three-fold decrease in kMT growth and shortening velocities (Supplemental Movie 2). Because of this decrease, simulated kMT plus-end excursion lengths were reduced, and there were significantly fewer instances of kMT plus-end depolymerization to the SPB (Figure 4.6A, B; Supplemental Movies 1 and 2). As a result, the simulated distribution for plus-end visits to each spindle position was narrowed, indicating a reduction in amplitude of kinetochore oscillations (Figure 4.6C, red histogram represents a 31% reduction in kMT length standard deviation). This was the result of reduced

excursions away from the average cluster position (Figure 4.1A, arrows). The narrowed distribution of plus-end visits to each spindle position in the β-tubulin mutant simulation predicted that the gradient in tubulin turnover rates over the spindle length will be preserved in spindles with reduced microtubule dynamicity (Figure 4.5B).

The β-tubulin mutation alters the distribution of kinetochore clusters

The experimentally observed location of most rapid FRAP was shifted slightly towards the spindle equator in the β-tubulin mutant (Figure 4.5B: arrows depict shift in approximate location of fastest FRAP). This shift indicated that kMTs are longer and thus kinetochore clusters in β-tubulin mutants would be predicted to be closer to the equator than in wild-type spindles. This result was confirmed experimentally by quantifying the centroid position of kinetochore-associated Cse4-GFP fluorescence relative to Spc29-CFP pole fluorescence in the β-tubulin mutant (Figure 4.7A, white arrows). The distance between kinetochore clusters was decreased by ~25% in the β-tubulin mutant while the average spindle length changed little (Figure 4.7B, C; Table 4.2). After correcting for the distance between Spc29-CFP and the kMT minus-ends (see above), the mean predicted kMT length was ~440 nm in the β-tubulin mutant, ~60 nm longer on average than wild-type kMTs.

As predicted by simulations with reduced kMT growth and shortening velocities, the experimentally observed distribution of kinetochore-associated fluorescence within each sister cluster was also narrowed in the β-tubulin mutant (31% reduction in the standard deviation of the experimental kMT lengths measured via variance in Cse4-GFP fluorescence, Table 4.2, Figure 4.7B). By quantifying Cse4-GFP fluorescence in the β-tubulin mutant, kinetochore clustering was found to be 31% more tightly focused on either side of the spindle equator as compared to wild-type spindles.

Reduced tension between sister kinetochores correlates with centromere plasmid mis-segregation

To test if reduced kMT dynamics and tension had an effect on the fidelity of chromosome segregation, we performed centromere-plasmid loss experiments in the β-

tubulin mutant. Centromere plasmids were lost at a 2.5-fold greater frequency in *tub2C354S* containing cells (wild-type 4.9±0.4% loss/generation, β-tubulin mutant 12.0±0.4% loss/generation). This suggests that there may be tension-dependent chromosome mis-segregation as a result of altered kMT dynamics.

Discussion

Using computer modeling and high-resolution FRAP, we predicted theoretically and observed experimentally the existence of a spatial gradient in kMT turnover in metaphase budding yeast cells. The methodology enabled detection of a gradient in GFP-tubulin FRAP over distances as small as ~65 nm. We found that the most rapid GFP-tubulin turnover occurred where the kMT plus-ends and kinetochores were located. A β-tubulin mutant with reduced microtubule dynamicity also exhibited a gradient in GFP-tubulin turnover and a tighter clustering of kinetochores. The tubulin mutant had slightly longer kMTs and less tension between sister kinetochores, as well as increased chromosome loss.

High-resolution FRAP analysis

Through the use of digital light microscopy experiments designed in concert with computational simulations, we have developed a spatially-resolved GFP-tubulin FRAP assay that simultaneously characterizes both the clustering of kMT plus-end locations and the dynamics of kMTs in the yeast metaphase spindle (Figure 4.2). kMT plus-end turnover is greatest at the site of kinetochore clustering in the yeast metaphase spindle, and GFP-tubulin FRAP proceeds in a "wave" towards each SPB. FRAP half-times at the SPB are nearly three-fold slower than FRAP half-times midway between the spindle equator and each SPB (the site of kinetochore positioning), indicating that kMT plus-ends infrequently depolymerize to the poles. Since half-times separated by one pixel, corresponding to ~65 nm, were in some cases statistically different ($p<0.01$ by t-test, Table B.1), the FRAP analysis can resolve differences in microtubule dynamics at distances less than the theoretical resolution of the microscope (~220 nm for 510 nm light). Thus, the light microscope has the ability to gain spatially-resolved information

on protein dynamics *in vivo* at nanometer-scale distances, limited only by the size of the data set and the distance projected onto single detector elements of the digital camera detector array.

Using two color digital imaging with model convolution techniques, we quantified the average distance between the centroid of Spc29-RFP or CFP labeled SPBs and kMT minus-ends (~50 nm). Using this offset, we then estimated the average kMT length based on the separation between kinetochore clusters (Cse4-GFP) and kMT minus-ends (~380 nm in WT spindles). This length also corresponds well with kMTs length as measured by electron microscopy (~390 nm) [30]. The combination of approaches has now enabled high resolution length measurements of metaphase spindles using the light microscope.

High-resolution FRAP constrains simulation models of kMT dynamic instability

Our observation that kinetochore clustering corresponds to the location of most rapid FRAP in the yeast metaphase spindle indicates that kMT plus-ends are dynamic, and that kinetochores remain in close proximity to dynamic kMT plus-ends. Clustering of dynamic plus-ends on either side of the spindle equator with relatively infrequent excursions to the SPBs argues for precise regulation of kMT plus-end dynamics. The simulation, which relies on high catastrophe frequency at the spindle equator with rescue frequency promoted by tension generated via chromatin stretch between sister kinetochores, reproduces the kMT dynamics as were observed in the high-resolution FRAP experiments (Figure 4.5B). The GFP-tubulin FRAP simulation constrains kMT growth and shortening rates to a narrow range of values (Table 4.1), and also rules out simpler models, such as simple stochastic dynamic instability (Figure 4.1B), for the regulation of kMT dynamic instability in both wild-type and β-tubulin mutant yeast spindles. Both the wild-type and β-tubulin mutant simulation parameter values are similar to the growth and shortening rates that were experimentally observed for cytoplasmic microtubules (Table 4.1, [74]). However, the estimated catastrophe and rescue frequencies are much higher for kMTs than for cytoplasmic MTs, indicating that the kinetochore regulates growth and shortening excursions within the spindle. Changes in

plus-end dynamics have also been observed for kinetochore attached MTs compared to cytoplasmic microtubules in G1 cells [105]. In addition, the catastrophe and rescue frequencies used to model the wild-type and β-tubulin mutant were nearly identical, indicating that the oscillations associated with dynamic instability are dictated by the kinetochore, and robust with respect to perturbation of tubulin itself.

Estimation of an upper limit to poleward kMT flux

Recently, experimental and modeling studies have highlighted the importance of poleward microtubule flux in creating tension at the kinetochores [15, 106]. It was proposed that chromosome oscillations occur in systems with little or no flux, such as in yeast, to compensate for the lack of poleward flux to generate tension at the kinetochore [59, 99]. Although poleward kMT flux has not been detected previously in budding yeast [59, 99], it may be that the spatial resolution was insufficient to detect flux in an intact wild-type spindle.

By calculating a FRAP half-time specifically at the SPB, our analysis places a theoretical upper limit on the rate of poleward kMT flux in yeast metaphase spindles. If the spindle depended only on poleward flux for recovery, then the fastest flux rate that would be consistent with the GFP-tubulin FRAP data is approximately 0.10 μm/min. We estimated this upper limit as follows: assuming total 220 sec. to achieve recovery at poles (twice the experimentally observed half-time), and an average kMT length of ~380 nm, (~380 nm mean kMT length) / (220 sec. to recovery) = 1.7 nm/sec = 0.10 μm/min rate of poleward flux. The flux rate would be even slower with a combination of kMT plus-end dynamics and poleward flux. The theoretical maximum rate (0.1 μm/min) is significantly slower than the rate of polymerization and depolymerization at kinetochores based on measurements of centromere movements using lacO-GFP markers placed ~1 kb from the centromere (1.5 μm/min; [19]), and based on the growth and shortening rates used here to match the observed tubulin FRAP recovery rates (Table 4.1). Therefore, the theoretical flux limit calculated here would not significantly contribute to the observed chromosome motility.

A bias toward kMT assembly results in loss of tension at the kinetochore

The decrease in GFP-tubulin turnover rate near the SPB in the β-tubulin mutant suggests that kMT plus-end excursion lengths are significantly reduced in frequency compared to wild-type spindles (Figure 4.6), with a shift of kMT plus-ends toward the spindle equator (Figure 4.7). While we do not understand the mechanism for this shift, these observations suggest that reduced kinetochore tension in the β-tubulin mutant results specifically from a net increase in kMT plus-end polymerization (Figure 4.7C). This result is consistent with cells treated with taxol or low concentrations of nocodazole where MT dynamics and centromere tension are also decreased (Vasquez *et al.*, 1997; Waters *et al.*, 1998). Thus, force-generating kMT plus-end dynamics are critical to establish separation between sisters and to maintain tension at the kinetochore.

Loss in kinetochore tension and the fidelity of chromosome segregation

The β-tubulin mutation resulted in tighter kinetochore clustering and a moderate loss of tension at the kinetochore (~25% loss in tension; Figure 4.7A-C). The observed increase in centromere plasmid loss in the mutant suggests that even a subtle loss in tension at the kinetochore has consequences for the fidelity of chromosome segregation. We hypothesize that a persistent loss in tension at the kinetochore may result in transient kinetochore-kMT detachment via a tension-dependent mechanism [25, 107]. At least two alternative possibilities exist for how chromosome loss occurs in the β-tubulin mutant. First, it may be that kMT plus-end dynamics and, therefore, excursions are required for error correction. Tight clustering of kinetochores indicates that kMT plus-ends are more constrained than in normal conditions (~31% reduction in the standard deviation of the kMT length). Robust kMT plus-end dynamics may allow for mechanical detachment of improper attachments and subsequent error correction. Second, it is possible that reduced MT dynamicity could affect "search and capture" for unattached kinetochores, resulting in a decreased number of attached kinetochores. We do not believe that erroneous search and capture is the dominant cause for chromosome loss because kinetochores are tightly clustered in the location of most rapid FRAP in the β-tubulin mutant, suggesting that MT plus-ends are localized with and attached to kinetochores.

In conclusion, we have combined simulation and experimental methodologies to improve the resolution of GFP-tubulin FRAP to detect a spatial gradient in kMT turnover at distances of ~65 nm. Analysis of fluorescence recovery patterns enabled high resolution tracking of kinetochore and kMT plus-end positions in the yeast metaphase spindle. Although kMT plus-ends remain highly dynamic during yeast metaphase, these dynamics are tightly regulated to allow for proper kinetochore positioning and separation. We find that regulated kMT plus-end dynamics are necessary for normal sister separation and accurate chromosome segregation by defining the position of kinetochores on the spindle axis. Spatially-resolved FRAP on the nanometer-scale will be a valuable tool for future studies aimed at characterizing fluorescent protein dynamics and localization in this genetically tractable organism. In addition, it will aid studies of submicrometer-sized structures within larger cells.

Acknowledgements

I thank Drs. Dick Himes and Moe Gupta for generous contribution of the β-tubulin strains. I thank Julian Haase for help with strain construction. Thanks to Drs. Paul Maddox, Jennifer Deluca, and Jason Stumpff for critical comments on the manuscript and discussions. This work was supported by NIH grants GM32238 (KB), GM071522 (DJO) and GM24364 (EDS). CGP is supported by a Damon Runyan Fellowship. MKG is supported by a NIH pre-doctoral fellowship. LVP is supported by a SPIRE fellowship (GM00678).

Tables and Figures

TABLE 4.1. Simulation Parameters

	Wild-Type Experimental, Cytoplasmic Microtubules	Wild-Type Simulation, kMT Dynamics	*tub2-C354S* Experimental, Cytoplasmic Microtubules	*tub2-C354S* Simulation, kMT Dynamics
Growth Rate (Vg) (μm/min)	1.30 ± 0.42	1.20 ± 0.10[a]	0.23 ± 0.11	0.40±0.10[d]
Shrinkage Rate (Vs) (μm/min)	1.98 ± 0.68	1.20 ± 0.10[a]	0.42 ± 0.18	0.40±0.10[d]
Catastrophe Frequency (k_c) (min^{-1})	0.46 ± 0.10	0.25-27[a]	0.024 ± 0.009	0.25-27[b]
Basal Rescue Frequency (k_r) (min^{-1})	0.21 ± 0.07	9[c]	0.036 ± 0.012	11[c]

[a]Calculated probability of fits (p-value): Vg=Vs=1.2 μm/min, p=0.42; Vg=Vs=1.1 μm/min, p=0.36; Vg=Vs=1.3 μm/min, p=0.08. p-values calculated as described in [29]. Growth and shortening velocities assumed to be equal for all simulations.
[b]Model catastrophe frequency depends on spindle position, (Supplemental Material and [96]).
[c]Model rescue frequency depends on tension between sister kinetochores, as measured by distance between assigned sister kinetochores in the simulation, (Supplemental Material and [96]). Reported value is for lowest basal rescue frequency in the absence of tension.
[d]Calculated probability of fits (p-value): Vg=Vs=0.40 μm/min, p=0.40; Vg=Vs=0.30 μm/min, p=0.14; Vg=Vs=0.50 μm/min, p=0.24.

TABLE 4.2. Spindle Statistics

Spindle Description	Mean GFP-Tub1 FRAP half-time ($t_{1/2}$) (sec)[a]	Mean spindle length (nm)	Mean SPB to kinetochore distance (nm)[b]	Mean kinetochore cluster spacing (nm)[c]	Corrected mean kMT length (nm)	n
Wild-type Spindles	65±31 sec (n=22)	1610±200	430±130	750±280	380±130	79
tub2C354 Spindles	146±64 sec (n=10)	1530±230	490±90	560±230	440±90	121

[a]Mean calculated over 10 pixel span from SPB towards equator.
[b]Estimated by multiplying the normalized spindle location of peak mean kinetochore-associated fluorescence by the mean spindle length.
[c]Calculated as follows: (mean spindle length) - (2*SPB to kinetochore distance).
All mean values are presented +/- standard deviation.

FIGURE 4.1: Simulation of yeast metaphase predicts kMT plus-end clustering and a spatial gradient in kMT tubulin turnover (A) In a model with spatial catastrophe and rescue gradients, kMT plus-ends and kinetochores cluster on either side of the spindle equator, even though kMT growth and shortening rates are constant. In this model, there is an approximately Gaussian distribution of kMT plus-end positions over the half-spindle, with kMT plus-ends frequently midway between the SPB and the spindle equator (left, yellow arrows). The cartoon represents a yeast mitotic spindle with kinetochore clustering on either side of the spindle equator. (SPB (red), Microtubules (green), Kinetochores (grey)). A spatial gradient in tubulin turnover rate was predicted from this model. Turnover was most rapid at the location of plus-end clustering (right, yellow arrow; (bleached half-spindle only)) (B) In a stochastic dynamic instability model where catastrophe and rescue frequencies are constant and equal over the spindle length there is approximately a uniform distribution of kMT plus-ends (left), and no spatial gradient in tubulin turnover was predicted (right). The cartoon represents a theoretical mitotic spindle with no obvious kinetochore clustering and plus-ends are randomly distributed along the spindle length.

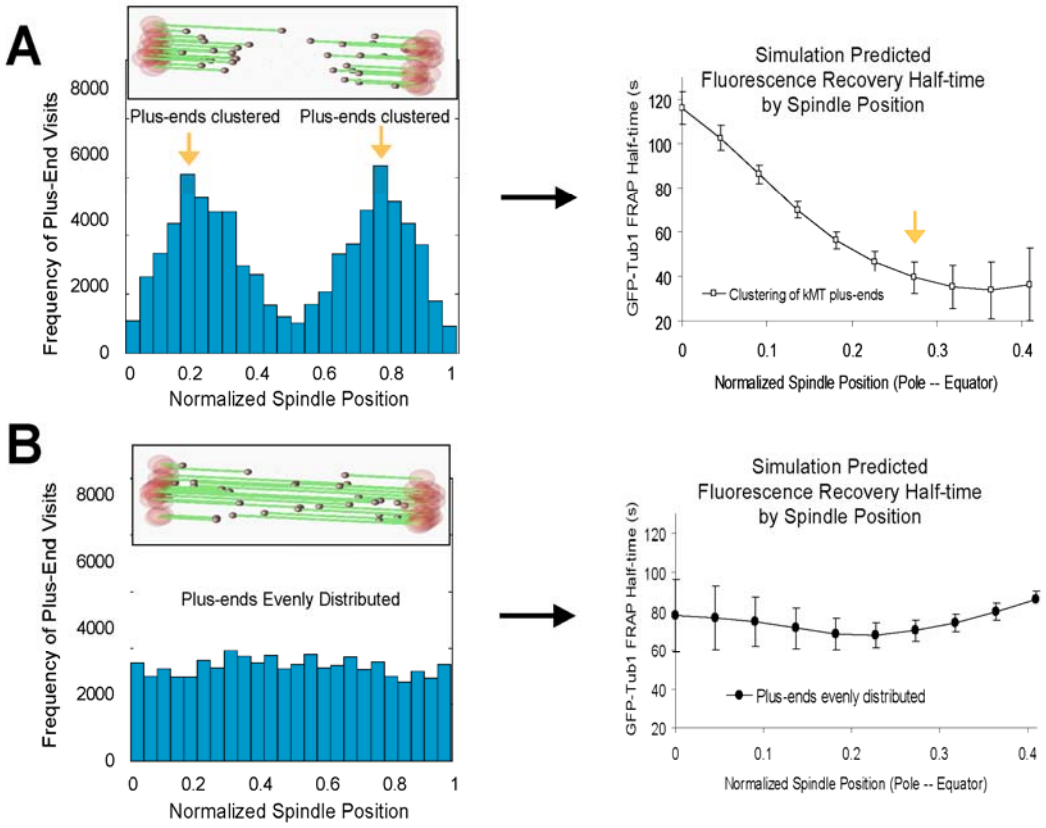

FIGURE 4.2: Spindle microtubules exhibit a spatial gradient in tubulin turnover rate. (A) Experimental images of the GFP tubulin FRAP experiment (SPB (red), MTs (green)). Experimental fluorescence recovery was monitored in ~65 nm "bins" along the photobleached half of the mitotic spindle (white boxes are unscaled representative bins). Scale bar, 1000 nm (B) Representative raw experimental data from a bin near the SPB (left, bin "0"), and a bin midway between the spindle equator and the SPB (right, bin "6"). Theoretical exponential fit curves calculated based on bin experimental recovery half-times are drawn through each plot (solid line). (C) Quantitative experimental results for GFP-tubulin FRAP half-time by spindle location. Normalized spindle position 0 represents the bin nearest the SPB, whereas normalized spindle position 0.45 represents the bin near the spindle equator. FRAP was most rapid at spindle positions midway between the spindle equator and each SPB, where plus-ends were clustered in the metaphase spindle (~ bin 6).

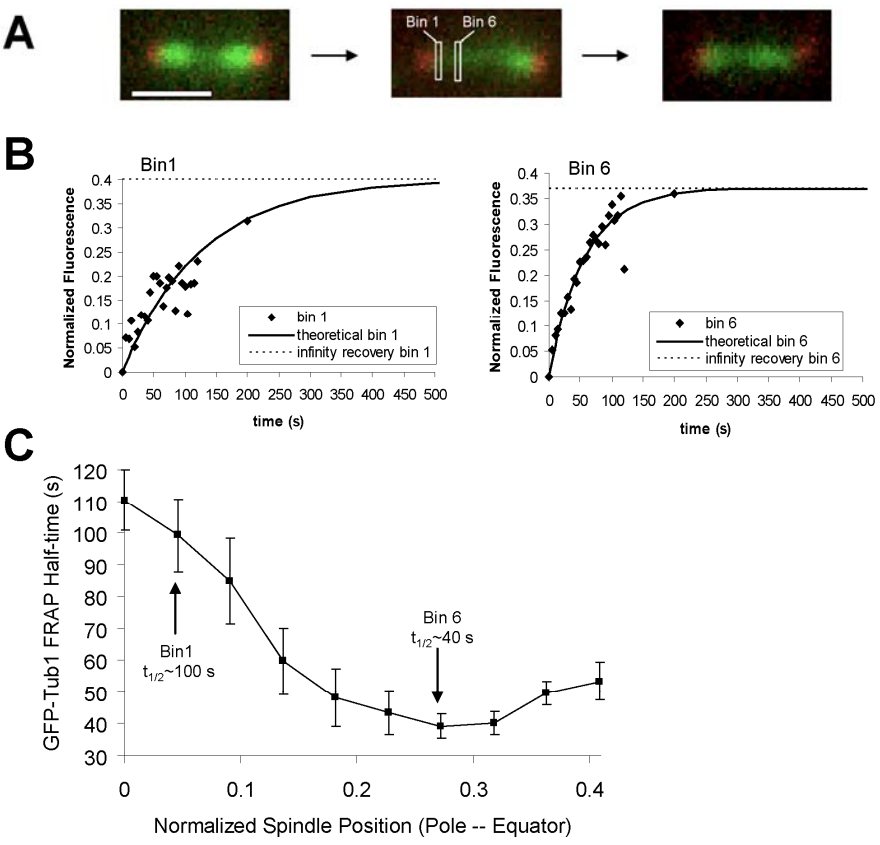

FIGURE 4.3: Kinetochores are clustered at positions of most rapid GFP-tubulin exchange**.** (A) The animated simulation output revealed a link between GFP-tubulin FRAP and kinetochore positioning, such that turnover is predicted to be most rapid in locations of kinetochore clustering (white box, Supplemental Movie 1) (SPB (red), unbleached kMTs (green), kinetochores (grey) and photobleached kMTs (violet)). (B) Representative experimental spindle images of Tub1-GFP with Spc29-RFP spindle pole markers (left) and Cse4-GFP with Spc29-CFP spindle pole markers (right). (C) Comparison of kinetochore position (Cse4-GFP) with GFP-tubulin FRAP. The peak in kinetochore localization corresponds to the site of most rapid GFP-tubulin FRAP.

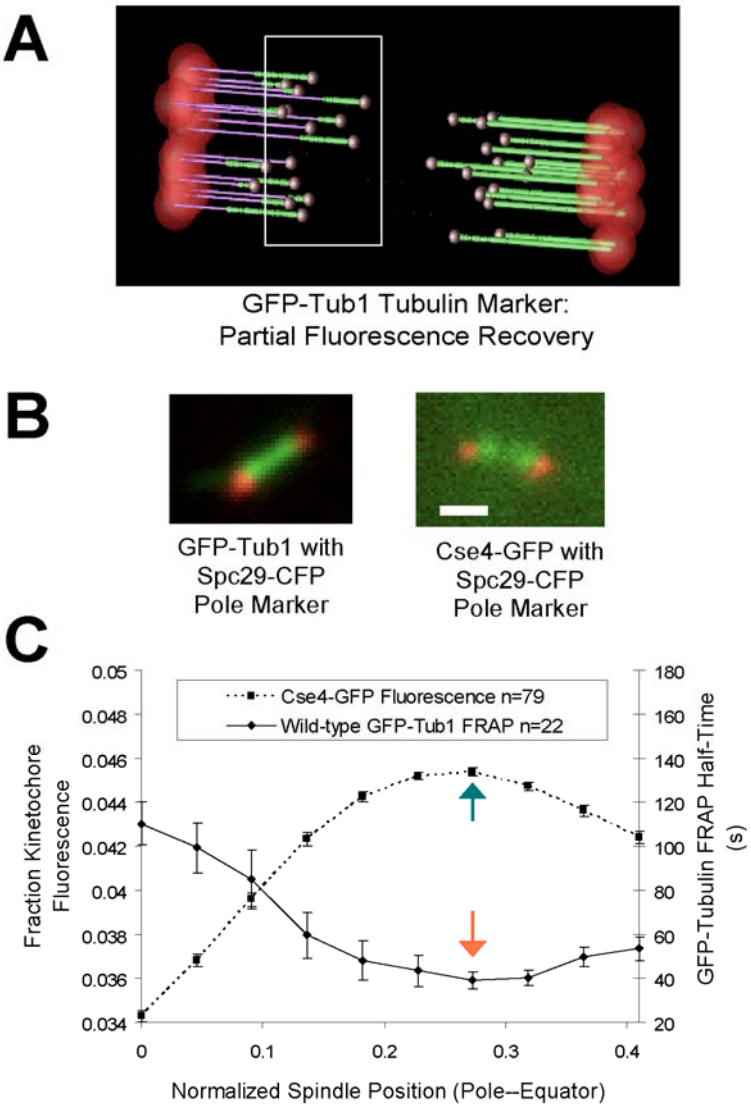

FIGURE 4.4: The microtubule minus ends are on average ~50 nm from the SPB**.** (A) Box 1: the upper spindle depicts an offset of ~10 nm between the SPB marker and the kMT minus-end in a theoretical image with no spreading of light through the microscope lens (point spread function (PSF)). In the box 1 lower image, the spreading of light due to PSF is depicted, resulting in a relatively intense GFP-Tub1 signal near the SPB marker. Box 2: the upper spindle depicts an offset of ~50 nm between the SPB marker and the kMT minus-end in a theoretical image with no spreading of light through the microscope lens (PSF). In the box 2 lower image, the spreading of light due to PSF is depicted, resulting in a relatively weak GFP-Tub1 signal near the SPB marker. (B) Images were simulated via model-convolution with 10 nm and 50 nm of offset between the SPB marker and kMT minus-ends (left two panels). A representative experimental image is displayed on the right. (C) Quantitative fluorescence analysis for mean GFP-tubulin fluorescence values by spindle position. Experimental and simulated curves represent average values over 92 spindles. All simulations assume that ipMT lengths are 89±10% of spindle length, and that the SPB marker is aligned at the edge of the starting bin during image analysis, such that offsets up to 65 nm are fully contained within bin "0". Red arrow denotes relative GFP-tubulin fluorescence in bin "0" near the SPB. By comparing experimentally measured GFP-tubulin at the poles to simulated image predictions the kMT minus-end position is estimated to be ~50 nm from the centroid of the Spc29-RFP fluorescence.

Figure 4.4

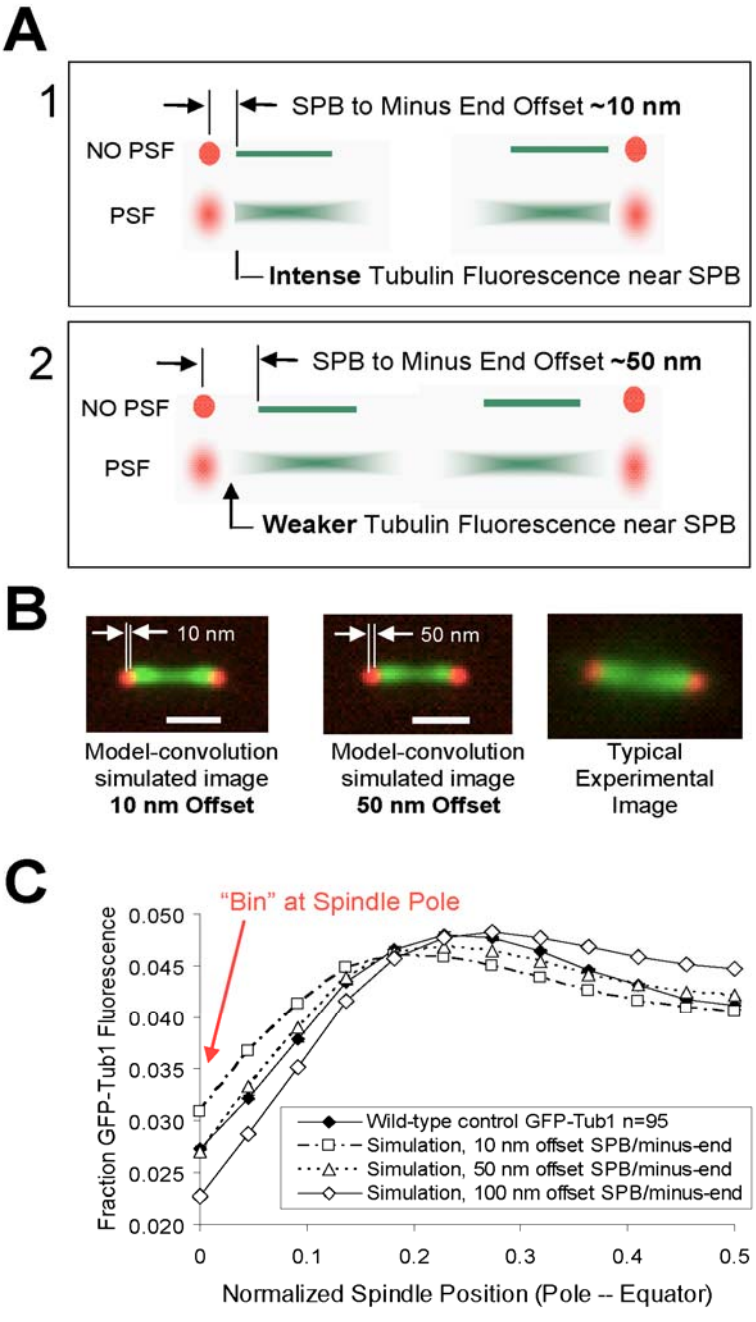
A
1
SPB to Minus End Offset ~10 nm
NO PSF
PSF
Intense Tubulin Fluorescence near SPB
2
SPB to Minus End Offset ~50 nm
NO PSF
PSF
Weaker Tubulin Fluorescence near SPB
B
10 nm
50 nm
Model-convolution simulated image 10 nm Offset
Model-convolution simulated image 50 nm Offset
Typical Experimental Image
C
"Bin" at Spindle Pole
Fraction GFP-Tub1 Fluorescence
0.050
0.045
0.040
0.035
0.030
0.025
0.020
0
0.1
0.2
0.3
0.4
0.5
Normalized Spindle Position (Pole -- Equator)
Wild-type control GFP-Tub1 n=95
Simulation, 10 nm offset SPB/minus-end
Simulation, 50 nm offset SPB/minus-end
Simulation, 100 nm offset SPB/minus-end

FIGURE 4.5: Reduced microtubule dynamicity alters the spatial gradient in tubulin turnover and kinetochore localization**.** (A) Representative raw GFP-Tub1 FRAP data for a β-tubulin (*tub2C254S*) mutant from a bin near the SPB (left), and another bin midway between the spindle equator and the SPB (right). Theoretical exponential fit curves calculated based on best-fit half-times by bin are drawn through each plot (solid line). (B) Experimental and simulated GFP-Tub1 FRAP for the β-tubulin mutant with reduced microtubule dynamicity compared to wild-type spindles. The rate of tubulin turnover was decreased in the β-tubulin mutant, especially near the SPB. The position of most rapid FRAP was shifted towards the spindle equator in the β-tubulin mutant (arrows). Simulation parameters and probability-of-fit (p-values) for the fit of the experimental data to the simulation are listed in Table 4.1.

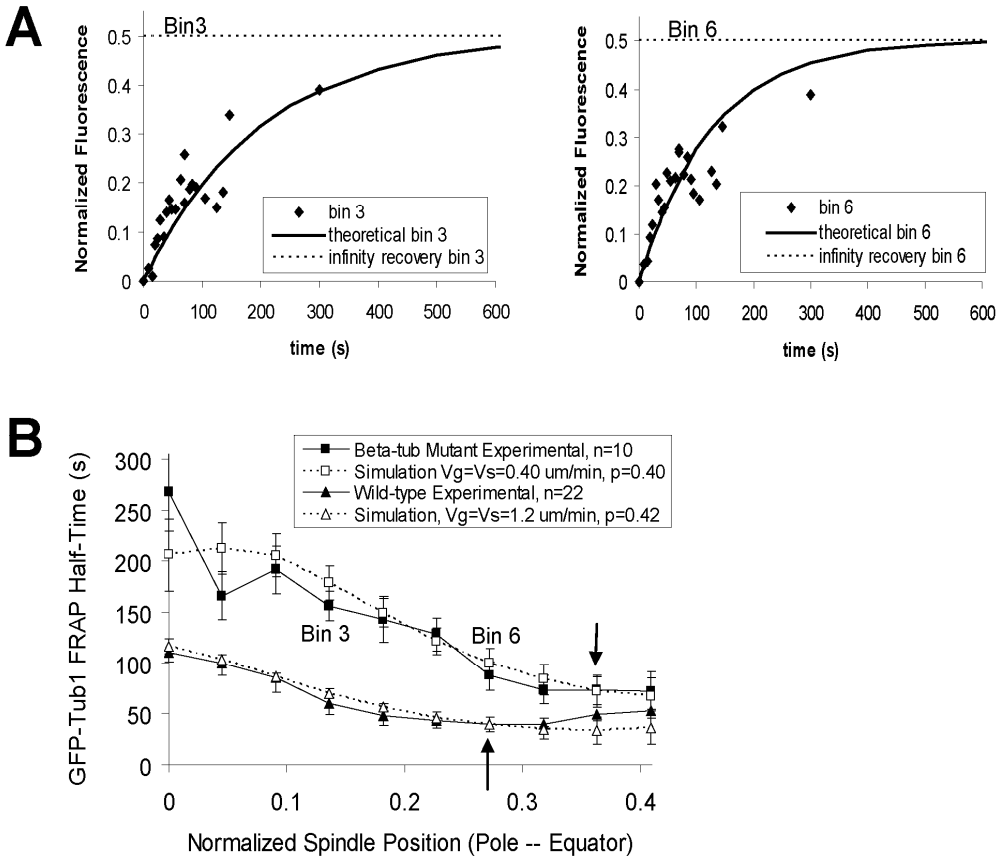

FIGURE 4.6: Simulation of kMT plus-end dynamics with reduced kMT growth and shortening velocity**.** (A) Spindle positions of a typical sister kinetochore pair over time in a wild-type simulation (Table 4.1; Simulation parameters) (B) Spindle positions of a typical sister kinetochore pair over time in a simulation with kMT growth and shortening velocities reduced three-fold (Table 4.1; Simulation parameters). Kinetochores in the simulation with reduced kMT velocities made shorter excursions as compared to wild-type controls. (C) Simulated frequency of plus-end positions by spindle location (Frequency of simulated wild-type plus-end position by spindle location (blue), Frequency of plus-end position by spindle location in simulation with reduced kMT growth and shortening velocities (red), Overlap zone between wild-type and slow velocity histograms (purple)). In simulations with reduced growth and shortening velocities, the distribution of plus-end positions by spindle location is narrowed (36% reduction in the standard deviation of kMT length).

Figure 4.6

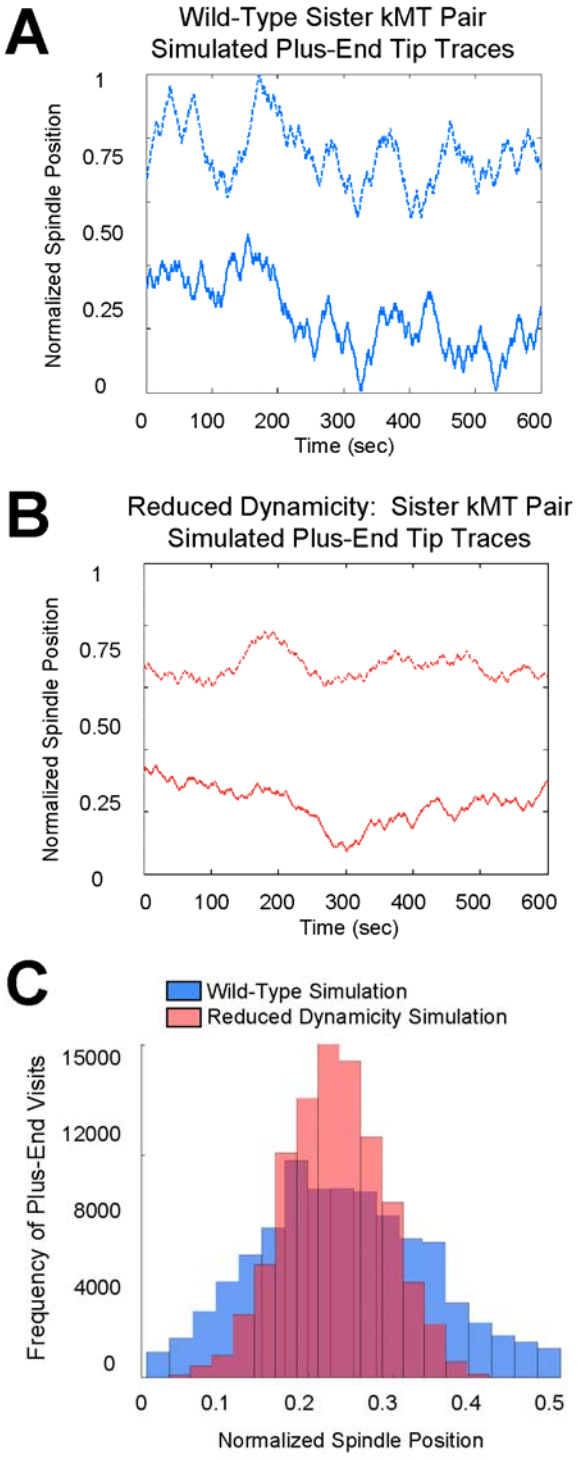
A
Wild-Type Sister kMT Pair
Simulated Plus-End Tip Traces
Normalized Spindle Position
1
0.75
0.50
0.25
0
0
100
200
300
400
500
600
Time (sec)
B
Reduced Dynamicity: Sister kMT Pair
Simulated Plus-End Tip Traces
Normalized Spindle Position
1
0.75
0.50
0.25
0
0
100
200
300
400
500
600
Time (sec)
C
Wild-Type Simulation
Reduced Dynamicity Simulation
Frequency of Plus-End Visits
15000
12000
8000
4000
0
0
0.1
0.2
0.3
0.4
0.5
Normalized Spindle Position

FIGURE 4.7: A β-tubulin mutation with reduced microtubule dynamicity has tightly clustered kinetochores and reduced kinetochore tension (A) Wild-type and β-tubulin mutant spindles (Cse4-GFP (green), Spc29-CFP (red)). Scale bar, 1000 nm. White arrows denote kinetochore clusters, which is shifted towards the spindle equator in the β-tubulin mutant. (B) Experimental and simulated comparison of kinetochore fluorescence (Cse4-GFP) in the β-tubulin mutant compared to wild-type. The peak kinetochore position is shifted towards the spindle equator in the β-tubulin mutant, such that sister kinetochore spacing is reduced. In addition, the kinetochore-associated fluorescence distribution curve reveals a sharp peak in Cse4-GFP fluorescence in the β-tubulin mutant, indicating that kinetochores are more tightly clustered within a half-spindle in the β-tubulin mutants as compared to wild-type spindles. (C) Representative simulated animations of wild-type and β-tubulin mutants (Supplemental Movies 1 and 2). In the simulation, a slight bias toward plus-end assembly of the β-tubulin mutant resulted in longer kMTs and reduced chromatin stretch (chromatin "spring" shown in yellow).

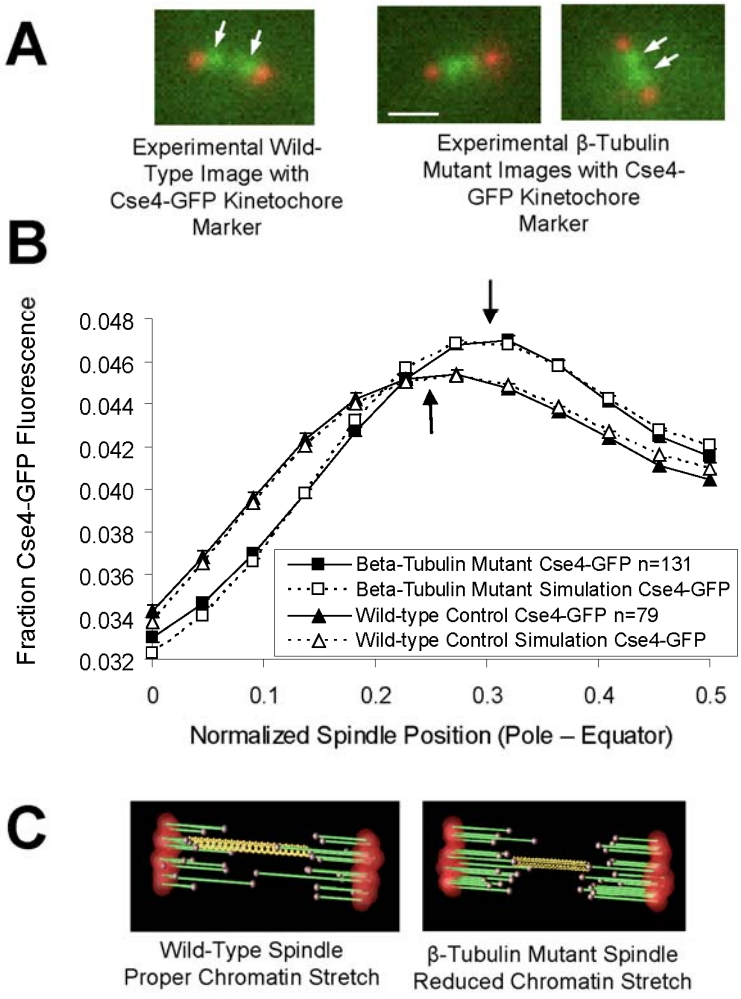

CHAPTER FIVE

CHROMOSOME CONGRESSION BY KINESIN-5 MOTOR-MEDIATED DISASSEMBLY OF LONGER KINETOCHORE MICROTUBULES

(Contributing Authors: Melissa Gardner, David Bouck, Leocadia Paliulis, Janet Meehl, Eileen O'Toole, Julian Haase, Adelheid Soubry, Ajit Joglekar, Mark Winey, E.D. Salmon, Kerry Bloom, and David J. Odde: *MG performed simulations, experiments, and image/data analysis; DB, JH, LP, and AS assisted with mutant strain construction, AJ performed protein counting experiments; JM and ET performed Electron Microscopy*)

Abstract

During mitosis, sister chromatids congress to the spindle equator and are subsequently segregated via attachment to dynamic kinetochore microtubule (kMT) plus-ends. A major question is how kMT plus-end assembly is spatially regulated to achieve chromosome congression. Here we find in budding yeast that the widely-conserved kinesin-5 sliding motor proteins, Cin8p and Kip1p, mediate chromosome congression by suppressing kMT plus-end assembly of longer kMTs. Of the two, Cin8p is the major effector and its activity requires a functional motor domain. In contrast, the depolymerizing kinesin-8 motor Kip3p plays a minor role in spatial regulation of yeast kMT assembly. Our analysis identified a model where kinesin-5 motors bind to kMTs, move to kMT plus ends, and upon arrival at a growing plus-end promote net kMT plus-end disassembly. In conclusion, we find that length-dependent control of net kMT assembly by kinesin-5 motors yields a simple and stable self-organizing mechanism for chromosome congression.

Introduction

A central question in biology is how replicated chromosomes are properly segregated during mitosis, such that exactly one copy of each chromosome moves to each of the two daughter cells [25]. In eukaryotes, chromosome-associated kinetochores attach to dynamic microtubule (MT) plus ends, while MT minus ends in turn generally attach to spindle poles [55]. Once properly bioriented, so that one kinetochore is mechanically

linked via one or more MTs to one pole and its sister kinetochore linked to the opposite pole, the sister chromosomes move toward the equator of the mitotic spindle, a process known as congression (Fig. C.1). In budding yeast, congression of bioriented sister chromosomes requires that the associated kinetochore microtubule (kMT) plus ends add tubulin subunits efficiently when they are near the poles (i.e. when kMTs are short), but inefficiently when near the equator (i.e. when kMTs are relatively long; [29, 50, 108]. The origin of this spatial gradient in net kMT plus end assembly is currently unknown.

One possible explanation for the spatial gradient of kMT net assembly derives from studies with the budding yeast kinesin-8 molecular motor Kip3p, which showed that processive plus-end directed depolymerizing motors could result in length-dependent disassembly of MTs *in vitro* [109]. However, to date there has not been an *in vivo* observation of length-dependent MT regulation via Kip3p or any other motor. Previous *in vivo* studies of Kip3p showed that cytoplasmic microtubule dynamics are altered by Kip3p, and that *KIP3* deletion results in spindle positioning defects [110]. Whether these *in vivo* effects resulted from the length-dependent control of MT assembly as proposed by Varga et al. (2006) was not clear. As a result, it is not clear at this point whether this interesting phenomenon identified *in vitro* by Varga et al. plays an important role in a biological process.

We now find that the kinesin-5 molecular motors, mainly Cin8p and, to a lesser extent, Kip1p, exhibit length-dependent control of MT assembly, and so mediate the spatial gradient in kMT plus end net assembly that drives congression during mitosis. Since their discovery, kinesin-5 motors have been viewed as mitosis-specific sliding motors that cross-link antiparallel MTs and exert outward extensional forces on the poles [111-116]. The results were surprising to us because kinesin-5 (Eg5 in vertebrates) is not known to affect microtubule assembly. Surprisingly, the disassembly-promoting activity that we now report is not specific to kMTs, since we found that Cin8p promotes disassembly of cytoplasmic astral MTs (aMTs) as well.

Because the kinesin-5 mediated length-dependent kMT disassembly is similar to that described by Varga et al. for Kip3p on MTs *in vitro*, we examined the role of Kip3p in controlling kMT assembly *in vivo*. We found that Kip3p only weakly affects kMT

dynamics and is not a major mediator of congression. Our computer simulations show that the difference in kinesin-5 and kinesin-8 behavior can be accounted for simply by the ability of tetrameric kinesin-5 to cross-link microtubules, a property lacking in dimeric kinesin-8. This naturally biases kinesin-5 towards kMT plus ends and kinesin-8 toward interpolar MT plus ends. Together, the results presented here suggest a simple explanation for metaphase chromosome congression in budding yeast by identifying a microtubule length-dependent disassembly-promoting activity *in vivo* that is associated with kinesin-5 molecular motors.

Results

Simulated phenotypes of a disrupted gradient in net kMT plus end assembly

MTs self-assemble from αβ-tubulin heterodimers via an unusual process called "dynamic instability" where MTs grow at a roughly constant rate, then abruptly and stochastically switch to shortening at a roughly constant rate, and then switch back to growth again and so forth. The switch from growth to shortening is called "catastrophe" and the switch from shortening to growth is called "rescue" [117]. Together, the four parameters of dynamic instability, growth rate (V_g [=] μm/min), shortening rate (V_s [=] μm/min), catastrophe frequency (k_c [=] 1/min), and rescue frequency (k_r [=] 1/min), define the net assembly state of MTs. If the mean length added during a growth phase ($L_g=V_g/k_c$ [=] μm) exceeds the mean length lost during shortening ($L_s=V_s/k_r$ [=] μm), then, there will be net growth, otherwise there will be net shortening. If the parameters depend upon position in the cell, then there can exist net growth in one part of the cell, and net shortening in another part of the cell. At the transition between these regions there will be no net growth, and this will create an attractor for plus ends, provided net growth is favored for short MTs and net shortening favored for long MTs (Fig. C.1).

Our previous studies showed that net kMT plus-end assembly in budding yeast metaphase spindles is favored for plus-ends located near the spindle pole bodies (SPBs) (i.e. for short kMTs), and inhibited for plus-ends near the equator (i.e. for longer kMTs) (Fig. C.1)[29, 50, 51, 108]. This spatial control over net kMT assembly was most readily explained using a catastrophe gradient in kMT plus-end assembly that creates two

attractor points where there is no net assembly, one attractor in each half-spindle (Fig. 5.1A, left, dotted line denotes the location of the attractor point for one half-spindle). These two attractors establish the bilobed distribution of kinetochores into the two distinct clusters that are characteristic of the congressed metaphase spindle (Fig. C.1).

We were interested in identifying the molecules responsible for this net assembly gradient, and so we simulated the expected phenotypes for changes in expression level of a putative spatial regulator of net kMT plus-end assembly. Fig 5.1A (left) shows a simulation of a wild-type budding yeast metaphase spindle where kMT plus-end assembly is favored near the SPB (where kMTs are short), and suppressed near the spindle equator (where kMTs are longer). Note that in the haploid budding yeast there are 16 kMTs emanating from each SPB, for a total of 32 kMTs, and ~8 longer interpolar MTs (ipMTs), for a total of 40 MTs in the metaphase spindle (for the sake of clarity the ipMTs are omitted from the animation in Fig.5.1). If a molecule promoted disassembly of longer kMTs in wild-type cells, and was then deleted, the predicted phenotype would be longer kMTs with kinetochores more broadly distributed along the spindle, as depicted in Fig. 5.1A, center. Conversely, overexpression of a spatial assembly regulator would produce very short kMTs with highly focused clusters of kinetochores near the SPBs, as depicted in Fig. 5.1A, right. These model predictions establish specific requirements for experimental identification of a spatial kMT plus-end assembly regulator.

The yeast kinesin-5 motors, Cin8p and Kip1p, control kinetochore positions

While studying various deletion mutants, we observed that *cin8Δ* mutants lost the clustering of kinetochores within each half spindle (measured by labeling of a kinetochore component, Cse4-GFP, in live cells), as shown in Fig. 5.1B, consistent with an earlier report [118]. Quantitative analysis of experimental Cse4-GFP fluorescence revealed that the peak fluorescence intensity also shifted toward the spindle equator, as predicted by simulations used to model deletion of a molecule that promotes net kMT plus-end disassembly of longer kMTs (Fig. 5.1B, p= 0.82, where p is the probability that the experimental Cse4-GFP fluorescence distribution curve is consistent with the simulated curve; see Methods for calculation procedure). The simulated Cse4-GFP

fluorescence distribution was obtained by convolution of the simulated fluorophore positions with the imaging system point spread function and noise, a computational process we call "model-convolution" [29, 119]. Deletion of the other yeast kinesin-5 motor, *KIP1*, had a similar, but weaker, phenotype to *cin8Δ*, with a moderate shift of kinetochores towards the spindle equator (Fig. C.4A). We note that the effects of *CIN8* deletion were not due to the well known moderate decrease in steady-state spindle length [114, 116, 120, 121], since we selected spindle lengths that were equal for both wild-type and *cin8Δ* cells (although results were similar regardless of the spindle length population analyzed (Fig. C.2)). To further establish that the effects of *CIN8* deletion were not due to changes in metaphase spindle lengths, we performed separate experiments using histone H3 repression mutants, which make centromeric chromatin more compliant and thus increase average spindle length [122]. In these longer spindles, wild-type kinetochores were still bilobed while *cin8Δ* kinetochores were still disorganized (Fig. C.4B), showing an insensitivity of the disorganization phenotype to spindle length. In addition, *bim1Δ* mutant spindles with short spindle lengths (similar to *cin8Δ* mutant spindle lengths, Fig. C.3) did not result in spindle disorganization (Fig. C.3). We conclude that kinetochores are declustered in kinesin-5 deletion mutants, independent of the spindle length.

If Cin8p mediates net kMT plus-end disassembly, then Cin8p overexpression will result in short kMTs with focused clusters of kinetochores, one near to each SPB (Fig. 5.1A, right). As shown in Fig. 5.1C, kinetochore clusters were indeed tightly focused within each half-spindle and much closer to each SPB. Spindles overexpressing Cin8p also have increased length due to increased motor sliding between oppositely oriented central spindle non-kMTs (also known as interpolar MTs) [121] (Fig. C.7). Despite the spindles being longer, kinetochores in Cin8p overexpressing cells were still ~50% closer to SPBs than wild-type controls (Fig. 5.1C), consistent with Cin8p overexpression resulting in shorter kMTs (Fig. C.7). We conclude that Cin8p, and, to a lesser extent, Kip1p, promote net kMT plus-end disassembly as judged by kinetochore position.

GFP-tubulin fluorescence confirms that kMTs are longer in cin8Δ mutants

If Cin8p promotes net kMT plus-end disassembly, then *CIN8* deletion will result in longer kMTs, producing a continuous "bar" of fluorescent tubulin along the length of the spindle (Fig. 5.2A, right), rather than the wild-type fluorescent tubulin "tufts" that emanate from each of the two SPBs (Fig. 5.2A, left). In experiments with GFP-Tub1, quantitative analysis of tubulin fluorescence in *cin8Δ* mutants revealed a shift in fluorescence towards the spindle equator, indicating that kMT length was increased (Fig. 5.2A, bottom). The distribution of GFP-Tub1 was quantitatively predicted in simulations using the same parameter set used to model kinetochore organization in *cin8Δ* mutants (Fig. 5.2A, p=0.22, Table C.2). In addition, we found that the ratio of spindle tubulin polymer signal to free tubulin signal outside of the spindle area is 2.0:1 in wild-type spindles (n=27), and 3.2:1 in *cin8Δ* mutant spindles (n=35), which represents an increase in tubulin polymer relative to free tubulin of ~62% in *cin8Δ* mutants as compared to wild-type cells ($p<10^{-5}$). This suggests that the increased kMT length in *cin8Δ* spindles is not the result of an overall increase of tubulin level, but rather reflects a thermodynamic shift toward increased net kMT assembly.

Cryo-electron tomography confirms that kMTs are longer in cin8Δ mutants

To directly visualize individual spindle MTs, we used cryo-electron tomography to reconstruct complete mitotic spindles from wild-type and *cin8Δ* mutant spindles (Fig. 5.2B, supplemental movies 1,2). To control for the moderate spindle length shortening in *cin8Δ* mutants, we selected spindles of similar length in the wild-type and mutant cell populations. Consistent with model predictions, we found a substantial increase in mean MT length in *cin8Δ* mutant spindles as compared to wild-type spindles (Fig. 5.2B, 41% increase in mean overall length, p=0.0007, statistical consistency between cells confirmed by ANOVA in Table C.1). Total non-kMT number also increased in *cin8Δ* as compared to wild-type spindles (42 % increase in total MT number, p=0.002), demonstrating that the total polymer level in the *cin8Δ* cells is increased relative to wild-type cells. Interestingly, the mean length of the 8 longest MTs in each spindle, presumably interpolar MTs (ipMTs), is not statistically different between wild-type and *cin8Δ* mutant cells (wild-type = 931 +/- 81 nm (mean±s.e.m., n=33 MTs); *cin8Δ* = 1141

+/- 25 nm (n=41 MTs), p=0.05).This result suggests that deletion of *CIN8* most significantly affects the kMT length rather than ipMT length.

In summary, the electron microscopy results independently confirm the model predictions and the light microscopy studies by demonstrating that kMTs are indeed longer in *cin8Δ* cells. We conclude that Cin8p participates in a process that promotes net kMT disassembly.

A Cin8p motor-domain mutant has increased kMT length

To test whether kMT length regulation requires the Cin8p motor domain, the organization of fluorescent tubulin was examined in the *cin8-F467A* mutant [123]. Previous studies found that the *cin8-F467A* mutation reduced the binding of Cin8p to microtubules *in vitro* by 10-fold [123] . Similar to the *cin8Δ* mutants, analysis of GFP-Tub1 distribution in the *cin8-F467A* mutants produced a continuous "bar" of fluorescent tubulin along the length of the spindle (Fig. 5.2C, right), rather than the wild-type fluorescent tubulin "tufts" (Fig. 5.2C, left). The similarity between the *cin8Δ* and the *cin8-F467A* mutant phenotypes suggests that the kMT disassembly promoting activity of Cin8p requires motor binding to kMTs. Furthermore, since our previous studies showed that net kMT assembly is promoted when kMTs are short and suppressed when kMTs are long (i.e. when kMT plus ends extend into the equatorial region, Fig 5.1A), we also conclude that Cin8p-mediated suppression of kMT assembly is specific to longer kMTs.

Cin8p mediates the gradient in net kMT assembly as measured by GFP-tubulin FRAP

To further test whether Cin8p specifically suppresses assembly of longer kMTs and thus mediates a gradient in net kMT assembly, we measured the spatial gradient in tubulin turnover within the mitotic spindle. In our previous work, we found that tubulin turnover, as measured by spatially resolved GFP-tubulin Fluorescence Recovery After Photobleaching (FRAP), is most rapid where kMT plus ends are clustered in wild-type cells [108] . If Cin8p mediates a gradient in net kMT assembly, then its deletion is predicted to result in loss of the gradient in FRAP half-time. As shown in Fig. 5.2D, deletion of *CIN8* results in loss of the tubulin turnover gradient, as predicted by the model

(Fig 5.1A, center). In general, the kMTs remain dynamic (overall $t_{1/2}$=46±15 s integrated over the half-spindle in *cin8Δ* (n=11), compared to $t_{1/2}$=63±30 s for wild-type [108], (n=22; p=0.03; Fig. C.5), and have a high fractional recovery (~90% for *cin8Δ*, compared to ~70% for wild-type [59, 108]).

In simulating the *cin8Δ* GFP-tubulin FRAP experiment, the best fit between theory and experiment is achieved with a flattened spatial gradient in net kMT plus-end assembly (e.g. a flattened catastrophe gradient), and with values for MT plus-end growth and shortening rates that are slightly higher than in wild-type simulations (Table C.2). This result explains why FRAP is relatively rapid along the entire length of the half-spindle in the *cin8Δ* mutants, and is consistent with recent studies that find increased chromosome oscillation velocities upon deletion of the human kinesin-8 motor Kif18A [124]. (reviewed in [125]). Although simulations suggest that Cin8p acts to weakly suppress MT plus-end growth and shortening rates in wild-type cells, the higher MT plus-end growth and shortening rates in *cin8Δ* simulations are not by themselves sufficient to reproduce the *cin8Δ* mutant phenotype in Figures 5.1B and 5.2A. In summary, we find that the tubulin-FRAP studies confirm that Cin8p mediates a spatial gradient in kMT assembly dynamics.

Deletion of the kinesin-8 motor Kip3p does not perturb congression

Recent studies found that the kinesin-8 molecular motor Kip3p acts as a length-dependent depolymerase both i*n vitro* and *in vivo* [109], and further studies have implicated the human kinesin-8 molecular motor Kif18A in the regulation of chromosome oscillation amplitude [124] and chromosome congression [126]. Thus, we asked whether Kip3p deletion would perturb kMT length organization in the yeast mitotic spindle. Interestingly, deletion of *KIP3* does not produce the continuous "bar" of fluorescent tubulin along the length of the spindle that is characteristic of *cin8Δ* spindles, but rather shows wild-type fluorescent tubulin "tufts" (Fig. 5.2E). Although microtubule organization appears wild-type, spindle lengths are moderately increased in *kip3Δ* cells, as previously reported [127] (mean spindle lengths in Fig. 5.2E, : WT: 1.60±0.22; *kip3Δ*: 1.97±0.15 μm). Thus, Kip3p regulates spindle length, possibly through regulation of

ipMT lengths, while Cin8p regulates kMT length without a measurable effect on ipMT lengths. Regardless of effects on ipMTs, the effect of Kip3 on kMTs is weak compared to the effect of Cin8, and is insufficient to establish congression.

Cin8p promotes shortening of astral MTs in the cytoplasm

MTs are densely packed in the yeast mitotic spindle (Fig.5.2B), and so it is difficult to resolve individual spindle MTs via fluorescence microscopy. In contrast, yeast astral MTs (aMTs) are normally much fewer in number (1-3) and splayed apart (Fig. 5.3A) [73, 74]. Because Kip3p is known to affect aMT dynamics, [110, 128, 129], but the effect of Cin8p is not known, we then examined the effect of motor deletion on aMTs outside of the mitotic spindle. Indeed, we found that aMT lengths were statistically longer in *kip3Δ* mutants as compared to wild-type cells (Fig. 5.3B,C), consistent with previous studies [110, 128].

A recent report suggests that Cin8p plays a role in spindle positioning through an aMT-dependent mechanism, and so, coupled with our results for kMTs, we hypothesized that Cin8p also suppresses aMT assembly [130, 131]. Using GFP-tubulin fluorescence microscopy, we measured the length of individual aMTs in the cytoplasm (Fig. 5.3B) [70, 73, 74]. Consistent with the behavior of kMTs, aMTs were longer in *cin8Δ* mutants relative to wild-type cells (Fig. 5.3 B,C; Fig. C.6). In addition, a previous study showed that aMT numbers are not decreased in *cin8Δ* mutants [130], consistent with an overall increase in both kMT and aMT polymer in *cin8Δ* mutants. Interestingly, aMT lengths in the *cin8-F467A* mutants with reduced binding of Cin8p to microtubules were also statistically longer than wild-type aMTs (Fig 5.3C). Conversely, overexpression of Cin8p resulted in shorter aMTs (Fig 5.3 B,C, Fig. C.6).

Since the tubulin polymer level in the *cin8Δ* cells increases in both the nucleus and in the cytoplasm, these results argue against a simple repartitioning of tubulin (or some other Cin8p-dependent assembly-promoting factor) from the cytoplasm into the nucleus in response to *CIN8* deletion. Conversely, MT polymer levels decrease in both compartments upon Cin8p overexpression.

One possible reason why both kMTs and aMTs are longer in *cin8Δ* cells is that *CIN8* deletion indirectly promotes MT assembly globally. To test this hypothesis, we shifted Cin8p from the nucleus to the cytoplasm while keeping the overall Cin8p expression level approximately constant. This shift was achieved by deleting the nuclear localization sequence (NLS) of Cin8p (as previously described) [132]. Because budding yeast undergoes a closed mitosis, deleting the NLS decreases the nuclear Cin8p concentration and increases the cytoplasmic Cin8p concentration [132]. We found that *cin8-nlsΔ* spindle MTs had a flat GFP-Tub1 fluorescence distribution, similar to *cin8Δ* cells (i.e. no tufts, Fig. 5.8A). This result is consistent with net kMT assembly in the absence of Cin8p locally in the nucleus (Figs. 5.3B, C.8A). Importantly, and in contrast to *cin8Δ* cells, aMT lengths in *cin8-nlsΔ* cells were shorter than in wild-type cells (Fig. 5.3 B,C; $p<0.001$, Fig. C.8C), consistent with elevation of Cin8p concentration locally in the cytoplasm. These results indicate that Cin8p acts locally in a given cellular compartment, rather than globally throughout the entire cell, to influence the local MT assembly state.

Together, these results suggest that Cin8p and Kip3p act similarly to suppress assembly of aMTs outside of the mitotic spindle. We then asked how Cin8p could act to promote kinetochore congression through suppression of kMT plus-end assembly, while Kip3p appears to regulate spindle length, possibly through suppression of ipMT plus-end assembly.

A model for Cin8p motor interaction with kMTs

Because Cin8p requires microtubule binding to promote length-dependent kMT plus-end disassembly, we hypothesized that Cin8p acts directly on kMT plus ends, either by itself or with a binding partner. To test the direct-interaction hypothesis, we first predicted the spatial distribution of Cin8p motors on kMTs via computational modeling. As a starting point, we extended our previous model for individual kMT plus-end dynamics [50] to also include the dynamics of microtubule-associated kinesin-5 molecular motors. This motor model assumes that motors reversibly attach and detach,

cross-link MTs, and move toward MT plus ends (supplemental movies 3,4; Fig. C.9, C.10) [112, 123, 133, 134].

Cin8-GFP is distributed in a gradient along kMTs

As shown in Fig. 5.4A, this simple model for motor dynamics predicts that, at steady-state, a substantial fraction of the motors cross-link parallel kMTs emanating from the same SPB (green). In the simulation, these motors walk to a kMT plus end and follow the end as it grows until catastrophe occurs, at which point the motor head detaches (supplemental movie 4). By repetitive photobleaching of Cin8-3XGFP labeled spindles, we were able to experimentally observe spindle-associated Cin8p motor dynamics in the "speckle" regime. Similar to the motor model simulation, we observed motor movement in the spindle with a mean velocity of 58 +/- 24 nm/sec (mean +/- s.d., n=10) (Fig. 5.4B; see Fig. C.9 and supplemental material).

To test the motor model, we predicted the distribution of Cin8-GFP fluorescence in live cells as a function of spindle position, and then measured it experimentally. As shown in Fig. 5.4C, the motor model is able to quantitatively reproduce the experimentally observed Cin8-GFP motor fluorescence distribution (green) relative to kinetochores as measured by Ndc80-cherry fluorescence (red) ($p=0.35$). We found that in order to correctly reproduce the Cin8-GFP fluorescence distribution, simulated motors are required to track growing but not shortening kMT plus-ends, resulting in a slight, but detectable, shift in the peak of motor-associated fluorescence away from kinetochores and towards SPBs (see supplementary material for analysis of various alternative models, Fig. C.10). In the motor model, this shift is the result of the increased motor off-rate imposed by shortening kMT plus-ends within the kinetochore clusters (Fig. 5.4C, red). In benomyl-treated spindles with stabilized microtubules, this shift is decreased, such that the motor-associated fluorescence is nearly coincident with kinetochores (Fig. C.13). Thus, the results with benomyl further support the hypothesis that kMT plus-end assembly dynamics control motor dynamics, in particular motor detachment from kMT plus ends.

The Kip1-GFP fluorescence distribution was qualitatively similar to the Cin8-GFP fluorescence distribution, but was relatively less focused into two clusters, consistent with a weaker affinity of Kip1p for MTs (Fig. C.11).

By normalizing the Cin8-GFP fluorescence to the local kMT density, we then calculated the Cin8-GFP density on a per kMT basis (see methods for details). As shown in Fig. 5.4D, Cin8-GFP concentration per kMT gradually increases with increasing distance from the SPB, as predicted by the motor model. We conclude that αβ-tubulins at the plus ends of longer kMTs are more likely to be associated with Cin8-GFP than αβ-tubulins at the plus ends of shorter kMTs.

A Cin8-GFP FRAP half-time gradient mirrors the GFP-tubulin FRAP half-time gradient

If motors rapidly detach from shortening kMT plus ends, then the rate of Cin8-GFP turnover on the spindle should be fastest in the vicinity of shortening kMT plus ends. Specifically, the motor model predicts there will be a spatial gradient in Cin8-GFP FRAP half-time that is very similar to the GFP-tubulin FRAP half-time gradient that we reported previously [108] (Fig. 5.2C). Alternatively, the Cin8-GFP FRAP half-time could be longest where kMT plus-ends are clustered, indicative of high affinity binding to the kinetochore [118] , which would also in principle explain the gradient in Cin8-GFP intensity observed experimentally in Fig. 5.4C. We performed kinesin-5-GFP FRAP experiments, and found that motor turnover is most rapid in the location of kMT plus-end clustering, (Figs. 5.4E, S12; $p<1x10^{-10}$ as compared to half-times near the SPBs), suggesting that Cin8p motors rapidly detach from shortening kMT plus ends. Mean Kip1-GFP FRAP half-times were ~50% faster than Cin8-GFP recovery half-times (Fig. C.12), again suggesting that Kip1p has a lower affinity for microtubules than Cin8p. The Cin8-GFP FRAP results are all consistent with a model in which motors frequently interact with kMT plus-ends in a length-dependent manner.

To summarize our studies of spindle-bound kinesin-5 dynamics, we find that kMT-bound kinesin-5 motors are distributed in a spatial gradient along kMTs, with their concentration increasing with increasing distance from the SPB. Consistent with the observed gradient, we also find that kinesin-5 motors frequently interact with, and are

controlled in their detachment from the MT lattice by, dynamic kMT plus ends. Because Cin8p suppresses assembly of longer kMT to mediate kinetochore congression, while Kip3p acts primarily to regulate metaphase spindle length, we then asked how the behavior of the kinesin-5 motor Cin8p compares to the behavior of the kinesin-8 motor Kip3p in the mitotic spindle environment.

Cin8-GFP concentrates near kMT plus-ends, while Kip3-GFP distribution is diffuse

As shown in Fig. 5.5A and described above, Cin8-GFP concentrates near kMT plus-ends. This localization is reproduced in simulation because a substantial fraction of the homotetrameric Cin8 motors cross-link parallel kMTs emanating from the same SPB, and then walk efficiently towards the plus-ends of both cross-linked microtubules. In contrast, motors crosslinking anti-parallel microtubules in the simulation (i.e., microtubules attached to opposite SPBs, Fig 5.4A, magenta) are not able to make progress towards the plus-ends of either microtubule to which they are attached, as the motor heads walk in opposite directions. These anti-parallel attached motors quickly stall, and remain stationary until the detachment of one or both heads. Interestingly, since ipMTs run nearly the full length of the spindle, their plus-ends reside in a highly anti-parallel environment, with ~4 ipMT plus-ends surrounded by ~20 anti-parallel MTs attached to the opposite SPB. Thus, the cross-linking properties of the tetrameric kinesin-5 motor naturally limit their processivity near to ipMT plus-ends.

In contrast, dimeric Kip3p motors attach to a single microtubule, and thus their processivity is not hindered by crosslinking to anti-parallel microtubules. In this case, the longer ipMTs acts as larger antennas, attracting larger numbers of plus-end directed Kip3p motors to their ends [109]. As shown in Fig 5.5A, while Cin8-GFP is specifically concentrated near to kMT plus-ends, Kip3-GFP is more diffusely distributed along the length of the spindle. Importantly, the relative concentration of Kip3-GFP is higher near to where the ipMT plus-ends are located (Fig 5.5A) as compared to Cin8-GFP, whose relative concentration is higher near to where kMT plus-ends are located (Fig 5.5A).

To test this interpretation of the localization data, simulations were run that reproduced both Cin8-GFP and Kip3-GFP localization in the spindle (Fig 5.5A). In these

simulations, Cin8-GFP is a MT crosslinking motor with simulation parameters as described above, and Kip3p is a slightly faster non-crosslinking motor (Kip3p motor velocity = 75 nm/sec) [110]) with otherwise identical simulation parameters. In these simulations, ~90% of Cin8p motor visits to all MT plus-ends were to kMT plus-ends specifically, while the majority of Kip3p plus-end visits were to ipMT plus-ends (~60%, Fig. 5.5B). Thus, Cin8p molecular motors mediate congression by suppressing the assembly of kMT plus-ends, while Kip3p acts primarily to limit assembly of ipMT plus-ends. The two different outcomes can be modeled simply by either including cross-linking (Cin8p) or not (Kip3p).

Cin8-GFP motors on aMTs

Because Cin8p promotes aMT disassembly (Fig. 5.3), we considered whether the motor model applies to cytoplasmic aMTs as well. In contrast to the densely packed kMTs, 1-3 individual aMTs can be readily observed in the cytoplasm so that individual motor interaction with aMTs should also be readily observable. Using time-lapse microscopy we were able to visualize Cin8-NLSΔ-3XGFP interacting with 1-3 individual aMTs. As shown in Fig, 5.6A (left), Cin8-NLSΔ-3XGFP moves persistently in the plus-end direction along stationary mcherry-Tub1 labeled aMTs (supplemental movie 6). Motors did not move in the minus end direction, consistent with the motor model and the inferred motor behavior on kMTs. The mean motor velocity was 15 +/- 3.3 nm/sec (mean +/- s.d., n=8), which is similar to previously reported aMT plus-end growth rates of 8 - 23 nm/sec [70, 73, 74, 110, 135], suggesting that motors track growing aMT plus ends. Since Cin8-GFP was distributed along kMTs in a gradient of increasing motor with increasing distance from the SPB, we were interested to see whether a similar motor gradient occurs on aMTs. As expected from the motor model and similar to the behavior of motors on kMTs, we found that Cin8-NLSΔ-GFP fluorescence is distributed along the length of aMTs with a peak fluorescence shifted slightly away from aMT plus ends (Fig. 5.6B,C). We then normalized the motor fluorescence to the aMT density, and, as shown in Fig. 5.6D, found a spatial gradient of Cin8-NLSΔ-GFP that is very similar to the gradient observed on kMTs and to the gradient predicted by the motor model. An

interesting feature of both the model and the experiment is a slight dip in the motor concentration at the peak aMT plus ends location (gray arrow in Fig. 5.5D). This dip was also apparent in the kMT data and simulation, and again suggests that dynamic MT plus ends mediate motor detachment from the MT lattice. We conclude that Cin8p interacts frequently with aMT plus ends in a manner similar to its interaction with kMT plus ends, and consistent with the motor model. We then asked if the spatially regulated interaction of Cin8p with kMT plus-ends, together with the disassembly-promoting activities of Cin8p, could act to mediate chromosome congression in the yeast metaphase spindle.

Cin8p-mediated "self-organized" model for metaphase kinetochore organization

The model for kinesin-5 motor dynamics that best agrees with the experimental data described above is one in which motors bind randomly to kMTs (Fig. 5.7A, top) and then walk toward kMT plus-ends, where they act to promote net kMT disassembly (Fig. 5.7A, middle). The longer the MT, the more sites there are for motors to attach, which results in more motors at the plus end, and the more that assembly will be disrupted. Once net disassembly occurs (e.g. via a catastrophe), then motors detach from the shortening kMT plus-end (Fig. 5.7A, bottom). Importantly, because simulated motors bind randomly to microtubules and are plus-end directed, the motor model predicts that the number of motor interactions at kMT plus-ends will increase with increasing kMT length, as shown recently for kinesin-8 molecular motors *in vitro* [109, 126] (Figs. 5.4D, 5.6D).

To determine if simulated Cin8p motors could mediate chromosome congression via their disassembly-promoting activity at kMT plus-ends, we allowed the Cin8p motors to promote catastrophe as they concentrate on kMT plus-ends in the motor model simulation as described above. In this "self-organized" model, there is no externally imposed "catastrophe gradient" to regulate kMT lengths (as in Fig. 5.1A), but rather the catastrophe-promoting motors naturally concentrate on kMT plus-ends in a length-dependent manner. Thus, by starting the simulation with a random organization of motors and kMT lengths (Fig 5.7B, top), we found that self-organization of kinetochores into a bi-lobed metaphase configuration arises naturally when Cin8p motors promote

catastrophe at kMT plus-ends (Fig. 5.7B, bottom; supplemental movie 5). Here, the catastrophe-promoting Cin8p motors self-organize a simulated bi-lobed spindle in which both Cin8-GFP and Ndc80-cherry fluorescence distributions are qualitatively consistent with experimental results (Fig. 5.7C). By allowing motor presence at the kinetochore to directly promote catastrophe, the theoretical kMT plus-end "catastrophe gradient" model (Fig 5.1A) is closely reproduced (Fig. 5.7D). As in Fig 1A, this gradient serves to establish the bilobed distribution of kinetochores into the two distinct clusters that are characteristic of the congressed metaphase spindle (Fig. C.1). Similar to experimental results in *cinΔ* mutants, reducing the motor number in the "self-organized" simulation disrupts the gradient in kMT assembly and thus leads to disorganization of the spindle (Fig. C.14).

Discussion

Our results demonstrate that kinesin-5 motors, in particular Cin8p, promote net kMT and aMT disassembly *in vivo*. Since net kMT assembly is specifically suppressed for longer kMTs (i.e. whose plus ends are near the equator) during yeast metaphase, kinesin-5 motors must be mediating their effect, either alone or with binding partners, most strongly on longer kMTs. It is this length-dependent regulation of net kMT plus end assembly that establishes the congressed state of chromosomes that is characteristic of metaphase. These results are surprising to us, since the only established activity of kinesin-5 is its well known antiparallel MT sliding activity, and, to our knowledge, no effect on MT assembly has been reported previously. We also found that Cin8-GFP interacts frequently with MT plus ends in vivo, and exists in a spatial gradient on MTs. The close correspondence of the gradient in net kMT assembly and the gradient in motor distribution strongly suggests that Cin8p, either alone or with a binding partner, directly promotes kMT disassembly via its presence at the kMT plus-end. In addition, this conclusion is strengthened by the close similarity between the *cin8Δ* mutant and the cin8 motor-domain mutant (*F467A*) phenotypes.

It is interesting to consider the consequences of the disassembly promotion for spindle length regulation. It is well established that kinesin-5 promotes spindle pole

separation by generating an outward extensional force, presumably via cross-linking of antiparallel MTs. The newly identified disassembly-promoting activity shortens kMTs, and thereby should generate an inward pulling force on the spindle poles via stretching of the intervening chromatin between the sister kMT plus ends. Thus, the two activities of Cin8p antagonize each other, and are expected to result in stable spindle pole separation during yeast metaphase.

As described above, the model for kinesin-5 motor dynamics in the metaphase budding yeast mitotic spindle that best agrees with experimental data is one in which motors bind randomly to kMTs (Fig. 5.7A, top), and then walk toward kMT plus-ends where they act to promote net kMT disassembly (Fig. 5.7A, middle). Here, because longer kMTs have a larger number of possible motor binding sites, the motor model predicts that the number of motor interactions at kMT plus-ends will increase with increasing kMT length, as shown recently for kinesin-8 molecular motors *in vitro* [109, 126]. Interestingly, the plus-ends of ipMTs, which are the longest MTs in the yeast mitotic spinde, may attract fewer Cin8p motors than the plus-ends of kMTs, simply because ipMT plus-ends are surrounded by potential anti-parallel motor attachments, frustrating the plus-end motility of crosslinking Cin8p motors. This explanation is supported by results for the non-crosslinking depolymerizing motor Kip3p, whose localization and deletion phenotypes are distinct from that of Cin8p. We found that Kip3-GFP behavior could be reproduced by taking the Cin8-GFP simulation and turning "off" the cross-linking. In this case, the non-crosslinking motor tends to accumulate more onto ipMTs, and less so onto kMTs. The simple physical feature of MT crosslinking, enabled in the tetrameric Cin8p, and disabled in the dimeric Kip3p, is sufficient to explain all the experimental results.

There have been numerous *in vitro* studies examining the interaction of kinesin-5 motors from various species with MTs and none have previously noted an effect on MT assembly [111, 112, 123, 133]. However, these studies were focused largely on motor properties, such as force and velocity, and used hyperstabilized MTs for the assay (e.g. with GMP-CPP or taxol added to the MTs), so motor-dependent depolymerization would have been difficult to detect.

Other studies have focused on the *in vivo* role of kinesin-5, most typically on Eg5 [136] [137]. Again, there has not been any report of an effect on MT assembly. Instead the primary phenotype of Eg5-inhibited cells or extracts is monopolar asters, instead of bipolar spindles. To our knowledge the quantitative effects on MT length and total polymer have not been measured. We suspect that our ability to discern an effect on kMT disassembly in budding yeast is facilitated by the presence of two kinesin-5 genes (*CIN8* and *KIP1*). In this case the deletion of one gene is not sufficiently severe to prevent bipolarity of the spindle.

The simplest molecular mechanism for length-dependent MT disassembly is that the kinesin-5 motor itself acts directly to promote MT plus-end disassembly. We speculate that mechanical stress between walking motor head domains would stress tubulin-tubulin bonds to destabilize the lattice and promote MT disassembly. In contrast to the strong depolymerase activity of kinesin-13 [138-140], the disassembly-promoting activity of kinesin-5 is likely to be relatively weak, with its effect likely exerted on growing plus-ends to stimulate disassembly. Alternatively, kinesin-5 could carry a disassembly-promoting binding partner to promote net disassembly at MT plus-ends, although to our knowledge there are no known cargoes that are transported by kinesin-5 motors.

It is interesting to consider the possibility that perhaps all kinesins, to some extent, possess intrinsic MT destabilizing activity due to some degree of mechanical stress between the head domains. Determining whether the destabilization of MT plus ends is via kinesin-5 itself or mediated through another molecule will be an important future effort. Either way, the role of kinesin-5 motors in regulating kMT assembly dynamics is a new property that we have now identified for a motor previously known only as a sliding motor that acts between antiparallel MTs. Because of the potent effect that *CIN8* deletion has on kinetochore organization, it seems unlikely that a significant Cin8p-independent pathway will be found to also promote length-dependent disassembly. The effects of kinesin-5 on MT assembly will be important to consider as anticancer drugs directed toward inhibiting kinesin-5 sliding activity are presently in clinical trials [141].

Experimental Procedures

Yeast Strains and Cell Culture

All relevant genotypic information can be found in Table C.8. Genes of fusion proteins remained under control of their endogenous promoter. Cell growth techniques and conditions were performed as previously described [50, 51, 60, 122]. The *CIN8* NLS deletion was performed as previously described [132]. Overexpression of Cin8p from the P_{GAL1} promoter was performed as previously described [121]. The CIN8-3xGFP was made by PCR amplification of 3xGFP from a plasmid, and then the linear PCR product was integrated at the endogenous *CIN8* gene. The cin8-F467A strain was made as previously described [123]. Benomyl treatment for stabilization of kMT plus-end dynamics was performed as previously described [60].

Fluorescence Imaging and Photobleaching

Fluorescence imaging and photobleaching experiments were performed as previously described [19, 108]. Astral MT lengths were assessed by measuring the length of GFP-Tub1 or mCherry-Tub1 labeled aMTs in which both the plus- and minus- ends were clearly visible within one focal plane. Counting of Cin8p and Kip1p on the mitotic spindle was completed as previously described [142].

Image Analysis

Average fluorescence distributions calculated over normalized spindle lengths were obtained as previously described [50].

In FRAP experiments, FRAP half-times were resolved according to spindle position, as previously described [59, 108]. Reported half-spindle FRAP half-times were calculated by averaging over all spindle positions in the photobleached half-spindle.

Cin8-GFP fluorescence normalized to the number of tubulin binding sites (Fig 5.4C and 5.5D) is calculated as follows. For Fig 5.4C, the tubulin decay function was calculated by assuming a tubulin binding site fraction of 1.3 at the SPBs, which decays inversely with increasing Ndc80-Cherry fluorescence such that there remains a fraction

of 0.3 binding sites at the spindle equator (representing interpolar MTs). Then, Cin8-GFP fluorescence was normalized to the number of tubulin binding sites by dividing Cin8-GFP signal minus background by the tubulin decay function at each spindle position. A similar method was used for Fig. 5.5D, except that the tubulin decay function was calculated directly from the distribution of aMT plus-ends as is shown in Fig. 5.5C (red).

All p-values for relative comparisons of experimental data sets were calculated using Student's t-test, unless otherwise noted. Quantitative comparisons of simulations to experimental results were completed as previously described [29].

Simulation Methods

All simulations were run using MATLAB R7.1 (Natick, MA). Detailed simulation methods are provided in the supplemental materials.

Tomography methods

Cells were prepared for electron microscopy using high pressure freezing followed by freeze-substitution as previously described [30]. Dual axis electron tomography was carried out as described previously [143].

In total, we recorded 4 wild-type spindles and 5 *cin8Δ* spindles. Individual microtubules and the position of the SPB central plaque were modeled from the tomographic volumes. A projection of the 3D model was then displayed and rotated to study its 3D geometry. Microtubule lengths were extracted from the model contour data using the program, IMODINFO.

Acknowledgements

I thank Dominique Seetapun for providing matlab kymograph code, Drs. Tom Hays and Leah Gheber for helpful discussions, Dr. Jeff Molk for comments on the manuscript, and Marybeth Anderson for assistance with *bim1Δ* images. Plasmids and strains were kindly provided by Drs. S. Reed, B. Errede, M.A. Hoyt, L. Gheber, and D. Pellman. This work was supported by NIH grant GM071522 to D.J.O. K.B. is supported by NIH grant GM32238 and M.K.G. is supported by NIH NRSA grant EB005568. E.T.O. is supported in part by grant RR-00592 from the National Center for Research Resources of the NIH to A. Hoenger.

Figures

FIGURE 5.1: Cin8p organizes metaphase yeast kinetochores in a manner consistent with length-dependent suppression of net kMT plus-end assembly. (A) A computational model of yeast metaphase kMT plus end dynamics, identified in our previous studies, predicts that deletion of the length-dependent promoter of kMT disassembly (modeled here as length-dependent catastrophe frequency (k_c)) will result in longer kMTs and disorganized kinetochores. Conversely, overexpression will result in shorter kMTs and focused kinetochore clusters. Here, mean rescue frequency (k_r) is dependent on tension between sister kinetochores, as described previously [50]. All model parameters as in Table C.2. (B) *CIN8* deletion results in kinetochore disorganization and the net shifting of kinetochores towards the spindle equator, suggesting that kMTs are on average longer than they are in wild-type cells (red, Spc29-CFP pole marker; green, Cse4-GFP kinetochore marker) (scale bar 1000 nm, error bars, s.e.m.) All model parameters as in Table C.2. Note that since k_r is dependent on tension between sister kinetochores in the model, disorganization of kinetochores naturally results in reduced separation between sister kinetochores and lower mean values for k_r. (C) Cin8p overexpression results in clusters of kinetochores near the SPBs, suggesting that kMTs are shorter than in wild-type cells.

Figure 5.1

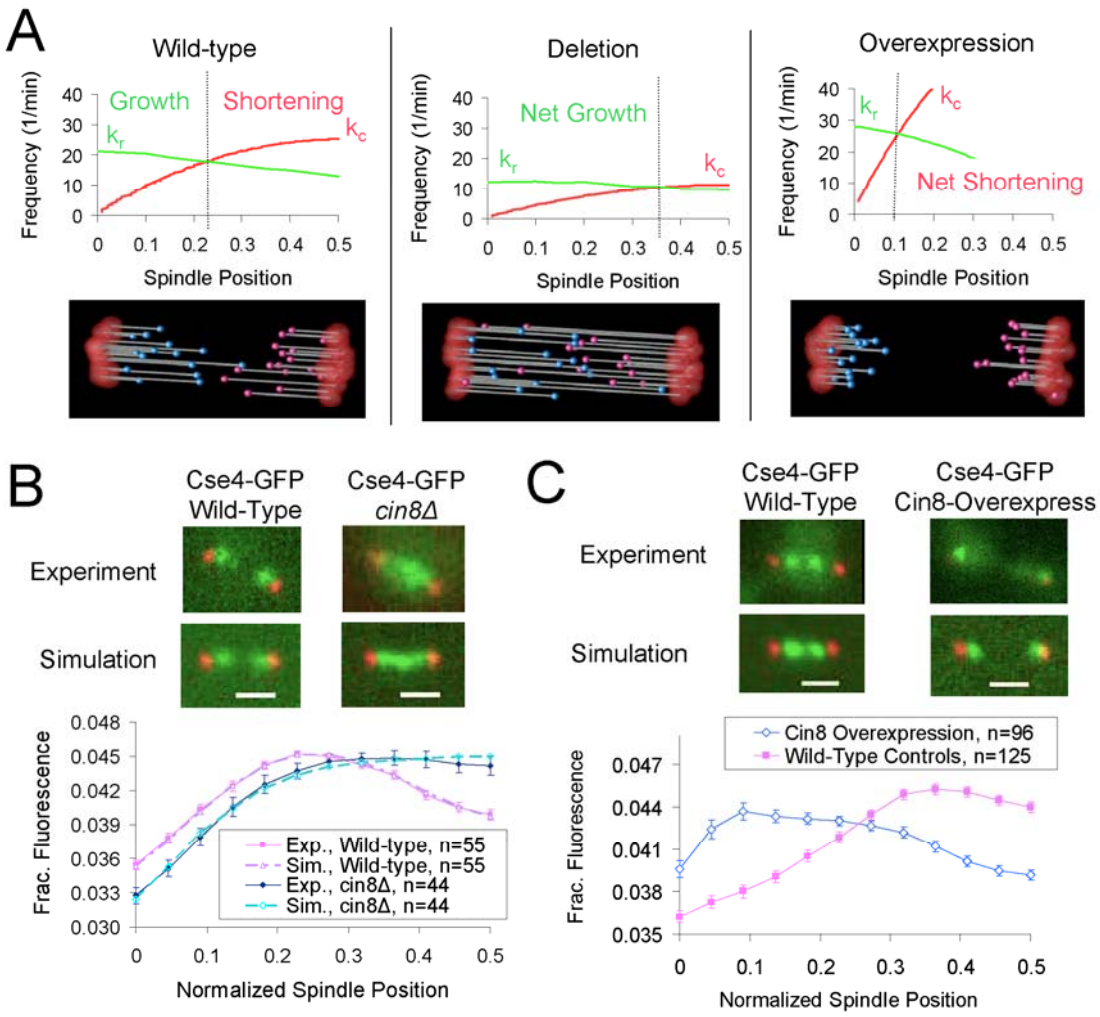
A
Wild-type
Growth
Shortening
k_r
k_c
Frequency (1/min)
Spindle Position
Deletion
Net Growth
Overexpression
Net Shortening
B
Cse4-GFP
Wild-Type
Cse4-GFP
cin8Δ
Experiment
Simulation
Frac. Fluorescence
Exp., Wild-type, n=55
Sim., Wild-type, n=55
Exp., cin8Δ, n=44
Sim., cin8Δ, n=44
Normalized Spindle Position
C
Cse4-GFP
Wild-Type
Cse4-GFP
Cin8-Overexpress
Cin8 Overexpression, n=96
Wild-Type Controls, n=125

FIGURE 5.2: Cin8p promotes kMT disassembly. (A) *CIN8* deletion results in flattening of the GFP-tubulin fluorescence distribution and shifting of fluorescence towards the spindle equator, suggesting that kMT lengths are increased in the mutant. (Red, Spc29-CFP SPB marker; Green, GFP-Tub1 MT marker) (scale bar 1000 nm, error bars, s.e.m.) All model parameters as in Table C.2. (B) Cryo-electron tomography reveals increased mean MT length and number in *cin8Δ* spindles (n=5 spindles, mean spindle length =1387 nm), relative to wild-type spindles (n=4 spindles, mean spindle length=1265 nm). (C) Similar to the CIN8 deletion mutant, the motor domain mutant, *cin8-F467A*, which has reduced affinity for MTs, results in flattening of the GFP-tubulin fluorescence distribution and shifting of fluorescence towards the spindle equator. (D) *CIN8* deletion eliminates the characteristic gradient in GFP-tubulin FRAP recovery half-time, consistent with disruption of the gradient in net kMT assembly. All model parameters as in Table C.2. (E) In contrast to the *cin8Δ* mutants, deletion of the kinesin-8 depolymerase *KIP3* does not significantly perturb kinetochore microtubule (kMT) organization.

Figure 5.2

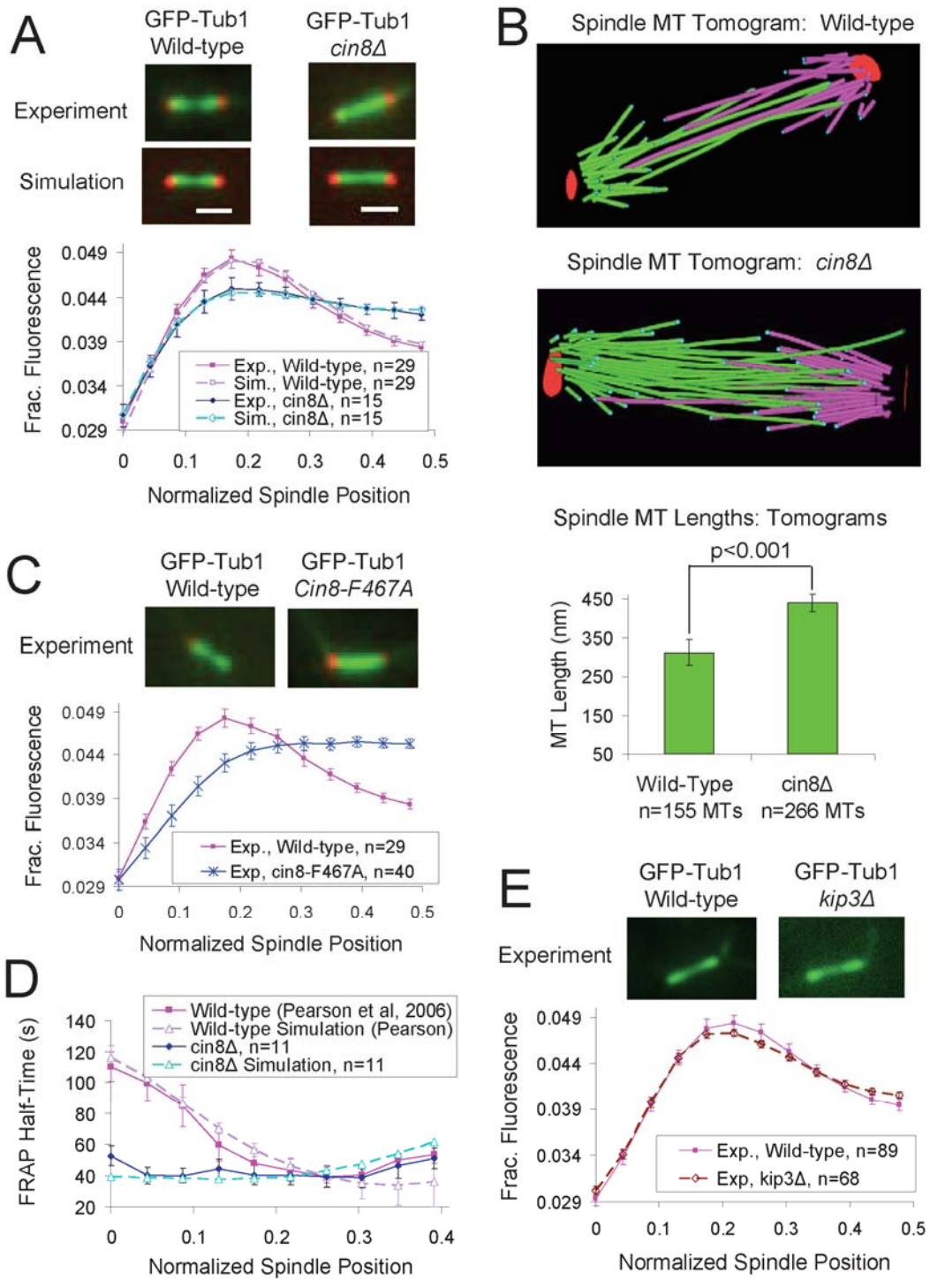
A
GFP-Tub1
Wild-type
GFP-Tub1
cin8Δ
Experiment
Simulation
Frac. Fluorescence
0.049
0.044
0.039
0.034
0.029
Exp., Wild-type, n=29
Sim., Wild-type, n=29
Exp., cin8Δ, n=15
Sim., cin8Δ, n=15
0
0.1
0.2
0.3
0.4
0.5
Normalized Spindle Position
B
Spindle MT Tomogram: Wild-type
Spindle MT Tomogram: cin8Δ
Spindle MT Lengths: Tomograms
p<0.001
MT Length (nm)
450
350
250
150
50
Wild-Type
n=155 MTs
cin8Δ
n=266 MTs
C
GFP-Tub1
Wild-type
GFP-Tub1
Cin8-F467A
Experiment
Frac. Fluorescence
Exp., Wild-type, n=29
Exp, cin8-F467A, n=40
Normalized Spindle Position
D
FRAP Half-Time (s)
140
120
100
80
60
40
20
Wild-type (Pearson et al, 2006)
Wild-type Simulation (Pearson)
cin8Δ, n=11
cin8Δ Simulation, n=11
Normalized Spindle Position
E
GFP-Tub1
Wild-type
GFP-Tub1
kip3Δ
Experiment
Frac. Fluorescence
Exp., Wild-type, n=89
Exp, kip3Δ, n=68
Normalized Spindle Position

FIGURE 5.3: Cin8p promotes astral MT disassembly. (A) Astral MTs (aMTs) extend from the SPBs into the cytoplasm, are outside the nucleus, and are fewer in number than spindle microtubules. (B) Fluorescence images of GFP-tubulin in living wild-type and *CIN8* mutant cells. aMT lengths were measured via GFP-tubulin fluorescence (white arrows point to plus ends; red, Spc29-CFP pole marker; green, GFP-tubulin) (scale bar 500 nm). (C) aMT lengths are increased in *cin8Δ* cells as compared to wild-type spindles. Cytoplasmic overexpression of Cin8p results in shorter aMTs, whether overexpression is global, as in *GAL1-CIN8* overexpression experiments, or if overexpression is local in the cytoplasm, as in experiments with mutant Cin8p lacking the nuclear localization signal (*cin8-nlsΔ*). Both *kip3Δ* and *cin8-F467A* mutants have increased aMT lengths relative to wild-type cells, similar to *cin8Δ* cells

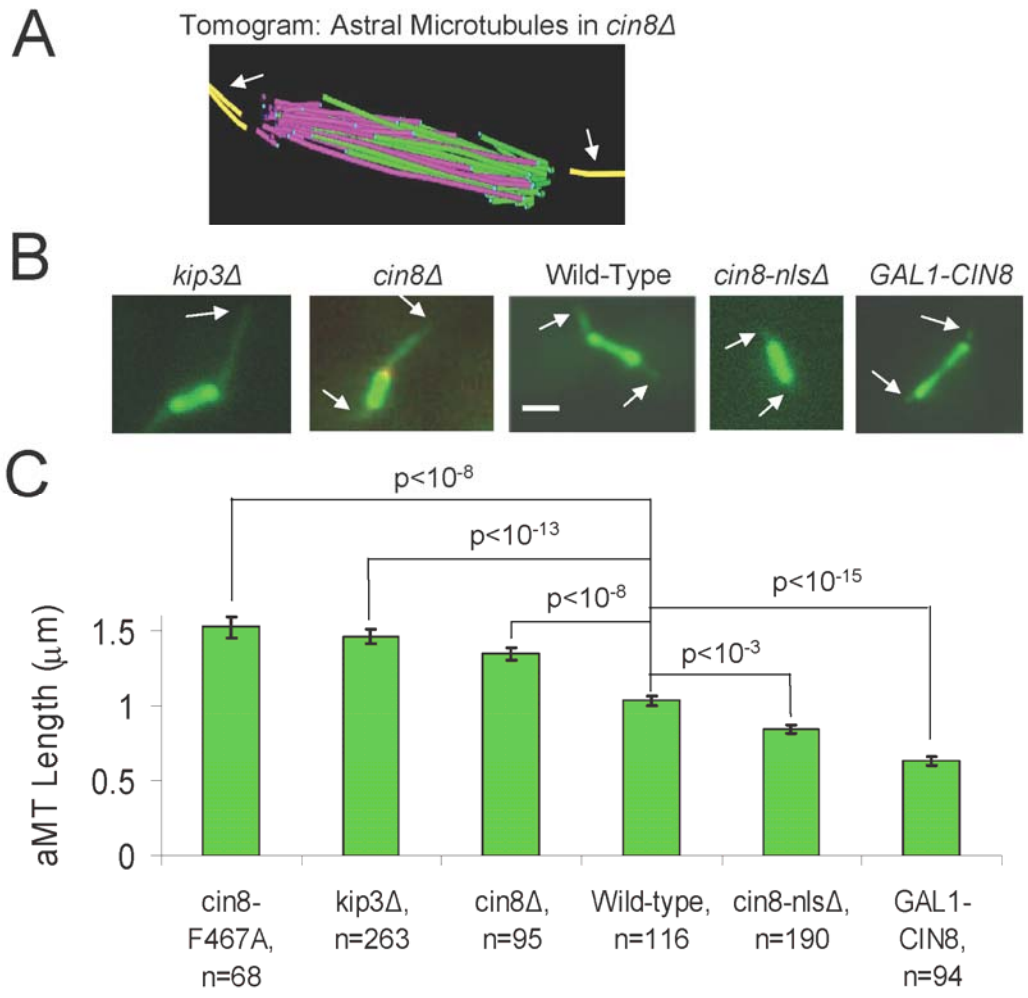

FIGURE 5.4: Cin8p accumulates on kMTs in a length-dependent manner and frequently interacts with kMT plus ends. (A) In simulation, kinesin-5 motors crosslink both anti-parallel-oriented microtubules (left, magenta) and parallel-oriented microtubules (right, green). Simulated motors crosslinking parallel-oriented microtubules move to and frequently interact with kMT plus-ends. (B) By repetitive photobleaching of spindles labeled with Cin8-3XGFP, spindle motor movement can be observed (kymograph: horizontal scale bar, 1000 nm; vertical scale bar, 20 sec). The three arrows (yellow, cyan, and magenta) indicate three time points in the movement of a Cin8-3XGFP fluorescent spot that moves in the plus end direction. (C) Cin8p motors concentrate near kinetochores both experimentally and in simulation, with a slight offset that is accounted for in the motor model by assuming motors detach from shortening kMT plus-ends (Red, Ndc80-Cherry kinetochore marker; green, Cin8-GFP) (scale bar 500 nm, error bars, s.e.m.). (D) Experimentally and in simulation, Cin8-GFP fluorescence normalized to the number of tubulin polymer binding sites increases for longer kMTs (data calculated from (C)). (E) Cin8-GFP FRAP half-time gradient. As expected from the motor model, the rate of Cin8-GFP turnover is most rapid where shortening kMT plus ends are located. The gradient closely mirrors the gradient observed in GFP-tubulin FRAP half-time (Fig. 2C), confirming the close connection between motor dynamics and kMT plus end dynamics.

Figure 5.4

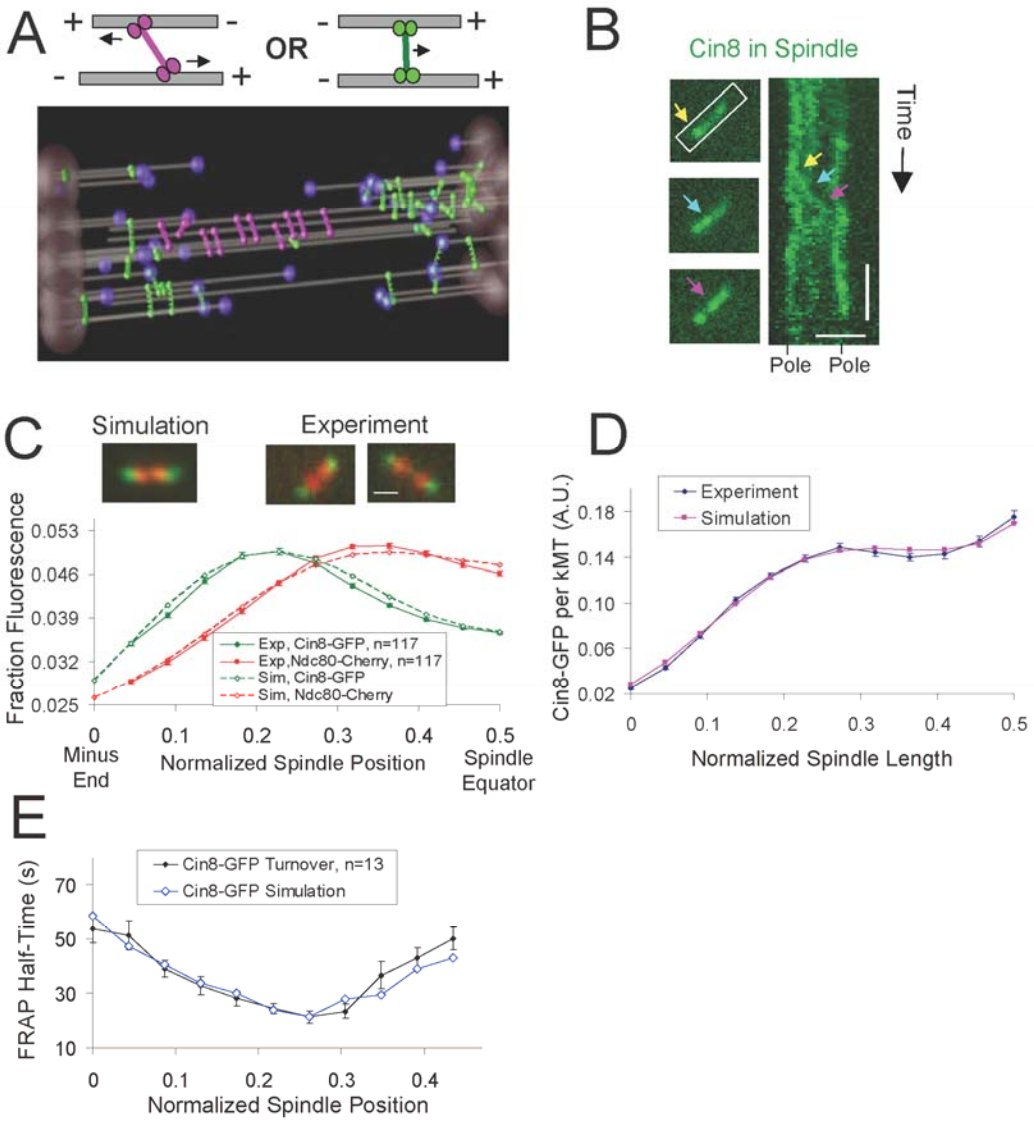
A
OR
B
Cin8 in Spindle
Time
Pole
Pole
C
Simulation
Experiment
Fraction Fluorescence
0.053
0.046
0.039
0.032
0.025
Exp, Cin8-GFP, n=117
Exp,Ndc80-Cherry, n=117
Sim, Cin8-GFP
Sim, Ndc80-Cherry
0
0.1
0.2
0.3
0.4
0.5
Minus End
Normalized Spindle Position
Spindle Equator
D
Cin8-GFP per kMT (A.U.)
0.18
0.14
0.10
0.06
0.02
Experiment
Simulation
0
0.1
0.2
0.3
0.4
0.5
Normalized Spindle Length
E
FRAP Half-Time (s)
70
50
30
10
Cin8-GFP Turnover, n=13
Cin8-GFP Simulation
0
0.1
0.2
0.3
0.4
Normalized Spindle Position

FIGURE 5.5: Relative Distribution of Cin8-GFP and Kip3-GFP (A) The experimental and simulated distribution of Cin8-GFP and Kip3-GFP. Cin8-GFP concentrates near to kMT plus-ends, while Kip3-GFP is relatively more prevalent where ipMT plus-ends are typically clustered. (B) In simulations, the crosslinking properties of Cin8p frustrates its processivity toward the plus-ends of interpolar (ipMT) plus-ends, such that Cin8p visits to ipMT plus-ends are rare relative to kMT plus-end visits. In contrast, the non-crosslinking motor Kip3p is predicted to visit ipMT plus-ends more frequently than kMT plus-ends, likely because the longer ipMTs act as larger attractors for the motors within the spindle and the lack of crosslinking relieves the frustration experienced by Cin8p motors.

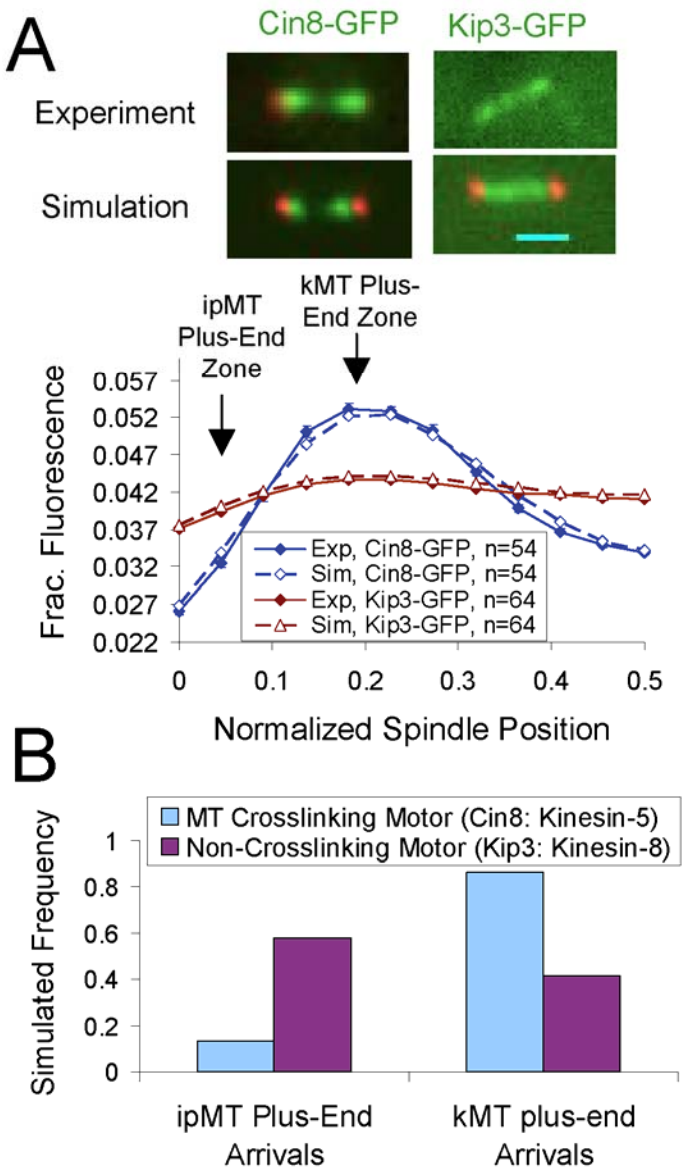

FIGURE 5.6: Cin8p walks processively towards MT plus ends, and its distribution on aMTs mirrors its distribution on kMTs. (A) Consistent with model predictions, Cin8-NLSΔ-3XGFP (left, green is Cin8p) moves in the plus end direction on aMTs, and frequently interacts with aMT plus-ends. The three arrows (yellow, cyan, and magenta) indicate three time points in the movement of a Cin8-GFP fluorescent spot that moves in the plus end direction (red, tubulin-cherry aMT aligned at its minus-end, although rapid photobleaching results in loss of the tubulin signal) (kymograph: horizontal scale bar, 1500 nm; vertical scale bar, 50 sec) (B) Cin8-NLSΔ-3XGFP (green) on aMTs (tubulin-cherry, red). (C) Cin8-NLSΔ-GFP concentrates near the plus-ends of longer aMTs with a slight off-set that mirrors the distribution of Cin8-GFP relative to kMT plus-ends. Here, the distribution of 155 aMT lengths is shown as the red line, with averaged Cin8-NLSΔ-GFP fluorescence as a function of aMT length shown as the green line. (D) Experimentally and in simulation, Cin8-GFP fluorescence normalized to the number of tubulin polymer binding sites increases for longer aMTs (data calculated from (C)).

Figure 5.6

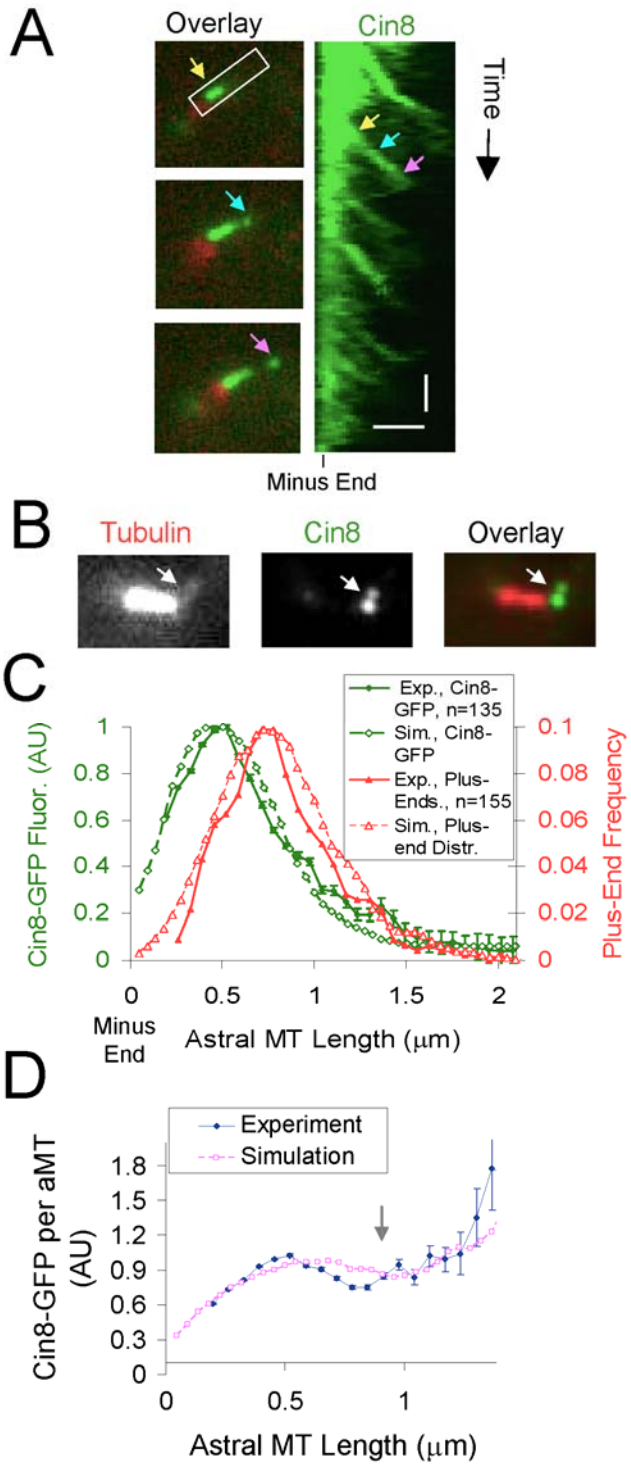
A
Overlay
Cin8
Time
Minus End
B
Tubulin
Cin8
Overlay
C
Exp., Cin8-GFP, n=135
Sim., Cin8-GFP
Exp., Plus-Ends., n=155
Sim., Plus-end Distr.
Cin8-GFP Fluor. (AU)
Plus-End Frequency
Minus End
Astral MT Length (μm)
D
Experiment
Simulation
Cin8-GFP per aMT (AU)
Astral MT Length (μm)

FIGURE 5.7: A "self-organized" model for Cin8p motor mediated spindle organization (A) A model for interaction of Cin8p motors with kMT plus-ends: Cin8p motors that crosslink parallel microtubules are plus-end directed (top). Cin8p concentrates on longer kMT plus-ends to directly promote kMT disassembly (middle), either by itself or possibly with an unidentified binding partner (not shown). kMT depolymerization then promotes motor detachment (bottom). (B) Simulation of motor-mediated spindle self-organization. Starting with a random distribution of kinetochores and motors in the spindle (top), motor-mediated promotion of kMT plus-end disassembly can organize the spindle into a typical metaphase bi-lobed kinetochore configuration as motors concentrate in a length-dependent fashion onto kMT plus-ends (bottom and Supplemental Movie 5). (C) Simulated images of Cin8-GFP (green) and Ndc80-cherry (red). At simulation start (t=0), motor and kinetochore fluorescence is randomly distributed in the spindle (left). After t=135 sec, simulated fluorescence distributions qualitatively reproduce experimental results (top right, simulated image; bottom, quantitative comparison to experimental data). Model parameters Table C.7. (D) In this self-organized model, the catastrophe frequency is assumed to be proportional to the number of motors at the plus end (see supplemental material simulation methods), resulting in a gradient of catastrophe frequency (red triangles) that is similar to the theoretical catastrophe gradient depicted in Fig. 5.1A (red line).

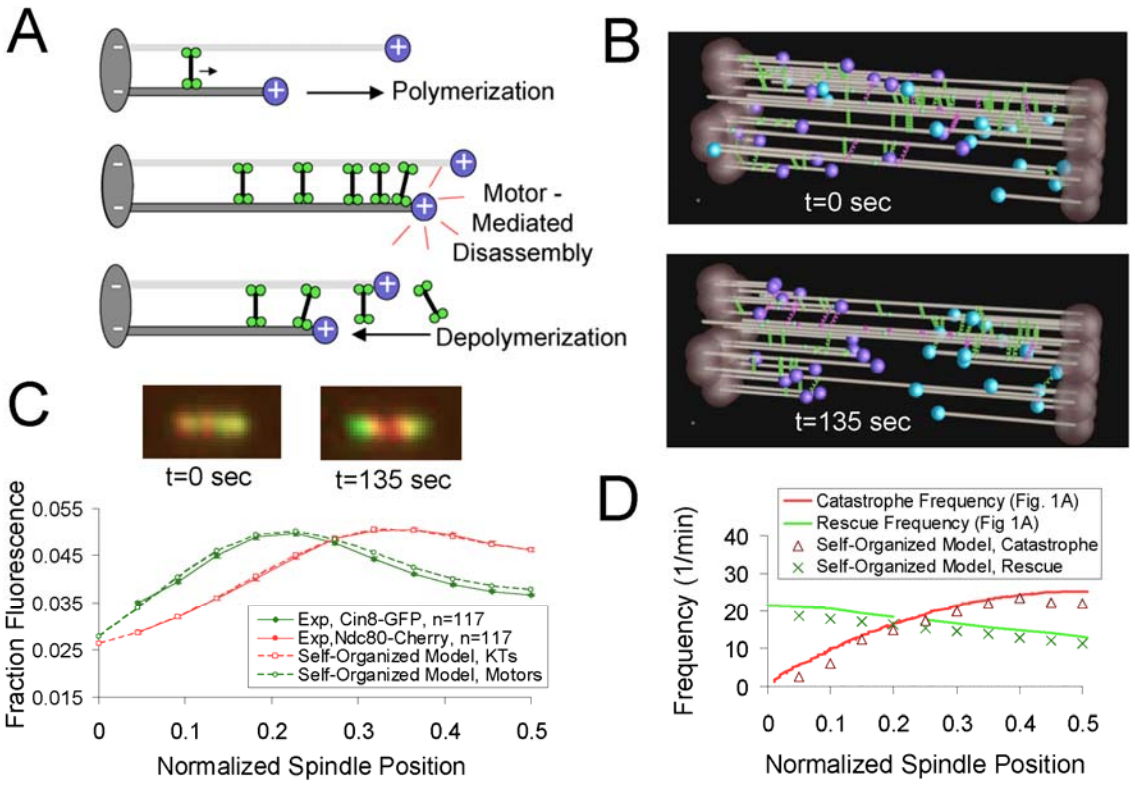

CHAPTER SIX

MICROTUBULE ASSEMBLY DYNAMICS AT THE NANOSCALE

(Contributing Authors: Melissa Gardner*, Henry Schek*, Jun Cheng, David Odde**, and Alan Hunt**)
(*Co-first authors: *MKG performed simulations and data analysis, HTS and JC performed experiments*)
(**Co-directed project)
(Reprinted with permission from *Current Biology* 41(2) (2007))

Abstract

Background: The labile nature of microtubules is critical for establishing cellular morphology and motility, yet the molecular basis of assembly remains unclear. Here we use optical tweezers to track microtubule polymerization against microfabricated barriers, permitting unprecedented spatial resolution.

Results: We find that microtubules exhibit extensive nanometer-scale variability in growth rate, and often undergo shortening excursions, in some cases exceeding 5 tubulin layers, during periods of overall net growth. This result indicates that the GTP cap does not exist as a single layer as previously proposed. We also find that length increments (over 100 ms time intervals, N=16,762) are small, 0.81 +/- 6.60 nm (mean +/- s.d.), and very rarely exceed 16 nm (~two dimer lengths), indicating that assembly occurs almost exclusively via single subunit addition rather than via oligomers as was recently suggested. Finally, the assembly rate depends only weakly on load, with the average growth rate decreasing only 2-fold as the force increases 7-fold from 0.4 pN to 2.8 pN.

Conclusions: The data are consistent with a mechanochemical model where a spatially extended GTP cap allows substantial shortening on the nanoscale, while still preventing complete catastrophe in most cases.

Introduction

Microtubules mediate a myriad of functions in the cell, including chromosome segregation and organelle transport, and serve broadly as scaffolding for transport and morphological changes. To respond and adapt to changing cellular demands,

microtubules undergo an unusual self-assembly mechanism, called dynamic instability, where the end of the microtubule switches stochastically between alternate periods of slow growth and rapid shortening such that individual αβ-tubulin heterodimeric subunits undergo net addition and loss, respectively [12]. This allows the microtubule cytoskeleton to rapidly reconfigure to support morphologic changes, and microtubules can probe the intracellular environment to explore possible arrangements [144]. Microtubules presumably "sense" the local environment by interaction with microtubule-associated proteins, which can vary spatially through, for example, kinase-phosphatase and GEF-GAP-mediated spatial gradients [93, 145]. Understanding how these microtubule-associated proteins control microtubule assembly depends on understanding dynamic instability in the pure microtubule polymer as this is the substrate over which all regulation is layered.

The current model for dynamic instability is based on the concept of a stabilizing GTP-tubulin "cap" at the growing plus end of the microtubule. As new GTP-tubulin subunits add to and become embedded in the growing microtubule tip, they subsequently hydrolyze to GDP-tubulin, thereby forming a labile inner core of GDP-tubulin that is stabilized by a "cap" of GTP-tubulin at the tip. If the GTP cap is lost through hydrolysis events and stochastic dissociation of GTP-tubulin, then the inner labile core of GDP-tubulin is exposed, leading to outward protofilament curling that antagonizes lateral bonds between neighboring tubulin subunits. These events ultimately promote a switch into a phase of extensive tubulin subunit loss. Switching from a growing GTP-tubulin tip to a shortening GDP-tubulin tip is called “catastrophe”, and the switch from shortening to growth is called “rescue”. Together, the rates of catastrophe and rescue, as well as the rates of growth and shortening, determine the extent of microtubule polymerization through rounds of dynamic instability, and ultimately control the spatial organization of microtubules. Critical to understanding the intrinsic dynamics of microtubules is an understanding of the size and nature of the GTP cap.

A series of studies have argued that the GTP cap is small [32{Drechsel, 1994 #1771, 146, 147]}, even as small as a single layer of GTP-tubulin [148-152]. These conclusions, which involve a variety of experimental approaches, have been shaped

substantially by light microscopy studies of microtubule assembly dynamics with spatial resolution of ~200 nm and temporal resolution of ~30 Hz. Recent studies established the use of optical tweezers in combination with a microfabricated chamber [153, 154] as a method for tracking microtubule assembly dynamics, with spatial resolution at least an order of magnitude better than traditional video microscopy achieved through video analysis [153]. In this assay, individual microtubules are held with optical tweezers and allowed to polymerize under compressive load (without buckling) against the chamber wall, achieving resolution of ~5-10 nm at 25 Hz by video-based tracking of a microtubule-attached bead [153]. These data exhibited unexpectedly large fluctuations in the assembly rate, with the interpretation being that there are often discrete "steps" of assembly corresponding to the addition of tubulin oligomers, about 20-30 nm in size.

Here we report results from experiments using a similar optical-trapping arrangement, but with the much higher temporal resolution of 5 kHz, which is achieved using back focal plane interferometry [155]. This higher temporal resolution allows for temporal filtering to average out thermal motion, providing unprecedented spatial resolution of <3.5 nm at 10 Hz temporal resolution, while still retaining the ability to examine records at higher bandwidth. We observed large fluctuations in the assembly rate under compressive loads (0-2.5 pN), with persistent periods of growth and shortening that resulted in addition and loss of many tubulin subunits. The net length change during these periods is broadly distributed according to a Gaussian, with r.m.s. length changes of +/- 10-15 nm per period and regular length change observations of +/- 40 nm. These length changes do not exhibit step-like character, and are qualitatively accounted for by a mechanochemical model that assumes addition and loss by single subunits, rather than oligomers. The experimentally observed tubulin loss of ~40 nm or more during a shortening period indicates that a single-layer cap model is insufficient to explain microtubule dynamic instability. Computational modeling qualitatively accounts for these dynamics, including shortening periods, by assuming simple first-order GTP hydrolysis resulting in ~40 tubulins in the GTP state on average comprising the GTP cap. In addition, the model suggests that GTP-tubulin has an approximately exponential decay in

concentration with increasing depth, much like the "comets" characteristic of many plus end tip-tracking proteins.

Overall, we found that microtubule growth is highly variable, weakly dependent on force, and can persist even after the loss of more than 5 layers of tubulin from the "growing" plus end. Thus, to minimize confusion we use "growth-phase" to refer to periods of average growth, previously broadly classified as "growth" in lower resolution studies. Growth-phase shortening excursions are distinct from rapid-shortening [12, 32], which is more than an order of magnitude faster and typically persists for micrometers rather than nanometers.

Results

Experimental measurement of microtubule dynamics at the nanoscale

To follow polymerization, dynamic microtubules are grown from bead-linked microtubule seeds, and abut against engineered barriers [154], as shown schematically in Fig. 6.1 A and 6.C. The microtubule polarity is inferred from the growth rate, determined by light microscopy (Fig. 6.1B) prior to the microtubule tip contacting the barrier. In this study we focused only on plus ends, identified by their faster growth [32]. The bead is held by optical tweezers [155] modified with the addition of a piezo-actuated mirror for high-precision trap steering. If the bead is held in a stationary trap as it is displaced by microtubule polymerization, some of the microtubule length change accumulates in the compliant biotin-streptavidin link between the bead and the microtubule, thus changes in microtubule length are underestimated {Svoboda, 1993 #1774). However, force at the microtubule tip is still equal and opposite to that of the trap on the bead, allowing accurate force measurements. Applying a force clamp, which adjusts the laser position at 10 Hz to maintain a constant force at the microtubule tip (Fig. 6.1C), fixes the strain in the compliant link and thereby increases the precision of growth measurements . This experimental method enables detection of variations in polymerization behavior at the nanoscale over very short time scales.

Simulations with a distributed GTP cap model predict growth-phase shortening events

In previous work, we described a three-dimensional mechanochemical model for microtubule self-assembly that recapitulated experimentally observed microtubule tip structures and assembly rates {VanBuren, 2002 #1546}. In this model, GTP-tubulin subunits stochastically hydrolyze to GDP-tubulin subunits via first order kinetics (hydrolysis rate constant of ~1 s^{-1}) subsequent to their incorporation into the tips of growing microtubules. This model predicts a variable GTP cap depth with an exponential decay in lattice-incorporated GTP-subunits from the tip of a given protofilament (Fig. 6.2A). In addition, the growing tips of simulated microtubules vary in structure from blunt tips with protofilaments of similar lengths (Fig. 6.2C) to sheet-like tips with a large variation in protofilament length (Fig. 6.2A-B).

By adapting the simulation to reproduce experimental conditions used in the bead-tracking assembly assay (see supplementary material), simulated microtubule assembly behavior could be directly compared to experimental results. In particular, we modeled not only the assembly dynamics of the microtubule, but also the thermal fluctuations and elastic forces in the system and the observation of the dynamics as detected by the experimental apparatus. Thus, we were able to predict the behavior of microtubule assembly as it would be observed with fast temporal resolution at nanometer precision. In simulations, highly variable microtubule tip structures with relatively long spatially distributed GTP caps allow for frequent shortening excursions during microtubule growth phases, as individual leading protofilaments are able to depolymerize and then subsequently recap without microtubule catastrophe. A typical simulated growth-phase shortening excursion, in which shortening and subsequent recapping of the leading protofilament occurs without microtubule catastrophe, is shown in Fig. 6.2. Note that the simulated GTP cap remains intact during the microtubule shortening event, never being less than 20 GTP-tubulin subunits. In the simulation, the GTP cap is typically exponentially distributed, reminiscent of the "comets" associated with many tip-tracking proteins, such as EB1, albeit with a shorter decay length. In contrast, shortening of a microtubule tip prior to catastrophe (Fig. 6.2D-E) results in a minimal GTP cap of ~3 subunits, which we previously found was typical of simulated shortening microtubules

[156].

Growth-Phase Microtubule Shortening Gives Rise to Polymerization Variability

Using the experimental assay described above, we examined microtubule growth behavior; in total we analyzed 35 growth-phase periods from 15 microtubules over a total of 1676.2 s, which at 5 kHz raw acquisition rate yielded 8,381,000 individual observations with sub-nanometer precision. Using temporal averaging of the raw data at 10 Hz to filter diffusive movements, we obtained 16,762 individual microtubule length measurements for subsequent analysis (complete data set given in supplementary material, Figs. D.3-D.5). This technique exposes highly-variable polymerization behavior over short time scales, even during periods where microtubule assembly appears stalled when observed with lower spatial or temporal resolution. Fig. 6.3A highlights nano-shortening events that occurred over 20 seconds of microtubule growth. In each case the microtubule does not proceed into a rapid shortening phase, but rather resumes growth. The magnitude and frequency of the growth-phase shortening events are roughly similar to those predicted by the mechanochemical model (Fig. 6.3A). Simulated and experimental force clamp data from a GMP-CPP stabilized control microtubule are also shown in Fig. 6.3A, demonstrating that the shortening events can be distinguished from thermal fluctuations of the growing microtubule's position. To quantify this behavior, we calculated the length of growth and shortening excursions over multiple experimental runs. Here, a microtubule length excursion is defined by summing successive positive or negative microtubule length displacements at sequential time points, as shown by the green and red arrows, respectively, in Fig. 6.3B. For example, three sequential 10 Hz time points with length changes of -1.0, -2.0, and -2.0 nm followed by a positive increment would result in a length excursion of -5.0 nm. This method provides a convenient and objective way to summarize nanoscale microtubule polymerization behavior over many different experimental runs without fitting the data to any particular model, although it will underestimate microtubule growth excursions since thermal fluctuations will obscure length excursions to some extent. Note, however, that this noise is explicitly included in the model, so that it is accounted for in the simulated dynamics.

Likewise, the absolute extent of growth-phase shortening is also underestimated due to intervening periods of actual lengthening above the noise. For example, the absolute peak to trough shortening in Fig. 6.3B exceeds 50 nm, but the maximum detected shortening is 32 nm by this method. In summary, excursion size analysis provides a model-independent, conservative estimate of nanoscale fluctuations in microtubule assembly.

Microtubule Growth Under Low Force (0-1 pN)

As shown in Fig. 6.4A, shortening excursions are common during microtubule growth under low load (0-1 pN). The shortening excursions can be quite large, in some cases 40 nm or larger, corresponding to ~5 layers of tubulin. Similarly, the growth excursions can also be quite large, again 40 nm or more. For both shortening and growth excursions, the model, which only permits tubulin addition and loss via single αβ-tubulin subunits, predicts that excursions of ~40 nm for both growth and shortening will be observed in this assay. Typically the excursions in the experiment and the simulation are relatively small, corresponding to roughly one layer of tubulin. Experimentally we find a mean shortening excursion length under low load of -9.7 nm, and a mean growth excursion length of +13.3 nm (n=7,617, Table 6.1), resulting in net growth of +3.6 nm per growth excursion-shortening excursion cycle. Shortening and growth excursions for GTP microtubules (-9.7 nm and +13.3 nm, respectively) are larger than those observed for GMP-CPP controls (-4.4 nm and +4.7 nm, respectively), differences that were statistically significant ($p<10^{-57}$ via one-tailed t-test). Thus, the growth and shortening excursions observed in the presence of GTP reflect the dynamics of microtubule assembly, rather than simply the thermal fluctuations in the experimental system. Low force summary statistics are given in Table 6.1.

Microtubule Growth Under High Force (1-2.5 pN)

Increasing the force on a microtubule has surprisingly little effect on the overall behavior of assembling microtubules. As shown in Fig. 6.4B, microtubules grown under high force (1-2.5 pN) exhibit a distribution of growth and shortening excursions during

growth phases that is qualitatively similar to that observed at low force (Fig. 6.4A). However, we find a number of statistically significant effects of increasing force. First, we find that the range of excursions is diminished. As expected, the mean growth excursion length decreases to +9.5 nm, which is significantly less than the low force value of +13.3 nm ($p<10^{-3}$). Surprisingly, the mean shortening excursion length decreases (in magnitude) at high force to –6.4 nm, which is significantly less (in magnitude) than the low force value of –9.7 nm ($p<10^{-6}$). Taken together, this means that the range of observed growing and shortening excursions during microtubule assembly is narrower at high force, and that fluctuations are generally suppressed (Fig. 6.4B, Table 6.1). Despite the suppression of fluctuations, the GTP dynamics are still statistically different than the GMP-CPP dynamics (see Table 6.1, $p<10^{-19}$ for growth excursions, and $p<10^{-5}$ for shortening excursions). These results, which are qualitatively reproduced by the model, suggest that at low forces the microtubule tip tends toward structures that promote larger shortening events. In the simulation, we found that microtubules under low force (0.5 pN) had an average difference between the leading and lagging protofilaments of ~5-6 tubulin subunits (40-48 nm), whereas under high force (2.5 pN), this difference was only ~2-3 tubulin subunits (16-24 nm). The reason for this is simple: at high force the addition rate to the leading protofilaments is more strongly suppressed, relative to the lagging protofilaments, than at low force. This creates a narrowing of the distribution of excursions, consistent with the experimental data. In low force simulations (0.5 pN) there are typically ~3 protofilaments whose tubulin addition rate is significantly suppressed by the wall at any point in time (defined as >2-fold reduction in on-rate constant), while in high force simulations (1.5 pN) there are ~6 protofilaments whose growth is influenced by the wall. In the model, the failure to grow significantly faster at low force is the result of sheet-like projections that often fail to be stabilized and are therefore lost, as in Fig. 6.2 time points A and B. At high force, model microtubules are relatively blunt and thus resistant to both growth and shortening excursions, consistent with the experimental data.

In summary, we find that microtubules exhibit large fluctuations in assembly during growth phases, including shortening excursions that correspond to loss of up to ~5

tubulin layers. These fluctuations are somewhat larger at low force than at high force, indicating that they are a natural feature of microtubule assembly in the absence of force.

Single time increment microtubule length changes do not reflect oligomer addition or loss

Since we found that large growth and shortening excursions occur during growth phases, we were interested in assessing whether these events were the result of tubulin oligomer addition, as recently suggested by Kerssemakers et al. [153]. Kerssemakers et al. reported step-like behavior that they attributed to oligomers, and these steps could be 30 nm or more. If oligomers were significant, then we ought to be able to detect them over single 0.1 s time intervals as large jumps corresponding to 16, 24, or 32 nm if the oligomer were a dimer, trimer, or tetramer of subunits, respectively (a single subunit being one αβ-tubulin heterodimer having length 8 nm). To test whether oligomers were accounting for the large growth and shortening excursions, we calculated the length increment over a single time interval (see Fig. 6.3B, "single time increment"). As shown in Fig. 6.5, there was a broad distribution of single time increments. Only very rarely were these single increments large enough to suggest addition or loss of an oligomer. In fact, increments exceeding 16 nm in magnitude were observed less than 1% of the time, and increments larger than 22 nm in magnitude were never observed in any of the 16,762 increments. Furthermore, when the unfiltered 5 kHz data was examined for increments exceeding 16 nm, these larger increments appeared to be periods of rapid growth rather than abrupt steps (data not shown). The mean length change for a single 0.1 s time increment was 0.81 nm, with a standard deviation of 6.60 nm (Table 6.2, N=16,762 individual increments). Over the same time interval, stable GMP-CPP controls had a mean length change of 0.00 ± 3.50 nm (Table 6.2, N=2,442 individual increments), demonstrating the ability to detect net growth from the single increment data ($p<10^{-20}$, one-tailed t-test comparing single time step length increments for GTP vs GMP-CPP microtubules). The standard deviation of the GMP-CPP control increments, 3.50 nm, largely reflects the variability due to thermal fluctuations in each increment, and so is appropriately regarded as a measure of the spatial resolution for detecting length changes

at 0.1 s sampling intervals. We find that the standard deviation of the GTP single time increments, 6.60 nm, is significantly larger than GMP-CPP control ($p<10^{-20}$), demonstrating the ability to detect tubulin addition-loss in single time increments. As shown in Fig. 6.5, simulations produced a distribution of single time point microtubule length increments similar to experimentally observed results (red line, Fig. 6.5). Notably, it was found that large increments of 16-24 nm were occasionally produced in the simulation, even though subunit addition in the model was strictly via single subunits. In the simulation there are on average ~26 tubulin arrival events and ~25 departure events, for a net gain of ~1 tubulin per 0.1 s, which matches well the experimentally observed mean increment of 0.81 nm (1 tubulin added corresponds to 8 nm/13 protofilaments = 0.6 nm average length added). The actual number of arrivals and departures in any 0.1 s interval is approximately binomially distributed, meaning that the distribution of increments will in turn be approximately Gaussian and sufficiently broad in their distribution so as to occasionally allow 16 nm increments via single subunit addition only. The simulation never produced increments larger than 22 nm, consistent with the experiment. Thus, we conclude that the variability in growth phase events is not likely due to tubulin oligomer addition or loss.

Microtubule Polymerization Rate is Weakly Dependent on Force

The analysis of growth and shortening excursions (Fig. 6.4 and Table 6.1) revealed that the assembly is only weakly dependent on force. From the individual traces obtained under force-clamp conditions (Fig. 6.2, Supplementary Figs. D.3-D.5) it appears that the variability within a given trace is as large as the variability across the population. The weak force dependence observed above predicts that even within a single microtubule there should be weak dependence of assembly rate on force. As shown in Fig. 6.6A, this is indeed the case when the force is progressively decreased from 1.6 pN to 0.7 pN, and it was found that there is no obvious relation between force and growth rate; short term variability apparently overwhelms any effect of force.

Examination of all the traces reveals a weak decrease of average growth rate with increasing force, as shown in Fig. 6.6B. The decrease was statistically significant

($p<0.008$), but was only about 2-fold, even though the force increased 7-fold. The simulation results are consistent with the experiment in both variability and weak force dependence (Fig. 6.6B). Thus, we conclude that assembly is only weakly dependent on force, and the relationship between them can be obscured by the high variability in growth rate and is only discerned through averaging over many microtubule growth phases.

Discussion

By combining optical tweezers with custom-engineered microscale barriers to microtubule polymerization, we are able to track tubulin addition and loss events at the growing tip of a compressively loaded dynamic microtubule. Using back focal plane interferometry for high temporal and spatial resolution, and applying force-clamping to increase the accuracy and resolution of displacement measurements, we attain unprecedented nanometer scale precision. We find that microtubule growth rates are highly variable with polymerizing microtubules frequently experiencing shortening excursions that can remove up to ~5 layers of tubulin from the microtubule tip. That microtubules can sustain such extensive tubulin loss and remain in the growing state argues against a single-layer GTP cap and is consistent with simulations that assume an exponentially-distributed multilayer GTP cap. Growth rate variability persists over a wide range of forces, and even over longer time scales the average growth rate is only weakly dependent on force. We find that these newly observed features of assembly under load arise naturally from a simple mechanochemical model.

Implications for Models of Microtubule Dynamic Instability

Understanding the molecular mechanisms of microtubule dynamic instability is critical for understanding how microtubule-associated proteins (e.g. EB1, APC, tau, Op18/stathmin, and XMAP215/TOG) control microtubule behavior in normal, diseased, and injured cells. The GTP cap hypothesis is central to our understanding of microtubule assembly [12], and is widely accepted even though the cap itself has not been directly visualized. The central premise is that αβ-tubulin heterodimers are stable in the

microtubule lattice when their beta subunit is bound to GTP, and relatively unstable when their beta subunit binds GDP. The relative instability of the GDP subunits is believed to derive from the intrinsic tendency of GDP subunits to form bent protofilaments that prefer to kink radially outward. This kinking then mechanically antagonizes lateral bonds within the microtubule lattice and thus promotes disassembly. Conversely, GTP-tubulin subunits are believed to form relatively straight protofilaments, thus reducing the mechanical stress on lateral bonds and thereby stabilizing the microtubule [34, 157-159]. Tubulin adds to the microtubule lattice as GTP-tubulin, and is subsequently hydrolyzed to GDP-tubulin. This maintains a cap of straight, relatively unstrained GTP-tubulin that holds the microtubule tip together, thus preventing the GDP subunits from destabilizing the lattice by assuming their preferred bent conformation; if the cap is lost, rapid shortening ensues. Depending on the relative rates of tubulin addition, tubulin loss, and GTP hydrolysis, the cap could be small and confined to the very tip of the microtubule.

A substantial body of work has argued that the GTP cap is very small, possibly as small as a single layer of tubulin [148-152], or only slightly larger [32, 146, 147, 160] (see review in [117]). Our observation of highly variable microtubule growth, with shortening excursions of up to ~5 layers or more of tubulin during a growth phase, is difficult to reconcile with a single layer GTP cap model, since the entire GTP cap would be frequently lost during these growth-phase shortening excursions. However, measuring the size of the GTP cap is very challenging, and after careful consideration of the arguments, experimental methodology, and data, we argue that the resolution in these earlier studies is probably insufficient to rigorously differentiate between a single discrete cap at the tip, versus a cap that is distributed over several layers of GTP at the end of a microtubule. In addition, in many cases these earlier studies estimated the *minimum* cap required for maintenance of the growth phase, rather than the *actual* size of the cap during growth. Importantly, upper bounds have also been placed on cap size via analysis of microtubule catastrophe subsequent to dilution, which resulted in the cap being rapidly lost within 1-2 sec, and led to estimates of the cap being at most 60-100 subunits deep if both hydrolysis and subunit loss are accounted for [32, 147]. Also, many of these studies implicitly assumed that GTP subunits form a discrete cap, with hydrolysis proceeding as

an induced wave that follows polymerization. This model implicitly assumes coupling or cooperative behavior between tubulin subunits. This is a substantially more complicated picture than the physically direct and simple assumption that GTP hydrolysis events are independent and stochastic first-order events as originally proposed by Mitchison and Kirschner [12]. By assuming uncoupled hydrolysis, the cap becomes effectively deeper for given number of GTP-tubulin units, as the GTP-tubulins are distributed throughout the tip region, rather than confined only to the last layer or two. The consequence is that the tip is expected to fluctuate on the nanoscale while remaining in the growth state.

Our theoretical treatment of microtubule dynamic instability assumes uncoupled hydrolysis [87, 156], and is approximately consistent with the newly observed nanoscale dynamics reported here. This mechanochemical model reasonably approximates: 1) the variability in the assembly during growth on the nanoscale, 2) the range of excursion sizes including occasional shortening excursions of 5 layers, 3) the reduction in excursion size (both growing and shortening) at high load, 4) the variability in the single time increments, and 5) the relative insensitivity of assembly on load. The model assumes that hydrolysis obeys a first-order reaction once a GTP-tubulin is buried in the lattice with a rate constant of ~1 s^{-1}[87, 156]. That the terminal GTP-tubulin would be spared hydrolysis is consistent with the β-tubulin subunit being exposed at the plus end with the GTP exposed to the solvent rather than to neighboring tubulin dimers [161]. Once another tubulin adds onto the protofilament, the formerly terminal GTP-tubulin is now the penultimate subunit and its GTP experiences a completely different biochemical environment. In the model, these buried subunits then undergo random hydrolysis leading to a spatially decaying distribution of GTP-tubulin near the tip, with progressively fewer GTP-tubulins as a function of distance away from the microtubule tip. In fact, the predicted approximately exponential decay of GTP-tubulin with increasing depth is reminiscent of, and mathematically similar to, the ‘comets’ observed with fluorescently tagged “tip tracking” proteins such as EB1. The first-order GTP hydrolysis for buried subunits and the resulting approximately exponential decay of GTP-tubulin spatially is also very similar to how Mitchison and Kirschner first hypothesized the cap structure might behave in their original report on dynamic instability [12]. The number of GTP-

tubulins in the microtubule lattice is predicted by the model to typically be ~40-60 (Fig. 6.2) [87, 156], consistent with the previous estimates of *maximum* cap size from dilution studies (60-100, discussed above). In addition, caps as small as 10-20 GTP-tubulins are sufficient to prevent complete catastrophe in most cases (Fig. 6.2), which is consistent with previous estimates of *minimum* cap size. When the cap falls below ~10, it is very likely that a catastrophe and subsequent rapid disassembly will occur (Fig. 6.2). In summary, the mechanochemical model of VanBuren et al.[87, 156] is a physically straightforward model that is in reasonable agreement with the new nanoscale assembly data. Future work is required to more thoroughly test the mechanochemical model to account for such phenomena as lattice defects and the microtubule seam, and their potential role in dynamic instability.

In principle, other models could explain these data as well. However, there have been relatively few attempts to construct models that explicitly account for dynamic instability at the nanoscale via explicitly accounting for individual tubulin dimer addition and loss. The first such models were constructed by Chen and Hill in the 1980s [162], and these were followed by the 'Lateral Cap' model of Bayley and co-workers [148]. The main problem with the models of Chen and Hill is that they predicted large cap sizes (~200) that later turned out to be inconsistent with experimental measurements. Bayley and co-workers attempted to address this issue in the Lateral Cap model by assuming that addition of an incoming GTP-tubulin instantly forced hydrolysis of an underlying GTP. This ensured that the cap was at most one layer deep. However, the present nanoscale fluctuation results, where shortening excursions of multiple tubulin layers do not necessarily result in catastrophe (Fig. 6.3A and Fig. 6.4A), stand in contradiction to the assumptions of the Lateral Cap model (see supplemental material for Lateral Cap model simulations as compared to nanoscale experimental results). Other models have attempted to describe cap dynamics without describing the details of the individual tubulin dimers [163, 164]. At the time, a coarse-grained modeling approach could be considered appropriate given the relatively low resolution with which microtubule assembly could be observed via light microscopy. However, such coarse-grained models are unable to aid in interpreting the present interferometry-based measurements with 3.5

nm resolution (Fig. 6.5, Table 6.2). As experimentation has now been pushed to the nanoscale, it is necessary for the modeling to push to the nanoscale as well.

Microtubule Growth is Highly Variable, but Does Not Involve Oligomeric Steps

Using an approach similar to ours, though with lower spatial and temporal resolution, a recent study reported stepwise growth of microtubules, and steps were attributed to addition of oligomers of tubulin subunits (i.e. a "dimer" has two subunits of length 16 nm, a "trimer" has three subunits of length 24 nm, etc.) [153]. Our data shows no evidence of this, though we find events with a similar step-like appearance when we process our data similarly to Kerssemakers et al. However, when viewed at higher bandwidth these events are clearly not steps (see supplemental information, Fig. D.6). Similar events of relatively rapid length change, producing an appearance that could be considered step-like, are also present in simulations of lower bandwidth data (e.g. at ~6 s in Fig. 6.2), despite the fact that only single subunit additions are modeled. These results illustrate the difficulty in discriminating steps in highly variable data. A step is by definition a period of rapid movement, and without a fundamental physical expectation for the structure of a step, it is only possible to say that events occurred more quickly than can be resolved on a given time scale. Because microtubule growth is highly variable, periods of rapid length change by successive net addition of subunits can be easily misinterpreted as steps, especially by algorithms that do not test the null hypothesis that steps do not exist. This naturally leads to the expectation that for a given criterion, steps will be identified more frequently if the average growth rate is rapid, as seen in Kerssemakers et al.'s interpretation of microtubule growth accelerated by the presence of XMAP215. Of course it is possible that oligomers do occasionally add to the tip of a microtubule. Strictly speaking, some oligomers will exist in equilibrium with the individual subunits in solution, although using the estimated value for ΔG^{0*}_{Long}=-7 k_BT ($K_{dimer\ formation}$=2200 M^{-1}) and a free tubulin-GTP subunit concentration of 5 μM, we estimate the concentration of dimers (i.e. two subunits associated head to tail) to be ~50 nM (if ΔG^{0*}_{Long}=-9 k_BT, then $K_{dimer\ formation}$=16,000 M^{-1}, and dimer concentration is ~300

nM at 5 μM total tubulin concentration). In our simulation, assuming dimers exhibit the same on-rate as monomers, this would result in an expected addition of a dimer once every 0.4 s, or ~1 out of 100 addition events (if ΔG^{0*}_{Long}=-9 k_BT, then a dimer would be added ~1 out of 15 addition events, or ~1-2 out of the ~26 addition events per 0.1 s observation period). In addition, the bimolecular on-rate constant for addition of dimers to the microtubule tip will likely decrease somewhat for the larger complexes owing to their slower translational and rotational diffusion, which will diminish the role of oligomers. Further, it might be expected that longitudinal association of the two subunits in solution would promote the hydrolysis of the beta subunit on the minus end of the dimer [161], so that the dimer can no longer form the full complement of lateral bonds with the microtubule lattice because of the kink induced by hydrolysis. Thus, from thermodynamic and biochemical arguments we expect the contribution of even the most common oligomers (2 subunits) to be negligible in our assay, occurring in less than 1 out of 100 addition events. This is both consistent with our results, and also with the most straightforward interpretation of the extremely steep, exponent 12 ± 2, dependence of microtubule nucleation on the concentration of tubulin, which suggests that oligomers are highly unstable and very short lived below the critical concentration for nucleation (~15 μM under our experimental conditions). However, we note that under some experimental conditions, for example high concentrations of magnesium or tubulin, oligomers become more prevalent [165, 166]. We expect that the study of Kerssemakers et al. had a similar oligomer concentration to our study, because both studies had about the same microtubule growth rate (~10 nm/s) despite using different tubulin concentrations, magnesium concentrations, and temperatures. Finally, the length fluctuations that we observed experimentally in single time increments were fully accounted for by a mechanochemical model that assumes assembly via single subunits (Fig. 6.5).

Previous observations of fluctuations during growth

These results show that the microtubule growth-phase is composed of a previously unobserved series of lengthening and shortening events. Indeed microtubules that would be described as growing in lower resolution studies, in fact are shortening

much of the time. The variability of microtubule growth rates that was identified in lower-resolution microscopy studies [167, 168] is now revealed to be largely due to frequent interspersion of shortening excursions during overall net growth. States that appear as "pauses" at low resolution are in fact composed of repeated switches between growth and shortening excursions. Conversely, filtering our high resolution data to data rates characteristic of microscopy based studies produces traces with similar variability.

Shortening excursions require the loss of many subunits during growth phases. Using light microscopy, Walker et al. [32] estimated the off-rate during growth to be 44 s^{-1}. From our simulations, we estimate that the off-rate of subunits is ~250 s^{-1}. However, the vast majority of these departures were of subunits that had no lateral neighbors, which would be difficult to detect by light microscopy. By contrast, simulated subunits with 1 or more lateral neighbors dissociated at a rate of 18 s^{-1}. Thus, we expect that light microscopy would yield an off-rate during growth of between 18 s^{-1} and 250 s^{-1}, consistent with the value estimated by Walker et al. of 44 s^{-1}.

We find that growth-phase shortening persists through the loss of many subunits, indicating that periods of polymerization and depolymerization during growth reflect different structural/chemical states at the tip of a microtubule, and not the tails of a Gaussian distribution arising from simple on and off kinetics, consistent with conclusions from previous analysis at lower resolution [167, 168]. These observations indicate that the tip of a microtubule dynamically transitions through a range of quasi-stable states with different polymerization rates (Fig. 6.2). Over short time periods (<1 s) such changes are revealed by transitions between growth and shortening, while over longer periods microtubules can evolve quasi-stable conditions during which transitions to shortening are more frequent or relatively suppressed.

Implications for microtubule assembly in vivo

The occurrence of shortening excursions during growth suggests that the specific suppression of these excursions in vivo might account for the high growth rates that are observed in vivo (reviewed in [117]). The large intrinsic variability of microtubule growth rates clearly expands the range of mechanisms available for rapid restructuring of

the microtubule cytoskeleton, and for controlling the force of microtubule polymerization during processes such as directing chromosome movements [17], organelle positioning such as nuclear positioning in yeast [169], or in the outgrowth of neuronal processes. Another interesting implication of our studies is a relatively weak dependence of velocity on compressive load, suggesting that if microtubule assembly is regulated by compressive load in vivo, it is likely through the catastrophe frequency rather than the assembly rate. The likely reason for the weak dependence of the load is that there are many protofilaments available "in reserve", that are close to the leading protofilament but not close enough to the wall to be significantly affected in their tubulin addition rate. In fact, our modeling indicates that only a relatively few protofilaments, typically ~3 out of 13 protofilaments (at 0.5 pN), are affected by the wall on average . This stands in contrast to actin filaments, which have only two protofilaments, and so their growth rate would be expected to be affected more strongly by compressive load than microtubules.

The greatly improved resolution of these studies reveals growth-phase variability paramount to microtubule dynamics. Our data builds on earlier studies examining variability of growth [167, 168] and provides a new experimental test that supports a simple mechanochemical description of microtubule growth [87, 156]. By achieving nanometer scale precision, we are able to resolve complex underlying behaviors that were obscured by longer time or ensemble averaging, including nanoshortening events, and variability of the relation between force and growth-rate. This has important implications for considering how external factors (e.g. drugs, MAPs, forces) alter the behavior of individual microtubules, as many details of the events occurring at the tip of a growing microtubule can disappear in lower resolution averages. Our assay, combined with the computational modeling, provides an integrated platform for further investigation of microtubule-associated protein regulation of microtubule assembly at the nanoscale. Going forward, the application of high-resolution techniques in the presence of MAPs or microtubule drugs promises to reveal details of physiologic microtubule and MAP behavior, including tip tracking, and actions of drugs that modulate microtubule behavior, such as the chemotherapy agents taxol and vinblastine.

Experimental Procedures

Microtubule seeds

Unless otherwise specified, all samples are in BRB-80 (80 mM pipes, 1 mM $MgCl_2$, 1 mM EGTA, pH=6.8). All reagents are from Sigma unless otherwise specified. Microtubules are polymerized from thrice-cycled bovine brain tubulin, taxol stabilized and pelleted in an airfuge (Beckman) for 5 minutes at 28 psi, resuspended, and biotinylated by 15 minutes incubation in 1.7 mM biotin succinimidyl ester. The biotinylation reaction is quenched with 3 volumes of 400 mM glycine for 10 minutes. Microtubules are pelleted, resuspended and passed through a 30 gauge needle 5-7 times to break the microtubules into ~ 3 μm lengths. Finally the microtubules are pelleted and resuspended three times in buffer not containing taxol. A conservative estimate of remaining taxol in an experimental solution is below 10 pM, far below the concentration required to detectably change microtubule behavior [170] (~100 nM) or for significant microtubule binding [171] (Kd = 10 nM).

Silica microspheres

Silica beads (0.6 micron diameter; Bangs Labs), suspended at 10 mg/ml, are incubated with 20 μg/ml bovine albumin biotin at room temperature for five minutes. Beads are pelleted, resuspended at 1 mg/ml, and incubated in 20 μg/ml streptavidin (Molecular Probes) at room temperature for five minutes. Finally beads are pelleted and resuspended four times before being aliquoted, flash frozen and stored at 10 mg/ml.

Optical tweezers

The optical tweezers are identical to those described previously [155] with two exceptions. First, the acousto-optic deflectors used to steer the beam in the original instrument were replaced by a tip-tilt mirror (Physik Instrumente). Second, the entire room that housed the instrument was temperature controlled to 36° C by use of a small radiant heater controlled via a feed back circuit reading a thermocouple positioned near the microscope stage. To prevent drift due to temperature differentials across the large thermal mass of the optical table and additional equipment, the entire room was held

within a range of one degree Celsius. Device calibration was carried out by fitting the power spectral density with a Lorentzian. Agreement with more direct calibration by laminar flow around the trapped particle was also checked, and agreed within 10%. Calibrations of stiffness and detector sensitivity across the range that a bead could be expected to traverse during an experiment varied less than 2 %. Finally, the stiffness and sensitivity were verified in the presence of barrier patterned coverglasses.

Polymerization assays

Microtubule seeds are diluted in BRB-80 buffer containing labeled glass microspheres (0.5 mg/ml), GTP (1 mM), Mg^{2+} (2 mM), catalase (0.12 mg/ml), glucose oxidase (0.6 mg/ml), glucose (30 mM), dithiothreitol (2 mM) and αβ-tubulin (5 μM). This polymerization mixture is introduced into a chamber created using a standard slide, aluminum foil spacers, and a coverslip with microfabricated barriers [154]. A suitable bead is located, trapped, and inspected by differential interference contrast microscopy for a microtubule. The bead and microtubule are brought to one of the barrier structures using the laser tweezers, and the microtubule is oriented toward the barrier by maneuvering the optical trap.

Stationary trap experiments simply allow the microtubule to polymerize into the barrier. Once the microtubule encounters the barrier, polymerization is tracked by recording bead position at 5 kHz. As the microtubule polymerizes against the barrier, its additional length pushes the bead from the center of the trap resulting in a force at the tip.

Feedback controlled experiments (force-clamp) are performed by updating the trap to maintain a constant force at the microtubule tip. Typically bead position and force data are collected at 5 kHz. The average position of the bead is calculated and the laser position is updated at 10 Hz. The force clamp is only initiated after the microtubule has grown to the barrier and displaced the bead.

Microtubule Dynamics Simulations

Simulations were run using MATLAB (The Mathworks, Natick, MA) as previously described [87, 156], except for the following. (1) Modifications were made

to the simulation program to account for the experimental force clamp routine, and (2) the simulation output was modified to match the experimental bead tracking method as described above. Details are provided in supplemental materials.

Acknowledgements

I would like to thank Dr. Edgar Meyhofer for valuable discussion and comments on this work, and Drs. Yan Chen, Joachim Mueller, and Erkan Tuzel for helpful discussions. The chemical engineering clean room at the University of Michigan supplied lithography equipment and expertise. This work was supported by the grants to AJH from the Burroughs Wellcome Fund and the National Science Foundation MCB-0334835. HTS was supported by the Whitaker Foundation, MKG is supported by National Institutes of Health NRSA grant EB005568. DJO is supported by National Institutes of Health grant GM071522 and by National Science Foundation grant MCB-0615568. I am grateful to the Minnesota Supercomputing Institute for providing computing resources, and to David Do for technical assistance in lateral cap

Tables and Figures

TABLE 6.1: Nanoscale Assembly Excursion Lengths

Experimental Force Clamp	Microtubule Description	Number of Excursions Measured	Mean Growth Excursion Length	Mean Shortening Excursion Length
0-1 pN	GTP	7,617	13.3±14.1[a] nm	-9.7±10.5[a] nm
	GMP-CPP	1,733	4.7±3.5 nm	-4.4±3.7 nm
1-2.5 pN	GTP	2,087	9.5± 10.5 nm	-6.4±6.7 nm
	GMP-CPP	167	4.7±3.2 nm	-4.5±3.2 nm

[a]mean +/- standard deviation

TABLE 6.2: Nanoscale Assembly Single Time Length Increments

Experimental Force Clamp	Microtubule Description	Number of Single Time Increments Measured	Mean Single Time Increment Length	Standard Deviation Single Time Increment Length
0-2.5 pN	GTP	16,762	0.81 nm	6.60 nm
0-2.5 pN	GMP-CPP	2,442	0.00 nm	3.50 nm

FIGURE 6.1: Observation of microtubule assembly at the nanoscale. (A) Schematic top view of the experimental geometry. A dynamic microtubule extension polymerizes from a bead-linked microtubule seed. The bead is held in the optical trap (magenta) such that when the growing microtubule contacts the barrier (gray), it polymerizes against the force of the trap. Lateral constraint of the microtubule is accomplished with the vertex seen in the top view while the undercut shown in the side view (Figure 1C) prevents the microtubule from slipping down off of the barrier. The barriers were carefully designed to avoid interference with the tightly focused laser and to allow high quality imaging. (B) Differential interference contrast micrograph of an experiment showing the bead, microtubule, and barrier. Two images are superimposed to show the microtubule straight before it is loaded, and later buckled to demonstrate that the tip is constrained and under load. Data is only analyzed for unbuckled microtubules. (C) Applying a force clamp allows an approximately constant load to be maintained at the microtubule tip. The laser position is updated to maintain the desired position of the bead relative to the center of the trap and therefore provides a constant average force. The positional changes of the laser trap are a direct measurement of microtubule length changes. The position of the laser is updated at 10 Hz, which is more than sufficient to follow polymerization. At this rate, the average position of the bead and hence the necessary change in laser position is determined with resolution smaller than the size of a single tubulin subunit (8 nm).

Figure 6.1

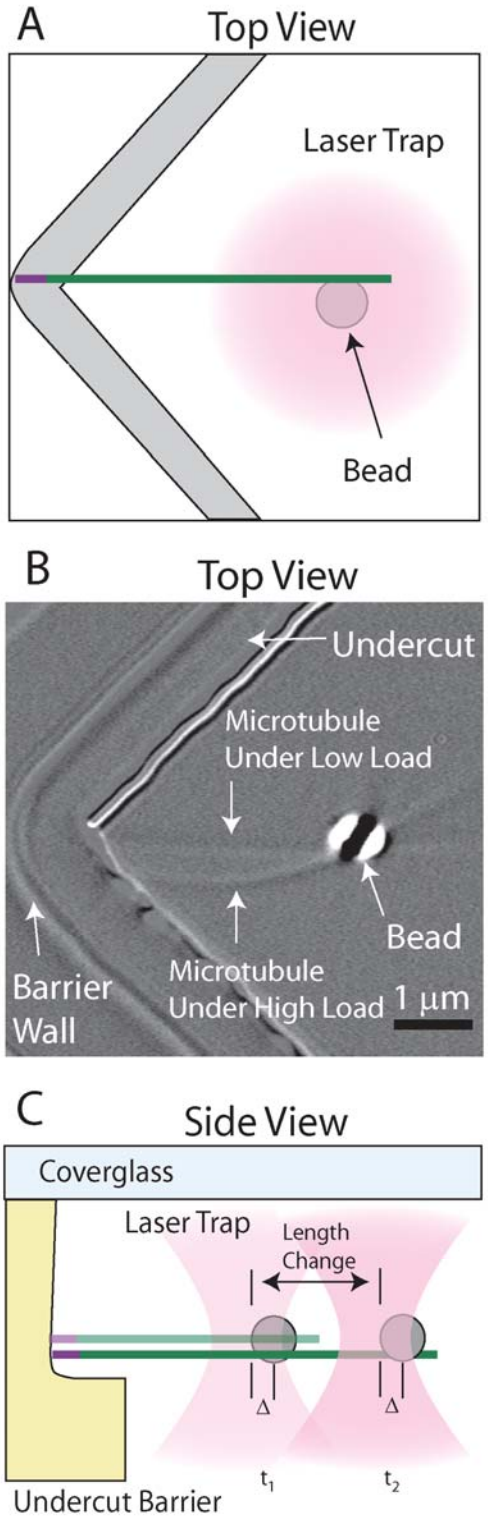
A
Top View
Laser Trap
Bead
B
Top View
Undercut
Microtubule
Under Low Load
Bead
Barrier
Wall
Microtubule
Under High Load
1 µm
C
Side View
Coverglass
Laser Trap
Length
Change
Δ
Δ
t1
t2
Undercut Barrier

FIGURE 6.2: Simulation of microtubule assembly at the nanoscale. At time (A), the microtubule tip has a multiprotofilament extension with a relatively long and spatially-distributed GTP cap (magenta) of 35 subunits on average. The leading protofilaments then depolymerize and recap, resulting in a growth-phase shortening event, as shown in (B). Note that the GTP cap remains intact, never being less than 20 GTP-tubulin subunits during the shortening phase. Subsequently, the microtubule polymer continues growth, as shown in (C). Catastrophe occurs after 10 sec, as shown in (D-E), at which point the GTP cap has only 3 subunits on average.

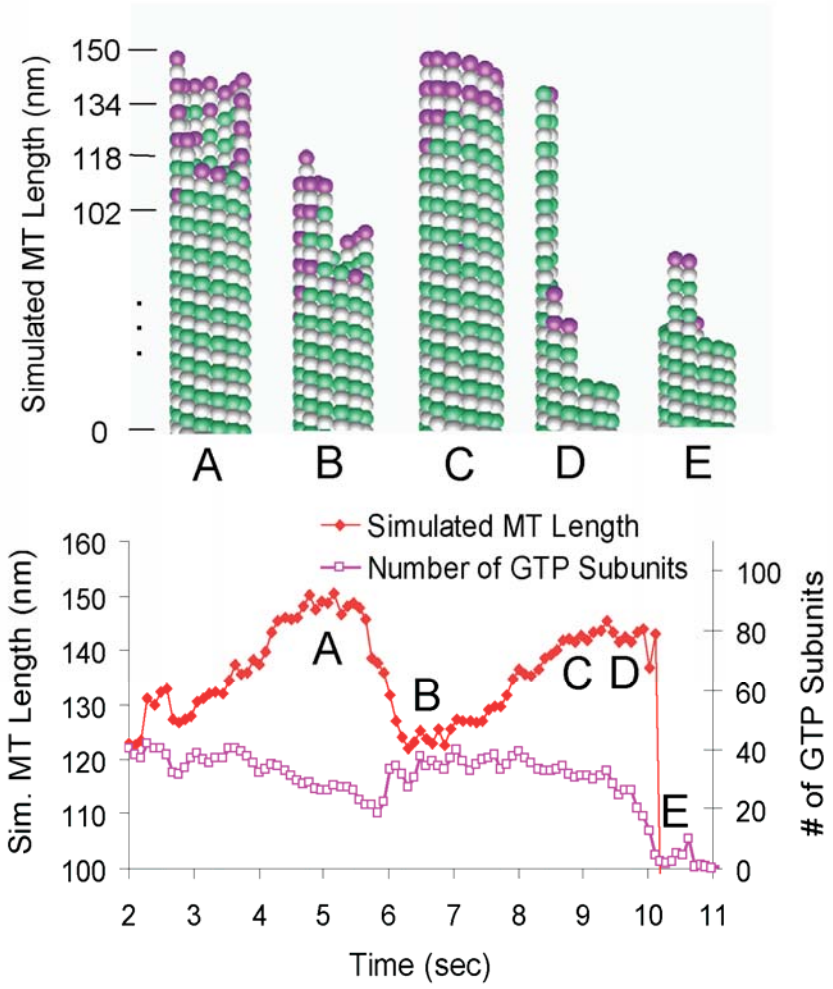

FIGURE 6.3: Microtubule assembly at the nanoscale. (A) Experimental and simulated individual traces of microtubule plus-end assembly behavior at 1.5 pN clamp force are shown as compared to GMP-CPP control traces. Slow net assembly at the microtubule tip is highly variable both experimentally and in simulation. There are clearly retreats during microtubule assembly that are larger than a single layer of tubulin subunits, or even a few layers. Traces from GMP-CPP stabilized microtubules are not highly variable, indicating that the variability is intrinsic to microtubule growth behavior, and not an artifact of the data collection method. (B) Quantification of microtubule assembly at the nanoscale. To quantify the variability in microtubule assembly, growth and shortening excursions are defined as the total number of consecutive displacements in either the positive or the negative direction (shown by green and red arrows, respectively). The length of these multiple time step excursions are then recorded as a measure of growth variability. In contrast, single time-step length increments are also recorded as a measure of microtubule growth activity within a short time interval (sampling interval = 0.1 s), as shown by the black arrows.

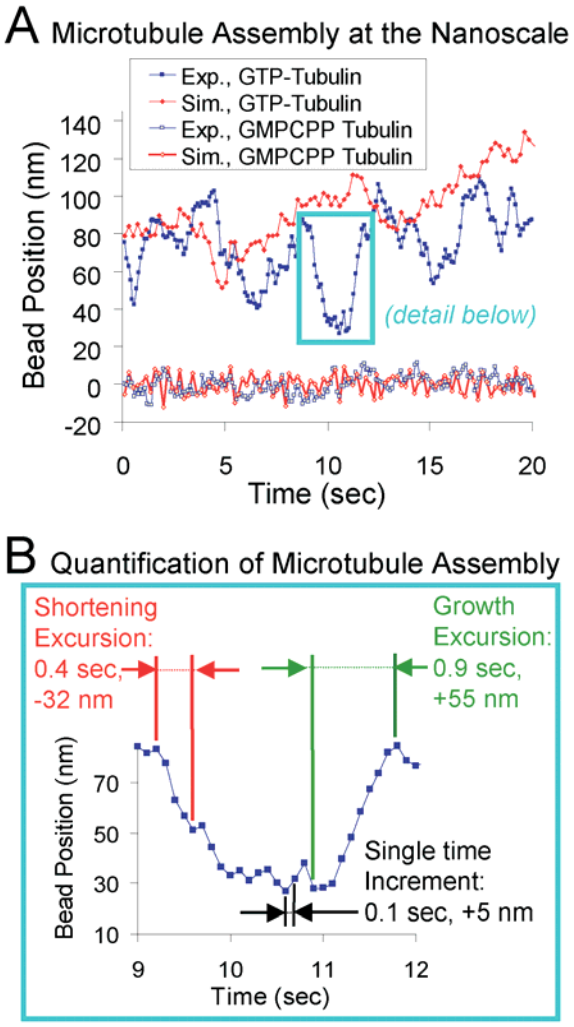

FIGURE 6.4: Microtubule assembly is highly variable, with frequent growth-phase shortening events. (A) A histogram of microtubule growth-phase excursion lengths for 0-1 pN force clamp as compared to GMP-CPP controls. Excursion lengths are defined in this analysis as sequential negative or positive microtubule length changes (no fitting), as shown in 3B. Growth-phase shortening events are large compared to GMP-CPP controls, indicating that experimental noise cannot account for the observed behavior. The model qualitatively accounts for the extent of positive and negative excursions (red) (B) A histogram of microtubule growth-phase length changes for 1-2.5 pN force clamp experiments, as compared to GMP-CPP controls. At higher clamp forces, both growing and shortening excursions are restricted as compared to low clamp force results ($p=9.7\times10^{-4}$ for growth, $p=3\times10^{-7}$ for shortening), reducing the overall variability in observed microtubule assembly behavior. This result suggests that the microtubule tip structure is influenced by the force on a microtubule, possibly by limiting the propensity of a few protofilaments to extend beyond their neighbors. The model (red) is qualitatively consistent with the extent of fluctuation and predicts the reduction in variability.

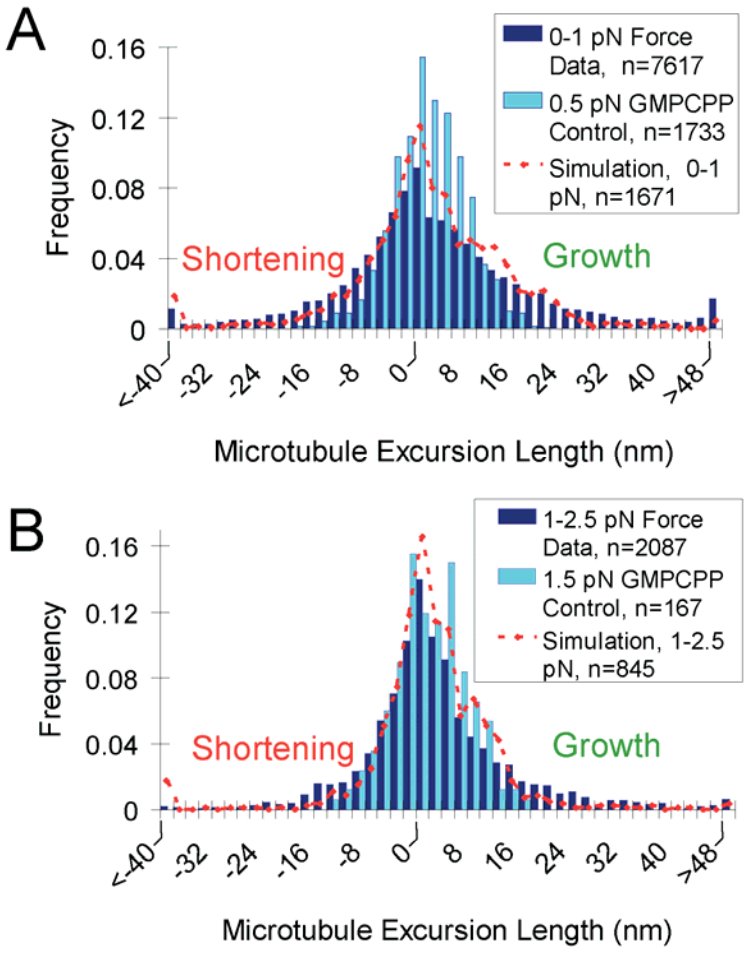

FIGURE 6.5: Distribution of microtubule growth-phase single time increments. Single 0.1 second time increment sampling demonstrates that tubulin dimers add as single subunits, not oligomers. Single time microtubule length increments are summarized for individual time steps during assembly. Both GTP microtubules and GMP-CPP control microtubules show small, Gaussian-distributed length fluctuations at single time steps, indicating that tubulin oligomer addition and loss is highly unlikely. The increments in the presence of GTP are larger than in GMP-CPP controls, and the model accounts for the extent of fluctuations observed experimentally while assuming that tubulin addition occurs via single subunits only.

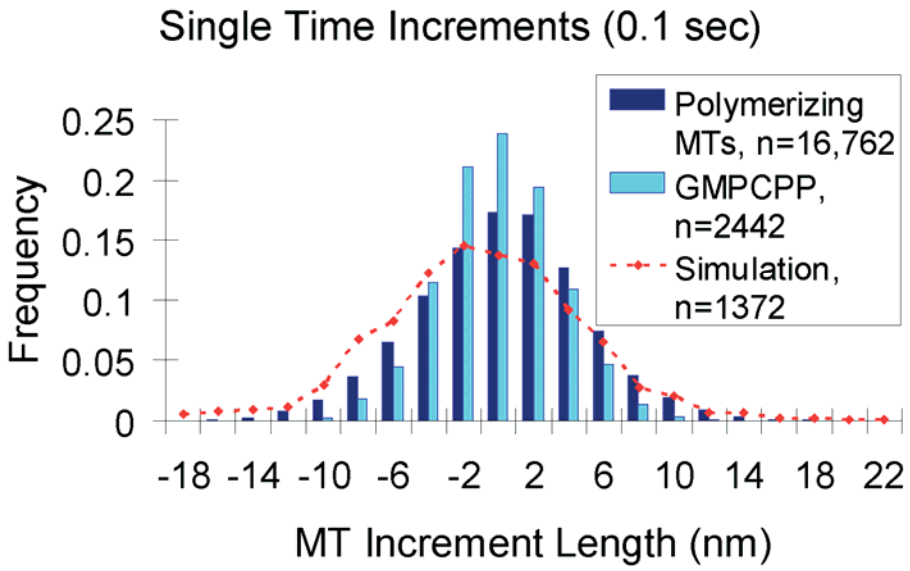

FIGURE 6.6: Growth velocity depends weakly on force. (A) A microtubule length history tracked under a range of loads held constant using the force clamping routine. The growth rate is variable at all loads, with no dramatic increases in rate as the load is reduced. (B) Dependence of microtubule growth velocity on applied force. Microtubule growth velocity is weakly dependent on force (applied in force-clamp mode) both in simulation and experiment. The high variability is the result of variability in assembly at the nanoscale.

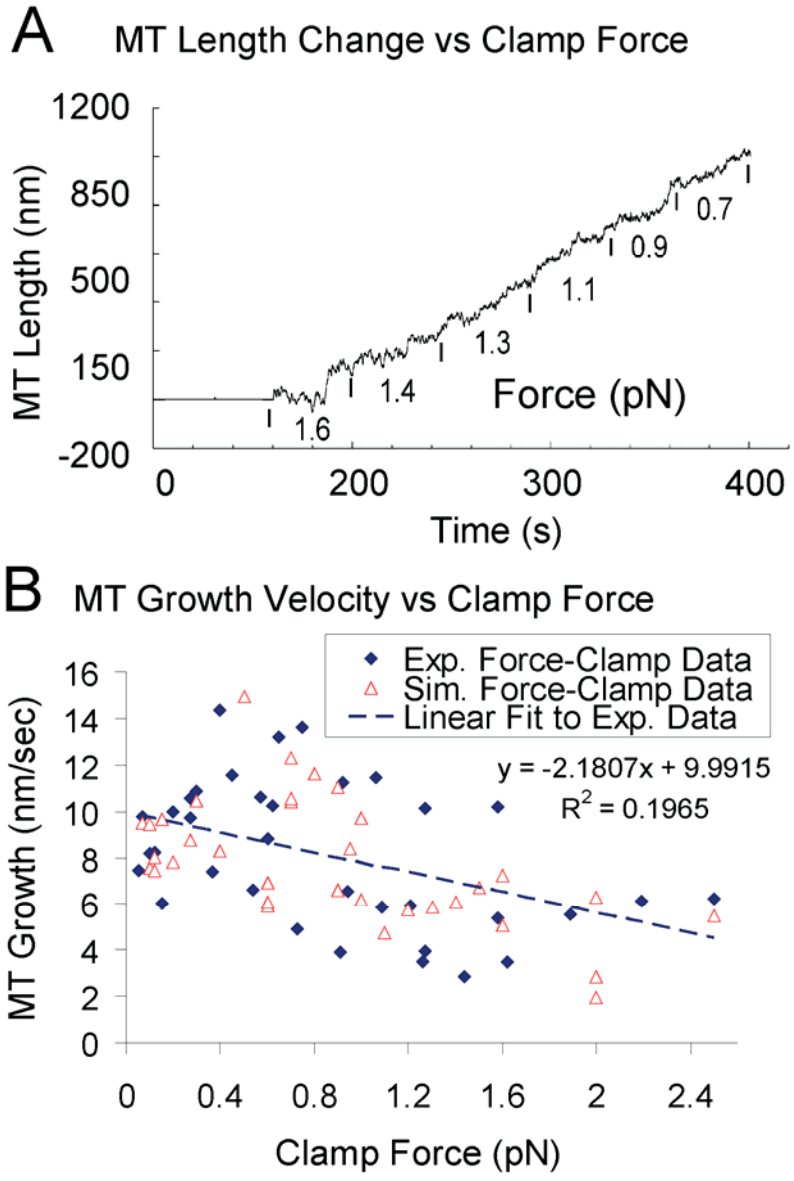

CHAPTER SEVEN

THE MICROTUBULE-BASED MOTOR KAR3 AND PLUS-END BINDING PROTEIN BIM1 PROVIDE STUCTURAL SUPPORT FOR THE ANAPHASE SPINDLE

(Contributing Authors: Melissa Gardner, Julian Haase, K. Mythreye, Jeffrey Molk, MaryBeth Anderson, Ajit Joglekar, Eileen O'Toole, Mark Winey, E.D. Salmon, David Odde, and Kerry Bloom: *MG performed simulations and data analysis; JH, KM, JM, MB, and AJ performed experiments and data analysis; ET performed EM*)
(Reprinted with permission from *The Journal of Cell Biology* 180(1) (2008))

Abstract

In budding yeast, the mitotic spindle is comprised of 32 kinetochore microtubules and ~8 interpolar microtubules. Upon anaphase onset, kinetochore microtubules shorten to the pole, while interpolar microtubules increase in length. Overlapping microtubules are responsible for the maintenance of spindle integrity during anaphase. To dissect the requirements for anaphase spindle stability we introduced a conditionally functional dicentric chromosome into yeast. When centromeres from the same sister chromatid attach to opposite poles, anaphase spindle elongation is delayed and a DNA breakage-fusion-bridge cycle ensues that is dependent upon DNA repair proteins. We find that cell survival following dicentric chromosome activation requires the microtubule binding proteins Kar3p, Bim1p and Ase1p. In their absence, anaphase spindles are prone to collapse and buckle in the presence of a dicentric chromosome. Our analysis reveals the importance of Bim1p in maintaining a stable ipMT overlap zone by promoting polymerization of ipMTs during anaphase, while Kar3p contributes to spindle stability by cross-linking spindle microtubules.

Introduction

Mitotic chromosome segregation requires the formation of a stable bipolar spindle. Interpolar microtubules (ipMTs) from opposing Spindle Pole Bodies (SPBs) form an organized array by cross-linking with each other [30]. ipMTs may be cross-linked by microtubule-based motor proteins and/or microtubule associated proteins. This arrangement contributes to the structural stability of the two halves of the mitotic spindle

during metaphase and provides the means by which SPBs are rapidly separated from each other during anaphase B. Deletions of the plus-end directed microtubule based motor proteins *CIN8* or *KIP1* lead to abnormally short metaphase spindles [121], suggesting that these plus-end directed motors generate outwardly directed extensional forces on the SPBs via the sliding of ipMTs against each other. Cells lacking both Cin8p and Kip1p are not viable, but deletion of *KAR3* suppresses this lethality, suggesting that the minus-end directed motor Kar3p provides an inward force that opposes the outward force generated by Cin8p and Kip1p [114]. In support of the prediction that Kar3p provides an inwardly directly spindle force, over-expression of Kar3p produces shorter spindles [121]. However, in contrast to this prediction, spindles in *kar3*Δ mutants are short [172-174]. Thus, the role of Kar3p in the balance of spindle forces that determines mitotic spindle length and stability is unclear.

In addition to Kar3p generating inwardly directed spindle forces, it could be that Kar3p functions passively as an ipMT cross-linker, thus resisting spindle collapse [175]. For example, the MT plus end binding protein Ase1p acts to bundle MTs and thus stabilize the anaphase spindle [176-178]. Similarly, Bim1p, the yeast EB1 homolog, may contribute to ipMT interactions through its function at microtubule plus-ends [71]. It has been difficult to test the function of various microtubule binding proteins during mitosis due to the complexity of forces generated between parallel and anti-parallel microtubules and the forces generated between oppositely oriented sister chromatids.

The structure of the anaphase spindle in yeast provides a unique system to address the function of microtubule binding proteins in the maintenance of spindle stability. By anaphase, sister chromatids have separated and kinetochore microtubules (kMTs) have shortened to the spindle poles (kMTs ~ 50 nm in length) [30]. Thus, the ipMTs are responsible for maintaining spindle integrity throughout anaphase.

In this work, we used a conditionally functional dicentric chromosome to test the structural stability of the anaphase spindle. When centromeres from sister chromatids attach to opposite poles, tension across the DNA strand satisfies the spindle checkpoint [69]. Cohesin is degraded, anaphase onset ensues, sister centromeres migrate to opposite poles (anaphase A) and sister chromatids segregate. However, segregation of centromeres

on sister chromatids of a dicentric chromosome are restrained via their covalent linkage. Anaphase spindle elongation is delayed until the error is resolved. In wild-type cells, resolution is characterized by DNA breakage, with greater than 70% survival. Alternatively, if spindle breakage precedes DNA breakage, the entire chromosome is mis-segregated. Mis-segregation of the entire chromosome leads to aneuploidy and subsequent cell death.

Using the conditionally functional dicentric assay, we find that cell survival following dicentric chromosome activation requires the microtubule binding proteins Kar3p, Bim1p and Ase1p. In their absence, anaphase spindles have poor structural stability and therefore collapse and break in the presence of a dicentric chromosome. Our analysis reveals the importance of Bim1p in maintaining a stable ipMT overlap zone by promoting growth of ipMT plus-ends during anaphase, while Kar3p contributes to spindle stability by acting to cross-link spindle microtubules.

Results

Viability in response to activation of a dicentric chromosome requires spindle-associated proteins

Strains with an activated dicentric chromosome that lacked the spindle-associated proteins Bim1p, Kar3p, Cik1p, Ase1p, or Bik1p were 20-300 fold reduced in viability as compared to wild-type cells with an activated dicentric chromosome (Figure 7.1A,B, Table E.1). The most severe defect was observed in *bim1*Δ and *kar3*Δ, followed by *bik1*Δ, *cik1*Δ, and *ase1*Δ. The loss of viability in these mutants is comparable to mutants in DNA repair (*rad52*), indicating that an essential function is abrogated in their absence.

Although several of these microtubule-binding proteins have been implicated in kinetochore function [118], two pieces of evidence argue that kinetochore defects are not the cause of the decreased viability in the presence of a dicentric chromosome. First, our findings with mutations in spindle associated proteins are different than those previously reported for kinetochore mutants. Specifically, kinetochore mutant cells with activated dicentric chromosomes do not have decreased viability (Fig. 7.1B) [179-181]. Second,

the microtubule-associated binding protein Ase1 has no known kinetochore function, but is required for ipMT function during anaphase [177, 178].

Dicentric chromosome breakage is reduced in cells lacking these spindle- associated proteins

If the structural integrity of the anaphase spindle is compromised, dicentric chromosome activation may result in spindle breakage and/or failure rather than dicentric chromosome breakage. To test whether dicentric chromosomes break and rearrange in bim1Δ mutants, wild-type and bim1Δ cells were transformed with the conditionally dicentric minichromosome pGAL-CEN^2. DNA breakage and rearrangement products can be detected by transformation into bacteria and subsequent gel electrophoresis [182]. Monocentric rearrangements occurred in 50/50 minichromosomes recovered from wild-type cells (wt Figure 7.2A), with loss of one of the two centromeres (CEN3 or CEN4). In contrast, ~50% of dicentric minichromosomes recovered from bim1Δ cells contained both centromeres (bim1Δ Figure 7.2A; rearrangement products in first two lanes 23/50, last six lanes unrearranged 27/50). Thus, the reduced viability of bim1Δ mutants is accompanied by an increase in propagation of the intact dicentric chromosome. The appearance of rearrangement products in 23/50 cells indicates that reduced viability in bim1Δ mutants is not due to a deficiency in DNA repair.

To examine the rearrangement frequency of a dicentric chromosome we introduced *GAL-CEN3* into *HIS4* on ChrIII in wild-type and *bim1*Δ mutants [179]. In wild-type cells, a 1.1 kb repair product diagnostic of breakage and recombination between *GAL-CEN3* and *CEN3* on ChrIII [183] was observed within 2.5 to five hours after dicentric chromosome activation (Figure 7.2B). The 1.1 kb repair product was not apparent until 12 to 24 hours after switching *bim1*Δ cells to glucose (Figure 7.2B). Quantitative analysis indicated 7.4% of *GAL-CEN3* was intact after wild-type cells were switched to glucose for 30 hours while 36% of *GAL-CEN3* remained in *bim1*Δ cells (Figure 7.2C). Intact *GAL-CEN3* was elevated five-fold and the 1.1 kb rearrangement product decreased four-fold in *bim1*Δ cells, indicative of reduced chromosome breakage (Figures 7.2C and 7.2D). A decrease in the 1.1 kb repair product was also observed in

*ase1*Δ and *kar3*Δ cells (Figure E.2). These data reveal that dicentric chromosomes are physically stable in *bim1*Δ, *ase1*Δ, and *kar3*Δ mutants.

Dicentric chromosomes mis-segregate in spindle-associated protein mutants

To determine if the loss of viability after dicentric chromosome activation in *bim1*Δ mutants reflects mis-segregation of the intact dicentric chromosome, we utilized the lacO- LacI-GFP system to visualize the dicentric chromosome in live cells [184, 185]. The LacO coding sequence was integrated between the two centromeres on Chr III at *LEU2*; LacI fused to GFP was expressed to image the dicentric chromosome. In wild-type cells with an activated dicentric chromosome, chromosome spots at *LEU2* remain as a single focus of fluorescence between the spindle poles until sister chromatids separate in anaphase and two spots are visible (Figures 7.3A and 7.3B). However, in *bim1*Δ cells the dicentric chromosome is found proximal to one SPB in 48.5% of cells (vs. 6% in wild-type cells, Fig. 7.3A), while 17.5% cells had >2 Chr III spots (vs 2% in wildtype cells, Figures 7.3A and 7.3B). Thus, the frequency of mis-segregation of the intact dicentric chromosome is highly elevated in *bim1*Δ mutants.

Spindle-associated protein mutants have unstable spindles in the presence of a dicentric chromosome

We imaged microtubules (GFP-Tub1p) in mitotic spindles to assess the structural stability of wild-type and mutant cells in the presence of an activated dicentric chromosome. In >95% of wild-type cells with an activated dicentric chromosome, GFP-Tub1p was continuous along the length of the spindle in both preanaphase and anaphase (Figure 7.3C; n = 57 cells). However, 38% of mitotic *bim1*Δ cells displayed discontinuous GFP-Tub1p fluorescence that appeared as two foci (Figure 7.3C; n = 166 cells). The two GFP-Tub1p fluorescent foci could separate >5 μm before moving back together (data not shown). Thus, when the anaphase spindle is constrained by a dicentric chromosome bridge the *bim1*Δ ipMTs cannot maintain a continuous overlapping array. The gap in GFP-Tub1p could result from spindle destabilization, possibly related to a change in ipMT length [71] or cross-linking defects. In either case, ipMT function is

required in anaphase for cells to resolve the dicentric chromosome into monocentric derivatives. In contrast, weakening of mitotic spindle structural stability via loss of ipMT function favors chromosome mis-segregation and/or spindle breakage rather than dicentric chromosome breakage and rearrangement.

ipMT-associated tubulin polymer is reduced in bim1*Δ cells, but not in* kar3*Δ cells*

If both Bim1p and Kar3p contribute to spindle stability, as is predicted by the dicentric assay, then the loss of these proteins should result in a quantifiable defect in anaphase spindle morphology. To test this prediction we examined the distribution of GFP-Tub1p in anaphase spindles of wild-type and mutant cells using quantitative microscopy and model convolution. In wild-type cells, there is a uniform distribution of GFP-Tub1p fluorescence along the entire length of the anaphase spindle (Figure 7.4A). Anaphase GFP-Tub1 fluorescence levels in *kar3*Δ mutants are comparable to wild-type spindles (Figure 7.4A), suggesting that reduced spindle stability upon *KAR3* deletion is not due to improper length regulation of ipMTs. In contrast, there is a sharp drop in GFP-Tub1p fluorescence outside of the kMT-dense area very near to the SPBs in *bim1*Δ anaphase spindles (Figure 7.4A). These results suggest that the tubulin polymer associated with ipMTs during anaphase may be reduced in *bim1*Δ mutants as compared to wild-type spindle*s*. In contrast, another spindle defect may prevail in the absence of Kar3p.

Bim1-GFP is concentrated at the spindle midzone in anaphase (Figures 7.4B and S1A), suggesting that Bim1p is bound near to ipMT plus-ends during anaphase. Bim1p promotes growth of astral microtubules in G1 [71] and is likely to have a similar mechanism of action when bound to ipMT plus-ends in anaphase.

During anaphase, bim1Δ *mutant ipMTs are shorter than wild-type ipMTs*

To quantify ipMT length, we used electron tomography to reconstruct microtubule length distributions in wild-type anaphase spindles. By normalizing all microtubule lengths to the individual spindle lengths of 2 anaphase spindles, we found one class of abundant, short microtubules. These microtubules exhibit an exponential

length distribution with their plus-ends clustered near to the spindle poles (mean ± sd is 7 ± 7.7 % of spindle length (absolute length 151 ±213 nm), n=64 MTs; Figure 7.5A left graph, probability of fit to exponential model (p-value)=0.59, see Methods for calculation procedure). Based upon the position of kinetochores at this stage of anaphase, this polymer class represents kinetochore microtubules. Longer ipMT lengths were also exponentially distributed, but extended the length of the spindle, with plus-ends clustered near the opposite SPB from their origin (mean±sd is 78±15 % of spindle length (absolute length 1555 ± 447 nm), n=14 MTs, Figure 7.5A right graph, p=0.27 for fit to exponential, see Methods for p-value calculation procedure).

To use model convolution to statistically compare tubulin distributions in different populations, we sampled the exponential fit curves from the tomograms (Figure 7.5A) to generate simulated GFP-Tub1p distributions of anaphase spindles. By convolving the experimentally observed microscope point spread function with the simulated GFP-Tub1p distributions (see methods and [119]), we could directly compare simulated images (Figure 7.5B, top) to GFP-Tub1p experimental images (Figure 7.5B, bottom). Simulated images based on electron tomography data qualitatively match experimental fluorescence images (p=0.07, Figure 7.5B graph). Thus the exponential wild-type ipMT length distribution obtained via quantitative analysis of electron tomography data is a reasonable approximation of wild-type anaphase spindles (Figure 7.5B, animation).

The theoretical length distribution of anaphase spindle microtubules that most closely reproduced the experimentally observed GFP-Tub1p fluorescence distribution in the absence of Bim1p is shown in Figure 7.5C. The best fit to experimental data could be obtained using a Gaussian ipMT length distribution with mean±sd equal to 52±7 % of spindle length (p=0.06, Figure 7.5C). Thus, we predict that the ipMT plus-ends in *bim1*Δ mutants are located very near to the spindle equator, resulting in a significant decrease in the anti-parallel ipMT overlap zone as compared to wild-type spindles (Figure 7.5C animation, cf Figure 7.5B animation).

The role of Bim1p in regulating MT length is consistent with previous observations [71]. The decrease in overlap of anti-parallel microtubules in *bim1*Δ

mutants would reduce the number of productive binding sites available for the kinesin-5 motors Cin8p and Kip1p, preventing *bim1*Δ spindles from achieving the outwardly directed force threshold that is required to break dicentric chromosomes. Interestingly, cell viability after activation with a dicentric chromosome was increased ~12 fold in a *bim*Δ*/kip3*Δ double mutant as compared to *bim*Δ mutants with an activated dicentric chromosome (*bim*Δ*/kip3*Δ dicentric viability, 6.8±0.73%, n=4 trials) This result suggests that an increase in ipMT length (in the absence of the microtubule depolymerizing motor Kip3p) is sufficient to stabilize the anaphase spindle, thus increasing viability after activation of a dicentric chromosome.

Kar3p regulates bundling of ipMTs during anaphase

Because deletion of *KAR3* did not have a significant effect on anaphase spindle tubulin polymer (Figure 7.4), we predicted that another spindle defect, such as the proper bundling of ipMTs, may prevail in the absence of Kar3p. To test this prediction, we examined mutant spindle morphology in *kar3*Δ mutants expressing GFP-Tub1p. As shown in Figure 7.6A, 47% of *kar3*Δ spindles showed splaying of MTs in anaphase. Thus, ipMTs are poorly bundled in *kar3*Δ mutants as compared to wild-type spindles (8% MT separation). Disrupting the organization of ipMTs may also disturb proper anti-parallel crosslinking of Cin8p and Kip1p, and suggests that Kar3p is required for efficient attachment of the kinesin-5 motors Cin8p and Kip1p to oppositely oriented ipMTs. Therefore, deletion of *KAR3* results in reduced outwardly directed spindle forces as mediated by kinesin-5 motors, even though Kar3p itself may act to antagonize Cin8p/Kip1p function in wild-type spindles.

Kar3p is known to interact with either Cik1p or Vik1p light chains *in vivo* and *in vitro* [173, 186, 187]. Because *cik1*Δ mutants have low cell viability in response to activation of a dicentric chromosome, we predicted that the Kar3p-Cik1p complex may regulate spindle integrity via the ipMT bundling mechanism as shown in Figure 7.6A, and thus localize near to ipMT plus-ends in the anaphase spindle. Indeed, Kar3-GFP in wild-type anaphase spindles is localized at the SPB, but more importantly, is also present in punctuate locations within the spindle (Figure 7.6B, left). To assess Kar3p-Cik1p

binding exclusively, we examined Kar3-GFP localization in *vik1*Δ spindles (Figure 7.6B center, Figure E.1B). Here, there is reduced fluorescence of Kar3-GFP near to the SPB, with increased fluorescence in punctuate spots near to putative ipMT plus-ends. Simulations in which fluorescent proteins are distributed at the plus-ends of MTs also resulted in punctuate spots along the length of the spindle (Figure 7.6C). In contrast, Kar3-GFP that is complexed with Vik1p (in *cik1*Δ cells) is focused at the SPBs with little fluorescence along the length of the spindle (Figure 7.6B right, Figure E.1B). These results demonstrate that the light chains Cik1p and Vik1p differentially regulate the localization and function of Kar3p to either the ipMT plus-ends (Cik1p) or spindle poles (Vik1p). In addition, our results suggest that Kar3p-Cik1p regulates ipMT bundling along the length of the spindle, and that poor ipMT bundling is the dominant mechanism for low cell viability in response to activation of a dicentric chromosome in *kar3*Δ mutants.

Discussion

There are two pathways required for cell survival in the presence of a dicentric chromosome. Dicentric chromosomes are physically unstable and undergo a breakage-fusion-bridge cycle that is required for cell survival (Figure 7.1A). We report a second pathway required for cell survival, which is the maintenance of spindle integrity. If the spindle is compromised, spindle breakage results in chromosome loss and the subsequent loss of cell viability.

Using the activated dicentric chromosome assay, we find that Bim1p and Kar3p both contribute to structural stability of the anaphase spindle. Interestingly, the mechanisms by which these proteins contribute to stability are distinct from each other, but appear to be of similar importance (Figure 7.1B). Specifically, deletion of BIM1 results in shorter ipMT lengths, which reduces the size of the anaphase anti-parallel overlap zone (Figure 7.7, right). The ipMT overlap zone is necessary for efficient anti-parallel binding of the kinesin-5 motors Cin8p and Kip1p, and so reducing its length likely has a direct effect on the ability of the kinesin-5 motors to provide the outwardly directed forces that are required to stabilize the elongating anaphase spindle.

In contrast, deletion of *KAR3* does not have a significant effect on the level of anaphase tubulin polymer (Figure 7.4). Rather, *kar3*Δ mutants show splaying of anaphase ipMTs, likely due to improper ipMT bundling as mediated by Kar3p-Cik1p complexes at the plus-ends of ipMTs (Figure 7.6). The differential localization of Kar3-GFP in *cik1*Δ mutants and *vik1*Δ mutants (Figure 7.6B) is consistent with the difference in activated dicentric lethality between the mutants (Figure 7.1B), suggesting that spindle-bound Kar3p acts to promote ipMT bundling. Similar to the *bim1*Δ mutants, poor ipMT bundling in *kar3*Δ mutants also likely prevents proper anti-parallel binding of the kinesin-5 motors and therefore results in reduced outwardly directed spindle forces (Figure 7.7, center). This effect explains the long-standing enigma of how spindle lengths could be shorter in *kar3*Δ mutants, even though Kar3p could act to resist outwardly directed spindle forces when ipMTs are properly bundled.

These results highlight the importance of the spindle midzone structure in maintaining anaphase spindle integrity. An important future effort will involve mechanistically linking the spindle localization of Kar3p and Bim1p to their specific functions within the anaphase spindle.

Materials and Methods

Media, growth conditions, and strain construction

Strains and plasmids used in this study are listed in Table E.2. Media and strains, including gene deletions and GFP fusions, were prepared as described previously [181, 188]. Deletions of *BIM1* were confirmed by PCR amplification and by sensitivity to 15 μg/mL of benomyl. Strains were maintained at 25°C except for some wild-type and *bim1*Δ cells carrying dicentric chromosomes that were grown at 32°C. *kar3*Δ cells expressing GFP fusion proteins were maintained at 25°C overnight and switched to 32°C for two to three hours prior to imaging. For imaging chromosome spots, cells were grown in galactose or glucose for two to four generations before analysis. Cells with a conditional dicentric chromosome were grown in YCAT-Gal (galactose – monocentric) overnight at 25°C to mid-logarithmic phase and diluted into YPD (glucose – dicentric) to analyze dicentric chromosome behavior. Approximately 1000 cells were diluted in water

and plated on YPG or YPD for viability assays. Plates were incubated at 25°C for up to 10 days before colonies were scored. Wild-type and *bim1*Δ cells were transformed with *pGAL-CEN*[2] on galactose and single transformants were grown for eight to ten generations in either galactose or glucose before plasmid DNA was isolated and transformed into *E. coli* for analysis.

Dicentric chromosome breakage analysis – Southern blotting and PCR

Time course experiments on glucose and Southern blotting were performed as previously described [179]. Wild-type and cells with conditional dicentric chromosomes were grown overnight in 50 mLs of YCAT-Gal or YPG media and switched to fresh YPD at the start of the experiment. At time points, yeast were collected by centrifugation and genomic DNA was prepared. For Southern blotting, the genomic DNA was digested with *BamH1* and, after transfer of the DNA, the blot was probed with ^{32}P-*GAL-CEN* that was generated by PCR with Klenow polymerase. The blot was stripped and re-probed for ^{32}P-*MET14* as a control. Band intensity was measured using ImageQuant. For PCR assays, 1 μL of genomic DNA was added to a 50 μL reaction (200 nM dNTP's, 4% DMSO, 400 nM primers), that was cycled as follows: 98°C, 1 min; melting temperature 95°C, 1min – annealing temperature 60°C, 1 min – extension temperature 72°C, 2 min for 27 cycles; final extension temperature 72°C, 5 min. 5 μL of each PCR reaction were loaded on a 1% agarose gel and stained for 15 min in 0.02% ethidium bromide before analysis.

Fluorescence image acquisition and data analysis

Wide-field [188] and confocal [15] images were obtained as previously detailed. The microscope used for wide-field imaging was a Nikon Eclipse TE2000E stand (Melville, NY) with 100 PlanApo NA 1.4 objective with a Hamamatsu Orca ER camera (Bridgewater, NJ). Images were acquired at room temperature with MetaMorph imaging software (Molecular Devices Corp., Downingtown, PA). Differential Interference Contrast (DIC) image exposure times were for 150 – 200 milliseconds (ms) and epi-fluorescence exposure times were 300 – 400 ms. LacI-GFP expression was induced as

described previously [185]. Images were processed as previously detailed [188]. To quantify the dicentric Chr III mis-segregation events, cells were grown overnight in glucose media, induced for LacI-GFP expression for two hours, and five-plane Z-series of the population were acquired. The percentage of mitotic cells in the population were also recorded at this time. Fluorescence intensity measurements by spindle position were performed as previously described [50]. All measurements were exported to Microsoft Excel (Microsoft Co., Seattle, WA) for further analysis.

Electron tomography

Cells were prepared for electron microscopy using methods previously described [30]. Briefly, log phase cultures were collected by vacuum filtration and high pressure frozen using a BalTech high pressure freezer. The frozen cells were freeze substituted in 1% OsO4 and 0.1% uranyl acetate in acetone and embedded in Epon resin. Serial, 250nm thick sections were collected onto formvar-coated slot grids and stained with lead citrate and uranyl acetate.

Dual axis tomography was carried out as described previously [143]. Colloidal gold (15nm) was affixed to each surface of the sections to serve as fiducial markers for tomography. The specimens were imaged using a TECNAI F30 microscope (FEI, Netherlands) operated at 300 kV. Images were captured every 1 degree over a +/- 60 degree range at a pixel size of 1nm about two orthogonal axes. The serial, tilted views were then aligned and dual axis tomograms computed using the IMOD software package [189, 190]. Tomograms were computed from adjacent, serial sections to reconstruct complete mitotic spindles.

In total, we reconstructed 2 wild-type anaphase spindles. Individual microtubules were modeled from the tomgographic volumes and a projection of the 3D model was then displayed to study its 3D geometry. Microtubule lengths were extracted from the model contour data using the program, IMODINFO.

Modeling of microtubule length distributions

MT length distributions obtained from electron tomography were fit to exponential models as follows. It was assumed that the 32 shortest MTs in each spindle were kMTs. The cumulative distribution of kMT lengths were then fit to an exponential distribution according to:

$$F(L) = 1 - e^{L/Lmean} \quad (1)$$

Where F(L) is the cumulative distribution function for MT length, L is MT length normalized to spindle length, and L_{mean} is the mean normalized MT length for the sample.

Then, all measured MTs longer than the 32 shortest in each spindle were assumed to be ipMTs. The cumulative distribution of ipMT lengths were fit to an exponential distribution according to:

$$F(L) = e^{-\{(L\max - L)/(L\max - Lmean)\}} \quad (2)$$

Where L_{max} is the maximum observed normalized MT length, which is 0.905. This correction takes into account an experimentally observed ipMT plus-end exclusion zone near to the SPBs, possibly due to entropic or steric exclusion originating from the high density of kMTs near to the poles.

A bootstrap method was used for calculating fit probability of experimental data to exponential models, as previously described [29, 119]. Here, a set of 100 simulated sum-of-squares error (SSE_{sim}) values were calculated by comparing each simulated MT length distribution curve (generated via sampling from the exponential fit curve) to the average curve over all 100 simulations. The experimental SSE value (SSE_{exp}) was then calculated by comparing the experimental data to the average simulation curve. The SSE_{exp} was ranked in the list of 100 simulated SSE_{sim} values to calculate the probability of fit (p-value).

Model-convolution simulations

Model-convolution of simulated fluorescence distributions was completed by convolving the experimentally observed microscope point spread function with the simulated distribution of fluorescent proteins, as previously described [29, 119]. Calculation of p-values for fit of simulated model-convolution images to experimental images was completed as previously described [29, 119].

Acknowledgements

I thank David Bouck, Jay Gatlin, Erin McCarthy, and members of the Bloom and Salmon laboratories for advice, assistance, and critical readings of the manuscript. This work was funded by the National Institutes of Health grants GM-32238 (K.B.), GM-071522 (D.J.O.),GM-24364 (E.D.S.), GM-60678 (E.D.S.), and the National Center for Research Resources of the National Institutes of Health RR-00592 to A. Hoenger (E.T.O.). MKG was supported by the National Institutes of Health (EB005568).

Tables and Figures

FIGURE 7.1. Dicentric chromosome activation results in decreased viability in MT plus end binding mutants. (A) Schematic of dicentric chromosome activation in wild-type cells. In approximately 50% of cells with an activated dicentric chromosome, the kinetochores will orient towards opposite SPBs. After anaphase onset, the bioriented dicentric chromosome will stretch between both SPBs, resulting in a midanaphase pause. To resume anaphase, the dicentric chromosome breaks and the DNA lesion is repaired to generate a monocentric derivative (chromosomes (blue), microtubules (green), spindle pole bodies (orange). (B) Histogram of the viability of cells with an activated dicentric chromosome. Centromeres on the dicentric chromosome were in the direct orientation except for *rad52Δ* cells, which, along with *ndc10-2*, have been reported previously [179, 181]. Error bars are the standard deviation for each determination. Data for both orientations can be found in Table E.1.

Figure 7.1

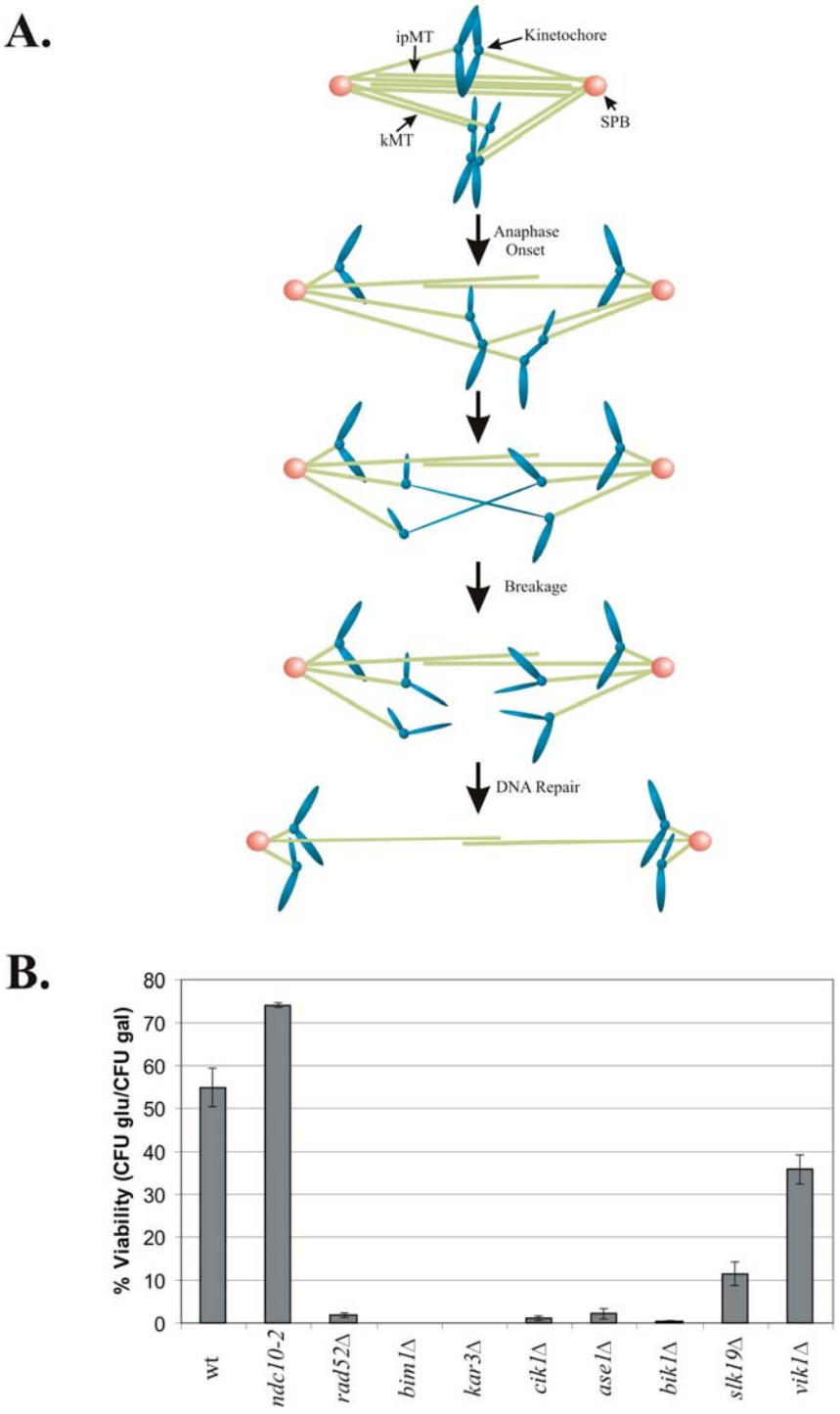
A.
ipMT
Kinetochore
SPB
kMT
Anaphase Onset
Breakage
DNA Repair
B.
% Viability (CFU glu/CFU gal)
0
10
20
30
40
50
60
70
80
wt
ndc10-2
rad52Δ
bim1Δ
kar3Δ
cik1Δ
ase1Δ
bik1Δ
slk19Δ
vik1Δ

FIGURE 7.2 *bim1*Δ suppresses dicentric chromosome breakage. (A) Restriction analysis of dicentric plasmid *pGAL-CEN*^{2} DNA [183] recovered from wild-type or *bim1*Δ cells maintained on galactose or glucose. Plasmid DNA derived from wild-type and *bim1*Δ cells was digested as previously described [183]. In wild-type cells, 0/50 cells had both centromeres intact after plasmid recovery and analysis; 27/50 dicentric plasmids derived from *bim1*Δ cells had both centromeres intact. Molecular weights of DNA fragments following restriction digestion of the unrearranged plasmid are indicated to the right of each gel (kilobase pairs, kb). CEN4 and CEN3 indicate the fragments containing the centromere fragment from chromosome IV or III, respectively. B) Time course for monocentric derivatives generated by recombination between the two centromeres on chromosome III. Wild-type and *bim1*Δ cells were cultured and the time course was performed as previously described [179]. Time (hours) indicates the time points after activating the dicentric chromosome (switch to glucose). At each time point, the chromosomal DNA was prepared and analyzed by Southern analysis (see Methods). The Southern blot was also probed for *MET14* that served as a loading control. Molecular weights for each of the respective fragments are indicated to the right. (C) Histogram of the percentage of radioactive *GAL-CEN3* relative to *MET14* over the time course for wild-type and *bim1*Δ cells as determined by ImageQuant analysis. There was a 13.5-fold decrease in the *GAL-CEN3* band in wild-type cells but only a 2.8-fold decrease in *bim1*Δ. (D) Histogram of the percentage of radioactive 1.1 Kb rearrangement product relative to *MET14* over the time course for wild-type and *bim1*Δ cells as determined by ImageQuant analysis. There was a 13.6-fold increase in the 1.1 Kb rearrangement product in wild-type cells but only a 3.8-fold increase in *bim1*Δ cells.

Figure 7.2

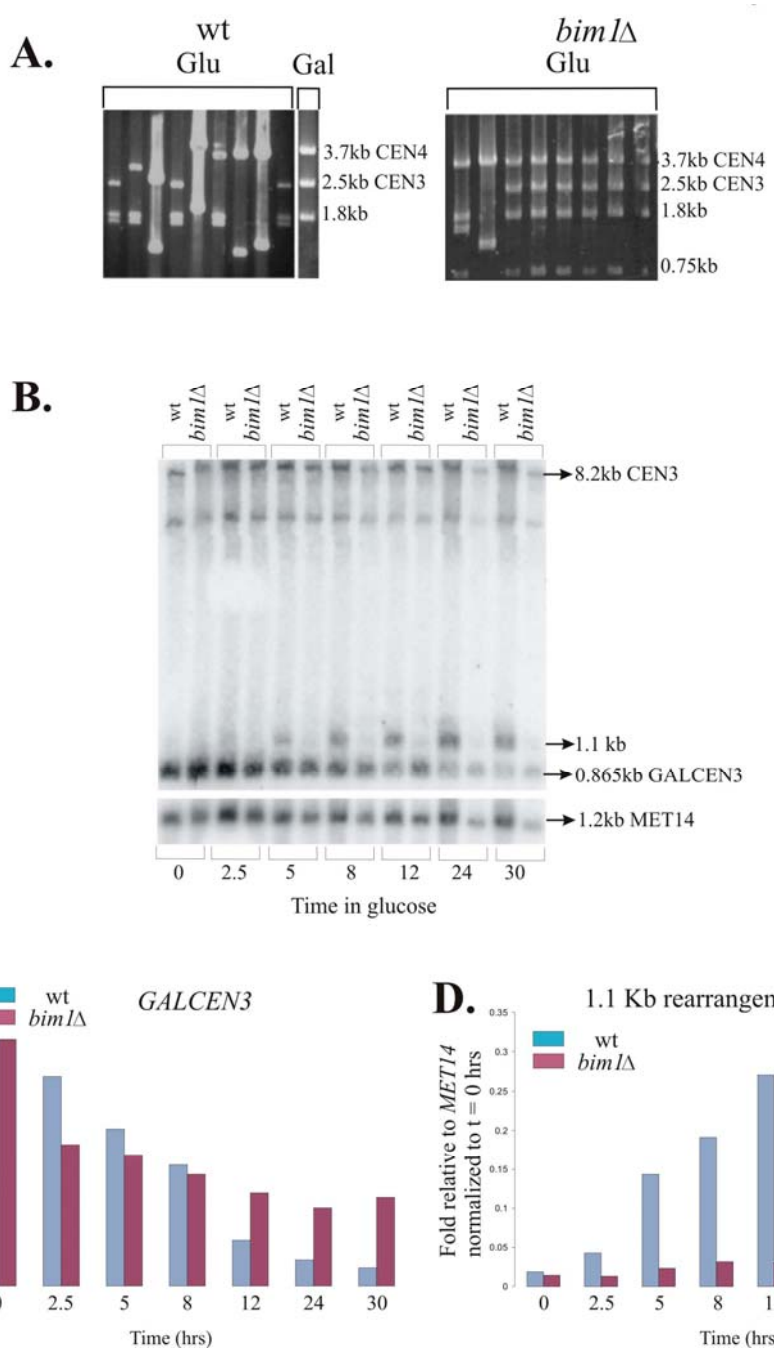
A.
wt
Glu
Gal
3.7kb CEN4
2.5kb CEN3
1.8kb
bim1Δ
Glu
3.7kb CEN4
2.5kb CEN3
1.8kb
0.75kb
B.
wt
bim1Δ
8.2kb CEN3
1.1 kb
0.865kb GALCEN3
1.2kb MET14
0 2.5 5 8 12 24 30
Time in glucose
C.
wt
bim1Δ
GALCEN3
Fold relative to MET14 normalized to t = 0 hrs
0 2.5 5 8 12 24 30
Time (hrs)
D.
1.1 Kb rearrangement product
wt
bim1Δ
Fold relative to MET14 normalized to t = 0 hrs
0 2.5 5 8 12 24 30
Time (hrs)

FIGURE 7.3. The dicentric chromosome is mis-segregated in bim1Δ cells. (A) Histogram of chromosome III segregation in wild-type, *bim1Δ* monocentrics, and *bim1*Δ dicentrics from cells expressing LacI-GFP with LacO integrated at *LEU2* on chr III. Bar, 2 μm. Unbudded or small budded cells were classified as G1/S. Medium to large budded cells were scored for one chr III spot, two chr III spots, two separated chr III spots in anaphase, or >2 chr III spots. Black bars – wild-type monocentrics (maintained on glucose; n = 91 cells); grey bars - *bim1*Δ monocentrics (grown on galactose; n = 139); white bars - *bim1*Δ dicentrics (cultured on glucose; n = 169). (B) Activated dicentric chr III behavior relative to SPBs. Arrow marks the position of chr III. Both cell types have LacO integrated at chr III and expressed LacI-GFP. Wild-type SPBs were marked with Spc72p-GFP. *bim1*Δ cell SPBs were marked with Spc29p-RFP. Population images were taken three hours after switching cells to glucose. Dicentric chr III position relative to the SPB was determined by measuring the distance of the chr III spot from the SPB and the distance between the two SPBs. Wild-type cells (n = 97) have 94% of chr III spots within the central one-third of the distance between SPBs. Only 51.5% of *bim1*Δ cells (n = 105) have the chr III spot in the central one-third of the spindle. Bar, 2 μm. (C) Spindle morphology in wild-type and *bim1*Δ cells with activated dicentric chromosomes. Upper panels – GFP-Tub1p images; lower panels – overlay of GFP-Tub1p (green) with DIC image (red). In wild-type cells, spindles are in preanaphase or arrest in midanaphase with continuous GFP-Tub1p fluorescence. In 38% of *bim1*Δ cells with activated dicentric chromosomes that entered anaphase, the GFP-Tub1p fluorescence was not continuous, suggesting spindles had broken. Bar, 2 μm.

Figure 7.3

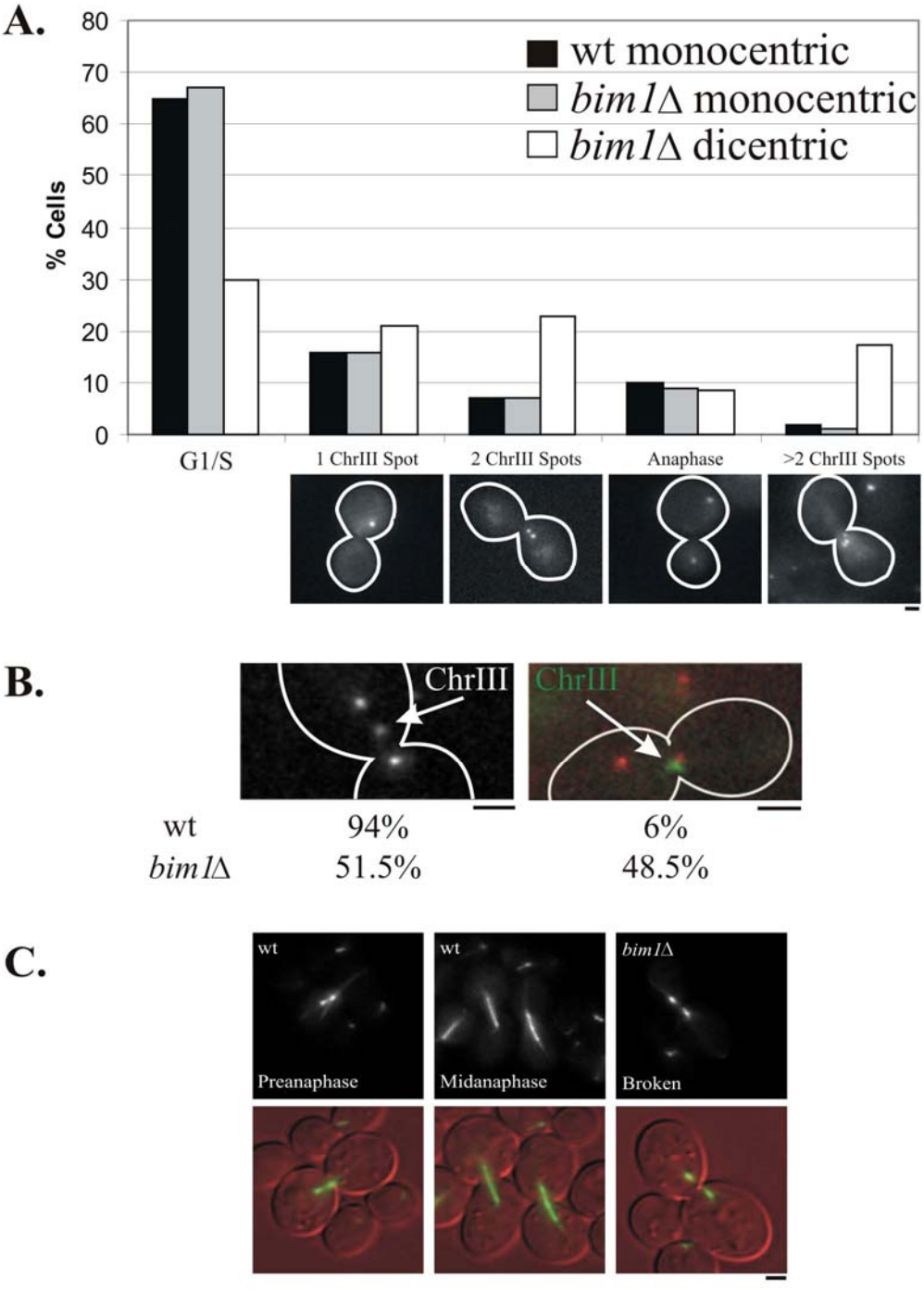
A.
80
70
60
50
40
30
20
10
0
% Cells
wt monocentric
bim1Δ monocentric
bim1Δ dicentric
G1/S
1 ChrIII Spot
2 ChrIII Spots
Anaphase
>2 ChrIII Spots
B.
ChrIII
ChrIII
wt
bim1Δ
94%
51.5%
6%
48.5%
C.
wt
Preanaphase
wt
Midanaphase
bim1Δ
Broken

FIGURE 7.4. Anaphase tubulin polymer is reduced in bim1Δ cells. (A) GFP-Tub1p fluorescence is nearly uniform along the length of wild-type anaphase spindles (top left, white arrows show approximate minimum intensity location), suggesting that ipMTs are nearly as long as the spindle itself (spindle length 5.04 ± 0.93 µm (mean ± SD)). In contrast, GFP-Tub1p fluorescence has decreased intensity in *bim1*Δ cells (top right, white arrows show approximate minimum intensity location, note comparison to wild-type spindle in similar location), suggesting that ipMTs have reduced length as compared to wild-type spindles (spindle length 5.15 ± 1.21 µm). Quantification of GFP-Tub1 fluorescence by normalized spindle position shows reduced GFP-Tub1p fluorescence in *bim1Δ* anaphase spindles as compared to wild-type spindles (bottom, spindle position normalized to total spindle length). (Scale Bar, 1000 nm; error bars, s.e.m.) (B) Bim1-GFP (green) is localized within the spindle midzone (blue arrows) (spindle lengths 4.66 ± 0.97 µm; quantification see Figure E.1A; Scale Bar, 1000 nm).

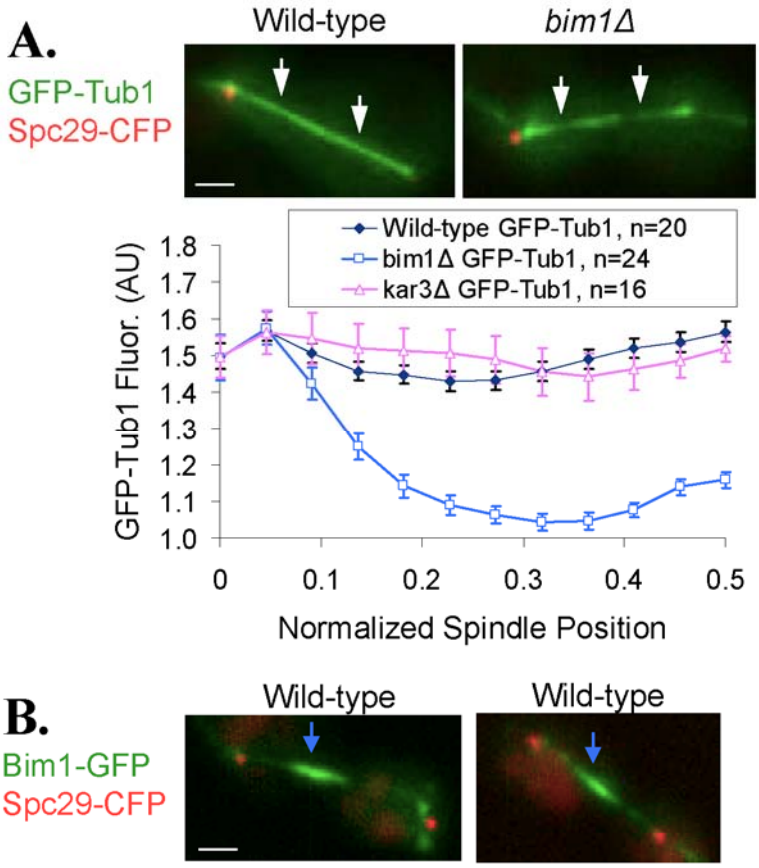

FIGURE 7.5. Model convolution analysis suggests that the midzone overlap zone in bim1Δ anaphase spindles is reduced as compared to wild-type spindles. (A) 3D model of a typical wild-type anaphase spindle using electron tomography (top). Individual microtubules from each spindle pole (magenta and green, respectively) were traced as model contours in a tomographic volume containing a complete spindle. The 32 shortest MTs were classified as kMTs in each of two spindles, and normalized cumulative length distribution is plotted (bottom left). The remaining longer MTs were then classified as ipMTs and plotted separately (bottom right). Both kMT and ipMT lengths followed exponential distributions, with kMTs short and near to each SPB, and ipMTs longer, running nearly the entire length of the spindle (orange and cyan lines, see text and Materials & Methods). (B) Exponential models derived from the wild-type tomogram analysis were sampled to produce simulated GFP-Tub1 fluorescence images via model-convolution (top left). Images simulated using wild-type kMT and ipMT tomogram length distribution models qualitatively reproduce experimental fluorescence images (top right); a typical animation is shown at bottom (kMTs, orange; ipMTs cyan). (Scale bar, 1000 nm; error bars, s.e.m.) (C) The ipMT length distribution was then modified in simulation to reproduce the experimentally observed distribution of GFP-Tub1 in *bim1*Δ anaphase spindles (top). The best-fit model predicts that ipMT length is reduced, resulting in a substantially shorter ipMT midzone overlap zone (animation, bottom). (Scale bar, 1000 nm; error bars, s.e.m.)

Figure 7.5

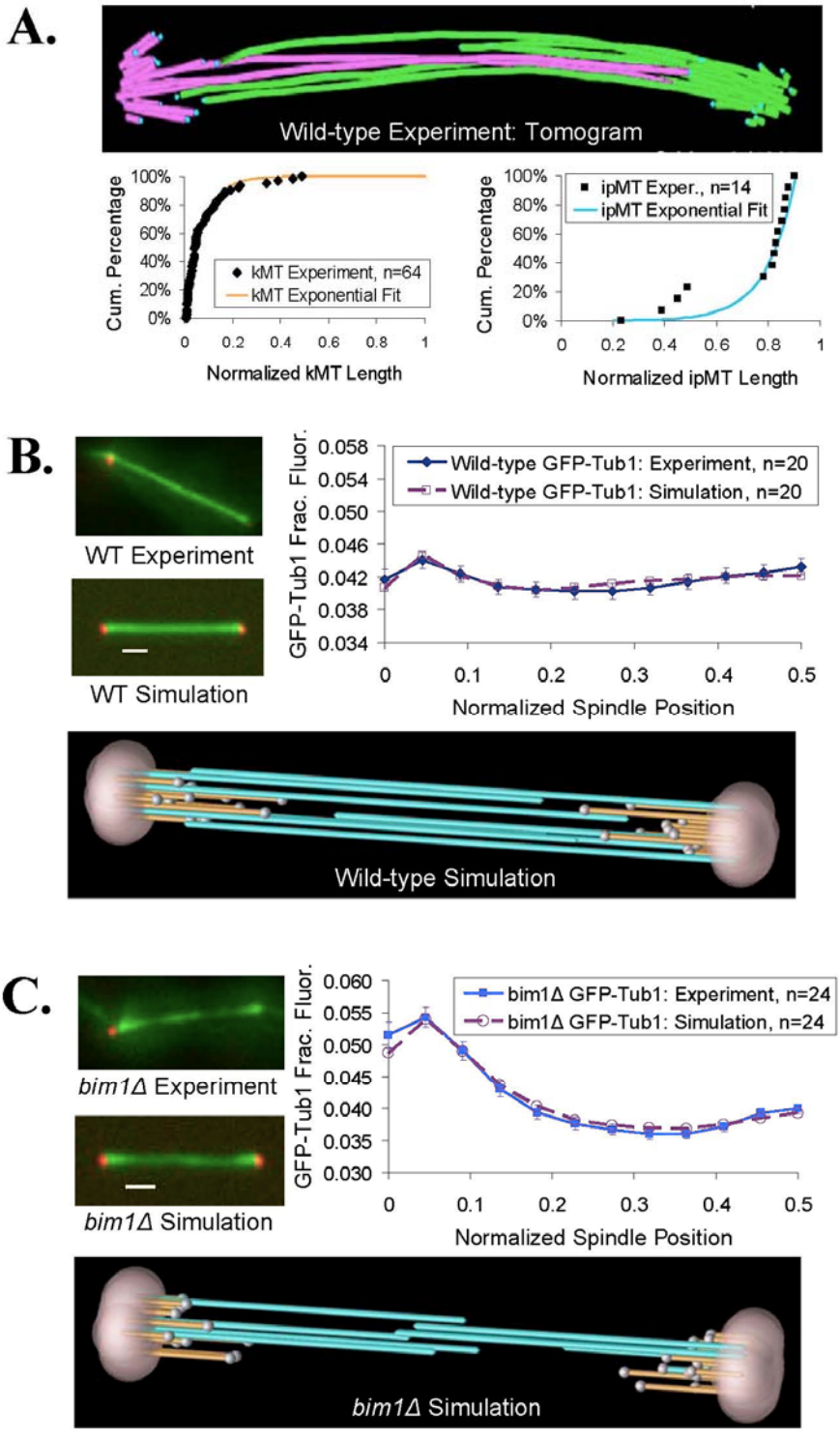
A.
Wild-type Experiment: Tomogram
Cum. Percentage
100%
80%
60%
40%
20%
0%
0
0.2
0.4
0.6
0.8
1
kMT Experiment, n=64
kMT Exponential Fit
Normalized kMT Length
ipMT Exper., n=14
ipMT Exponential Fit
Normalized ipMT Length
B.
WT Experiment
WT Simulation
GFP-Tub1 Frac. Fluor.
0.058
0.054
0.050
0.046
0.042
0.038
0.034
Wild-type GFP-Tub1: Experiment, n=20
Wild-type GFP-Tub1: Simulation, n=20
0.1
0.2
0.3
0.4
0.5
Normalized Spindle Position
Wild-type Simulation
C.
bim1Δ Experiment
bim1Δ Simulation
0.060
0.055
0.050
0.045
0.040
0.035
0.030
bim1Δ GFP-Tub1: Experiment, n=24
bim1Δ GFP-Tub1: Simulation, n=24
Normalized Spindle Position
bim1Δ Simulation

FIGURE 7.6. ipMT bundling is reduced in *kar3*Δ mutant anaphase spindles. (A) ipMT bundling is compared in wild-type, *bim1*Δ, and *kar3*Δ anaphase spindles by examining the splaying of MTs within the spindle. Splaying of ipMTs in *kar3*Δ spindles is readily apparent (right, white arrow) as compared to well-bundled wild-type and *bim1*Δ spindles (white arrow) (*kar3*Δ spindle length 5.49 ± 1.04 μm (mean ± SD), wild-type and *bim1*Δ spindle lengths are as in Fig. 7.4). (Scale bar, 1000 nm) (B) Kar3-GFP is localized near to the SPBs (magenta arrows) as well as in punctate spots within the spindle (green arrows) (left). Analysis of Kar3-GFP localization in *vik1*Δ and *cik1*Δ spindles suggests that the Kar3p-Cik1p complex is localized both near to the SPBs (magenta arrows) and within the spindle (green arrows) (center), while the Kar3p-Vik1p complex is localized near to the SPBs (magenta arrows) (right). (Scale bar, 1000 nm) (C) Modeling results are consistent with the prediction that the Kar3p-Cik1p complex is localized at the plus-ends of anaphase MTs. (Scale bar, 1000 nm)

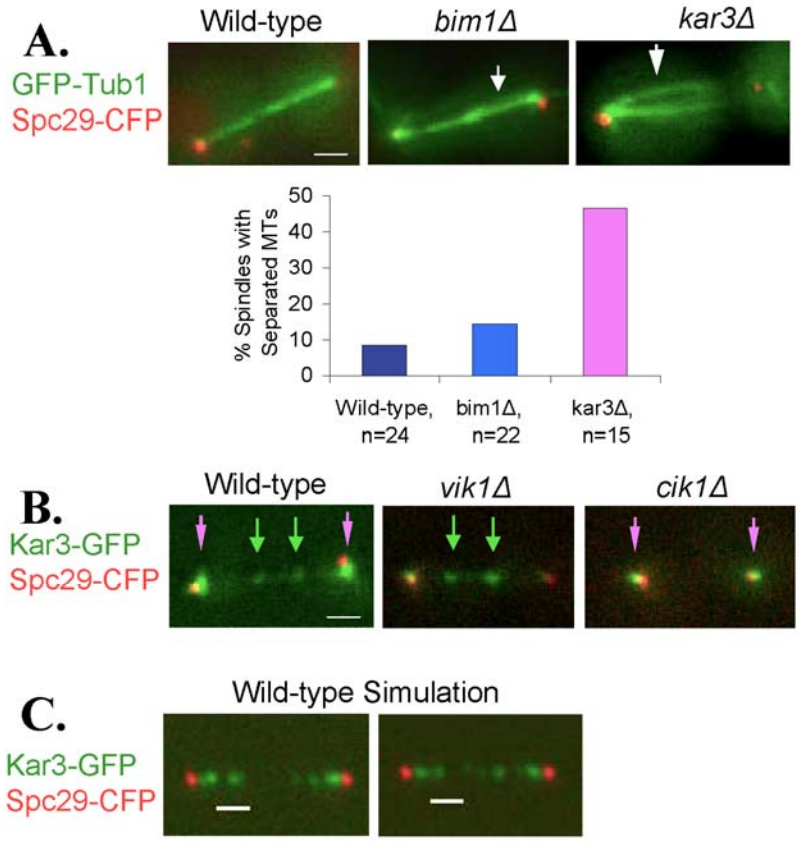

FIGURE 7.7. A model for the distinct roles of Kar3p and Bim1p in mechanically stabilizing the anaphase spindle. In wild-type spindles (left), Kar3p and Bim1p cooperate to maintain an ipMT midzone overlap zone of sufficient length and width. In *kar3*Δ mutants, ipMTs are splayed apart (center) compromising the robust structural stability of the anaphase spindle. In contrast, *bim1*Δ mutants are properly bundled, but have shorter ipMTs (right), reducing the length of the anti-parallel midzone overlap zone. Both improper bundling and a reduced midzone overlap zone likely frustrate proper attachment and cross-linking of the motor proteins that provide outwardly directed spindle forces during anaphase (Cin8p and Kip1p)

.

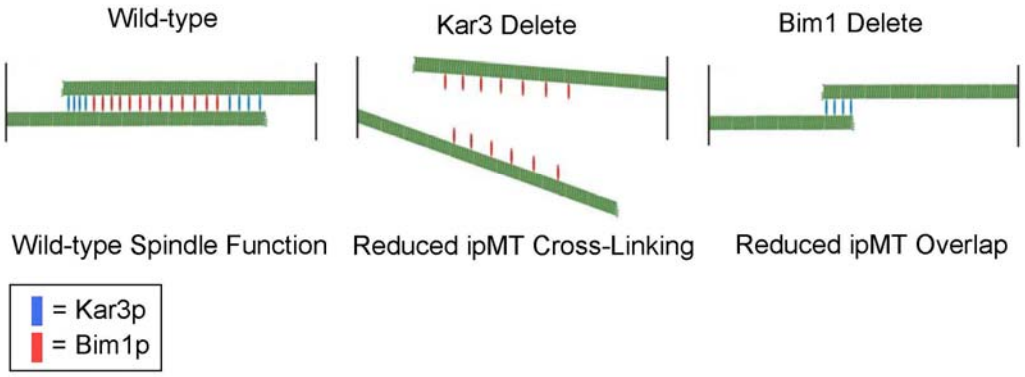

CHAPTER 8

SUMMARY AND CONCLUSIONS

The field of cell biology is rich in data, and sophisticated microscopy methods using fluorescent proteins now allow for an unprecedented view into the inner workings of the cell at the molecular level. A key challenge is in integrating biological data into physically realistic models for cellular processes. Thus, the emerging field of "systems biology" aims to integrate computational modeling methods with modern cell biology in order to advance the understanding of important biological processes. To successfully integrate computational methods with modern cell biology, a systematic approach is required. In chapter 2, an iterative approach was presented in which computational models were directly compared to experimental data. This approach has two major advantages, (1) models can be directly tested against multiple experiments, thus facilitating the evolution of the model as specific predictions are tested and the model is challenged in different ways, and (2) in turn, the model predictions can then be used to design new experiments. Furthermore, the model can be used to build intuitive understanding of the complex processes underlying cell behavior. In chapters 3-7, this approach, in which experiments and simulations are closely integrated, is demonstrated at multiple levels. Specifically, by "coarse-graining" the dynamics of multiple microtubules within the yeast mitotic spindle, the mechanism for kinetochore microtubule length regulation during mitosis was investigated (chapters 3-5). In performing molecular-level modeling of a single *in vitro* microtubule, the configuration and role of the GTP-cap in microtubule assembly was studied (chapter 6). Finally, the microtubule-based mitotic spindle structure was studied in chapter 7, as a first step in developing a mechanical model for the entire yeast mitotic spindle that includes multiple microtubules, together with microtubule-associated proteins, molecular motors, and chromosomes.

During cell division, accurate chromosome segregation is critical to preventing the occurrence of aberrant genomes that can result in cell death and disease [191]. As the plus-ends of kinetochore microtubules are responsible for the physical segregation of chromosomes into two daughter cells, an understanding of how their dynamics are

regulated to accomplish this feat is fundamental to the understanding of mitosis. In chapters 3-5, a series of studies utilized a combined experimental-theoretical approach to elucidate how kinetochore microtubule plus-ends are regulated during budding yeast mitosis.

In budding yeast, fluorescently labeled sister kinetochores are separated into two clusters on either side of the spindle equator. This clustering suggests not only that kMT plus-end dynamics are regulated to achieve similar lengths, but also that sister chromosomes attached at opposing kinetochores are stretched apart. Indeed, DNA markers placed near to the kinetochores show persistent separation throughout metaphase, suggesting that sister chromosomes are stretched apart [18, 19]. In chapter 3, I explored the role that this chromosome stretching may play in regulating kMT plus-end dynamics. There is evidence in higher eukaryotes that mechanical tension at the kinetochore, induced by the stretching of chromosomes between sister kinetochores, could regulate both kMT dynamics and the attachment stability of kMTs to the kinetochore [66]. However, because there are multiple kMTs attached to each kinetochore in these cells, the role of tension in regulating kMT plus-end dynamics, as opposed to simply affecting attachment stability, is unclear. In budding yeast, there is only one kMT attached to each kinetochore [30], and this attachment remains stable throughout metaphase [51].

By using computer simulation in combination with targeted experiments, I found that the stretching of chromosomes between sister kinetochores promotes rescue of depolymerizing microtubules, and that lack of tension suppresses kMT plus-end rescue frequency. Thus, when kMT plus-ends extend into and past the spindle equator area, tension due to sister chromosome stretching is low. This leads to suppression of rescue frequency, and thus prevents frequent equator crossing of kMT plus-ends. Consistent with this result, in mutant spindles with no chromosome duplication (and thus no tension from sister chromosome stretch) all kMTs are short. This data was the first direct *in vivo* evidence for tension-dependent regulation of kMT plus-end dynamics during mitosis, and provided a model for how tension could act to mediate congression of chromosomes during metaphase.

Subsequent to this work, models have been developed for other organisms that incorporate our tension-dependent model for regulating chromosome congression [27, 192]. In addition, this model inspired *in vitro* studies performed by Franck *et al*, in which the authors recreated the kinetochore-microtubule linkage outside the cell by isolating the Dam1 kinetochore protein. Interestingly, by pulling on the kinetochore complex at the tips of depolymerizing microtubules, the microtubule rescue frequency was increased by ~7 fold over control microtubules [193].

The model for yeast kinetochore congression as developed in chapter 3 predicts that kMT plus-end dynamics are spatially regulated in the yeast mitotic spindle, and therefore their dynamics should vary as a function of position within the spindle. In chapter 4, this prediction is tested explicitly by measuring the fluorescence recovery after photobleaching (FRAP) half-time for GFP-tubulin as a function of position within the mitotic spindle. If kMT dynamics are spatially regulated within the mitotic spindle such that their plus-ends are most frequently located on either side of the spindle equator, then GFP-tubulin should turn over most rapidly in this position, and slower elsewhere. Indeed, I found that there exists a gradient in GFP-tubulin FRAP half-times along the length of the spindle, such that the GFP-tubulin turnover is most rapid in the location of kinetochore clustering, and slower elsewhere. These experiments provide further data to support the model for kMT plus-end dynamics within the spindle, and describe a new method for collecting FRAP data at a spatial resolution of ~65 nm, well below the theoretical resolution limit of the light microscope (~200 nm). Subsequent to this work, other groups have used or are currently using a similar method to analyze FRAP of spindle components [194].

An essential component of the model as described in chapters 3 and 4 is that, in addition to a tension-dependent rescue frequency at kMT plus-ends, there also exists a spatial gradient in kMT plus-end catastrophe frequency. Because tension-dependent rescue frequency relies exclusively on the distance between sister kinetochores, and does not depend upon absolute position within the spindle, it is insufficient by itself to correctly organize the metaphase spindle. Thus, in chapter 5, the spatial catastrophe gradient aspect of the model for yeast chromosome congression was explored. By making

predictions regarding the spindle phenotype for a knock-out/knock-down of a hypothetical catastrophe gradient mediator, we were able to search experimentally for candidate molecules that could mediate a gradient in catastrophe frequency. Surprisingly, the candidate that produced the predicted phenotypes for a catastrophe gradient mediator was the kinesin-5 molecular motor, Cin8. This motor has been well-studied both in humans and in yeast, and a drug that targets the human homologue of Cin8 is currently in Phase II clinical trials as a cancer therapeutic. Because this motor has force-generating microtubule crosslinking activities, it plays a critical role in separating the spindle poles to maintain a constant spindle length during metaphase. Thus, although Cin8's role in separating spindle poles is well established, its role in regulating kMT plus-end dynamics is surprising. The fact that kinesin-5 motors are important both for force generation and in the regulation of kMT plus-end dynamics may be a key aspect of metaphase chromosome congression that has been overlooked until now.

As described in chapter 5, I then explicitly incorporated the stochastic dynamics of the plus-end directed Cin8 motor into the yeast metaphase kMT dynamics model in an effort to understand how a plus-end directed molecular motor could mediate a gradient in kMT plus-end catastrophe frequency. Interestingly, the plus-end directed activity of the motor naturally results in a length-dependent gradient at kMT plus-ends, such that longer kMTs are larger attractors and therefore have a higher concentration of Cin8 motors at their plus-ends. Conversely, shorter kMTs act as poor antennas, and thus attract fewer motors at their plus-ends. Although recent work described a similar length-dependent depolymerization effect for the kinesin-8 molecular motor Kip3 [109], this motor does not have a significant effect on the kMT length distribution in the mitotic spindle. As suggested by simulations of both motor types, this difference likely relies on the MT crosslinking properties of Cin8, which results in its specific concentration at kMT plus-ends, while the non-crosslinking motor Kip3 concentrates on the longer interpolar microtubules that run nearly the full length of the spindle, but are not associated with kinetochores.

Thus, through a series of three papers, a model for the regulation of kMT plus-end dynamics in the yeast metaphase spindle has been developed, molecular functions have been identified, and the model tested experimentally using a wide variety of fluorescent protein markers and mutations. Key future work will involve applying the general principles identified in this study to other organisms. In particular, the effect of a kinesin-5 knockdown in bipolar spindles will be interesting to study in mammalian cells.

Chromosome congression during mitosis depends on the dynamic plus-ends of kinetochore microtubules. In chapter 6, the molecular basis of the dynamic instability behavior that is at the heart of kMT dynamics is explored with molecular level detail. Specifically, simulations are run which take into account the stochastic addition of GTP-tubulin subunits at microtubule tips, hydrolysis of these subunits to GDP-tubulin, and then loss of both GTP- and GDP- tubulin subunits from the microtubule tip. A key assumption that is inherent in these simulations is that GDP- tubulin subunits have a preferred conformation in the microtubule lattice that is kinked outwardly relative to their longitudinal neighbor. This kinking tends to destabilize GDP-tubulin subunits that are exposed at the microtubule tip, increasing their off rate relative to GTP-tubulin subunits. Thus, the exclusive addition of GTP-tubulin subunits at the microtubule tip, combined with a stochastic delay prior to their hydrolysis into a GDP-containing subunit, results in a stabilizing GTP-cap at the tip of a growing microtubule.

Although the concept of a stabilizing GTP-cap at the tip of a growing microtubule is well established in the literature, the size and configuration of this cap remains controversial, especially because to date efforts at visualizing a GTP-cap have not been successful. By comparing new *in vitro* nanoscale data on microtubule growth (collected at 5 kHz temporal resolution and temporally filtered to achieve ~3.5 nm spatial resolution) to the stochastic model of microtubule dynamics, new insights were gained into the structure of the stabilizing GTP-cap, as described in chapter 6. Specifically, nanoscale shortening events were frequently observed during microtubule growth that were larger than a single layer of tubulin subunits, and often times larger than many layers of tubulin subunits. Similar nanoscale shortening events were observed in the simulation. Analysis of the GTP-cap structure in simulations that reproduce the nanoscale

growth variability of *in vitro* microtubules suggests that the GTP-cap is not a single layer of GTP-tubulin subunits as previously proposed, but rather is likely a long spatially-distributed cap that can support large nanoscale variability in growth-phase behavior.

These results are important in light of recent data that suggests plus-end binding proteins track microtubule ends via a tip recognition mechanism [195]. Thus is it likely that a longer, spatially distributed GTP-cap could contribute to the targeting of important plus-end binding proteins to the tips of *in vivo* microtubules.

Interesting future work will involve integrating the tension-dependent rescue model described in chapter 3 with the molecular-level microtubule dynamics simulations. Through this work, the molecular-level simulations could then be related to cellular level regulation of kMT dynamics.

During mitosis, *in vivo* microtubules perform their functions within the structure of a mitotic spindle. Important future work will involve integrating the models for microtubule dynamics described above into a higher-order self-organizing model to elucidate the proteins and mechanisms that organize the structure of the spindle itself. The results in chapter 7 represent a first step in this direction, as the key microtubule-associated proteins that regulate the mechanical integrity of the mitotic spindle are identified. In this work, additional mechanical stress is imposed on anaphase spindles via a dicentric chromosome mutation. In these spindles, sister chromosomes do not separate properly, which results in stresses induced from chromosome stretching as spindle poles separate during anaphase. The comparative viability of deletions in various microtubule-associated proteins allows for identification of the proteins that are important in maintaining spindle integrity during mitosis. Interestingly, the contributions of the minus-end directed motor protein Kar3 and the plus-end binding protein Bim1 appear to be equally important to Ase1, a microtubule-associated protein previously thought to be the major contributor to structural spindle stability.

In conclusion, the feasibility of the experimental-theoretical approach has been demonstrated here. Future work will involve modeling increasingly complex systems in budding yeast, i.e. the mitotic spindle structure, and expanding these models to mammalian systems by applying the general principles identified in budding yeast.

APPENDIX A

SUPPLEMENTAL MATERIAL: TENSION-DEPENDENT REGULATION OF MICROTUBULE DYNAMICS AT KINETOCHORES

(Reprinted with permission from *Molecular Biology of the Cell* 16(8) (2005))

SUPPLEMENTAL RESULTS: ANALYSIS OF MODEL ASSUMPTIONS

Steady-state metaphase as determined experimentally by kinetochore-associated fluorescence imaging

In comparing yeast kinetochore-associated Cse4-GFP fluorescence images at different spindle lengths, it was qualitatively observed that shorter spindles exhibited kinetochore clustering distinct from longer metaphase spindles. The shorter spindles had a disorganized band of kinetochore-associated fluorescence across the spindle equator (Fig. A.1 (A)), whereas the longer metaphase spindles had relatively tight kinetochore-associated fluorescence clusters (green) on either side of the spindle equator (Fig. A.1(B)).

Quantitative statistical analysis relating kinetochore distributions to spindle length supported qualitative observations (Fig. A.1(C)). In this analysis, it was found that spindles of lengths 1.6-1.9 μm had a consistent pattern of separated kinetochore clustering (probability of fit >0.25, Fig. A.1(B, C)), and therefore represented a steady-state metaphase configuration. Spindles with lengths outside of this window had kinetochore clustering patterns which were not consistent with the putative metaphase steady-state data set (probability of fit <0.10, Fig. A.1(A, C)). We therefore considered spindles having lengths 1.6-1.9 μm as being in "metaphase," with the shorter spindles being in "prometaphase."

The data set used to calculate the metaphase distribution of kinetochore clustering was therefore redefined from earlier work [29] to limit metaphase spindle lengths to the range of 1.6-1.9 μm. The mean distribution of kinetochore-associated fluorescence (n=56 spindles, n=112 spindle halves) for the steady state metaphase spindles is shown in Fig. A.1(D). For comparison, the distribution of kinetochore-associated fluorescence in the elongating (and therefore unsteady-state) prometaphase spindles is shown as well (Fig. A>1(D)). The peak in kinetochore clustering midway between the pole and equator (i.e. at the quarter-spindle location) was more prominent using the redefined metaphase data set, with distinctly reduced kinetochore-associated fluorescence at the spindle equator. By redefining the metaphase experimental data set, models for regulation of kMT dynamics are more tightly constrained as compared to our previous work.

Analysis of the kinetochore marker Cse4-GFP for use in characterizing kMT plus-end dynamics

In order to test the model assumption that the kinetochore marker Cse4-GFP provides a reasonable approximation of kMT plus-end locations in the yeast metaphase spindle, quantitative electron microscopy data was forward-convolved to create simulated fluorescence images. Here, simulated green fluorescent markers were placed at the plus-end location of each putative kMT analyzed in electron micrograph reconstructions [30] and simulated red fluorescent markers were placed in the locations of the kMT minus ends. These images were then convolved with the measured microscope point spread function and typical background and noise levels in Cse4-GFP fluorescence images. Representative simulated images generated from electron microscopy data are shown in Fig. A.2(A), with typical experimental Cse4-GFP fluorescence images shown in Fig. A>2(B). A fluorescence distribution curve comparing the mean simulated plus-end fluorescence generated from electron microscopy data (n=4) to mean kinetochore-associated Cse4-GFP fluorescence (n=56) is shown in Fig. A.2(C). Reasonable agreement between the locations of simulated peak kMT plus-end associated fluorescence and peak Cse4-GFP kinetochore-associated fluorescence supports the assumption that Cse4-GFP locations can reasonably predict kMT plus-end locations in yeast metaphase spindles.

Analysis of the assumption of kMT dynamic instability

All models considered assumed that kMTs exhibit dynamic instability, as observed in yeast cytoplasmic microtubules [70]. Specifically, kMTs are assumed to be in either one of two states: growing or shortening, as produced by polymerization or depolymerization at kMT plus ends, respectively. Is it possible that the microtubules do not conform to a dynamic instability model? Lack of dynamic instability behavior has been previously observed in living cells [196]. However, this does not seem to be especially problematic as a more generalized model for assembly would be a "diffusion with drift" model as put forward by [197]. In this work, Maly showed that dynamic instability can be modeled as a special case of diffusion with drift in the limit of rapid switching, and that the two parameters of the diffusion with drift model (i.e. the drift velocity and the diffusion coefficient) can be calculated directly from the four parameters of dynamic instability. Therefore, yeast kMT self-assembly behavior via diffusion with drift can be modeled by the dynamic instability model with very high catastrophe and rescue frequencies.

Previous studies have documented a possible "pause" state in dynamic instability, which represents a third assembly state where there is no change in length during the pause phase [198]. Could pausing be regulated spatially, rather than catastrophe or rescue, to explain the experimental observations? Certainly if pausing were extensive near the quarter-spindle location, then there would be clustering of kinetochore fluorescence as observed experimentally. However, such a model would allow long-lived

equator crossing to occur, in conflict with the Cse4-GFP FRAP experiment. Finally, such an effect would not give rise to the phenotype observed in the cdc6 mutant cells. Therefore, spatially-dependent pausing would not explain the experimental results.

The only other documented phenomenon that could in principle give rise to the experimentally observed metaphase kinetochore clustering is that of "history-dependent" switching [31, 199, 200]. ,However our previous analysis documented that this model produces only qualitative agreement and cannot explain Cse4-GFP distribution quantitatively (Sprague et al., 2003).

SUPPLEMENTAL RESULTS: MODEL SCREENING

A number of models with varying complexity were considered and failed to reproduce one or more of the four experiments, as shown in Table A.1. As the Tubulin-GFP experiment did not invalidate any models, it is not included in Table A.1. However, this experiment did serve to constrain the values for V_g and V_s (see text). In this table, all tested individual models as well as model combinations are summarized. All models were first screened for their ability to correctly predict wild-type experimental metaphase kinetochore clustering (Exp 1). If a model or model combination failed to reproduce wild-type metaphase kinetochore clustering correctly (i.e. $p<.05$), it was ruled out, and therefore not tested through further simulations. Models and associated parameter value sets that qualitatively reproduced metaphase kinetochore clustering were then run through the Cse4-GFP FRAP simulation (Exp 2) and the simulation results compared to experimental Cse4-GFP FRAP percentages. Finally, all models that correctly reproduced both wild-type kinetochore fluorescence distributions and Cse4-GFP FRAP experiments were used to simulate tension-deficient *cdc6* mutant spindles by setting the mechanical spring constant in the simulation to 0 (Exp 3). Probabilities of fit (p-values) were calculated for all simulations through quantitative comparison of simulated and experimental data as described below. This approach effectively implemented a computer-based combinatorial screen of models having complexity similar to the catastrophe gradient with tension-dependent rescue model that was ultimately found to satisfactorily explain all of the experimental results.

SUPPLEMENTAL MATERIALS AND METHODS

Statistical Analysis of Kinetochore-Associated Fluorescence

Image analysis was completed by integrating the total kinetochore Cse4-GFP fluorescence over a 15 pixel wide band along the length of the spindle and then calculating the percentage of spindle fluorescence at each spindle position as a function

of relative distance along the spindle, as described previously [29]. Integrated Cse4-GFP fluorescence along the spindle for *cdc6* mutant cells was binned into 42 equal bins rather than the 24 equal intervals used for wild-type spindles, in order to account for the experimentally observed longer spindle lengths. For the Cse4-GFP FRAP and GFP-tubulin FRAP experiments, the total integrated fluorescence intensity was calculated for each half-spindle. Statistical comparison between simulated images and experimental images was completed as previously described [29].

Statistical Comparison of Simulated and Experimental FRAP Results

The simulated Cse4-GFP FRAP results were compared to the experimental results by running 50 simulated experiment sets (n=13 cells/experiment), and then calculating the mean recovery over all 50 simulated experiments. The sum-of-squares error (SSE) between each simulated experiment set and the 50-set mean was then calculated. The p value was calculated by ranking the sum-of-squares error between the mean experimental recovery and the 50-set simulated mean in the list of 50 simulated SSEs.

For each simulated GFP-Tub1 FRAP experiment, recovery half-times were calculated as described in [59]. P values for fit of simulated results to published experimental results were then calculated as described above, with n=6 cells/experiment.

Statistical Determination of Steady-State Metaphase Kinetochore Distribution

Simulated images of yeast metaphase spindles were generated only after a warm-up time was allowed (~10 minutes), such that the system was allowed to settle into a steady-state configuration prior to construction of simulated images. In order to ensure that experimental images represented steady state metaphase we performed a statistical analysis of the experimental Cse4-GFP fluorescence image data set, such that only steady-state metaphase experimental images were used for quantitative comparison to simulated images. To compare kinetochore-associated fluorescence distributions at various spindle lengths, experimental fluorescence image data was sorted by spindle length (in pixels, 1 pixel = 0.066 μm), and a mean fluorescence distribution calculated for each spindle length. By comparing the similarity of these fit curves, it was possible to build a combined “steady-state” mean fluorescence distribution curve for metaphase spindles. For example, starting with the data set for a 26 pixel spindle length, we statistically compared the 26 pixel length mean fit fluorescence distribution curve to the 25 pixel mean fit curve by performing a sum-of-squares error (SSE) comparison of fluorescence distribution curves between the individual 26 pixel data set and a randomly reshuffled 25-26 pixel merged data set. In each case, integrated kinetochore-associated fluorescence was calculated for each of 24 equal bins in the fluorescence distribution curve. If these curves were the "same" ($p>0.01$, calculated based on ranking of the merged 25-26 pixel data set mean SSE value in the individual 26 pixel data set SSE values), they would be combined into a "steady-state" distribution. Then, this new "steady-state" distribution was compared to the 24 pixel fluorescence mean fit curve.

Again, if the fit curves were not statistically distinct, the 24 pixel set would be added to the "steady-state" distribution. Once we came to a spindle length in which the probability of fit of its mean fit curve to the steady state mean fit curve was low ($p<0.01$), this spindle length and all spindle lengths shorter (or longer) than this were excluded from the steady-state data set.

Simulation of microtubule dynamics

A Monte Carlo technique was used to simulate individual kMTs undergoing dynamic instability using MATLAB (Version 6.0, The MathWorks, Natick, MA) as previously described [29], with the following exception. In previous work, a spindle length of 1500 nm was assumed for all simulated spindles. The current model has been updated to allow for flexibility in simulated spindle lengths. Rather than using a mean experimentally observed spindle length, the measured spindle length of each of the experimental spindles was used in the simulation. This spindle length was then held constant for the duration of the simulation for each cell.

Estimation of point spread function and background fluorescence

The point spread function of the microscope imaging system was determined as previously described [29]. The method for estimating background fluorescence was determined in a manner similar to previous work, with the following exception. Rather than determining the mean background fluorescence in 10 random cells, the mean and standard deviation of the background fluorescence was measured on each experimental image, and then reproduced in a simulation for that particular spindle. As background fluorescence was found to vary by location within the cell, the mean background fluorescence was calculated along the spindle length for each cell (15 pixel wide band 7 pixels away from the mid-line of the spindle) on both sides of the spindle. The background noise was then calculated based on the standard deviation of the background fluorescence and reproduced for each of the experimental images.

Models for MT dynamics

Models for a rescue gradient mediated by a polar ejection force and a catastrophe gradient mediated by a chemical gradient model were used as described by Sprague et al. (2003). Briefly, the rescue gradient model was defined such that the kMT rescue frequency was high at the spindle pole bodies and decreased rapidly as the kMT plus ends approached the spindle equator. The catastrophe gradient model, based on the theoretical gradient of a catastrophe promoting molecule, resulted in low kMT catastrophe frequencies at the spindle pole bodies, with a maximum in catastrophe frequencies at the spindle equator.

The tension-dependent catastrophe frequency and tension-dependent rescue frequency models were used as described by Sprague et al. Briefly, the tensile force between sister kMTs was modeled as a Hookean spring with a rest length between sister kinetochores of 200 nm,

$$F_{tensile} = \rho(s - s_r), \qquad (2)$$

where s is the separation distance between the tips of sister kMTs (units of m), s_r is the rest length between sister kMT tips (units of m), and ρ is the spring constant (units of N/m). The dependence of rescue frequency on tension was assumed to obey an exponential relationship, given by

$$k_r = k_{r,0}e^{(F_{tensile}/F_o)} \qquad (3)$$

where $k_{r,0}$ is the rescue frequency in the absence of tensional force (units of m^{-1}), $F_{tensile}$ is the tensional force between sister kinetochores (units of N),and F_o is the characteristic force at which the rescue increases e-fold (units of N). Combining Eqs. 2 and 3 yields that

$$k_r = k_{r,0}e^{(\rho^*(s-s_r))} \qquad (4)$$

where $\rho^* = \rho/F_o$, which has units of m^{-1} (note: this parameter was termed ρ in Sprague et al., 2003).

Simulation of the Cse4-GFP FRAP experiment

The FRAP of Cse4-GFP was recently reported by Pearson et al. [51]. In this study, one half of a metaphase spindle was bleached and the recovery in the bleached zone quantitatively measured over time. It was found that recovery of the spindles was barely detectable, even over long periods of time (>10 min). To simulate the Cse4-GFP FRAP experiment, a standard simulation of microtubule dynamics was allowed to run for 350 seconds (700 time steps) prior to simulation of Cse4-GFP laser photobleaching, in order to allow the system to first reach a steady-state. At the time of the bleach event (350 s), an array was generated with 32 elements, one element corresponding to each simulated kMT tip, to record the bleach status of each simulated kinetochore. If the length of a kMT attached to the left SPB (at 350 seconds) was less than or equal to ½ of the total spindle length, or if the length of a kMT attached to the right SPB was greater than or equal to ½ of the spindle length, the element in the bleach status array corresponding to that kMT tip was assigned as 0, indicating that the kinetochore Cse4-GFP attached to the plus-end of that kMT was bleached. All other kMT tips were assigned as 1 in the bleach status array, indicating that the kinetochore Cse4-GFP was not bleached. Thus, any kinetochores in the left half of the spindle were considered bleached, regardless of which pole their respective kMT was anchored to. This array was then stored, remaining unchanged, for the duration of the simulation. Simulated microtubule dynamics were allowed to continue for an additional 650 seconds after the

bleach event. Simulated fluorescence images were then generated as described above, with the following exception. Prior to generating images of the kinetochore position data array, each element in the bleach status array was multiplied by its corresponding element in the kinetochore position data array. In this way, all bleached kMT tips were assigned 0 values in the kinetochore position array, rendering bleached kinetochores nonfluorescent during the image simulation process.

In modeling of the Cse4-GFP FRAP experiment, it was assumed that one entire half-spindle was bleached during the experimental bleaching event. In addition, the model does not account for Cse4-GFP turnover on the kinetochore or diffusion of free (unbleached) Cse4-GFP into or out of the bleached spindle half. The observed lack of recovery in Cse4-GFP FRAP experiments supports this assumption. A spindle length of 1.72 μm was used for all of the Cse4-FRAP simulations.

Analysis of the Cse4-GFP FRAP experiment and simulation

The calculation of Cse4-GFP FRAP was identical for both the experimental work as well as the simulation[51]. In each case, the baseline fluorescence bleach amount was established by measuring the integrated fluorescence intensity of the spindle half prior to bleaching, and then again immediately after laser photobleaching. Another total fluorescence intensity measurement was then obtained for the bleached spindle half after 10 minutes of simulation and/or experimental time had elapsed. The fluorescence recovery in each case was calculated according to the following formula:

$$\% \text{ Recovery} = ((F_{final} - F_{t=0})/(F_{pre} - F_{t=0})) * 100 \quad (1)$$

where F_{final} = integrated fluorescence intensity of bleached spindle half after 10 minutes, F_{pre} = pre-bleach fluorescence intensity of spindle half to be bleached , and $F_{t=0}$ = bleached spindle half fluorescence intensity immediately post-bleach. Any negative recoveries (due to stochastic fluctuations) were recorded as zero for the experiment as well as the simulation.

Simulation of the GFP-Tub1 FRAP experiment

GFP-Tub1 FRAP experiments were simulated using a method similar to the FRAP of Cse4-GFP, as described above. In the case of GFP-Tub1 FRAP, each tubulin subunit in a given kMT is simulated. During the bleach event, every incorporated tubulin subunit in the bleached half-spindle is assigned a value of zero in a bleach status array. Tubulin subunits are then exchanged with a free pool as kMTs depolymerize and then polymerize. A given percentage of the free tubulin pool is bleached during the bleaching event, as occurs in live cells [59], and the percentage of unbleached free units is updated as bleached or unbleached tubulin dimers are released from shortening kMTs and consumed by growing kMTs. It is assumed that free tubulin subunits can diffuse rapidly throughout the nucleus relative to the speed of MT polymerization, i.e. when bleached

subunits are released from kMTs in the bleached half they are well mixed into the nuclear free subunit pool so that kMTs anywhere in the nucleus have an equal probability of picking up a bleached subunit. This assumption is justified, as the rate of polymerization is slow relative to diffusion over the distance of the nucleus [201]. The probability of adding an unbleached subunit to a polymerizing kMT is equal to the fraction of unbleached subunits remaining in the free tubulin pool. Calculation of half-spindle integrated fluorescence is completed as described above for every time step in the simulation.

In the GFP-tubulin FRAP simulation, it is assumed that all incorporated GFP-tubulin subunits in the bleached half-spindle are rendered permanently nonfluorescent during the bleach event. In addition, 50% of the free GFP-tubulin pool, estimated to be $3.4x10^4$ molecules (Sprague, 2002), is bleached. All dynamics are assumed to occur at kMT plus-ends, with no minus end flux. The simulation is not corrected for experimental photobleaching due to image acquisition, as the Maddox et al. (2000) experimental data is already corrected to compensate for this effect.

TABLE A.1: Screening of Computational Models for kMT Dynamic Instability in Yeast

	Castastrophe Gradient Model	Rescue Gradient Model	Tension Dependent Rescue Model	Tension Dependent Catastrophe
Catastrophe Gradient Model	(single model) Exp 1[a]: p[d]<0.01 Exp 2[b]: p<0.02 Exp 3[c]: p<0.01	xxx	xxx	xxx
Rescue Gradient Model	Exp 1: p=0.04 Exp 2: p=0.08 Exp 3: p<<0.01	(single model) Exp 1: p<<0.01[e] Exp 2: p<<0.02	xxx	xxx
Tension Dependent Rescue Model	**Exp 1: p= 0.55** **Exp 2: p=0.24** **Exp 3: p= 0.11**	Exp 1: p<<0.01[e]	(single model) Exp 1: p<<0.01[e]	xxx
Tension Dependent Catastrophe Model	Exp 1: p=0.25 Exp 2: p=0.26 Exp 3: p<.01	Exp 1: p=0.27 Exp 2: p=0.05 Exp 3: p<<.01	Exp 1: p<<0.01[e]	(single model) Exp 1: p<<0.01[e]

[a]Exp 1: Experiment #1 is a comparison of the simulated mean wild-type kinetochore-associated metaphase Cse4-GFP fluorescence distribution to the experimental mean wild-type kinetochore-associated fluorescence distribution via statistical analysis of fluorescence distribution curves.

[b]Exp 2: Experiment #2 is a comparison of the simulated mean Cse4-GFP FRAP percentage to the experimental mean Cse4-GFP FRAP

[c]Exp 3: Experiment #3 is a comparison of the simulated mean *cdc6* mutant kinetochore-associated metaphase Cse4-GFP fluorescence distribution to the experimental mean *cdc6* mutant kinetochore-associated Cse4-GFP fluorescence distribution via statistical analysis of fluorescence distribution curves. No parameter value adjustments are allowed in simulating the *cdc6* mutant spindles from the wild-type parameter values, with the exception of reducing the tension spring constant to 0.

[d]p-values = probability of fit of simulated results to experimental results, calculated as described in supplemental materials and methods for each experiment

[e]Models that were unable to qualitatively reproduce metaphase kinetochore clustering were immediately ruled out and therefore not run through additional simulated experiments.

FIGURE A.1: Metaphase congression is correlated with spindle length. (A) Shorter spindle length "prometaphase" experimental image with indistinct kinetochore clustering (green; labeled with Cse4-GFP). Spindle poles are labeled with Spc29-CFP (red). (B) Metaphase spindle experimental image with distinct kinetochore clustering on either side of the spindle equator. Scale bar, 1000 nm (C) Statistical comparison of kinetochore localization by spindle length. Spindles between 1.6-1.9 μm had consistent kinetochore distributions ($p>0.25$), whereas spindle lengths outside of this range had decreased probabilities of fit. Kinetochores exhibit a "prometaphase" configuration at short spindle lengths (1.1 to 1.5 μm) and congress to a metaphase configuration at spindle lengths from 1.6 to 1.9 μm. (D) Quantitative comparison of experimental kinetochore clustering in prometaphase and metaphase spindles. Relative fluorescence at each point is given as mean ± standard error of the mean (SEM). Normalized spindle position equals 0.5 at the spindle equator. Prometaphase spindles have less organized kinetochore clusters, whereas metaphase spindles have a distinct peak in kinetochore-associated fluorescence at the "quarter spindle" location, with a definite reduction of fluorescence at the spindle equator.

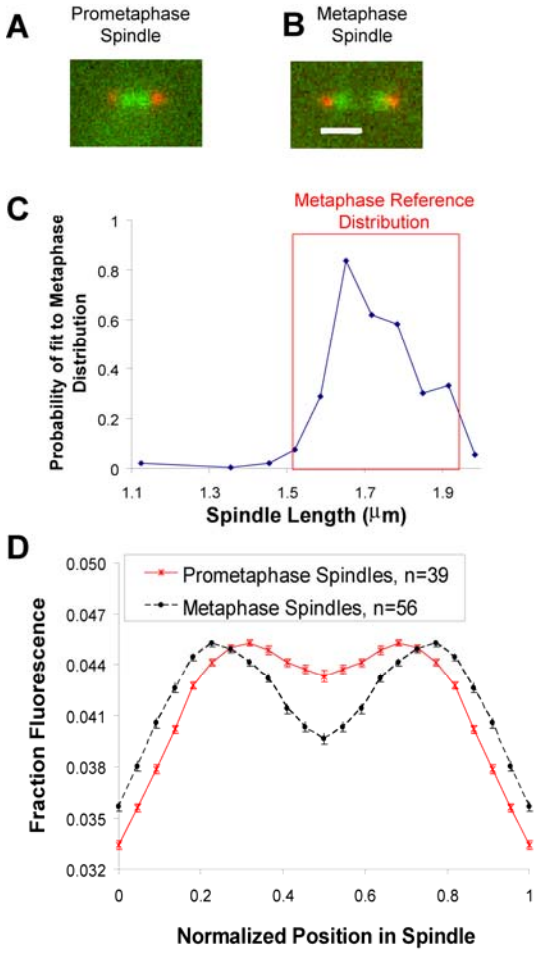

FIGURE A.2: Kinetochore-associated Cse4-GFP clustering provides a reasonable approximation for kMT plus-end locations. (A) Representative simulated images generated by placing green fluorescent markers at putative kMT plus-ends as measured in electron micrograph reconstructions [30], and red fluorescent markers at kMT minus ends (Scale bars, 1000 nm). Absolute kMT lengths are increased by ~30 nm in the simulated images to account for the distance between the kMT minus ends as measured in electron micrograph reconstructions and the Spc29-CFP spindle pole marker used in experimental fluorescence images [202]. All simulated images have been convolved with the measured microscope point spread function and typical noise levels in the Cse4-GFP fluorescence images. (B) Typical Cse4-GFP experimental fluorescence images (Scale bar, 1000 nm) (C) Quantitative analysis of average simulated kMT plus-end fluorescence clustering with comparison to mean experimental Cse4-GFP kinetochore-associated fluorescence clustering. Thus, Cse4-GFP fluorescence provides a good approximation of the kMT plus-end positions as evaluated by electron micrograph reconstructions.

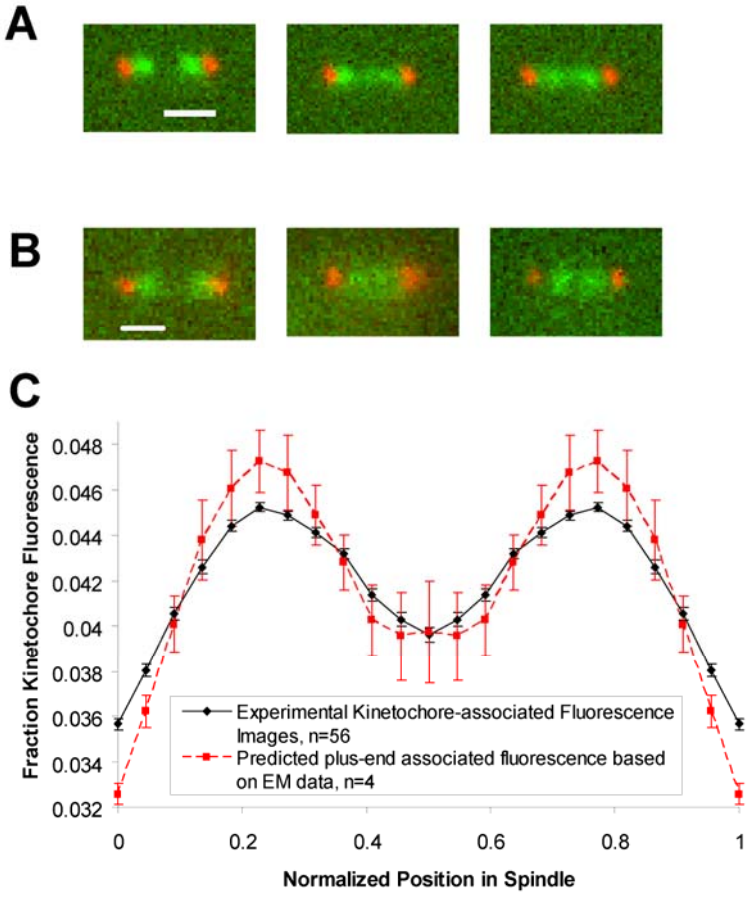

APPENDIX B

SUPPLEMENTAL MATERIAL: MEASURING NANOMETER SCALE GRADIENTS IN SPINDLE MICROTUBULE DYNAMICS USING MODEL CONVOLUTION MICROSCOPY

(Reprinted with permission from *Molecular Biology of the Cell* 17(9) (2006))

Supplemental Tables and Figures

TABLE B.1: p-values for Spatially-Resolved FRAP Experimental Data

Bin Number	Normalized Spindle Position[a]	p-value adjacent bins (65 nm resolution)[b]	p-value alternating bins (130 nm resolution)[c]
0	0.000	0.2830	**0.0193**
1	0.043	0.2263	**0.0007**
2	0.087	**0.0008**	**0.0001**
3	0.130	**0.0018**	**0.0261**
4	0.174	0.3681	0.2560
5	0.217	0.4627	0.5505
6	0.261	0.8188	**0.0248**
7	0.304	**0.0377**	**0.0335**
8	0.348	0.3375	**0.0341**
9	0.391	0.0919	**0.0192**

[a]Normalized spindle position represents the value between 0 and 1 that defines relative location within the yeast mitotic spindle. Spindle position 0 is at the centroid of the Spc-29 SPB marker, and spindle position 0.5 is in the center of the spindle at the spindle equator. FRAP half-times are not reported at the spindle equator for half-spindle bleaches, as this area represents the point where the fluorescence recovery in the bleached half-spindle equals the fluorescence loss in the unbleached half-spindle, and thus does not contain useful information.

[b]p-values were calculated via a t-test for comparison of raw data in adjacent bins (~65 nm resolution). For example, p-values for bin "0" were calculated by comparing raw experimental FRAP half-times for bin "0" to the data for bin"1". Bold values represent bins where $p<0.05$.

[c]p-values were calculated via a t-test for comparison of raw data in alternating bins (~130 nm resolution). For example, p-values for bin "0" were calculated by comparing raw experimental FRAP half-times for bin "0" to the data for bin"2". Bold values represent bins where $p<0.05$.

FIGURE B.1: Simulated ipMT dynamics dominate recovery at the equator, but have little effect on recovery rates near the SPBs. (A) Recovery rates in the spindle zone with high kMT density (blue arrows) were not affected by the addition of robust ipMT dynamics to the simulation, assuming growth and shortening rates were similar between ipMTs and kMTs (range from 0.9 μm/min – 2.0 μm/min tested). Frequent depolymerization of ipMTs to the spindle equator does affect FRAP half-times towards the equator (red arrows). (B) Experimentally observed FRAP half-times at the equator limit theoretical ipMT plus-end excursion lengths, such that it is likely that ipMT plus-ends rarely visit the equator. The histogram shows the distribution of ipMT plus-end positions as a function of spindle position for (1) simulations where ipMTs are dynamic, and yet depolymerization to the equator is limited such that experimentally observed half-times are reproduced (blue and purple bars), and (2) for a simulation where ipMT dynamics result in a failure to reproduce experimental results because ipMT plus-end depolymerization leads to reduced FRAP half-times towards the equator (red and purple bars) (for ipMTs, $k_c = 0.25\ min^{-1}$, $V_g = 1.2$ μm/min, $V_g = 1.2$ μm/min). These simulation results indicate that if ipMTs are dynamic, they must have plus ends that are confined to be close to the opposite pole. Otherwise, they must be non-dynamic compared to kMTs.

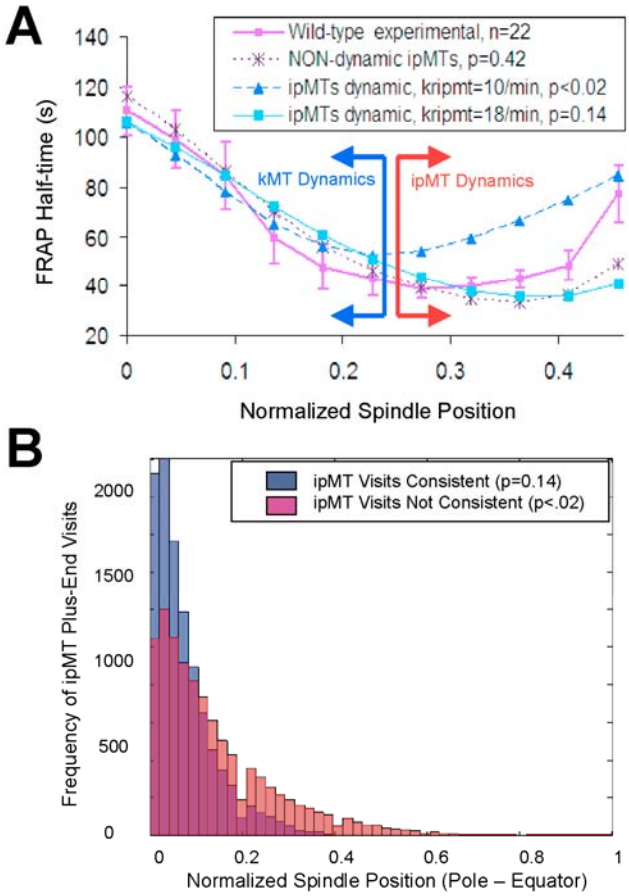

APPENDIX C

SUPPLEMENTAL MATERIAL: CHROMOSOME CONGRESSION BY KINESIN-5 MOTOR-MEDIATED DISASSEMBLY OF LONGER KINETOCHORE MICROTUBULES

Introduction

During metaphase in the budding yeast mitotic spindle (Fig. C.1) sister mitotic chromosomes (blue) are still physically attached to one another. Each chromosome is mechanically linked via a single kinetochore (cyan) to the plus end of a single kinetochore microtubule (kMT, black) whose minus end is in turn linked to a spindle pole body (SPB, grey) [19, 30, 51, 58, 61, 102, 142]. The sister chromosome is similarly linked to the opposite SPB. Kinetochores move as their associated kMT plus ends dynamically exchange αβ-tubulin subunits with the soluble pool in the nucleus, while kMT minus end assembly remains non-dynamic [59, 99, 108]. In all, there are 16 sister chromosome pairs in haploid cells, for a total of 32 kinetochores and 32 kMTs, although for schematic simplicity we show only a single pair in Fig. C.1.

The mechanical linkage that runs from pole to pole via the kMTs and kinetochores is almost always under tension in metaphase [18, 19, 61, 102]. As a result, kinetochores constrain chromosomes to congress at the equator, provided each kinetochore remains in its respective half of the spindle. Since each kinetochore is persistently attached to a single kMT plus end during metaphase in budding yeast [50, 51], kMT plus end assembly must be limited so that each kMT plus end generally remains in its own half-spindle. If subunit exchange at the kMT plus end were unfavorable everywhere in the spindle, then kinetochores would tend to cluster around their respective poles, as the pole would be the most probable position for a kMT plus end. In fact, kinetochores do not cluster near their poles, but instead cluster about midway between their pole and the equator [19, 29, 50, 61, 108, 118, 203]. Therefore, kMT plus ends should have net assembly favored near the SPBs, but net disassembly near the equator, which together establish a gradient in net kMT assembly.

Through a series of fluorescence and electron microscopy studies, we confirmed the existence of the gradient in net kMT plus end assembly [29, 50, 51, 108, 203]. This gradient is depicted in Fig. C.1 as a region near the SPB where net assembly is favorable (green, i.e. when kMTs are relatively short), and another region near the equator where assembly is unfavorable (red, i.e. when kMTs are relatively long). As a result of this gradient in net assembly, kMT plus ends grow efficiently away from poles, but rarely cross the equator. In between these two regions is an intermediate region where net assembly is close to zero, and this region constitutes an attractor zone for kMT plus ends and their associated kinetochores (Fig. C.1, yellow arrows). A key question, that we now address, is how the kMT plus end net assembly gradient is established.

FIGURE C.1: A spatial gradient in net kMT plus-end assembly mediates kinetochore congression in yeast**.** Kinetochores (cyan) congress to attractor zones (yellow arrows) on either side of the spindle equator (dotted line) during yeast metaphase via the plus-end assembly dynamics of kMTs (black). The kMT plus-end assembly dynamics are spatially regulated such that plus-end assembly is favored near the poles when kMTs are relatively short (grey, favorable assembly zone shown as green gradient), and suppressed near the spindle equator when kMTs are relatively long (dotted line, assembly suppression zone shown as red gradient).

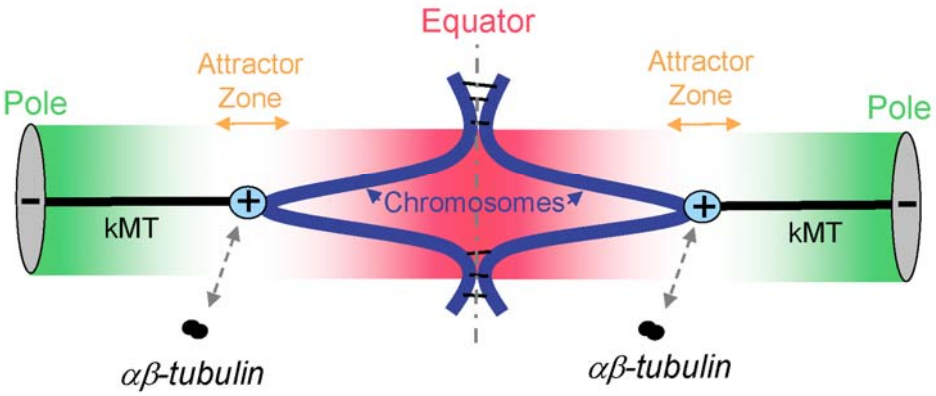

Supplemental Results

Spindle Length Distributions

In this study, we focused on the regulation of kMT plus-end microtubule dynamics by kinesin-5 molecular motors, independent of their role in generating outward extensional sliding forces on the poles to establish a steady-state metaphase spindle length. As Cin8p and Kip1p are redundant for the microtubule sliding function in yeast, deletion of either molecular motor by itself results in metaphase spindles with either a modest reduction in spindle length (*cin8Δ*) or little change in spindle length (*kip1Δ*) (Fig. C.2A). To ensure that our analysis of kMT plus-end dynamics was not affected by differences in spindle lengths between wild-type and mutant cells, we selected a subset of the total distribution of wild-type and *cin8Δ* spindle lengths for analysis (Fig. C.2B). This selection was made by selecting all wild-type and mutant spindles within the range of 1.5-1.7 μm for analysis, such that the mean and standard deviation of both wild-type and mutant spindle lengths were similar. This sub-selection represents a substantial fraction of all the spindles (~30-40%), and results in a mean spindle length only slightly different than the mean of the parent population (~5-15% different). A similar process was used for both Cse4-GFP and GFP-Tub1 fluorescence analysis experiments.

For comparison, the Cse4-GFP kinetochore localization analysis was also performed on the entire wild-type and *cin8Δ* spindle length populations (Fig. C.2C, left). Although results in the main text are sub-selected to eliminate any spindle length bias in the analysis, nearly identical results were achieved using the entire spindle length population (Fig. C.2C, left). In addition, the longest 50% of spindle lengths for both populations were analyzed, with similarly indistinguishable results (Fig. C.2C, right).

As an added control, spindle microtubule organization was evaluated in a strain with reduced spindle lengths. In *bim1Δ* mutants, spindle lengths are shorter than in wild-type spindles, with a spindle length distribution that is similar to *cin8Δ* mutant cells (Fig. C.3A). However, in contrast to *cin8Δ* mutants, spindle microtubule organization is not disrupted in *bim1Δ* mutants, but rather is similar to the wild-type distribution (Fig. C.3B). Thus, we conclude that the disrupted spindle organization in *cin8Δ* mutant cells is not simply a consequence of reduced *cin8Δ* spindle lengths.

FIGURE C.2: Mutant spindle lengths are moderately shorter than wild-type spindle lengths**,** although kinetochore organization results are similar regardless of spindle length (A) Spindle length distributions for wild-type, *cinΔ*, and *kip1Δ* spindles. *cin8Δ* spindle lengths are moderately shorter than wild-type spindle lengths. (B) To control for spindle length, a subset of the total distribution of spindles is selected for analysis of kMT dynamics, as shown. (C) Cse4-GFP kinetochore organization analysis of alternate spindle length populations produced similar results.

A Spindle Length Distribution

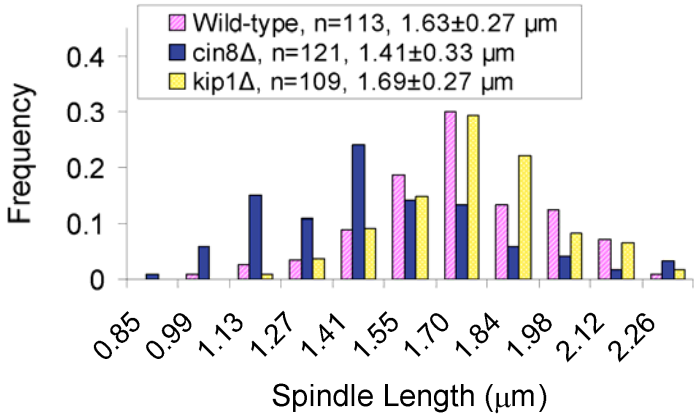

B Spindles Selected for Analysis of Cse4-GFP Distribution

Spindle Type	Spindle Length (µm)	N, All spindles	Spindle Length Selected for Cse4-GFP Analysis (µm)	N, Spindles Selected for Analysis
Wild-type	1.63 ± 0.27[a]	113	1.69 ± 0.11[a]	55
cin8Δ	1.41 ± 0.33[a]	121	1.61 ± 0.15[a]	44

[a]mean ± standard deviation

C Alternate Populations: Cse4-GFP Distribution

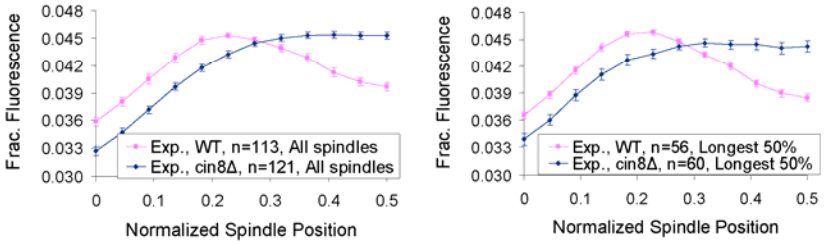

FIGURE C.3: A bim1Δ mutant with similar spindle lengths to cin8Δ mutants does not have disrupted spindle microtubule organization (A) *bim1Δ* spindle lengths are shorter than in wild-type cells, but similar to *cin8Δ* spindle lengths. (B) GFP-Tub1 organization is similar in wild-type and *bim1Δ* spindles, but disrupted in *cin8Δ* spindles.

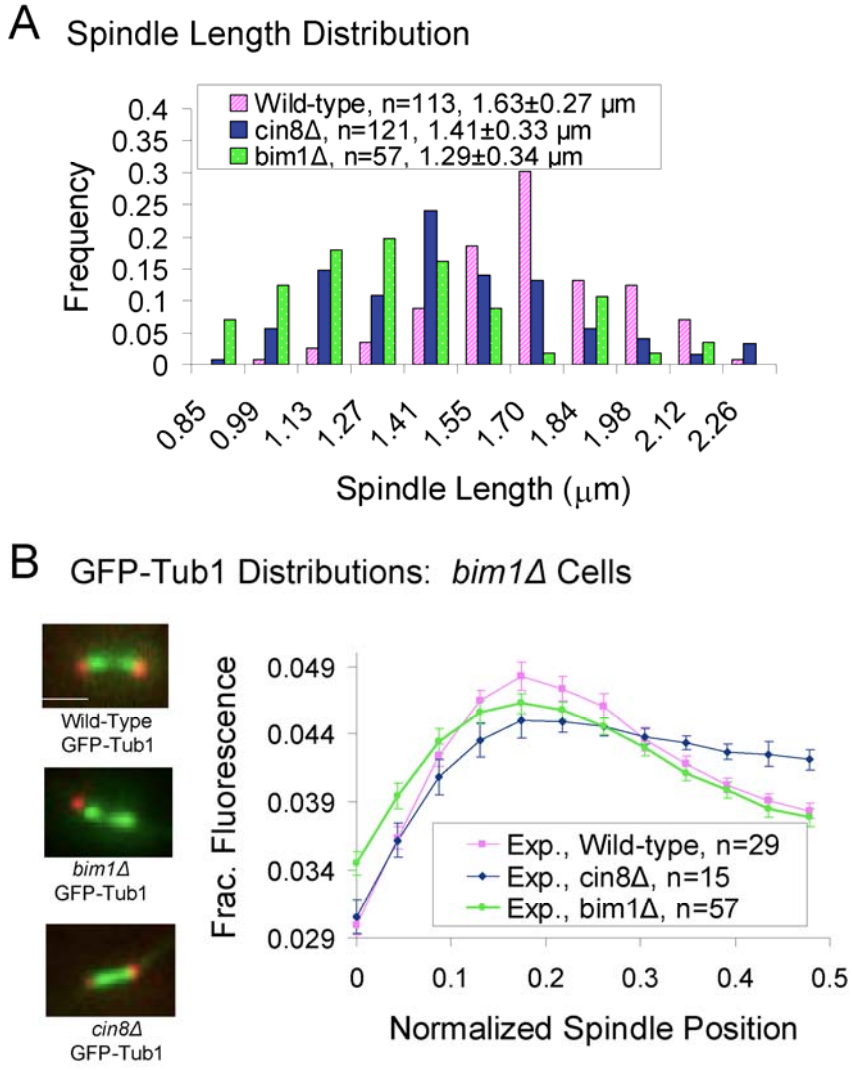

Kinetochore Position Distribution in kip1Δ Spindles

There are two kinesin-5 motors in budding yeast, Cin8p and Kip1p. Kip1p is considered the less important of these two motors [113, 118, 120, 121], as *kip1Δ* phenotypes are less severe than those of *cin8Δ* cells. Nevertheless, we quantified kinetochore organization in *kip1Δ* mutants via Cse4-GFP fluorescence analysis, similar to the analysis for *cin8Δ* mutants. Here, *kip1Δ* mutants had a similar, but moderated, effect on kinetochore organization as compared to *cin8Δ* mutants (Fig. C.4A). The peak in kinetochore-associated fluorescence is shifted towards the spindle equator, indicating that kMTs are longer in *kip1Δ* mutants as compared to wild-type spindles. This shift is less significant than in *cin8Δ* mutants, though, suggesting that Kip1p ultimately has a more moderate effect on kMT assembly than Cin8p (Fig. C.4A).

FIGURE C.4: kip1Δ mutants have a similar, but attenuated, kinetochore disorganization phenotype as compared to cin8Δ mutants. (A) As shown in experimental images (left), kinetochore organization is mildly disrupted in *kip1Δ* mutant spindles (Cse4-GFP, green; Spc29-RFP pole markers, red). By quantifying Cse4-GFP fluorescence over a large number of spindles (right) mean kinetochore positions suggest that kMTs in *kip1Δ* mutants are longer than in wild-type spindles, but shorter than in *cin8Δ* mutant spindles. (scale bar, 500 nm; error bars s.e.m.) (B) Similar results are obtained using histone-repression mutants, where the spindle length is longer than in wild-type spindles.

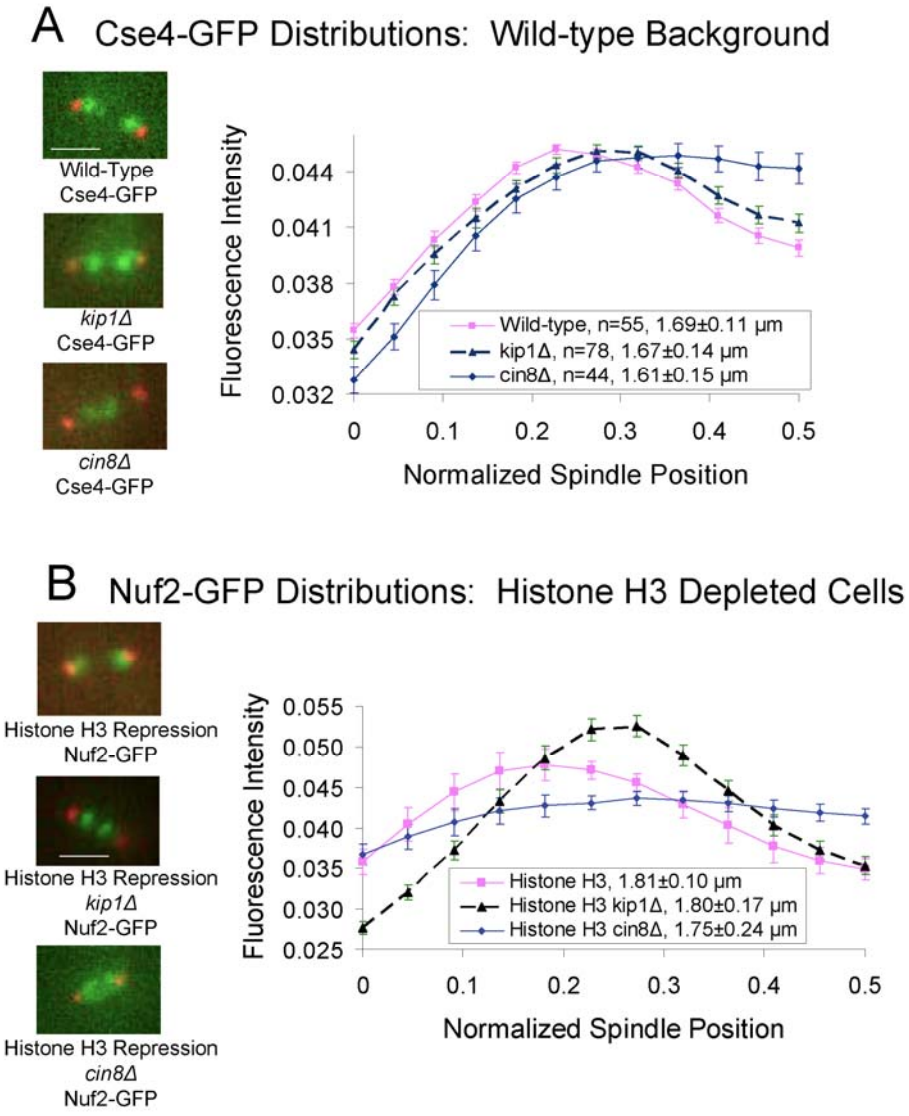

Kinetochore Distribution in Histone H3-repressed Cells: Wild-type vs cin8Δ

To further ensure that reduced spindle length was not responsible for the observed kinetochore organization changes in *cin8Δ* mutants, we repeated the kinetochore localization experiments in histone H3 repression mutants. As reported previously, histone H3 repression results in longer metaphase spindles, apparently by making the chromatin between sister kinetochores more compliant [122]. Thus, *cin8Δ* spindles in a histone H3 repressed mutant have lengths typical of wild-type cells [122]. In these cells, although the entire range of spindle lengths is within the typical wild-type range, loss of kinetochore clustering and shifting of kinetochores toward the equator are still apparent, similar to *cin8Δ* spindles in a wild-type background (Fig. C.4B). Thus, deletion of Cin8p affects metaphase kinetochore organization independent of its role in regulating spindle length.

Although spindle lengths are increased in the histone H3 repressed spindles, *kip1Δ* mutants again show a moderate shift in kinetochore-associated fluorescence towards the spindle equator (Fig. C.4B).

ANOVA Analysis of MT Length Distributions Measured via Cryo-Electron Microscopy

A single-factor ANOVA analysis of MT length distributions between cells was performed for the wild-type and *cin8Δ* spindles to ensure that all MT lengths could be analyzed as independent entities (Table C.1, below). All cells were statistically indistinguishable from each other.

TABLE C.1: Single-Factor ANOVA Analysis: Wild-type and *cin8Δ* Mutant Spindles

SUMMARY: cin8Δ

Groups	*Count*	*Sum*	*Average*	*Variance*
Cell 01	65	28474	438	111571
Cell 02	60	25952	432	214142
Cell 03	60	22995	383	151855
Cell 04	49	19667	401	137830
Cell 05	50	20388	408	90007

ANOVA: cin8Δ

Source of Variation	*SS*	*df*	*MS*	*F*	*P-value*	*F crit*
Between Groups	124701	4	31175.27	0.219	0.929	2.404
Within Groups	39760636	279	142511.2			
Total	39885337	283				

SUMMARY: Wild-type

Groups	*Count*	*Sum*	*Average*	*Variance*
Cell 01	43	12061	280.4884	67832.87
Cell 02	37	11260	304.3243	120916.2
Cell 03	38	15334	403.5263	395248.5
Cell 04	42	9823	233.881	54929.23

ANOVA: Wild-type

Source of Variation	*SS*	*df*	*MS*	*F*	*P-value*	*F crit*
Between Groups	606519.2	3	202173.1	1.309854	0.273	2.663
Within Groups	24078257	156	154347.8			
Total	24684776	159				

GFP-Tubulin Fluorescence Recovery After Photobleaching: Half-Spindle Time Series Recovery

GFP-Tubulin FRAP is robust in both wild-type and *cin8Δ* cells, as shown by the representative time series in Fig. C.5. Recovery obeys a single exponential, and summary statistics are as shown.

FIGURE C.5: GFP-Tubulin FRAP in wild-type and cin8Δ spindles. As shown by the FRAP time series, half-spindle FRAP recovery rate is similar in both wild-type and *cin8Δ* cells (p=0.03), indicating that kMT self-assembly remains dynamic in *cin8Δ* spindles. The extents of recovery are also similar.

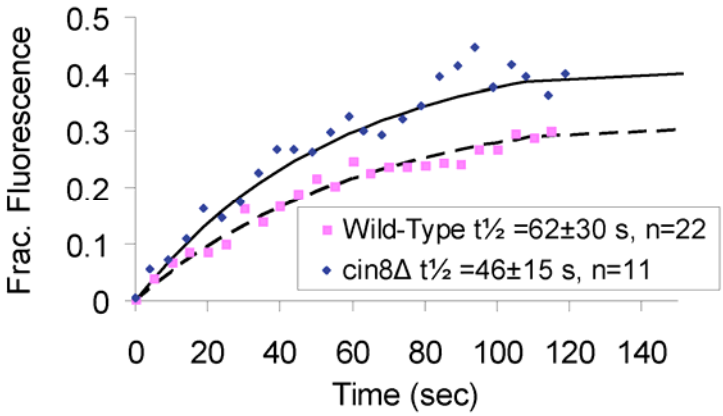

Astral Microtubule Length Distributions

In Fig.C.6 is shown the distribution of astral microtubule lengths for varying cytoplasmic concentrations of Cin8p. Although the distributions are broad, as expected, the distribution shifts toward increasing aMT length with decreasing Cin8p expression.

FIGURE C.6: Astral MT length distributions. Astral microtubule lengths are broadly distributed, although there is a shift in mean length depending on the Cin8p expression level. The mean aMT length correlates inversely with Cin8p expression level.

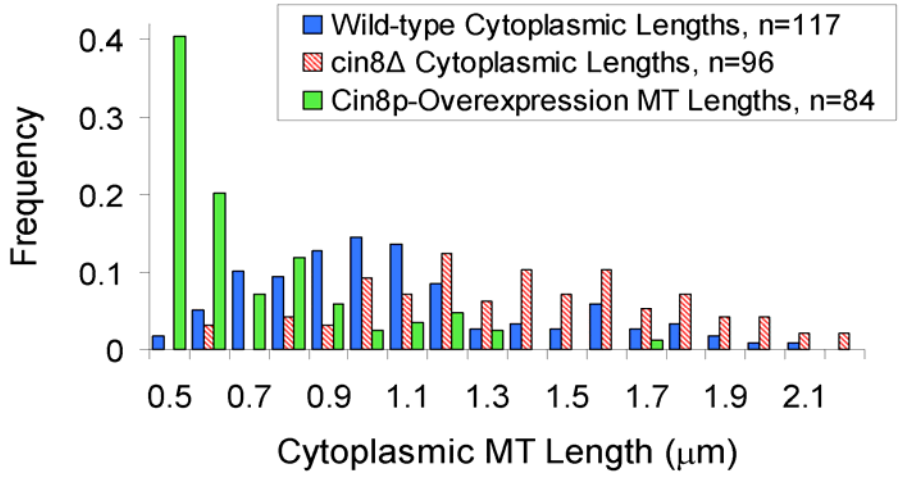

Cin8p Overexpression: Spindle Statistics

Similar to kinesin-5 deletion experiments, overexpression of kinesin-5 sliding motors has an effect on spindle length [121]. Here, an increased concentration of sliding motors in the nucleus results in longer spindle lengths (Fig. C.7A). Because the Cin8p overexpression assay had a substantial effect on spindle length (Fig. C.7A), it was not possible to compare equal spindle lengths between wild-type and Cin8p-overexpression in considering kinetochore organization. Thus, quantitative analysis was performed such that kinetochore fluorescence was recorded as a function of absolute distance from the pole, regardless of spindle length (Fig. C.7B). It was found that although spindle lengths were increased, the peak in kinetochore-associated fluorescence was ~50% closer to the poles in spindles with Cin8p overexpression than in control spindles. This result suggests that kMT length is substantially reduced in the presence of high concentrations of Cin8p. The kMT shortening occurs despite the increase in chromatin stretching between sister kinetochores, which by itself promotes kMT assembly [50, 193, 204]. Thus, the effect of Cin8p overexpression and its associated promotion of kMT disassembly is dominant over the tension-dependent promotion of assembly, and so net kMT shortening occurs.

Although the overexpression experiment results in increased Cin8p expression as evidenced by longer spindle lengths and shorter kMTs, it is difficult to predict the expression level quantitatively, and large fluctuations in expression level are likely [205]. For this reason, simulation results, although qualitatively predicted in Fig. 5.1A, are not quantitatively fit to the Cin8p overexpression experiment.

FIGURE C.7: Results for Cin8p overexpression studies. (A) Spindles are longer in Cin8p overexpression cells than in wild-type cells, although the estimated kMT length is reduced. (B) The Cse4-GFP fluorescence distribution as a function of absolute distance from one spindle pole body is similar to normalized results (Fig 5.1C).

A Cin8p Overexpression: Spindle Statistics

	Wild-Type Control	Cin8p-Overexpression
Number of Spindles Analyzed	N=125	N=96
Spindle Length	1.80 +/- 0.30[a] μm	2.48 +/- 0.96[a] μm
Estimated kMT Length (Mode)	573 nm	248 nm
% Spindle Length Change	---	+38%
% kMT Length Change	---	-57%

[a]mean ± s.d.

B Cse4-GFP Fluorescence in Cin8p Overexpression

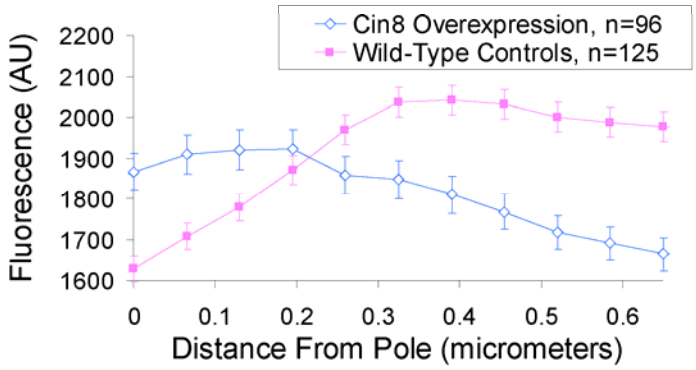

Experimental results for cin8-nlsΔ cells

We performed experiments using a mutant yeast strain in which the Cin8p nuclear localization signal (NLS) is deleted [132]. This mutation reduces the concentration of Cin8p in the nucleus, while increasing the cytoplasmic concentration of Cin8p. Fluorescent mCherry-tubulin images of metaphase spindles with associated aMTs were collected. Analysis of mcherry-tubulin distribution in the spindle produced results similar to *cin8Δ* cells (Fig. C.8A). Wild-type spindles had characteristic tubulin "tufts", with a peak in mcherry-tubulin fluorescence roughly midway between each pole and the spindle equator. In contrast, mcherry-tubulin fluorescence in *cin8-nlsΔ* spindles was

shifted towards the spindle equator, suggesting that kMT lengths were increased (Fig. C.8A). Spindle lengths were reduced in the mutation, similar to *cin8Δ* spindles, although comparable spindle lengths were used between wild-type and mutant cells for the mcherry-Tub1 spindle fluorescence analysis (Fig. C.8B). Importantly, and in contrast to *cin8Δ* spindles, aMT lengths in *cin8-nlsΔ* cells were shorter than in wild-type cells (Fig. C.8C). In general, the lengths of the MTs in a given compartment, either the nucleus or the cytoplasm, depended inversely on the relative amount of Cin8p in that compartment. This analysis indicates that the effect of Cin8p is mediated locally in a given cellular compartment, rather than globally.

FIGURE C.8: Spindle lengths, kMT lengths, and aMT lengths in cin8-nlsΔ spindles. (A) A comparison of mcherry-tubulin fluorescence distributions in wild-type and *cin8-nlsΔ* spindles. As shown in the images on the left, wild-type spindles have characteristic mcherry-Tub1 "tufts" (green) on either side of the spindle equator, while *cin8-nlsΔ* spindles have a single bar of mcherry-Tub1 fluorescence, similar to *cin8Δ* spindles. This result indicates that kMTs are longer in the *cin8-nlsΔ* cells. Quantification over many images produces similar results (right). (scale bar 500 nm, error bars s.e.m.) (B) Similar to *cin8Δ* mutants, spindle length is reduced in *cin8-nlsΔ* mutants, presumably due to the lower concentrations of anti-parallel-attached Cin8p motors that act to exert an outwardly directed sliding force to separate the SPBs. (C) In contrast to *cin8Δ* mutants, overexpression of Cin8p in the cytoplasm of *cin8-nlsΔ* mutants results in shorter aMTs, rather than the longer aMTs observed in *cin8Δ* mutants.

A Spindle Microtubule Distribution: WT vs *cin8-nlsΔ*

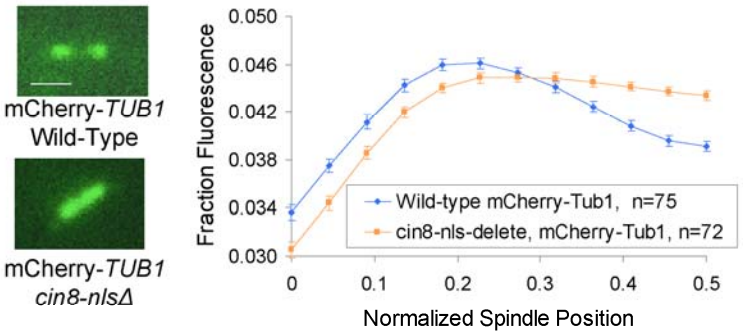

B Spindle Lengths: WT vs *cin8-nlsΔ*

Spindle Type	Spindle Length (μm)	N, All spindles	Spindle Length selected for Analysis in (A) (μm)	N, Spindles Selected for Analysis in (A)
Wild-type	1.46 ± 0.25[a]	75	1.46 ± 0.25[a]	75
cin8-nlsΔ	1.38 ± 0.15[a]	71	1.47 ± 0.08[a]	48

[a]mean ± standard deviation

C Astral Microtubule Lengths: WT vs *cin8-nlsΔ*

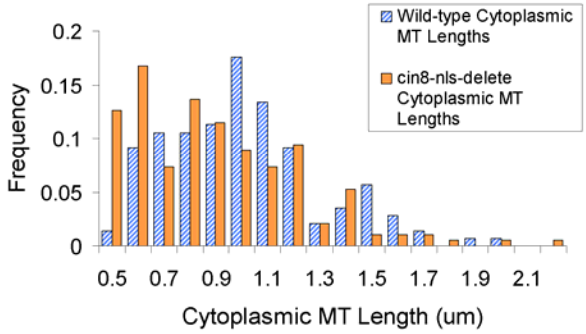

Experimental Evidence for ATP-Driven Motor Activity

Numerous studies have demonstrated that kinesin-5 motors, including Cin8p, have plus-end directed motor activity both *in vitro* and *in vivo* [111, 112, 115, 120, 123, 133, 134]. In addition, because of its bipolarity, the kinesin-5 motor Eg5 is capable of cross-linking adjacent MTs and motoring toward the plus ends of each MT, independent of the relative orientation angle between the two MTs [112]. Because of the results of [112] and the widely recognized torsional compliance of kinesins [206-208], it seems likely that kinesin-5 motors, which are largely regarded as sliding motors that push antiparallel MTs apart, could just as easily cross-link parallel MTs and motor toward the MT plus ends without generating sliding force between the parallel MTs.

To test the simulation assumption that motors walk toward MT plus-ends on parallel microtubules, we performed experiments to provide evidence for ATP-driven motility of kinesin-5 motors in the yeast spindle. As shown in Fig. C.9A (left), both simulated and experimental kymographs of spindle Cin8-GFP were generated to examine spindle-associated motor motility over time. Due to the density of motors in the spindle, it was not possible to detect individual Cin8p motility. However, motor dynamics on the spindle can be inferred from changes in half-spindle Cin8-GFP fluorescence intensity over time. As motors move along the spindle, they would eventually reach the ends of parallel kMTs and soon dissociate. The expected result is that the number of Cin8-GFP molecules will fluctuate over time due to motor-based turnover and movement on the spindle.

If the motor activity were inhibited, then the turnover would be less dynamic, and thus the fluctuations in number would be smaller. To assess whether the Cin8-GFP dynamics on the spindle were affected by inhibition of motor activity, Cin8-GFP spindle kymographs were then obtained for cells treated with azide [60], which will stall motor motility. Quantitative analysis showing the half-spindle standard deviation in Cin8-GFP fluorescence over time for both experiments is shown in Fig. C.9B. The variation in Cin8-GFP fluorescence intensity is reduced in azide-containing media as compared to control media, suggesting that motor motility is reduced. Experiments in low-dose benomyl had variability in half-spindle Cin8-GFP fluorescence that was intermediate between control spindles and azide media spindles, suggesting that kMT plus-end dynamics also contribute to motor exchange on the spindle. We conclude that ATP is required for normal Cin8p dynamics, and that the fluctuations in Cin8p on the spindle are consistent with a model that assumes plus-end directed motility along parallel spindle MTs.

As the density of Cin8-GFP motors in the spindle precluded identification of individual motor spindle movements, we then performed experiments in which we repeatedly photobleached spindles labeled with Cin8-3XGFP and then collected rapid time-lapse images of the spindle after Cin8-3XGFP fluorescence redistribution. This method reduced the fluorescent motor number, allowing for detection of individual Cin8-3XGFP movements. As is experimentally observed and is predicted via simulation (Fig. C.9C), motor movements in the spindle are apparent in both directions, as predicted by a model in which with motors walk along parallel kMTs and ipMTs. We observed a bimodal distribution of motor velocities that is consistent with faster intrinsic motor

velocities (Fig. C.9 C, left, and D), and slower MT polymerization-limited motor velocities (Fig. C.9 D, right, and D). The slower velocity values were similar to those observed on astral MTs where aMT assembly rate presumably limits motor velocity at the growing plus end (Fig. C.9, D).

FIGURE C.9: Experimental evidence for ATP-driven motor motility in the spindle. (A) Simulated and experimental kymographs of Cin8-GFP (green) in metaphase spindles over time show clear qualitative differences between Cin8p activity in control media (left) vs azide (right; horizontal scale bar, 1 μm, vertical scale bar, 4 sec) (B) Cin8-GFP kymographs are quantitatively compared by calculating the standard deviation in half-spindle fluorescence over time. The p-value (calculated via F-test) reflects a significant difference in the variation of Cin8-GFP fluorescence intensity over time in control conditions vs. azide. (C) Repetitive photobleaching of Cin8-3XGFP labeled spindles reveals Cin8p motor motility in the spindle. Rapid excursions (left, horizontal scale bar, 1 μm, vertical scale bar, 20 sec) are consistent with intrinsic motor motility on MTs, while slower excursions are consistent with MT-polymerization limited motor motility rates. (right) (D) The measured distribution of motor velocities is approximately bimodal. Slower spindle velocity measurements are consistent with motor motility rates as measured on astral MTs, and faster spindle velocities are consistent with previously measured in vitro motility assays for Cin8p.

Figure C.9

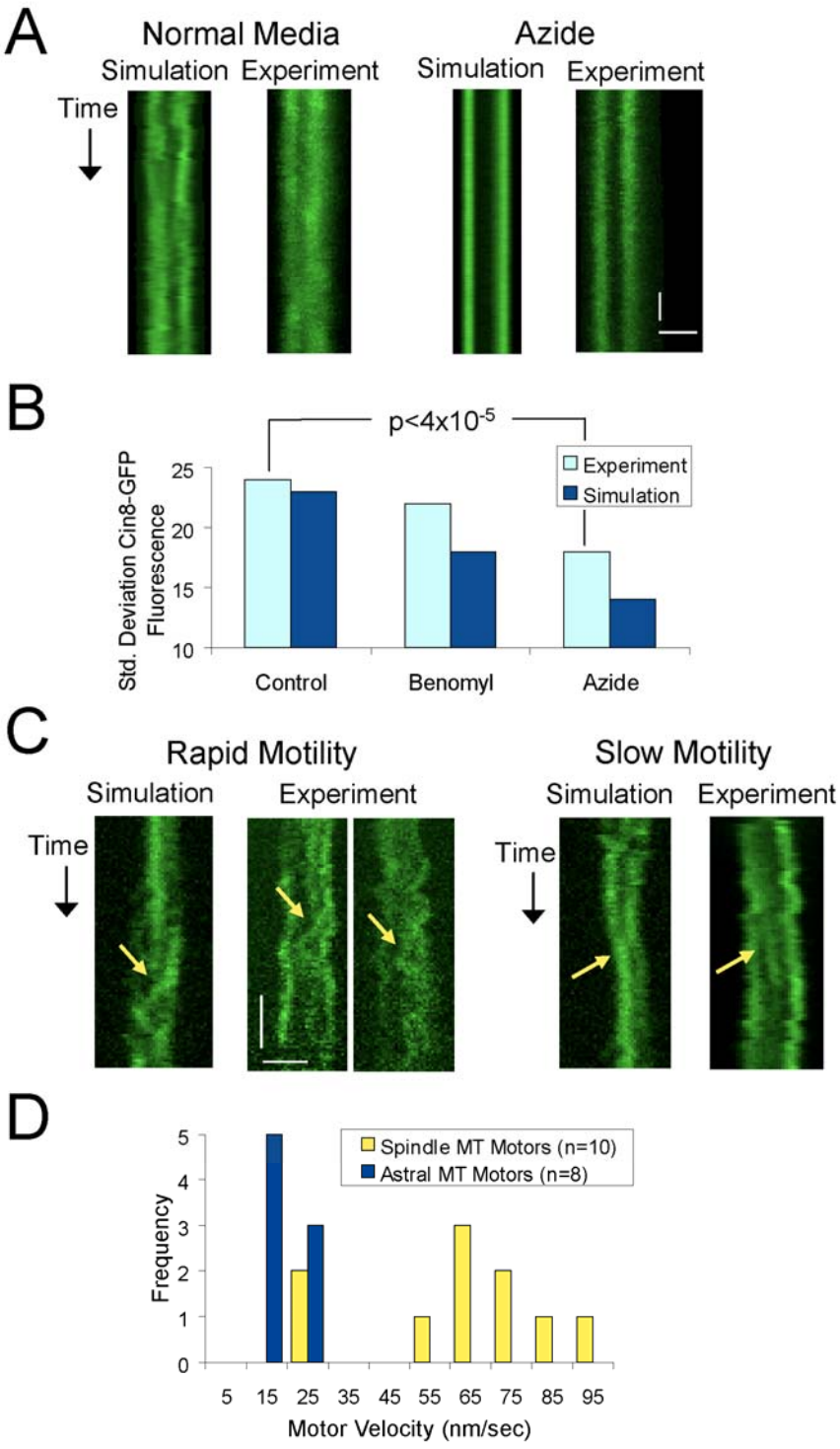
A
Normal Media
Simulation
Experiment
Azide
Simulation
Experiment
Time
B
p<4x10-5
Experiment
Simulation
Std. Deviation Cin8-GFP Fluorescence
25
20
15
10
Control
Benomyl
Azide
C
Rapid Motility
Simulation
Experiment
Slow Motility
Simulation
Experiment
Time
Time
D
Spindle MT Motors (n=10)
Astral MT Motors (n=8)
Frequency
5
4
3
2
1
0
5
15
25
35
45
55
65
75
85
95
Motor Velocity (nm/sec)

Alternate Models

The best fit between experiment and simulation was achieved with a model in which motors randomly attach to microtubules. In this model, motors cross-linking parallel-oriented microtubules walk towards and frequently interact with kMT plus-ends. As shown in Fig. C.10, the evidence for motor motility is further supported by simulation results with stationary motors. In this alternate model, motors stochastically attach to and detach from microtubules, without any plus-end directed motion. Quantitative analysis of Cin8-GFP simulation results from the stationary Cin8p motor model (Fig. C.10, green line) reveals a predicted Cin8-GFP fluorescence distribution that is inconsistent with the observed Cin8-GFP distribution. Rather, the predicted Cin8-GFP distribution for the stationary motor model is roughly similar to the experimentally observed fluorescence distribution for GFP-Tub1 (main text, Fig. 5.2A). The similarity in the predicted Cin8-GFP and the GFP-Tub1 fluorescence distributions arises because microtubule polymer density is a major factor in determining motor attachment positions on the spindle. However, the quantitative difference between the stationary motor model Cin8-GFP positions (Fig. C.10, green line) and the experimentally measured Cin8-GFP positions (Fig. C.10, indigo line) can be accounted for by assuming that Cin8-GFP has plus-end motor activity once attached. Note that if the motor were diffusing on the lattice, rather than actively motoring, then the motor fluorescence distribution would also appear to be very similar to GFP-tubulin fluorescence distribution (not shown).

An alternate model could be one in which motors are stably associated with the kinetochore, acting as "markers" of yeast kMT plus-ends, much like Cse4-GFP or Nuf2-GFP (or any other kinetochore component). In simulations where motors are stably associated with both polymerizing and depolymerizing kMT plus-ends, Cin8-GFP fluorescence is shifted, such that it is essentially coincident with kinetochore-associated fluorescence (Fig. C.10, blue line). Thus, the experimentally observed off-set between the peak in kinetochore-associated fluorescence and the peak in motor-associated fluorescence (main text, Fig. 5.4B) is inconsistent with Cin8p being a stable kinetochore component. Rather, the off-set suggests that dynamic kMT plus-ends increase motor dissociation near to the kMT tip so that the peak of Cin8-GFP fluorescence is shifted toward the pole relative to kinetochore fluorescence.

Another way in which the motor could associate with MTs is via copolymerization with tubulin, and then dissociation subsequent to incorporation into the microtubule lattice. This so-called "tip-tracking" mechanism is hypothesized to be used by EB-1 and other plus-end tip-interacting proteins (+TIPs). However, in this model the Cin8-GFP is again coincident with the kinetochore (results not shown), much like the distribution predicted by the kinetochore-associated model described above, and inconsistent with experimental observation.

The best fit between simulation and experiment is achieved when motors bind to and cross-link kMTs of the same polarity, move towards the kMT plus-ends, and track growing but not shortening plus-ends (Fig. C.10, red line). This model results in a steady

increase in the Cin8-GFP concentration along the kMT, but a decrease in Cin8-GFP concentration near to where the dynamic kMT plus ends are located (main text, Fig. 5.4B), thus quantitatively predicting the fluorescence distribution of Cin8-GFP using reasonable parameters for the motor (see values below).

Note that in this model Cin8p is allowed to randomly crosslink MTs, with no inherent preference for either parallel or anti-parallel binding. This assumption is consistent with the experimentally observed distribution of Cin8-GFP on the spindle, because if the motor had a preference for crosslinking anti-parallel oriented MTs, then the majority of the Cin8-GFP fluorescence would be located near the spindle equator. Since this is inconsistent with the observed Cin8-GFP localization, we conclude that there is no preference for antiparallel MTs. Instead, the model predicts that a substantial majority of cross-links will be between parallel MTs. This is because in the regions where the polymeric tubulin concentration is highest (i.e. in the vicinity of the pole), there is also a strong parallel alignment (>90% parallel). Near the equator the polymeric tubulin level is lower and alignment is mixed (50% parallel). Thus, the majority of Cin8p is expected to be bound to MTs somewhere between the pole and the kinetochores, and of these a substantial majority will likely cross-link parallel kMTs emanating from the nearby pole. This explanation is entirely consistent with both the Cin8-GFP distribution and the Cin8-GFP FRAP, including FRAP resolved by position (see below).

Kinesin-5 motor crosslinking of MTs only affects the model via the effect that crosslinking has on the ability of the motor to consistently interact with the MT plus-ends. Thus, in the kMT-dense spindle, even motors simulated with relatively low individual head processivity will tend to rebind to a nearby MT while the second head remains attached, so that the motor is less likely to completely dissociate from the spindle. Therefore, the "effective" motor processivity is increased due to motor crosslinking [133], ensuring that Cin8p motors frequently interact with the plus-ends of kMTs. A non-crosslinking motor would require a higher intrinsic processivity to consistently arrive at the plus-ends of longer MTs. So, although cross-linking will affect the motor interaction with kMT plus ends, it is not an essential component of the model and can be compensated for by changing other parameters within reasonable limits.

FIGURE C.10: Alternate models for Cin8p dynamics. Alternate models were considered for Cin8p behavior relative to dynamic spindle microtubules. For example, simulated motors that were non-motile (green line), or those that tracked both polymerizing and depolymerizing plus-ends (blue line) had distinct simulation results that differed from the experimentally observed Cin8-GFP fluorescence distribution. The only model considered that was consistent with the experimental Cin8-GFP distribution was one in which motors tracked polymerizing but not depolymerizing kMT plus-ends (red line) (scale bar 1000 nm).

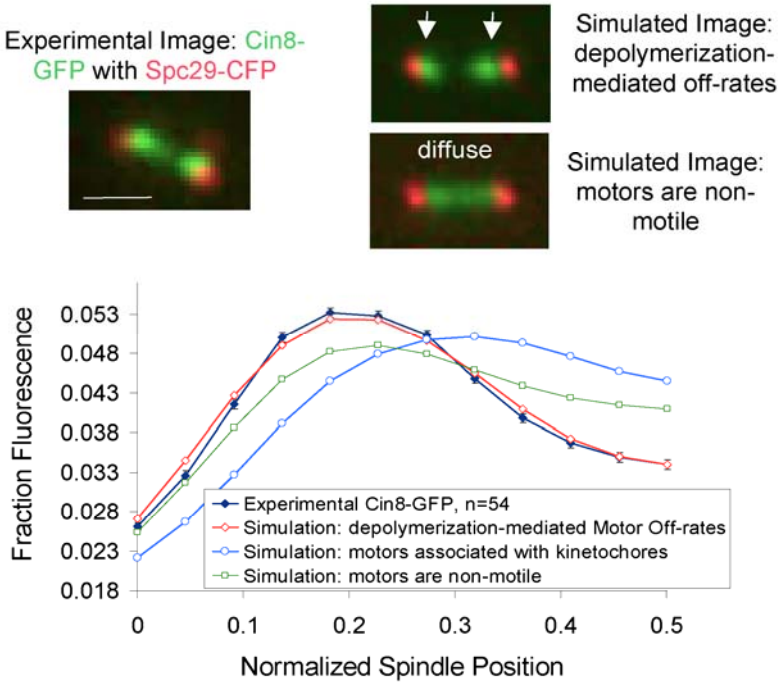

Kip1-GFP Spindle Localization

As shown in Fig. C.11, Kip1-GFP localization in the spindle is qualitatively similar to Cin8-GFP. However, Kip1-GFP is more diffuse than Cin8-GFP, suggesting that Kip1p affinity for MTs is lower than for Cin8p.

FIGURE C.11: Experimental Kip1-GFP fluorescence distribution in the spindle. The Cin8-GFP spindle fluorescence distribution (indigo line) is more tightly focused than Kip1-GFP distribution (maroon line). This result suggests that Cin8p has a higher affinity for microtubules than Kip1p, such that Cin8p has longer run lengths and thus concentrates more efficiently at the growing kMT plus-ends. Low affinity of Kip1p for MTs may result in short motor run lengths that decrease the likelihood of motor concentration at kMT plus-ends. (scale bar 1000 nm)

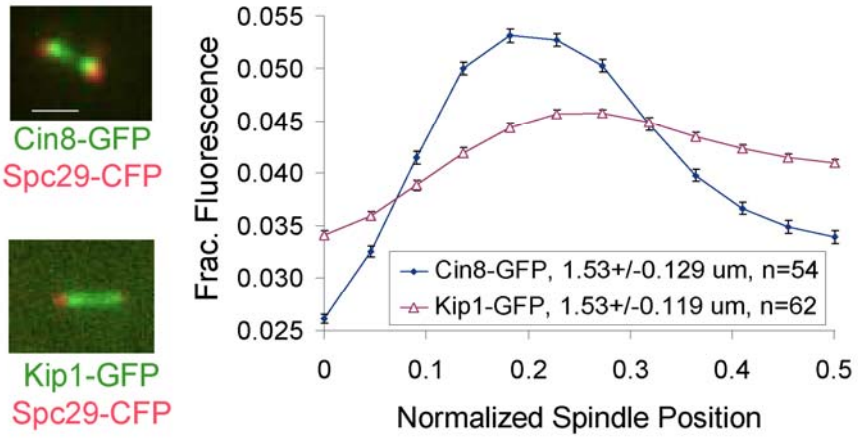

Kinesin-5 Motor Turnover on the Spindle

By measuring Cin8-GFP FRAP half-time as a function of spindle position (Fig. C.12, green line, we find that Cin8-GFP turns over most rapidly in the position of kMT plus-end clustering, suggesting that dynamic kMT plus-ends mediate motor off-rates. Kip1-GFP turnover (Fig C.12, violet line) is also most rapid where kMT plus ends are located. In addition, Kip1-GFP recovery is on average more rapid than Cin8-GFP turnover, again suggesting that Kip1p has a lower affinity for microtubules than Cin8p.

FIGURE C.12: Cin8-GFP and Kip1-GFP FRAP, resolved by spindle position. As was previously reported, FRAP half-time can be resolved by spindle position for GFP-tubulin[108]. There is a gradient in GFP-tubulin recovery half-times, such that recovery is most rapid in the location of kMT plus-end clustering (position 0.25). There is a similar gradient in Cin8-GFP FRAP half-times (green line), suggesting that kMT plus-end dynamics mediate Cin8p motor off-rates. Kip1-GFP FRAP half-time obeys a similar gradient as well. However, Kip1-GFP turns over more rapidly than Cin8-GFP, consistent with a model where Kip1p has a lower affinity for MTs, and thus interacts less frequently with kMT plus-ends. (error bars, s.e.m.)

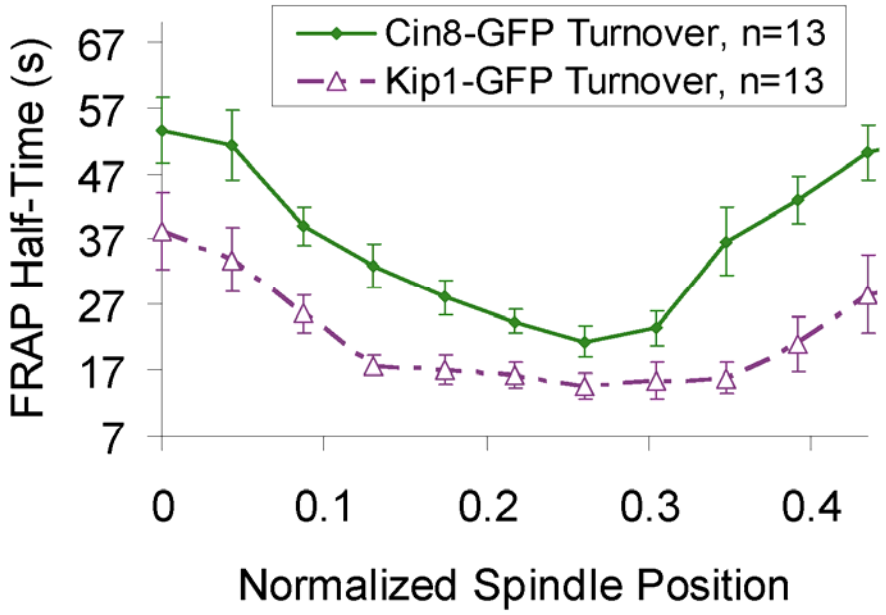

Experimental testing of the motor model: Cin8-GFP fluorescence distribution and turnover in benomyl-treated cells

In the motor model, motor detachment is largely mediated by disassembling kMTs. If the kMT disassembly rate were reduced, then motors should, on average, be bunched closer toward kMT plus ends and their turnover rate on the spindle should decrease. To test the first prediction, low-dose benomyl was used to experimentally stabilize kMT plus-end dynamics [60], and then Cin8-GFP distribution was measured relative to kinetochores. As shown in Fig. C.13A, Cin8-GFP clusters are nearly coincident with kinetochores in conditions of low-dose benomyl. To quantitatively measure the mean positions of motor and kinetochore clusters, fluorescence centroids were calculated as previously described [209] for Cin8-GFP and Ndc80-Cherry in each half-spindle. The distance between Cin8-GFP and Ndc80-Cherry centroids in control media was 54 ±2 nm (mean ± s.e.m., n=154 half-spindles), while the centroid separation was 19 ±3 nm in benomyl (n=78 half-spindles, $p<10^{-37}$; distribution shown in Fig. C.13A).

To test the second prediction, we measured the Cin8-GFP FRAP half-time in control and benomyl-treated cells. As predicted by the motor model and shown in Fig. C.13B, the $t_{1/2}$ for Cin8-GFP FRAP is increased where kMT plus-ends are located in benomyl-treated cells as compared to controls. We conclude that the experimentally observed Cin8-GFP distribution and dynamics are sensitive to kMT plus end dynamics, both of which are explained in the motor model by the assumption that motors fail to remain attached to shortening kMT plus ends. Furthermore, the observed motor sensitivity to kMT plus end assembly dynamics indicates that motors interact frequently with kMT plus ends.

FIGURE C.13: Cin8-GFP localization and dynamics in benomyl-treated cells (A) Cin8-GFP is nearly co-localized with kinetochores in spindles with benomyl-stabilized kMT plus-ends, as shown by the distribution of centroid spacing between Cin8-GFP and Ndc80-Cherry in spindles with dynamic kMT plus-ends (control media, indigo), and stabilized plus-ends (Benomyl, cyan). Modeling suggests that the observed off-set between kinetochore fluorescence and Cin8-GFP in conditions with dynamic kMT plus-ends is due to increased motor off rates from depolymerizing kMT plus-ends. (scale bar 500 nm) (B) Benomyl-stabilized kMT plus-ends results in Cin8-GFP FRAP half-times that are increased in the location of plus-end clustering relative to control cells. (error bars, s.e.m.)

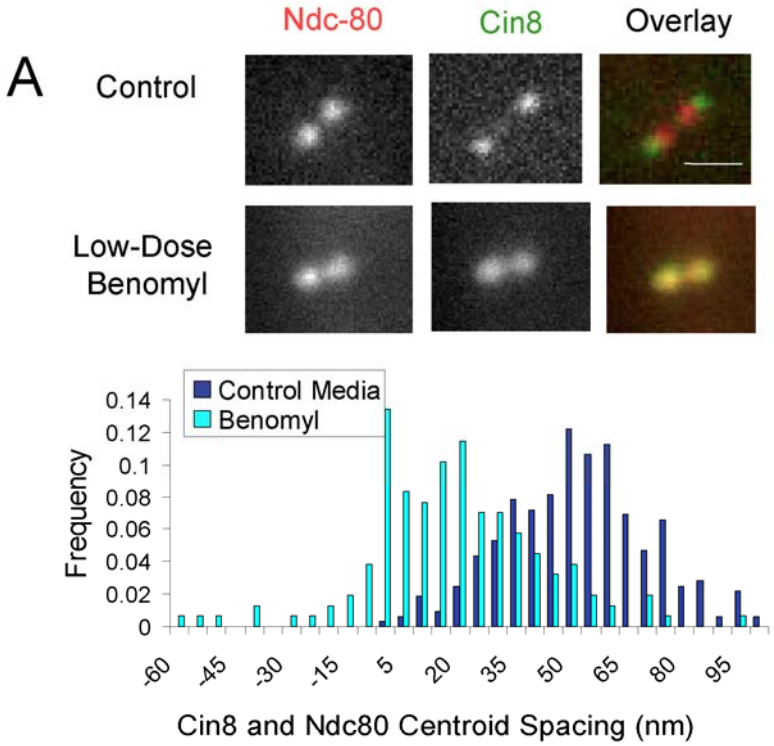

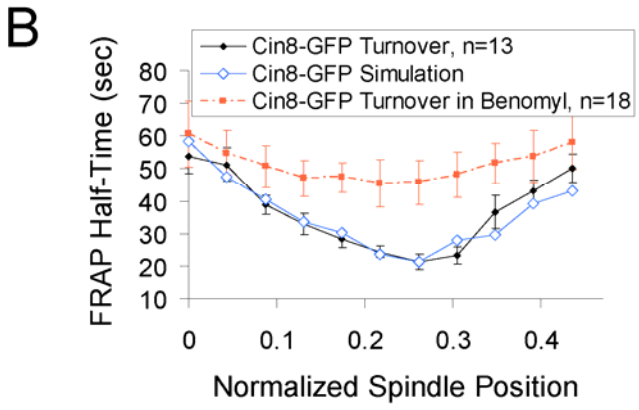

A "Self-Organized" Model: Kinetochore Organization via Kinesin-5 mediated MT Disassembly

In previous work, [29, 50] kMT dynamics were modeled using an imposed "catastrophe gradient". Although the kMT dynamics simulations in Figures 5.1-5.5 were performed as described previously, the results in Fig. 5.6 and Fig. C.14 are the result of a "self-organized" model (see also supplemental movie 5), in which the presence of kinesin-5 motors on kMT plus ends is assumed to increase the catastrophe frequency proportionally to their number at the plus end (see detailed description of model below in the methods section). We have used this self-organized model to test our hypothesis that, by this mechanism, kinetochores could self-organize into the characteristic bi-lobed metaphase configuration of kinetochores.

Typical results from the "self-organized" model are shown in Fig. C.14(A). In this model, both experimental wild-type Cin8-GFP localization as well as the experimentally observed bi-lobed Cse4-GFP kinetochore organization are qualitatively reproduced in simulation. In addition, by reducing the number of motors, such as in a *cin8Δ* mutant in which only Kip1p remains, the gradient in motor localization at the kinetochore is disrupted (Fig. C.14B), and thus the experimentally observed disruption of kinetochore disorganization is qualitatively reproduced by the model (Fig. C.14C). Similarly, by increasing the number of motors in the simulation, such as in the Cin8p-overexpression experiment, the experimentally observed depolymerization of kMTs can be qualitatively reproduced by the model (not shown). Therefore, it is no longer necessary to externally impose a catastrophe gradient on the system, but rather the catastrophe gradient is now a natural consequence of a model where kinesin-5 motors walk to plus ends and promote net disassembly upon arrival. Note that the model makes no assumption about whether the motor itself promotes disassembly, or whether it requires a cargo.

FIGURE C.14: Self-Organized model (A) Experimental Cse4-GFP localization as well as the experimental Cin8-GFP distribution is qualitatively reproduced via a "self-organized" model in which Cin8p promotes net disassembly at the kMT plus end. (scale bar, 1000 nm) (B) By altering the number of simulated motors, the gradient in motor presence at the kinetochore is reduced (indigo line, simulating *cin8Δ* mutants), and (C) kinetochore organization is disrupted, similar to experimental results (scale bar, 1000 nm).

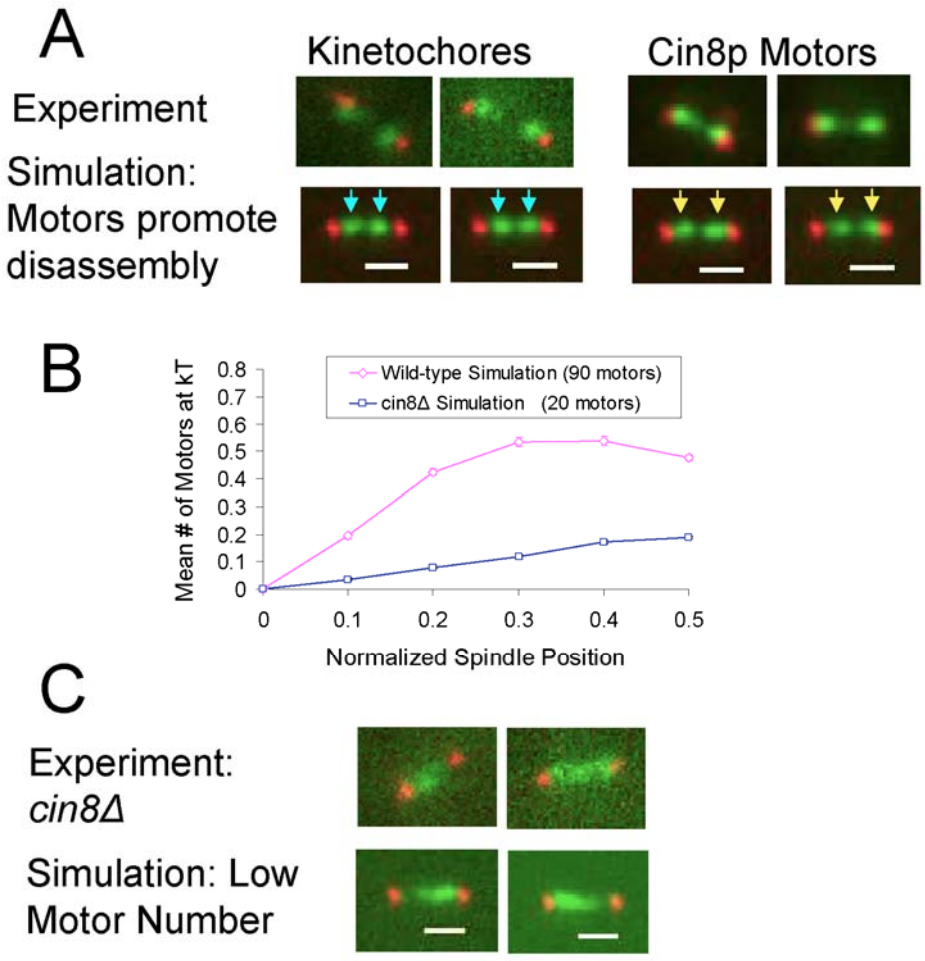

Simulation Methods

A stochastic simulation was developed to account both for dynamic kMT plus-ends in the yeast metaphase spindle as well as for dynamic plus-end directed kinesin-5 motors that interact with MTs, as described below.

Microtubule Dynamics: Model Description

As was previously described [29, 50], a Monte Carlo simulation was developed and run in MATLAB to simulate kMT plus-end dynamics. The model assumes that kMT plus-ends remain in one of two states, growing or shortening, at all times. Thus, their dynamics can be fully described via the four parameters of dynamic instability, where V_g and V_s describe rates of kMT plus-end polymerization and depolymerization, respectively, and k_c and k_r describe the probability of switching between these two states. Here, k_c is defined as catastrophe frequency, which is the rate at which a kMT plus-end will switch from a growing state to a shortening state, and k_r is defined as rescue frequency, which is the rate at which a kMT plus-end will switch from a shortening state to a growing state. Previously, we found that there does not exist a constant set of dynamic instability parameters that is able to reproduce kMT plus-end localization in the yeast metaphase spindle [29]. Rather, catastrophe and/or rescue frequency vary spatially along the length of the spindle in the model, with net assembly promoted for kMT plus-ends near the pole, i.e. when kMTs are relatively short, and net disassembly promoted for kMT plus-ends near the equator, where kMTs are relatively long [29, 50].

All wild-type simulations of kMT plus-end dynamics were run with models and parameter values as previously described [50], and as shown in Table C.2. Here, rescue frequency is regulated by tension between sister kinetochores, as measured by the separation distance along the spindle axis between the tips of sister kMTs. Thus, this tensile force, $F_{tensile}$, is defined as:

$$F_{tensile} = \rho^{*}(s - s_0) \qquad (1)\ [29]$$

Where ρ* is a Hookean spring constant for chromatin connecting sister kMTs with units μm^{-1}, s is the separation distance between the tips of sister kMTs, and s_0 is the rest length of the chromatin. Using this equation, rescue frequency is calculated as a function of tension between sister kinetochores at every time step using the equation:

$$k_r = k_{r,0} e^{(F_{tensile})} \qquad (2)[29]$$

In addition, catastrophe frequency in all simulations (except the final "self-organized" model) was calculated using a theoretical "chemical gradient" model, where k_c varies according to:

$$k_c = k_{c,0} + \beta c_B \qquad (3)[29]$$

Where β is an adjustable parameter that describes the magnitude of the catastrophe promotor's effect, and c_B is the concentration of a theoretical catastrophe promoter. In the model, c_B varies by spindle position via a reaction-diffusion process, in which the concentration of the theoretical catastrophe promoter is highest at the spindle equator and lower elsewhere [29].

kMT dynamics in *CIN8* deletion experiments were simulated by modifying the catastrophe gradient model to decrease the parameter β, with model parameters as listed in Table C.2. The best fit between experiment and theory was achieved with values for MT plus-end growth and shortening rates that were slightly higher than in wild-type simulations (Fig. 5.2C and Table C.2), which decreases FRAP half-times at all spindle positions in simulations of the *cin8Δ* GFP-Tub1 FRAP experiment. These results suggest that Cin8p may also have a slight effect on the suppression of plus-end growth and shortening velocities.

The parameters in Table C.2 were used for simulations across all experiments as shown in Figures 5.1-5.5.

Non-kMTs (ipMTs) were modeled both using non-dynamic plus-ends, and using a model in which $k_r >> k_c$, with constant values of V_g and V_s. The model for ipMT dynamics did not have a significant effect on simulation results where kMT density is high (not shown, but reviewed in [108](supplemental material)).

TABLE C.2: Model for kMT Dynamics: Simulation Parameters

Category	Symbol	Description	Wild-Type	*cin8Δ*
Parameter	ρ^*	Chromatin spring constant (μm^{-1})	0.9	0.9
Parameter	$k_{r,0}$	Basal rescue frequency (min^{-1})	9	9
Parameter	$k_{c,0}$	Basal catastrophe frequency (min^{-1})	0.25	0.25
Parameter	β	Catastrophe sensitivity factor for theoretical catastrophe promoter at kinetochore ($M^{-1}min^{-1}$)	680	300
Parameter	Vg	Growth Rate (Vg) ($\mu m/min$)	1.2[a]	1.9[a]
Parameter	Vs	Shortening Rate (Vs) ($\mu m/min$)	1.2[a]	1.9[a]
Parameter	N_{kMT}	Number of kMTs	32	32
Variable	k_c	Catastrophe Frequency (min^{-1})	0.25-30[b]	0.25-15[b]
Variable	k_r	Rescue Frequency (min^{-1})	9-24[c]	9-13[c,d]

[a]In all simulations, growth and shortening rates are assumed to be equal. GFP-Tub1 FRAP experiments constrain growth and shortening values in both wild-type and *cin8Δ* experiments.
[b]Catastrophe frequency depends on spindle position of kinetochore, as described in equation (3) and [29]
[c]Rescue frequency is dependent on distance between sister kinetochores, such that high tension at the kinetochore promotes rescue, as described in equations (1) and (2) and (Gardner et al., 2005).
[d]In the *cin8Δ* simulation, tension-dependent rescue frequency decreases near to basal (no tension) values as a natural consequence of reduced sister kinetochore separation distances.

Kinesin-5 Motor Dynamics: Model Description

A simulation was developed to explicitly model individual kMT dynamics as well as the dynamics of individual MT-associated homotetrameric kinesin-5 molecular motors, based on known properties of the motors [111, 112, 133, 134]. Each kinesin-5 homotetramer is modeled as a bipolar motor that has two motor "heads", one at each end of the complex, with each "head" consisting of a pair of motor head domains. As shown schematically in Table C.3, one motor head stochastically attaches to an individual MT (at rate k_{on}*), and subsequently crosslinks via the other head to an adjacent MT (at rate αk_{on}*). Once bound, motor heads move toward their respective MT plus ends (at velocity v), and eventually detach (each head detaching at rate k_{off}). The motor velocity is slowed by opposing force (Table C.3) [123, 133], and motor off-rate increases with increasing force [133, 210]. Additional model assumptions are reviewed in Table C.4, with variables and parameter values specified in Tables C.5 and C.6.

Load-dependent motor velocity results in two distinct motor behaviors depending on whether motors are crosslinking parallel oriented or anti-parallel oriented MTs. As shown in Table C.3 (top), motor heads crosslinking anti-parallel oriented MTs walk in opposite directions, stretching the motor and quickly increasing load. Thus, these motors are stationary on the spindle, and tend to concentrate in locations with increased density of anti-parallel MTs, such as at the spindle equator (supplemental movies 3,4). Because of the increasing load, motors bound to antiparallel MTs tend to detach more rapidly than motors bound to parallel MTs. In contrast, motor heads crosslinking parallel-oriented microtubules walk together towards the plus-ends of both microtubules (Table C.3 (top), supplemental movies 3,4). In this case, these motors do not stretch or generate load, but rather walk along the spindle at the unloaded motor velocity. In simulation, it is this behavior that results in the experimentally observed concentration of motors near the plus-ends of kMTs in the yeast mitotic spindle. Once one of the motor heads reaches the plus end, the head is assumed to travel at the rate of MT plus end growth, which is likely to be slower than the unloaded motor velocity [70, 74, 110, 123]. The differing rates for each of the two heads results in motor stretching and thus increases the detachment rate. If a plus end undergoes catastrophe, then any motor heads that are at the plus end are assumed to detach. Motor heads that encounter shortening plus ends are also assumed to detach.

TABLE C.3: Model for Kinesin-5 Motor Behavior

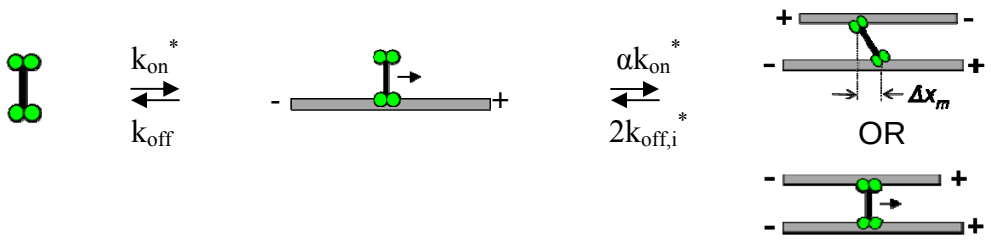

Behavior	Model Equation	Variables	Parameters
Motor Head Attachment	$k_{on}^* = k_{on}$ [Tubulin]	k_{on}^* = motor on-rate constant	[Tubulin] = polymer concentration α = second head on-rate correction
Motor Head Movement	$v_i = v_u(1- F_{L,i}/F_{stall})$	v_i = motor velocity $F_{L,i}$ = motor tension	F_{stall} = stall force v_u = unloaded velocity
Motor Stretching	$F_{L,i} = \rho_{motor} \Delta x_m$	Δx_m = stretch distance	ρ_{motor} = spring constant
Motor Head Detachment	$k_{off,i}^* = k_{off} e^{(FL,i / Fc)}$	$k_{off,i}^*$ = motor off-rate constant (force dependent)	F_c = critical force k_{off} = unloaded off-rate constant

Kinesin-5 Motor Dynamics: Model Assumptions

Model assumptions for simulation of kinesin-5 motor dynamics are summarized in Table C.4, along with references and explanations.

TABLE C.4: Model Assumption Summary

Behavior	Model Assumption	Reference or Explanation
First Head Motor Attachment	Weighted random attachment of first head along spindle according to local MT density	Diffusion in the nucleoplasm is expected to be fast relative to motor rebinding time. In simulation, x_{rms} ~ 2 μm prior to motor rebinding, length of spindle ~1.5 μm.
Second Head Motor Attachment	Random attachment of second head within a 40 nm radius of first head due to torsional flexibility of motor	[134] [112] [111]
Motor Attachment and MT Polarity	No preference of motor attachment to parallel vs anti-parallel attachments, or to kMTs vs the non-kMTs that generally run the length of the spindle (interpolar MTs)	[112] In general, the metaphase Cin8p motor distribution roughly mirrors MT density rather than enrichment of motors at the midzone
Motor Movement: Force	Motor heads move according to a force-velocity relationship	[133]
Motor Movement: Compliance	Motors act as Hookean springs	[211]
Motor Movement: Velocity	Singly-attached motors move at unloaded velocity	By definition
Motor Detachment: Both heads Attached to Adjacent MTs	Motor detachment is force dependent	[210] [133] [212] (for review, see [213])
Motor Detachment: Single Attachments	Singly-attached motors detach at unloaded off-rate	By definition

Kinesin-5 Motor Dynamics: Parameter Value Summary

All simulated parameter values are summarized in Table C.5, along with references and explanations. Average numbers of kinesin-5 motors on the mitotic spindle were experimentally determined for this study via analysis of fluorescence intensity (as described in [142]). We found that ~50 Cin8p motors and ~20 Kip1p motors are bound at any given time to the spindle.

In addition, Cin8p FRAP studies generally constrained motor off-rates in the simulation. Here, the model value for k_{off} was a 'fitting parameter' that was adjusted to reproduce Cin8-GFP spindle localization and FRAP half-times. For Cin8p movement along astral microtubules, the motor appears to processively walk along astral microtubules for 30-60 seconds (500-1000 nm), while the single-head k_{off} modeling parameter would predict single-head run lengths of 3-4 seconds. Because Cin8p is a homotetrameric crosslinking motor, though, motors with a relatively low individual head processivity may tend to rebind to a nearby MT while the second head remains attached, increasing the observed effective processivity of the motor [133]. Thus, it may be that motors observed walking along astral microtubules are in fact crosslinking two microtubules. Consistent with this interpretation of the results, recent *in vitro* studies measured a k_{off} of 12 sec^{-1} for Eg5, which is larger than the Cin8p simulated value of 0.3 sec^{-1}, even though the measured k_{off} on astral microtubules is ~0.02 sec^{-1} [133]. Therefore, the "effective" motor processivity may be increased due to either motor crosslinking or differing biochemical conditions in the various intracellular compartments/in vitro assays.

A free parameter (α) was defined to account for the diffusion and attachment of a second Kinesin-5 motor head once the first head has attached. The value of this parameter depends on the density of microtubules near the first-head attachment site, and is calculated as follows:

$$\alpha = \frac{\rho_M}{3} \qquad (4)$$

where α is the correction factor, and ρ_M equals the number of neighboring MTs (within a 40 nm radius in the yz plane) that are of sufficient length to allow for crosslinking of the motor at the first head location. In this way, the second head on-rate constant is moderately increased as compared to the first head on-rate constant, depending on the number of MTs in the vicinity of the first head attachment point.

A velocity of 50 nm/sec was used for Cin8p in simulations, to be consistent with *in vitro* measurements of Cin8p motility [123]. We hypothesize that the observed motor motility on astral MTs may be limited by MT polymerization, an interpretation that is consistent with the *in vivo* data obtained at rapid temporal resolution on Cin8p motors in the spindle (Fig. C.9). The value used in simulation is similar to the measured values for motor motility in the spindle (Fig. C.9).

All remaining parameter values are based on previous studies, as described in Table C.5.

Kinesin-5 Motor Dynamics: Variable Summary

Typical values for model variables, resulting from the equations in Table C.3 and the parameter values described in Table C.5, are listed in Table C.6. In general, modeling results were highly sensitive to the rules for motor behavior at kMT plus-ends, and it was necessary that parallel-attached motors were motile in order to reproduce experimentally observed motor localization. Simulation of motor FRAP experiments constrained motor off-rates, although on-rates are high enough that many of the simulated motors are attached throughout the simulation. Thus, parameter values and the resulting variable values were not highly constrained to narrow ranges, and it was possible to reproduce both motor localization and FRAP experiments with physically reasonable numbers.

TABLE C.5: Model Parameter Value Summary

Symbol	Description	Typical Value	Reference or Source
v_u	Unloaded Motor Velocity	50 nm/sec	[123] 57 nm/sec
F_{stall}	Motor Stall Force	6 pN	[133], 5-7 pN
ρ_{motor}	Motor Spring Constant	0.5 pN/nm	[214]
k_{off}	Unloaded Motor Off-rate Constant	0.3 sec^{-1}	Model Fit Parameter (via FRAP)
k_{on}	Motor On-rate Constant	1 $\mu M^{-1}sec^{-1}$	[215]
N_m	Number of Cin8p Spindle Motors	50	This study (via counting)
α	Second-head on-rate correction	0 – 8	Free parameter, depends on number of MTs in 40 nm attachment radius
r_M	Radius of 2nd Motor Head attach point relative to 1st Motor Head attach point	40 nm	[134] (53 nm)
F_c	Critical Force for force-dependent off-rates	6 pN	[133], 5-7 pN [210], 2 pN

TABLE C.6: Model Variable Summary

Symbol	Description	Typical Value
v_i	Velocity of i^{th} motor	0-50 nm/sec
$N_{m,att}$	Number of attached motors	~50
$F_{L,i}$	Load force on i^{th} motor	0 – 6 pN
$\Delta x_{m,i}$	Stretch of i^{th} motor in the x direction	0 - 30 nm
$k_{off,i}^*$	Force corrected off-rate constant for i^{th} motor	0.3 – 1.0 sec^{-1}
$k_{on,1}^*$	Pseudo first-order motor on-rate constant, 1st head	30-35 sec^{-1}
$k_{on,2}^*$	Pseudo first-order motor on-rate constant, 2nd head	0-500 sec^{-1}
[Tub]	Concentration of tubulin polymer in nucleus [=(1600 units/μm)x(total MT polymer length in μm), assuming a 1.5 μm diameter nucleus]	30-35 μM

Simulation Methods: "Self-Organized" Model

The effect of kinesin-5 motors on catastrophe frequency at kMT plus-ends is modeled according to the following:

$$k_c = k_{c,0} + \beta_m M_T \qquad (5)$$

where k_c is the catastrophe frequency for a given kMT plus-end, $k_{c,0}$ is the basal rescue frequency in the absence of kinesin-5 motors, M_T is the total number of kinesin-5 motors within 16 nm (1st or 2nd tubulin subunit) of the plus-end, and β_m is the sensitivity factor for the effect of motors on basal catastrophe frequency. Model parameter values and typical variable values for the results shown in Fig. C.14 and Fig. 5.6 are shown in Table C.7. Cin8p motor parameters and variables are as listed in Tables C.3-C.6. In addition to the model assumptions outlined in Table C.4, kMT plus-end catastrophe frequency is increased upon sister kinetochore crossing, which is unlikely to occur *in vivo* due to steric hindrance of kinetochores and chromatin [216].

TABLE C.7: "Self-Organized" Model for MT Dynamics: Simulation Parameters

Category	Symbol	Description	Wild-Type	*cin8Δ*
Parameter	$k_{c,0}$	Basal Catastrophe Frequency (no Motor) (min^{-1})	0.25	0.25
Parameter	β_m	Catastrophe Sensitivity Factor per Motor at Kinetochore (min^{-1})	20	20
Parameter	Vg	Growth Rate (μm/min)	1.2[a]	1.9[a]
Parameter	Vs	Shortening Rate(μm/min)	1.2[a]	1.9[a]
Parameter	N_{kMT}	Number of kMTs	32	32
Variable	k_c	Catastrophe Frequency (min^{-1})	0.25-30[b]	0.25-10[b]
Variable	M_T	Total Number of Motors at kinetochore	0.5±0.9[c] (out of 90 motors)	0.1±0.4[c] (out of 20 motors)[e]
Variable	k_r	Mean Rescue Frequency (min^{-1})	9-24[d]	9-13[f,d]

[a]In all simulations, growth and shortening rates are assumed to be equal.
[b]Catastrophe frequency depends on the number of motors near the kinetochore, as described in equation (5)
[c]mean±sd per kinetochore (typical in simulation)
[d]Rescue frequency is dependent on distance between sister kinetochores, such that high tension at the kinetochore promotes rescue, as in Gardner et al., 2005.
[e]In the *cin8Δ* simulation, Kip1p motors are still present, and so a smaller number of kinesin-5 motors are simulated.
[f]In the *cin8Δ* simulation, tension-dependent rescue frequency decreases near to basal (no tension) values as a natural consequence of reduced sister kinetochore separation distances).

TABLE C.8: Relevant Plasmids and Strains

Plasmid Name	**Description**	**Source**
pMA1214	*GAL1-CIN8* plasmid	M.A. Hoyt
pMA1186	*cin8Δ* plasmid	M.A. Hoyt
pB1585	3xGFP plasmid	D. Pellman
pRS406	mCherry-*TUB1* plasmid	S. Reed

Strain Name	**Description**	**Source**
YEF473A	*MATa trp1-63 leu2-1 ura3-52 his3-200 lys2-801*	J. Pringle
KBY2012	As YEF473A except *cse4::HYG SPC29-CFP-KAN pKK1*	C. Pearson
KBY2270	As YEF473A except *cin8::LEU2 cse4::HYG SPC29-CFP-KAN pKK1*	This Study
KBY2129	As YEF473A except *GFP-TUB1::leu2_1, SPC29RFPKAN*	C. Pearson
KBY2275	As YEF473A except *cin8::LEU2 GFP-TUB1::leu2_1,SPC29RFPKAN*	This study
KBY7001	As YEF473A except *kip1::NAT cse4::HYG SPC29-CFP-KAN pKK1*	This Study
KBY8030A	As YEF473A except *mCherry-TUB1:URA3*	This Study
KBY8023	As YEF473A except *Cin8-GFP:HIS3MX6, NDC80-Cherry:KAN*	This Study
KBY8052	As YEF473A except *CIN8-GFP:HIS3, SPC29RFP:HYG*	This Study
DCB 411.1	As YEF 473A except *CIN8-3GFP-HIS3 mCherry-TUB1-URA3*	This Study
DCB 421.1	As YEF473A except *CIN8-NLSdelta-3GFP-HIS mCherry-TUB1-URA3*	This Study
DCB 430	As YEF473A except *pGAL-CIN8-HIS3 cse4::HYG SPC29-CFP-KAN pKK1*	This Study
KBY8033A	As YEF473A except *pGAL cin8:HIS GFP-TUB1::leu2_1, SPC29RFPKAN*	This Study
DCB 204.1	As YEF473A except *HHT1::TRP1 KAN-GAL1p-HHT2 ura3::NUF2-GFP-URA3 SPC29-RFP HYG*	D. Bouck
DCB 208.1	As YEF473A except *HHT1::TRP1 KAN-GAL1p-HHT2 ura3::NUF2-GFP-URA3 SPC29-CFP-HIS3 cin8::LEU2*	D. Bouck

APPENDIX D

SUPPLEMENTAL MATERIAL: MICROTUBULE ASSEMBLY DYNAMICS AT THE NANOSCALE

(Reprinted with permission from *Current Biology* 41(2) (2007))

Supplemental Methods: Simulation of Force Clamp Experiment

The microtubule assembly dynamics simulation as developed by VanBuren *et al*.[87, 156] was adapted to simulate assembly under load, applied by laser tweezers in a microfabricated chamber. In general, this required updating the model to include (1) assembly of a thermally-driven microtubule under compressive loading in the presence of a rigid barrier, and (2) simulation of the data collection via bead tracking. All additional simulation parameters and methods are as described previously [87, 156]. Similar to previous work, it was assumed that all microtubules had 13 protofilaments in a B-lattice.

Simulation Coordinate System and Variables

In order to simulate the experimental assay and data collection method, a coordinate system was defined such that the bead, optical trap, and fabricated barrier positions could be tracked relative to length changes of the simulated microtubule (Table D.1, Figure D.1).

TABLE D.1: Coordinate System and Simulation Variables

Variable	Description	Definition
x	Axis along length of microtubule	x=0 at microtubule minus-end
x_{wall}	Position of microfabricated wall	x_{wall} = x distance from microtubule minus-end to wall
$L_{pf,i}$	Length of protofilament	$L_{pf,i}$ = x distance from microtubule minus-end to tip of each individual protofilament (i=1 to 13)
L_{MT}	Length of microtubule	L_{MT} = x distance from microtubule minus-end to the tip of the longest protofilament at the plus-end
$L_{gap,i}$	Gap between individual microtubule protofilament tips and the microfabricated wall	$L_{gap,i}$ = x distance from individual protofilament tips (i =1 to 13) to microfabricated wall
x_{trap}	Position of optical trap	x_{trap} = x distance from microtubule minus-end to center of trap
x_{bead}	Position of microtubule-attached bead	x_{bead} = x distance from microtubule minus-end to center of bead

FIGURE D.1: Coordinate system for simulation of microtubule dynamics under compressive load. The frame of reference is the microtubule, with the origin at the point of bead attachment (i.e. the minus end). For simplicity, the situation depicted here is for the lead protofilament, which requires an 8 nm gap to open up to allow tubulin subunit addition. Lagging protofilaments will require smaller gaps, and if they trail the lead protofilament by more than 8 nm, then they do not require a gap at all and so are unaffected by the presence of the wall. See text for further details.

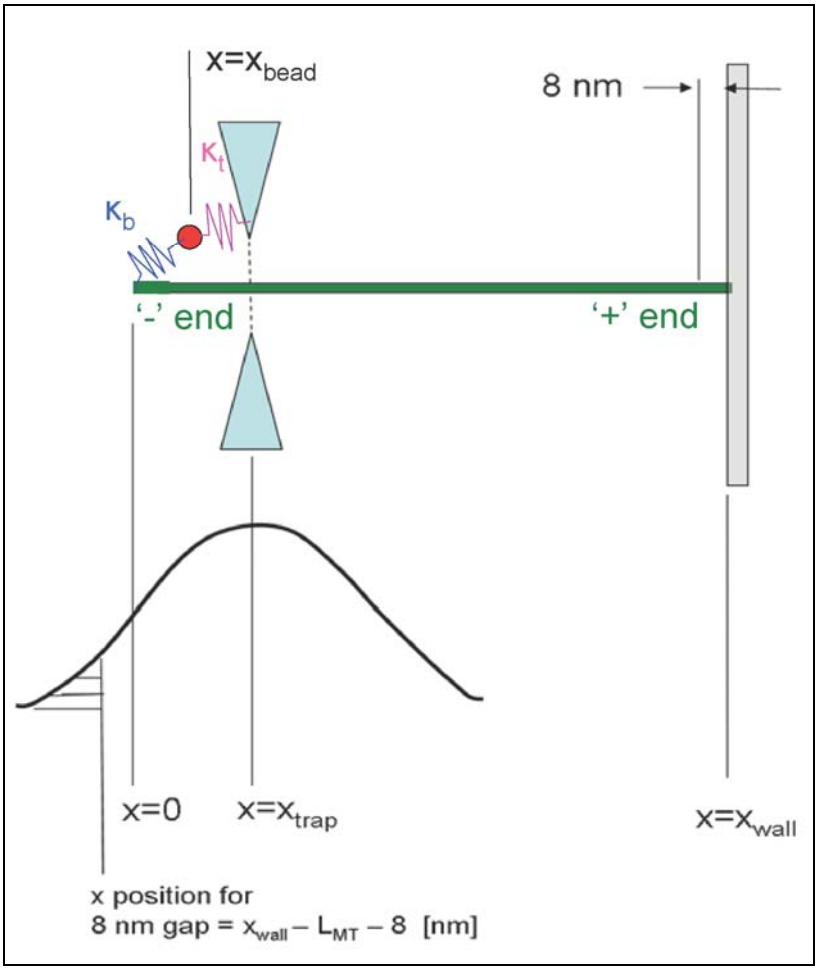

In this system, the microtubule-bead complex moves relative to the wall as a result of the optical force and thermal forces. The frame of reference chosen here is the microtubule with the origin chosen to be at the point of bead attachment, which is referred to for simplicity as the "minus end", even though the microtubule in practice extends beyond the attachment point. However, this minus-end extension does not affect the force balance calculation, and it is the length changes at the plus end that are of interest in the simulation and experiment. The minus end defines the origin in the

coordinate system, and positive values of x are in the direction of the plus end of the microtubule. As a result of thermal fluctuations, the wall is almost always further from the origin than the plus end of the microtubule ($x_{wall} > L_{MT}$), although strictly speaking if the leading protofilament is transiently in direct contact with the wall, then $x_{wall} = L_{MT}$. We considered the microtubule to be incompressible so that x_{wall} can never be less than L_{MT}. The variables listed in Table D.1 are shown in Figure D.1 relative to the position of the growing microtubule (green). A bead (red) is attached via a linear spring (blue) to the microtubule (green) at x=0, which is stretched to a position $x = x_{bead}$ by the optical force on the bead. An optical trap (cyan) centered at $x = x_{trap}$ acts as a linear spring (magenta) to apply a force on the microtubule in the direction of the barrier and constrain bead movement relative to the microtubule. Together, the trap stiffness (κ_t, magenta) and the bead linkage stiffness (κ_b, blue) define a series compliance that elastically links the optical trap to the microtubule minus end to create a harmonic potential well in the x-direction. If the trap center is displaced from the minus end ($x_{trap}>0$), then there is an elastic force on the microtubule that pushes the microtubule toward the wall. Addition of a tubulin subunit at the plus-end of an individual microtubule protofilament requires that the gap between the wall and the i^{th} protofilament ($L_{gap,i}$) is large enough to allow an ~ 8 nm tubulin dimer to enter (shown in Figure D.1 as 8 nm gap). Each protofilament has a length $L_{pf,i}$ and the length of the microtubule is defined as $L_{MT}=\max(L_{pf,i})$. The gaps between the individual protofilament tips and the wall open up as a result of thermal forces that drive the microtubule away from the wall, thus allowing polymerization under compressive load.

Simulation of Microtubule Assembly Under Load

In order to simulate microtubule assembly as the tip of the microtubule is forced against the microfabricated barrier via the bead/trap linkage, the probability of a gap opening up between the barrier and the tip of each microtubule protofilament that is large enough to add a tubulin dimer is calculated. For a thermally-driven spring, the probability density function obeys a Gaussian, which is experimentally observed for optical traps [217, 218]. In the simulation, the Gaussian has mean = x_{trap}, and variance

$$\sigma^2 = k_B T / \kappa_{effective} \qquad (1)$$

where $\kappa_{effective}$ is the effective spring constant of the bead/trap microtubule linkage. The effective spring constant of the bead/trap microtubule linkage is calculated based on two springs connected in series, and is given by

$$\kappa_{effective} = \kappa_b \kappa_t / (\kappa_b + \kappa_t) \qquad (2)$$

where κ_b is the spring constant of the bead/microtubule linkage, and κ_t is the spring constant of the bead in the trap.

Via random sampling from the Gaussian probability density function, the stochastic effect of gap opening probability on the event time for individual tubulin

heterodimer addition (by protofilament) is then calculated. The probability that the i^{th} protofilament will be at least a distance of 8 nm from the wall is given by

$$p_i = \frac{\int_{-\infty}^{x_{wall}-L_{pf,i}-8nm} f(x)dx}{\int_{-\infty}^{0} f(x)dx} \qquad x_{wall}\text{-}L_{pf,i} \le 8 \text{ nm} \qquad (3)$$

$$p_i = 1 \qquad x_{wall}\text{-}L_{pf,i} > 8 \text{ nm} \qquad (4)$$

where f(x) is the Gaussian probability density function with mean x_{trap} and variance σ^2 (as described above). The event time for each protofilament, t_i, is then calculated using

$$t_i = -ln(rand)/(p_i\, k^*_{on}) \qquad (5)$$

where k^*_{on} is the pseudo first-order rate constant for tubulin addition to the protofilament tip when there is no barrier ($k^*_{on}=k_{on}$[GTP-tub]), and *rand* is a uniformly distributed, uncorrelated random number over the range 0 to 1. These event times are then used as described by VanBuren *et al [87, 156]* to stochastically simulate microtubule assembly, with model parameters as listed in Table D.2 and described previously.

TABLE D.2: Model Parameters

Parameter	Description	Value
[GTP-tub]	Free GTP-Tubulin concentration	5.3 x10^{-6} M
k_{on}	Tubulin on-rate constant	4x10^6 $M^{-1}sec^{-1}$
$k_{hydrolysis}$	Hydrolysis rate constant	0.95 sec^{-1}
ΔG^{0*}_{Long}	Longitudinal chemical bond energy (tubulin polymer)	-6.8 k_BT
ΔG^{0}_{Lat}	Lateral chemical bond energy (tubulin polymer)	-5.7 k_BT
κ_b	Spring constant for bead-microtubule linkage	0.021 pN/nm
κ_t	Spring constant for trap	0.021 pN/nm
T	Temperature	309 K

Simulation of Data Collection via Bead Tracking

In order to accurately reproduce experimental observation conditions, bead positions are simulated and updated every 0.2 ms. The procedure for this update is as follows:

a) The probability density function (mean= x_{trap}, variance calculated via $\kappa_{effective}$, as described above) of possible microtubule minus-end positions is randomly sampled, to account for microtubule diffusion away from the wall in the potential well defined by the optical trap (positions where x<0).

b) Then, given the microtubule minus-end position and the trap position, a "rest" position of the bead is calculated. The entire (Gaussian) probability density function of available bead positions relative to the microtubule tip is then randomly sampled using a probability density function with the mean equal to the calculated "rest" position of the bead and the variance calculated via $\kappa_{effective}$, as described above.

c) Finally, error in bead measurement by the microscope-quadrant photodetector system was accounted for by adding Gaussian white noise with mean zero and standard deviation equal to the experimentally measured error in bead location (1 nm).

Finally, the simulation accounted for trap position reset (every 100 ms, used to maintain force clamp). In the case of a set point force (F), the trap position was reset every 100 ms (i.e. at 10 Hz) in the simulation according to:

$$x_{trap} = F/\kappa_t + mean(x_{bead,j}) \quad for\ j=1:500 \qquad (6)$$

where j is the index of the last 500 observations obtained at 5 kHz. This resets the simulation such that trap location is set to a new position that is x_{trap} nanometers in front of the bead, so that the trap moves along with microtubule assembly, and disassembly, as it occurs at the plus end of the microtubule. We found that the mechanical energy minimization routine used in VanBuren et al. [87], which is the slowest part of the algorithm, could be turned off without significantly altering the tip structure or simulation output. In our previous study [87], we found that there was little curling during the growth phase, consistent with our findings here. Therefore, for the sake of speed, we simulated without mechanical energy minimization.

Supplemental Results: Raw data (5 kHz) temporally filtered to force clamp resolution (10 Hz)

The force clamp routine averages the 5 kHz data stream and updates the position of the force clamp at a rate of 10 Hz, with the result that each update is based on 500

individual bead position measurements. To illustrate the effect of temporal averaging, we show an example trace in Figure D.2 (below) where both panels show full 5 kHz data streams (gray) and low-pass filtered streams (software implemented, 5th order low-pass filter, 10 Hz cutoff, black) with the only difference being the amount of data presented. Variability is evident in the trace filtered to match force clamp resolution, though the absence of the force clamp results in underestimation of microtubule length changes.

FIGURE D.2: Low pass filtered stationary trap data demonstrating that variability in growth is evident in raw data taken with a stationary trap. The lower trace shows a subset of the data from the upper trace.

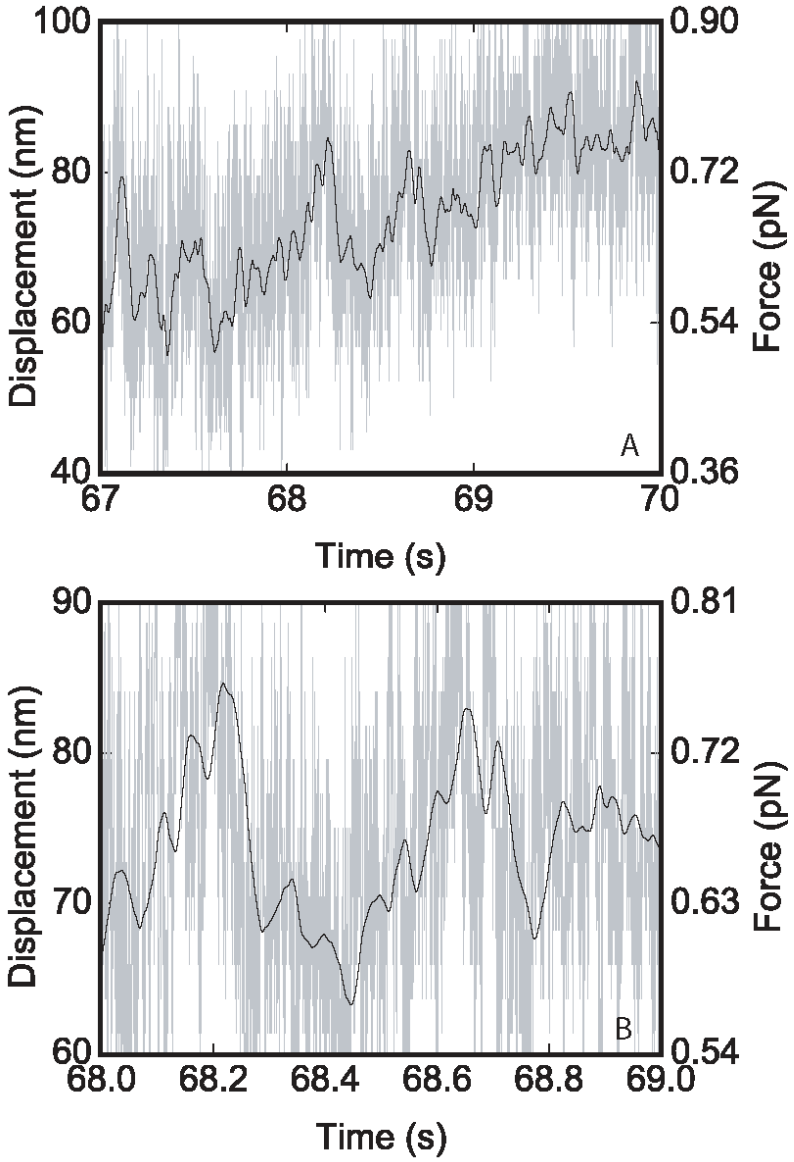

Supplemental Results: Additional traces of force clamp experimental data
All experimental data traces filtered at 10 Hz are sorted by force clamp value and summarized below.

FIGURE D.3: Experimental microtubule length-time traces (A) for short observation time 0-0.60 pN force clamp experiments. Traces are organized by force value, with lowest forces in the upper portion of the graph, and higher forces in the lower portion of the graph. (B) Experimental microtubule length-time traces for short observation time 0.62-1.0 pN force clamp experiments. Traces are organized by force value, with lowest forces in the upper portion of the graph, and higher forces in the lower portion of the graph.

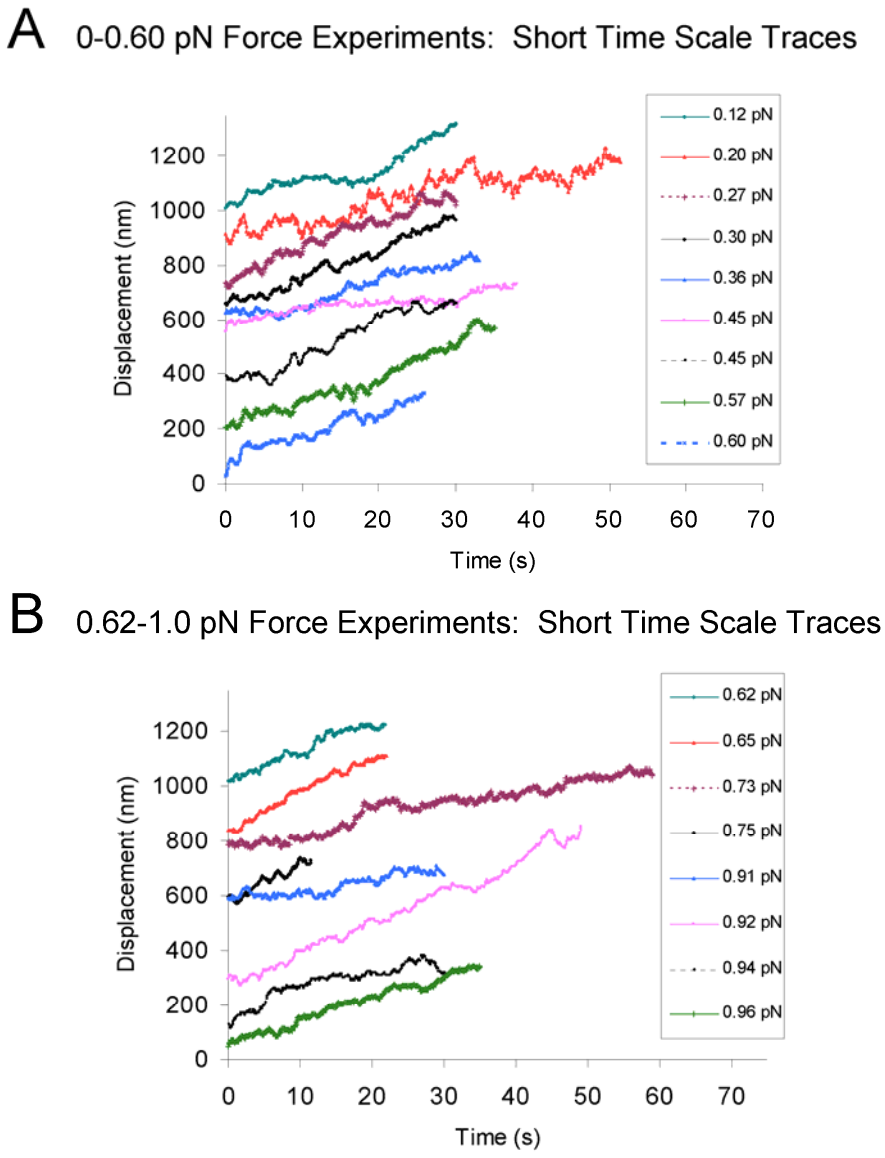

FIGURE D.4: Experimental microtubule length-time traces for long observation time 0-1 pN force clamp experiments. Traces are organized by force value, with lowest forces in the upper portion of the graph, and higher forces in the lower portion of the graph.

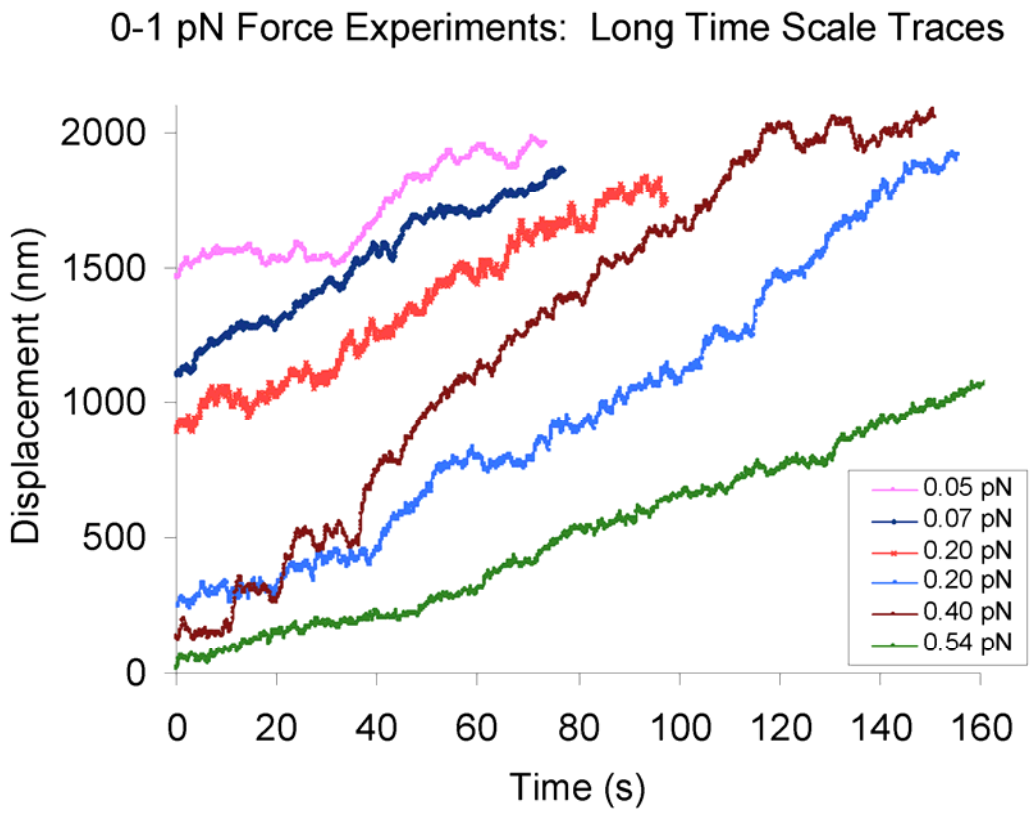

FIGURE D.5: Experimental microtubule length-time traces for 1.0 – 2.5 pN force clamp experiments. Traces are organized by force value, with lowest forces in the upper portion of the graph, and higher forces in the lower portion of the graph.

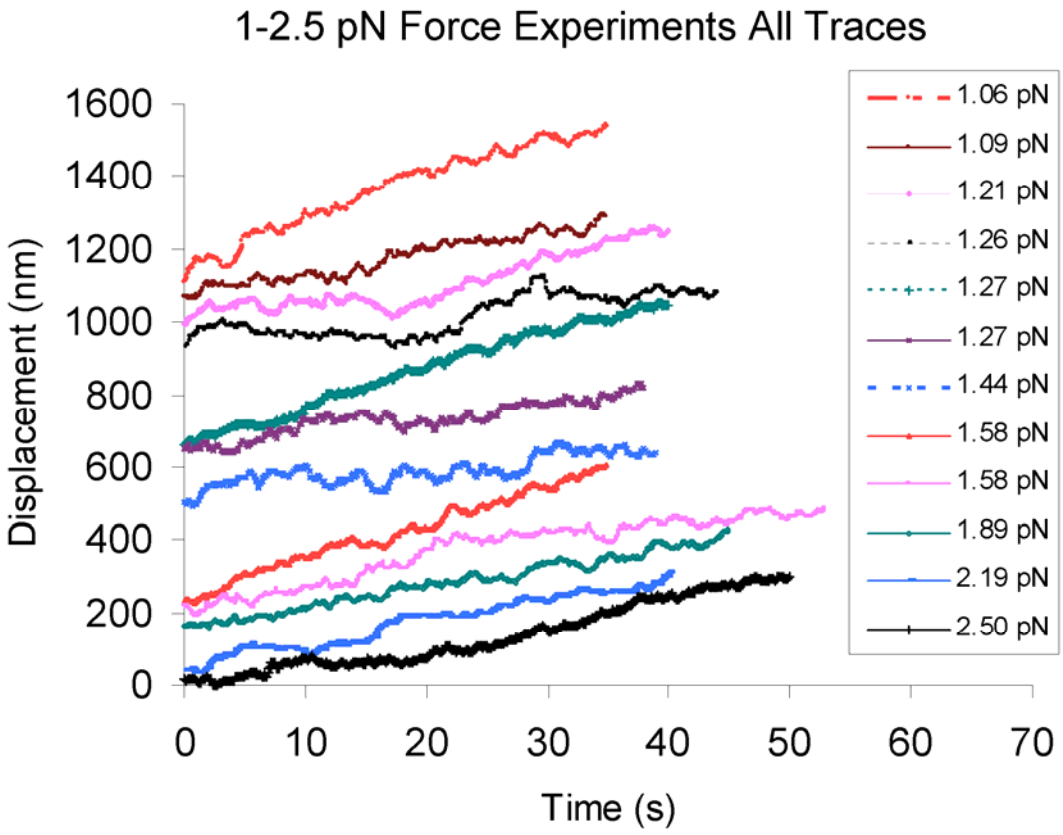

Supplemental Results: Example of apparent steps at low resolution

Figure D.6 shows an example of data that appears to be stepwise growth when viewed at the 25 Hz data rate of Kerssemakers *et al* [153], but is revealed to be rapid continuous growth at higher bandwidth (500 Hz). Similar to the data presented by Kerssemakers *et al* [153] , these data were taken using a stationary trap. For the most part we relied on the force clamp to eliminate the effect of the series compliance while Kessermakers *et al.* first measured the compliance of the linkage and then corrected for it. Hence, the changes in bead displacement shown in Figure D.6 reflect the microtubule length changes but underestimate their actual value. However, we can still use the high bandwidth data produced in stationary trap records to look for the appearance of stepwise growth by the addition of tubulin oligomers. In the left panel, low-pass filtered data (cut off=25 Hz, 5th order, software implemented Butterworth low-pass filter) is shown

resampled to 25 Hz (black trace with diamond markers) and super-imposed on data filtered with a 500 Hz cut-off (gray trace without markers). In this presentation, a step of ~20 nm is apparent in the filtered and resampled data. In the right panel, the portion of the higher bandwidth data (500 Hz cutoff) that contains the apparent step is shown on a longer x-axis. In this higher time resolution presentation, it is clear that this step is actually a period of fast microtubule growth. This analysis merely serves as an example showing how data processing or low bandwidth acquisition might lead to misinterpretation of a period of high speed growth as a stepwise addition to the polymer.

FIGURE D.6: Data averaging produces the appearance of step-wise growth which at higher time resolution is shown to be a period of rapid, continuous growth.

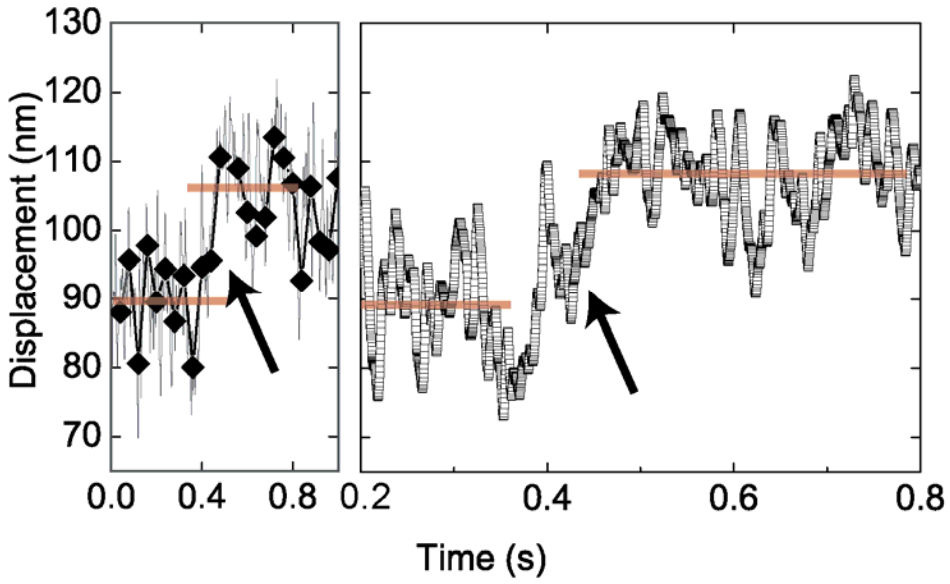

Supplemental Results: Lateral cap model simulations

A numerical model for microtubule dynamic instability that relied on a single layer of GTP-tubulin was previously developed by Bayley and coworkers [148, 219]. Termed the "Lateral Cap" model, this simulation assumed direct coupling of GTP-tubulin hydrolysis with addition of new tubulin subunits at the terminal end of a growing microtubule. Thus, a single layer of GTP-tubulin subunits in Lateral Cap model simulations could qualitatively account for the dynamic instability behavior of microtubules. Subsequently, further analysis of this model by Odde and coworkers [168]

verified that qualitative dynamic instability behavior could be reproduced by this model, including periodic deviations from linear growth. In order to compare results from the lateral cap model simulation for microtubule dynamic instability with our nanoscale experimental data, we ran simulations of dynamic instability using FORTRAN code that had been previously developed [168], and then added Gaussian white noise (mean = 0, standard deviation = 1 nm) to account for the experimental error in nanoscale microtubule length measurement. We then compared multiple time-step growth and shortening excursion lengths for nanoscale dynamic instability as predicted by the lateral cap model to experimental data for nanoscale excursion lengths (Figure D.7). We find that the blunt microtubule tip structure predicted by the single-layer GTP-cap model cannot account for the wide range of nanoscale growth fluctuations during microtubule assembly. Here, GTP-tubulin hydrolysis coupled to the distal addition of new tubulin subunits predicts a narrow range of growth and shortening excursions, similar to GMP-CPP stabilized microtubules.

FIGURE D.7: Lateral Cap model simulations as compared to nanoscale experimental microtubule assembly data. The single-layer lateral GTP-cap model is unable to account for the large fluctuations in nanoscale microtubule assembly that are observed experimentally.

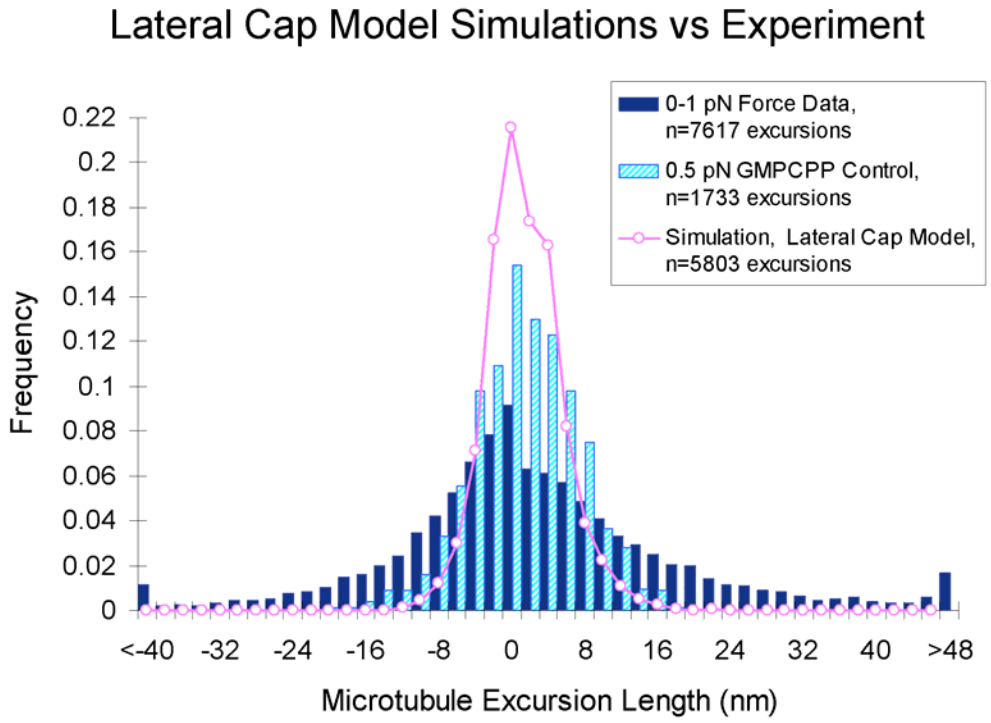

Supplemental Discussion: Assay variability in relation to growth-phase shortening events

Alternative explanations for the observed growth phase variability are most broadly rejected by the stable microtubule control data (main text; Figure 6.5, Table 6.2). The microtubule length standard deviation for GMP-CPP controls of 3.5 nm at measurement intervals of 0.1 second was, as expected, greater than that found when tracking a bead affixed to the coverslip surface ($\pm$1.5 nm, data not shown). The larger variation is principally due to increased thermal motion, but slow lengthening and shortening may contribute since the microtubule cannot be guaranteed to be entirely stable. Indeed, occasionally GMP-CPP microtubules were seen to exhibit very slow length changes that eventually became large enough for observation by DIC microscopy.

In addition to the relatively stable GMP-CPP microtubule control, physical arguments also reject likely alternate explanations: 1) the optical tweezers force clamp is unstable and as a result produces the perceived lengthening and shortening events, 2) the barriers themselves are sufficiently rough that the microtubule appears to shorten and lengthen as the tip moves about the surface and 3) microtubule bending fluctuations are large enough to make the microtubule appear to shorten and lengthen. In addition to the GMP-CPP controls showing that none of these possibilities is in fact an issue, each one can also be eliminated by further arguments.

In the case of the optical tweezers stability, tracking a bead attached to the surface of the coverslip demonstrates that the tweezers, and the routines that operate them, are capable of tracking a bead's position with an error of $\pm$ 1.5 nm (data not shown). This error is the result of the cumulative error of small air currents inside the optical tweezers enclosure, which cause very small error signals on the detector, and more significantly the fact that the bead was not perfectly immobilized but was capable of small movements while attached to the coverslip.

Simple physical arguments show that barrier roughness cannot be responsible for the shortening events. Imagine a rough barrier with several pits or crevices into which a microtubule can slide and remain. In some cases, as the microtubule grows, the tip will slip out of a local pit and the compressive force of the trap will push the microtubule down into the next minimum, eventually reaching a stable crevice. These events would then appear to be shortening. There are two fundamental arguments that reject this mechanism. First, the viscoelastic relaxation time of the microtubule-bead in the trap is ~2 msec. If the microtubule slipped from one crevice to a lower one, the travel time for the bead from its first equilibrium position to the lower would be of the order of the relaxation time. Since the force clamp routine updates every 100 msec, this event would appear as a sudden drop from one position to the next with a time interval of one update. This has never been observed in any of the records; all shortening events happen at speeds similar to growth: less than 50 nm/s.

A second argument starts with the observation that at some point the microtubule would reach a global minimum in the rough landscape. From there, it would first have to make an excursion from the minimum, against load, and then slip past the rough obstruction back to a new local minimum. At a typical clamping force of ~ 1.5 pN the energy necessary to work against the compressive force to a distance of 40 nm would be 60 pN-nm or equivalently ~15 k_BT, which from the Boltzmann distribution corresponds to a probability of ~10^{-7}. Dividing this probability into the correlation time of the trap, 1-4 msec, predicts the observation time necessary to see a single such event as 10000-40000 seconds, whereas in the experiments microtubules were observed for a total of 1,676 s. Shortening events are far more frequent than this and so must arise from another source.

Furthermore, each experiment began by guiding the microtubule tip into the microfabricated vertex where it would abut the microfabricated barrier by sliding the microtubule along the barrier wall. In no case was a stick-slip behavior observed during this process. Additionally, each observation began with a substantial observation in a stationary trap that usually achieved high force. These observations again produced no evidence of the microtubule sticking and slipping past a rough area in the barrier.

Finally, the possibility that the microtubule is changing shape on a time scale and in a fashion that could create the appearance of lengthening and shortening can be eliminated. Following Gittes and Howard [220], the first bending mode of a 5 μm microtubule would have a characteristic relaxation time on the order of 100 μs with the higher order mode relaxation times decreasing according to the inverse fourth power of the mode number. Microtubule shape fluctuations would therefore be heavily averaged because the force clamp is updated infrequently, once every 100 ms, equivalent to 1000 times the slowest viscoelastic relaxation time of the microtubule during thermally-driven bending. Accounting for the large variation in the reported flexural rigidity of microtubules [87], a worst case estimate of the relaxation time might be 20 times greater, but still far too short to be apparent in the force clamping records. Similarly, the motion that one would expect from compression of the microtubule due to thermal motion is quite small. Assuming that a microtubule wall is an isotropic material, one can calculate the elastic modulus from the flexural rigidity [87, 220]. Conservative estimation of the elastic modulus indicates that 5 pN would result in compression of much less than 1 nm. In addition, Kerssemakers *et al*. [153] considered the thermal fluctuations of protofilament extensions at the end of the microtubule, and estimated that such extensions are still very stiff and would only fluctuate a few nanometers at most.

A further consideration is the lack of thermodynamic stability of mechanically compliant structures. While it is formally possible for a single protofilament to protrude beyond the other protofilaments, it is very unstable. Using our base parameter set, we estimate that the mean lifetime of single subunit with no lateral neighbors is ~0.2 ms. By contrast the mean arrival time for an incoming subunit is about 50 ms. So the probability of adding another subunit onto one that lacks lateral neighbors is 0.004. Further addition without loss, necessary for building up a single protofilament extension, is even less

likely. For example, in the case of 4 tubulin subunits (32 nm long protofilament extension), the mean time for one of the 4 longitudinal bonds to break is ~50 μs. Therefore, we conclude that these structures will rarely occur, and if they do they will be extremely short-lived. Of course a two-protofilament extension could occur, as in Fig. 6.2E, but these are also very unstable, and in the simulation usually results in catastrophe. Even a two-protofilament extension that is 8 subunits long (64 nm) will be unlikely to buckle significantly. For example, given elastic modulus E=260 pN/nm^2 [1], and second moment of inertia of the cross-sectional area I=[(4 nm)^3(8 nm)]/12 = 43 nm^4, then the Euler critical buckling force is

$$F_{c,2pf}^{0} = \pi^2 EI / L^2 = 27pN \tag{7}$$

which is well below the maximum force of 2.5 pN used in this study (note that much of the data were collected at 0-1 pN). Accounting for thermal effects on the buckling will have only a modest effect on the predicted buckling force, since the length of the projection (L=64 nm) is small compared to the persistence length of the projection (L_p=EI/kBT=2600 nm). For the single protofilament extension (L=32 nm), the persistence is similarly large (L_p=510 nm), so that in neither case are thermal forces expected to play a significant role. In either case, (one or two protofilaments of 32 or 64 nm, respectively) the critical buckling force is still much more than the ~5 pN required to buckle the entire microtubule. Note that microtubule buckling was not observed at the forces used in this study (max 2.5 pN). Furthermore, the fluctuations were largely uncorrelated with the load, and were in fact *larger* in the low force experiments than in high force experiments, which is the opposite of what one might expect if the applied load were inducing structural changes in the tip. Finally, it is important to note that the manipulation system is very soft in the direction away from contact with wall, and very stiff when in contact with the wall. From Boltzmann's Law, this implies that the microtubule tip rarely contacts the wall, and so is unable to sustain deformed tip states. Therefore, neither thermal events nor the forces exerted in these studies would produce significant tip deformation.

APPENDIX E

SUPPLEMENTAL MATERIAL: THE MICROTUBULE-BASED MOTOR KAR3 AND PLUS-END BINDING PROTEIN BIM1 PROVIDE STUCTURAL SUPPORT FOR THE ANAPHASE SPINDLE

(Reprinted with permission from *The Journal of Cell Biology* 180(1) (2008))

TABLE E.1. Viability of cells carrying an activated dicentric chromosome

Relevant Genotype	Orientation	% Viability[A]	n
Wild-type	Inverted	77.6 +/- 8.3	8
	Direct	54.8 +/- 13	8
rad52Δ[B, C]	Inverted	2.0 +/- 0.2	6
ndc10-2 (33°C)[C]	Direct	74.5 +/- 1.0	6
bim1Δ	Inverted	0.100 +/- 1.00	4
	Direct	0.500 +/- 0.60	5
kar3Δ	Inverted	0.140 +/- 0.11	4
	Direct	0.150 +/- 0.070	4
kar3-1	Inverted	0.210 +/- 0.16	4
	Direct	5.84 +/- 1.0	3
cik1Δ	Inverted	1.08 +/- 0.58	4
	Direct	1.23 +/- 0.62	9
ase1Δ	Inverted	2.53 +/- 0.80	4
	Direct	2.24 +/- 1.4	4
bik1Δ	Inverted	2.08 +/- 2.2	4
	Direct	0.41 +/- 0.24	3
slk19Δ	Inverted	13.3 +/- 5.6	5
	Direct	11.4 +/- 5.7	3
vik1Δ	Inverted	39.9 +/- 2.6	3
	Direct	39.5 +/- 7.3	4

[A]Mean +/- Standard Deviation
[B][221]
[C][181]

TABLE E.2. *S. cerevisiae* strains used in this study

Strain Name	Relevant Genotype	Source/Reference
YEF 473A	MAT**a** *trp1Δ63 leu2Δ1 ura3-52 his3Δ200 lys2-801*	[222]
YEF 473B	MATα *trp1Δ63 leu2Δ1 ura3-52 his3Δ200 lys2-801*	[222]
J178-1D	MAT**a** *ade1 met14 ura3-52 leu2-3, -112 his3*	
SFY 280-20A	MAT**a** *ade2-1 ade3 can1-100 his3-11,-15 leu2-3,-112 trp1-1 ura3-1 lys2Δ::HIS3 vik1Δ::KAN^r GFP-TUB1::URA3*	T. Davis[A]
MS 1119	MAT**a** *ura3-52 leu2-3, -112 ade2-101 kar3-1*	[223]
GT1	MAT**a** *trp1Δ63 leu2Δ1 ura3-52 his3Δ200 lys2-801 GFP-TUB1::URA3*	P. Maddox[B]
KBY 2275	MAT**a** *trp1Δ63 leu2Δ1 ura3-52 his3Δ200 lys2-801*	C. Pearson[B]
KBY 4138	MAT**a** *ade1 met14 ura3-52 leu2-3, -112 his3 URA3::HB^r bim1Δ::KAN^r pJB2#7*	This Study
KBY 7003	MAT**a** *ade1 met14 ura3-52 leu2-3, -112 his3 URA3::HB^r bim1Δ::KAN^r GFP-TUB1::URA3 pJB2#7*	This Study
KBY 7004	MAT**a** *ade1 met14 ura3-52 leu2-3, -112 his3 URA3::HB^r GFP-TUB1::URA3 pJB2#7*	This Study
KBY 9282	MATα *trp1Δ63 leu2Δ1 ura3-52 his3Δ200 lys2-801 KAR3::GFP-HB^r*	This Study
KBY 9293	MAT**a** *trp1Δ63 leu2Δ1 ura3-52 his3Δ200 lys2-801 kar3Δ::TRP1*	Molk et al., 2006
KBY 9313	MAT**a** *trp1Δ63 leu2Δ1 ura3-52 his3Δ200 lys2-801 kar3Δ::TRP1*	Molk et al., 2006
KBY 9344	MAT**a** *trp1Δ63 leu2Δ1 ura3-52 his3Δ200 lys2-801 pJB2#4*	This Study
KBY 9345	MAT**a** *trp1Δ63 leu2Δ1 ura3-52 his3Δ200 lys2-801 pJB2#7*	This Study
KBY 9346	MAT**a** *trp1Δ63 leu2Δ1 ura3-52 his3Δ200 lys2-801 kar3Δ::TRP1 pJB2#4*	This Study
KBY 9347	MAT**a** *trp1Δ63 leu2Δ1 ura3-52 his3Δ200 lys2-801 kar3Δ::TRP1 pJB2#7*	This Study
KBY 9348	MAT**a** *ura3-52 leu2-3, -112 ade2-101 kar3-1 pJB2#4*	This Study
KBY 9349	MAT**a** *trp1Δ63 leu2Δ1 ura3-52 his3Δ200 lys2-801 cik1Δ::KAN^r pJB2#4*	This Study
KBY 9350	MAT**a** *trp1Δ63 leu2Δ1 ura3-52 his3Δ200 lys2-801 cik1Δ::KAN^r pJB2#7*	This Study
KBY 9351	MAT**a** *ade2-1 ade3 can1-100 his3-11,-15 leu2-3,-112 trp1-1 ura3-1 lys2Δ::HIS3 vik1Δ::KAN^r GFP-TUB1::URA3 pJB2#4*	This Study
KBY 9352	MAT**a** *ade2-1 ade3 can1-100 his3-11,-15 leu2-3,-112 trp1-1 ura3-1 lys2Δ::HIS3 vik1Δ::KAN^r GFP-TUB1::URA3 pJB2#7*	This Study
KBY 9353	MAT**a** *trp1Δ63 leu2Δ1 ura3-52 his3Δ200 lys2-801 TEM1::GFP-KAN^r ase1Δ::HB^r pJB#4*	This Study
KBY 9354	MAT**a** *trp1Δ63 leu2Δ1 ura3-52 his3Δ200 lys2-801 TEM1::GFP-KAN^r ase1Δ::HB^r pJB#7*	This Study
KBY 9355	MAT**a** *trp1Δ63 leu2Δ1 ura3-52 his3Δ200 lys2-801 bik1Δ::KAN^r*	This Study
KBY 9356	MAT**a** *trp1Δ63 leu2Δ1 ura3-52 his3Δ200 lys2-801 bik1Δ::KAN^r*	This Study
KBY 9357	MAT**a** *trp1Δ63 leu2Δ1 ura3-52 his3Δ200 lys2-801 TEM1::GFP-KAN^r*	This Study
KBY 9358	MAT**a** *trp1Δ63 leu2Δ1 ura3-52 his3Δ200 lys2-801 TEM1::GFP-KAN^r*	This Study
KBY 9359	MAT**a** *ura3-52 leu2-3, -112 ade2-101 kar3-1 pJB2#7*	This Study
KBY 9365	MAT**a** *trp1Δ63 leu2Δ1 ura3-52 his3Δ200 lys2-801 slk19Δ::KAN^r*	This Study
KBY 9366	MAT**a** *trp1Δ63 leu2Δ1 ura3-52 his3Δ200 lys2-801 slk19Δ::KAN^r*	This Study

Plasmid Name	Relevant Genotype	Source or Reference
pJB2#4	*his4::URA3 GAL-CEN3* (inverted orientation)	[221]
pJB2#7	*his4::URA3 GAL-CEN3* (direct orientation)	[221]
pAFS125	*GFP-TUB1::URA3*	[224]
pGAL-CEN[2]	*GAL-CEN3 CEN4 URA3*	[225]

[A]University of Washington, Seattle, WA; [B]University of North Carolina, Chapel Hill, NC

FIGURE E.1. Quantification of microtubule-associated protein localization during anaphase. (A) Localization of Kar3-GFP in *vik1Δ* mutants vs Bim1-GFP in wild-type spindles. The Kar3-GFP in the Kar3-Cik1 complex is present in punctate locations along the length of the spindle, while Bim1-GFP is concentrated near to the spindle midzone. (B) Kar3-GFP localization in *cik1Δ* and *vik1Δ* mutants. The Kar3-Cik1 complex is located at putative MT plus-ends, while Kar3-Vik1 is concentrated at the SPBs.

A.

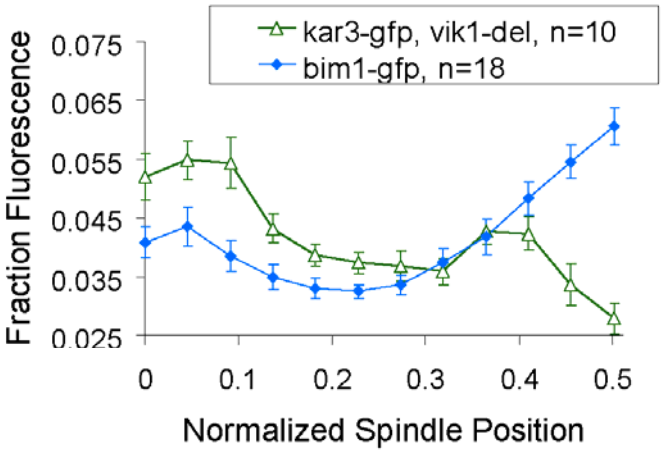

B.

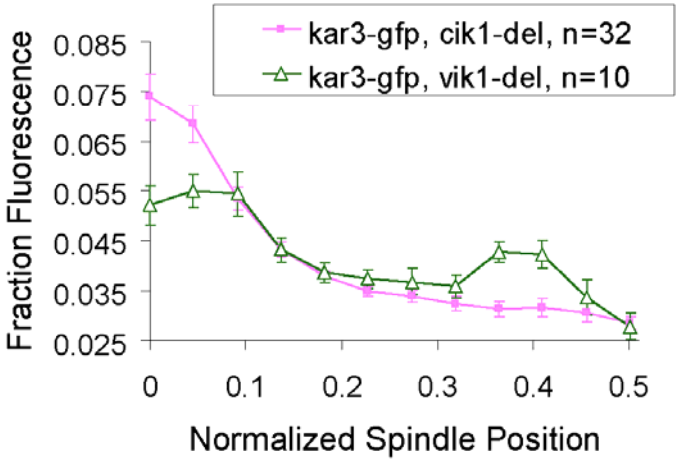

FIGURE E.2. Formation of repair products after activation of dicentric chromosome III is suppressed in ase1Δ and kar3Δ cells. (A) Ethidium bromide stained agarose gel of PCR amplification experiments that probed for the repair product formed after dicentric breakage (left lanes) and the *MET14* locus (right lanes) that was used as a control. Images were captured using the Alpha Innotech AlphaImager 2200 system. (B) Quantification of PCR products in (A). Image files were processed in MetaMorph 6.1. Lines were drawn through each band and the integrated intensity was recorded in a linked Microsoft Excel spreadsheet. The background was determined by averaging the intensity of 15 pixels surrounding the band and multiplying this value by the width of the band. This background figure was subtracted from the band intensity, yielding the corrected intensity. To compare PCR reactions, the ratio of repair band to the *MET14* control band was plotted.

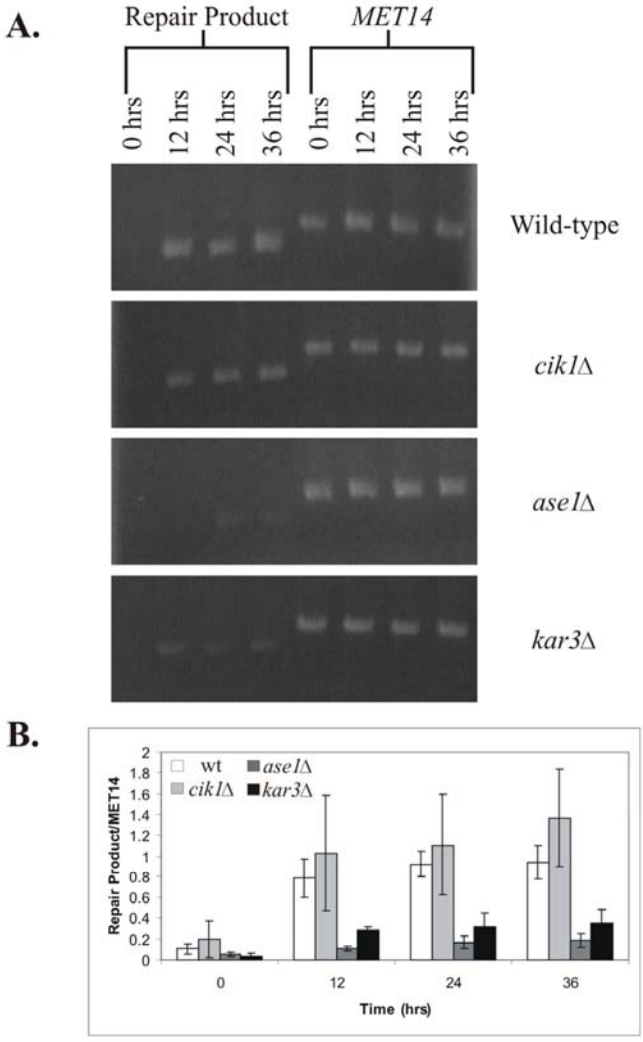

REFERENCES

1. Gardner, M.K., and Odde, D.J. (2006). Modeling of chromosome motility during mitosis. Curr Opin Cell Biol *18*, 639-647.

2. Gardner, M.K., Hunt, A.J., Goodson, H.V., and Odde, D.J. (2008). Microtubule assembly dynamics: new insights at the nanoscale. Curr Opin Cell Biol *20*, 64-70.

3. Karsenti, E., and Vernos, I. (2001). The mitotic spindle: a self-made machine. Science *294*, 543-547.

4. Scholey, J.M., Brust-Mascher, I., and Mogilner, A. (2003). Cell division. Nature *422*, 746-752.

5. Compton, D.A. (2000). Spindle assembly in animal cells. Annu Rev Biochem *69*, 95-114.

6. McDonald, K.L., O'Toole, E.T., Mastronarde, D.N., and McIntosh, J.R. (1992). Kinetochore microtubules in PTK cells. J Cell Biol *118*, 369-383.

7. Gordon, M.B., Howard, L., and Compton, D.A. (2001). Chromosome movement in mitosis requires microtubule anchorage at spindle poles. J Cell Biol *152*, 425-434.

8. McIntosh, J.R., Grishchuk, E.L., and West, R.R. (2002). Chromosome-Microtubule Interactions During Mitosis. Annu Rev Cell Dev Biol.

9. Maiato, H., DeLuca, J., Salmon, E.D., and Earnshaw, W.C. (2004). The dynamic kinetochore-microtubule interface. J Cell Sci *117*, 5461-5477.

10. Fukagawa, T. (2004). Assembly of kinetochores in vertebrate cells. Exp Cell Res *296*, 21-27.

11. Howard, J., and Hyman, A.A. (2003). Dynamics and mechanics of the microtubule plus end. Nature *422*, 753-758.

12. Mitchison, T., and Kirschner, M. (1984). Dynamic instability of microtubule growth. Nature *312*, 237-242.

13. Skibbens, R.V., Skeen, V.P., and Salmon, E.D. (1993). Directional instability of kinetochore motility during chromosome congression and segregation in mitotic newt lung cells: a push-pull mechanism. Journal of Cell Biology *122*, 859-875.

14. Nicklas, R.B., and Kubai, D.F. (1985). Microtubules, chromosome movement, and reorientation after chromosomes are detached from the spindle by micromanipulation. Chromosoma *92*, 313-324.

15. Maddox, P., Straight, A., Coughlin, P., Mitchison, T.J., and Salmon, E.D. (2003). Direct observation of microtubule dynamics at kinetochores in Xenopus extract spindles: implications for spindle mechanics. J Cell Biol *162*, 377-382.

16. Skibbens, R.V., and Salmon, E.D. (1997). Micromanipulation of chromosomes in mitotic vertebrate tissue cells: tension controls the state of kinetochore movement. Exp Cell Res *235*, 314-324.

17. Rieder, C.L., and Salmon, E.D. (1994). Motile kinetochores and polar ejection forces dictate chromosome position on the vertebrate mitotic spindle. Journal of Cell Biology *124*, 223-233.

18. Goshima, G., and Yanagida, M. (2001). Time course analysis of precocious separation of sister centromeres in budding yeast: continuously separated or frequently reassociated? Genes Cells *6*, 765-773.

19. Pearson, C.G., Maddox, P.S., Salmon, E.D., and Bloom, K. (2001). Budding Yeast Chromosome Structure and Dynamics during Mitosis. J. Cell Biol. *152*, 1255-1266.

20. Mitchison, T.J., and Salmon, E.D. (2001). Mitosis: a history of division. Nat Cell Biol *3*, E17-21.

21. Kapoor, T.M., and Compton, D.A. (2002). Searching for the middle ground: mechanisms of chromosome alignment during mitosis. J Cell Biol *157*, 551-556.

22. Kline-Smith, S.L., and Walczak, C.E. (2004). Mitotic spindle assembly and chromosome segregation: refocusing on microtubule dynamics. Mol Cell *15*, 317-327.

23. Rieder, C.L., and Salmon, E.D. (1998). The vertebrate cell kinetochore and its roles during mitosis. Trends in Cell Biology *8*, 310-318.

24. Arana, P., and Nicklas, R.B. (1992). Orientation and segregation of a micromanipulated multivalent: familiar principles, divergent outcomes. Chromosoma *101*, 399-412.

25. Nicklas, R.B. (1997). How cells get the right chromosomes. Science *275*, 632-637.

26. Cimini, D., Howell, B., Maddox, P., Khodjakov, A., Degrassi, F., and Salmon, E.D. (2001). Merotelic kinetochore orientation is a major mechanism of aneuploidy in mitotic mammalian tissue cells. J Cell Biol *153*, 517-527.

27. Civelekoglu-Scholey, G., Sharp, D.J., Mogilner, A., and Scholey, J.M. (2006). Model of chromosome motility in Drosophila embryos: adaptation of a general mechanism for rapid mitosis. Biophys J *90*, 3966-3982.

28. Joglekar, A.P., and Hunt, A.J. (2002). A simple, mechanistic model for directional instability during mitotic chromosome movements. Biophys J *83*, 42-58.

29. Sprague, B.L., Pearson, C.G., Maddox, P.S., Bloom, K.S., Salmon, E.D., and Odde, D.J. (2003). Mechanisms of Microtubule-Based Kinetochore Positioning in the Yeast Metaphase Spindle. Biophys J *84*, 1-18.

30. Winey, M., Mamay, C.L., O'Toole, E.T., Mastronarde, D.N., Giddings, T.H., Jr., McDonald, K.L., and McIntosh, J.R. (1995). Three-dimensional ultrastructural analysis of the Saccharomyces cerevisiae mitotic spindle. Journal of Cell Biology *129*, 1601-1615.

31. Odde, D.J., Cassimeris, L., and Buettner, H.M. (1995). Kinetics of microtubule catastrophe assessed by probabilistic analysis. Biophys J *69*, 796-802.

32. Walker, R.A., O'Brien, E.T., Pryer, N.K., Soboeiro, M.F., Voter, W.A., Erickson, H.P., and Salmon, E.D. (1988). Dynamic instability of individual microtubules analyzed by video light microscopy: rate constants and transition frequencies. J Cell Biol *107*, 1437-1448.

33. Chretien, D., Fuller, S.D., and Karsenti, E. (1995). Structure of growing microtubule ends: two-dimensional sheets close into tubes at variable rates. Journal of Cell Biology *129*, 1311-1328.

34. Mandelkow, E.M., Mandelkow, E., and Milligan, R.A. (1991). Microtubule dynamics and microtubule caps: a time-resolved cryo-electron microscopy study. J Cell Biol *114*, 977-991.

35. Nogales, E., and Wang, H.W. (2006). Structural mechanisms underlying nucleotide-dependent self-assembly of tubulin and its relatives. Curr Opin Struct Biol *16*, 221-229.

36. Wang, H.W., and Nogales, E. (2005). Nucleotide-dependent bending flexibility of tubulin regulates microtubule assembly. Nature *435*, 911-915.

37. Gigant, B., Curmi, P.A., Martin-Barbey, C., Charbaut, E., Lachkar, S., Lebeau, L., Siavoshian, S., Sobel, A., and Knossow, M. (2000). The 4 A X-ray structure of a tubulin:stathmin-like domain complex. Cell *102*, 809-816.

38. Muller-Reichert, T., Chretien, D., Severin, F., and Hyman, A.A. (1998). Structural changes at microtubule ends accompanying GTP hydrolysis: Information from a slowly hydrolyzable analogue of GTP, guanylyl (alpha,beta)methylenediphosphonate. Proceedings of the National Academy of Sciences of the United States of America *95*, 3661-3666.

39. Chen, K.C., Calzone, L., Csikasz-Nagy, A., Cross, F.R., Novak, B., and Tyson, J.J. (2004). Integrative analysis of cell cycle control in budding yeast. Mol Biol Cell *15*, 3841-3862.

40. Ciliberto, A., Novak, B., and Tyson, J.J. (2003). Mathematical model of the morphogenesis checkpoint in budding yeast. J Cell Biol *163*, 1243-1254.

41. de Jong, H. (2002). Modeling and simulation of genetic regulatory systems: a literature review. J Comput Biol *9*, 67-103.

42. Slepchenko, B.M., Schaff, J.C., Macara, I., and Loew, L.M. (2003). Quantitative cell biology with the Virtual Cell. Trends Cell Biol *13*, 570-576.

43. Loew, L.M. (2002). The Virtual Cell project. Novartis Found Symp *247*, 151-160; discussion 160-151, 198-206, 244-152.

44. Moraru, II, Schaff, J.C., Slepchenko, B.M., and Loew, L.M. (2002). The virtual cell: an integrated modeling environment for experimental and computational cell biology. Ann N Y Acad Sci *971*, 595-596.

45. Gillespie, J.H. (1972). The effects of stochastic environments on allele frequencies in natural populations. Theor Popul Biol *3*, 241-248.

46. Becskei, A., Kaufmann, B.B., and van Oudenaarden, A. (2005). Contributions of low molecule number and chromosomal positioning to stochastic gene expression. Nat Genet *37*, 937-944.

47. Dorn, J.F., Jaqaman, K., Rines, D.R., Jelson, G.S., Sorger, P.K., and Danuser, G. (2005). Yeast kinetochore microtubule dynamics analyzed by high-resolution three-dimensional microscopy. Biophys J *89*, 2835-2854.

48. Wollman, R., Cytrynbaum, E.N., Jones, J.T., Meyer, T., Scholey, J.M., and Mogilner, A. (2005). Efficient chromosome capture requires a bias in the 'search-and-capture' process during mitotic-spindle assembly. Curr Biol *15*, 828-832.

49. Odde, D.J. (2005). Chromosome capture: take me to your kinetochore. Curr Biol *15*, R328-330.

50. Gardner, M.K., Pearson, C.G., Sprague, B.L., Zarzar, T.R., Bloom, K., Salmon, E.D., and Odde, D.J. (2005). Tension-dependent Regulation of Microtubule Dynamics at Kinetochores Can Explain Metaphase Congression in Yeast. Mol Biol Cell *16*, 3764-3775.

51. Pearson, C.G., Yeh, E., Gardner, M., Odde, D., Salmon, E.D., and Bloom, K. (2004). Stable kinetochore-microtubule attachment constrains centromere positioning in metaphase. Curr Biol *14*, 1962-1967.

52. Shaw, S.L., Yeh, E., Bloom, K., and Salmon, E.D. (1997). Imaging green fluorescent protein fusion proteins in *Saccharomyces cerevisiae*. Current Biology *7*, 701-704.

53. Salmon, E.D., Shaw, S.L., Waters, J., Waterman-Storer, C.M., Maddox, P.S., Yeh, E., and Bloom, K. (2003). A high-resolution multimode digital microscope system. Methods Cell Biol *72*, 185-216.

54. Yeh, E., Skibbens, R.V., Cheng, J.W., Salmon, E.D., and Bloom, K. (1995). Spindle dynamics and cell cycle regulation of dynein in the budding yeast, Saccharomyces cerevisiae. Journal of Cell Biology *130*, 687-700.

55. Inoue, S., and Salmon, E.D. (1995). Force generation by microtubule assembly/disassembly in mitosis and related movements. Molecular Biology of the Cell *6*, 1619-1640.

56. Nasmyth, K. (2002). Segregating sister genomes: the molecular biology of chromosome separation. Science *297*, 559-565.

57. Peterson, J.B., and Ris, H. (1976). Electron-microscopic study of the spindle and chromosome movement in the yeast *Saccharomyces cerevisiae*. Journal of Cell Science *22*, 219-242.

58. O'Toole, E.T., Winey, M., and McIntosh, J.R. (1999). High-voltage electron tomography of spindle pole bodies and early mitotic spindles in the yeast Saccharomyces cerevisiae. Molecular Biology of the Cell *10*, 2017-2031.

59. Maddox, P., Bloom, K., and Salmon, E.D. (2000). Polarity and Dynamics of Microtubule Assembly in the Budding Yeast *Saccharomyces cerevisiae*. Nature Cell Biology *2*, 36-41.

60. Pearson, C.G., Maddox, P.S., Zarzar, T.R., Salmon, E.D., and Bloom, K. (2003). Yeast kinetochores do not stabilize Stu2p-dependent spindle microtubule dynamics. Mol Biol Cell *14*, 4181-4195.

61. He, X., Asthana, S., and Sorger, P.K. (2000). Transient Sister Chromatid Separation and Elastic Deformation of Chromosomes during Mitosis in Budding Yeast. Cell *101*, 763-775.

62. Tanaka, T., Fuchs, J., Loidl, J., and Nasmyth, K. (2000). Cohesin ensures bipolar attachment of microtubules to sister centromeres and resists their precocious separation. Nat. Cell Biol. *2*, 492-499.

63. Krishnan, V., Nirantar, S., Crasta, K., Cheng, A.Y., and Surana, U. (2004). DNA replication checkpoint prevents precocious chromosome segregation by regulating spindle behavior. Mol Cell *16*, 687-700.

64. Chen, Y., Baker, R.E., Keith, K.C., Harris, K., Stoler, S., and Fitzgerald-Hayes, M. (2000). The N Terminus of the Centromere H3-Like Protein Cse4p Performs an Essential Function Distinct from That of the Histone Fold Domain. MCB *20*, 7037-7048.

65. Meluh, P.B., Yang, P., Glowczewski, L., Koshland, D., and Smith, M.M. (1998). Cse4p is a component of the core centromere of Saccharomyces cerevisiae. Cell *94*, 607-613.

66. Nicklas, R.B. (1988). The forces that move chromosomes in mitosis. Annual Review of Biophysics & Biophysical Chemistry *17*, 431-449.

67. Skibbens, R.V., Rieder, C.L., and Salmon, E.D. (1995). Kinetochore motility after severing between sister centromeres using laser microsurgery: evidence that kinetochore directional instability and position is regulated by tension. Journal of Cell Science *108*, 2537-2548.

68. Cimini, D., Cameron, L.A., and Salmon, E.D. (2004). Anaphase spindle mechanics prevent mis-segregation of merotelically oriented chromosomes. Curr Biol *14*, 2149-2155.

69. Dewar, H., Tanaka, K., Nasmyth, K., and Tanaka, T.U. (2004). Tension between two kinetochores suffices for their bi-orientation on the mitotic spindle. Nature *428*, 93-97.

70. Carminati, J.L., and Stearns, T. (1997). Microtubules orient the mitotic spindle in yeast through dynein-dependent interactions with the cell cortex. J Cell Biol *138*, 629-641.

71. Tirnauer, J.S., O'Toole, E.O., Berrueta, L., Bierer, B.E., and Pellman, D. (1999). Yeast Bim1p promotes the G1-specific dynamics of microtubules. The Journal of Cell Biology *145*, 993-1007.

72. Kosco, K.A., Pearson, C.G., Maddox, P.S., Wang, P.J., Adams, I.R., Salmon, E.D., Bloom, K., and Huffaker, T.C. (2001). Control of microtubule dynamics by Stu2p is essential for spindle orientation and metaphase chromosome alignment in yeast. Mol Biol Cell *12*, 2870-2880.

73. Shaw, S.L., Yeh, E., Maddox, P., Salmon, E.D., and Bloom, K. (1997). Astral microtubule dynamics in yeast: A microtubule-based searching mechanism for spindle orientation and nuclear migration into the bud. Journal of Cell Biology *139*, 985-994.

74. Gupta, M.L., Jr., Bode, C.J., Thrower, D.A., Pearson, C.G., Suprenant, K.A., Bloom, K.S., and Himes, R.H. (2002). beta-Tubulin C354 mutations that severely decrease microtubule dynamics do not prevent nuclear migration in yeast. Mol Biol Cell *13*, 2919-2932.

75. Tirnauer, J.S., Salmon, E.D., and Mitchison, T.J. (2004). Microtubule plus-end dynamics in Xenopus egg extract spindles. Mol Biol Cell *15*, 1776-1784.

76. Biggins, S., and Murray, A.W. (2001). The budding yeast protein kinase Ipl1/Aurora allows the absence of tension to activate the spindle checkpoint. Genes Dev *15*, 3118-3129.

77. Cleveland, D.W., Mao, Y., and Sullivan, K.F. (2003). Centromeres and kinetochores: from epigenetics to mitotic checkpoint signaling. Cell *112*, 407-421.

78. Stern, B.M., and Murray, A.W. (2001). Lack of tension at kinetochores activates the spindle checkpoint in budding yeast. Curr Biol *11*, 1462-1467.

79. Zhou, J., Yao, J., and Joshi, H.C. (2002). Attachment and tension in the spindle assembly checkpoint. J Cell Sci *115*, 3547-3555.

80. Biggins, S., and Walczak, C.E. (2003). Captivating capture: how microtubules attach to kinetochores. Curr Biol *13*, R449-460.

81. Nicklas, R.B., and Ward, S.C. (1994). Elements of error correction in mitosis: microtubule capture, release, and tension. Journal of Cell Biology *126*, 1241-1253.

82. Nicklas, R.B., Waters, J.C., Salmon, E.D., and Ward, S.C. (2001). Checkpoint signals in grasshopper meiosis are sensitive to microtubule attachment, but tension is still essential. J Cell Sci *114*, 4173-4183.

83. Westermann, S., Avila-Sakar, A., Wang, H.W., Niederstrasser, H., Wong, J., Drubin, D.G., Nogales, E., and Barnes, G. (2005). Formation of a dynamic kinetochore- microtubule interface through assembly of the Dam1 ring complex. Mol Cell *17*, 277-290.

84. Miranda, J.J., De Wulf, P., Sorger, P.K., and Harrison, S.C. (2005). The yeast DASH complex forms closed rings on microtubules. Nat Struct Mol Biol *12*, 138-143.

85. Cheeseman, I.M., Drubin, D.G., and Barnes, G. (2002). Simple centromere, complex kinetochore: linking spindle microtubules and centromeric DNA in budding yeast. J Cell Biol *157*, 199-203.

86. McIntosh, J.R. (2005). Rings around kinetochore microtubules in yeast. Nat Struct Mol Biol *12*, 210-212.

87. VanBuren, V., Odde, D.J., and Cassimeris, L. (2002). Estimates of lateral and longitudinal bond energies within the microtubule lattice. Proc Natl Acad Sci U S A *99*, 6035-6040.

88. Caplow, M., and Shanks, J. (1996). Evidence that a single monolayer tubulin-GTP cap is both necessary and sufficient to stabilize microtubules. Mol Biol Cell *7*, 663-675.

89. Brower-Toland, B.D., Smith, C.L., Yeh, R.C., Lis, J.T., Peterson, C.L., and Wang, M.D. (2002). Mechanical disruption of individual nucleosomes reveals a reversible multistage release of DNA. Proc Natl Acad Sci U S A *99*, 1960-1965.

90. Brown, G.C., and Kholodenko, B.N. (1999). Spatial gradients of cellular phospho-proteins. FEBS Lett *457*, 452-454.

91. Van Breugel, M., Drechsel, D., and Hyman, A. (2003). Stu2p, the budding yeast member of the conserved Dis1/XMAP215 family of microtubule-associated proteins is a plus end-binding microtubule destabilizer. J Cell Biol *161*, 359-369.

92. He, X., Rines, D.R., Espelin, C.W., and Sorger, P.K. (2001). Molecular analysis of kinetochore-microtubule attachment in budding yeast. Cell *106*, 195-206.

93. Kalab, P., Weis, K., and Heald, R. (2002). Visualization of a Ran-GTP gradient in interphase and mitotic Xenopus egg extracts. Science *295*, 2452-2456.

94. Guacci, V., Hogan, E., and Koshland, D. (1997). Centromere Position in Budding Yeast: Evidence for Anaphase A. Mol. Biol. Cell *8*, 957-972.

95. Straight, A.F. (1997). Cell cycle: Checkpoint proteins and kinetochores. Current biology *7*, R613.

96. Gardner, M.K., Pearson, C.G., Sprague, B.L., Zarzar, T.R., Bloom, K., Salmon, E.D., and Odde, D.J. (2005). Tension-dependent Regulation of Microtubule Dynamics at Kinetochores Can Explain Metaphase Congression in Yeast. Mol. Biol. Cell *16*, 3764-3775.

97. Mitchison, T.J. (2005). Mechanism and function of poleward flux in Xenopus extract meiotic spindles. Philos Trans R Soc Lond B Biol Sci. *360*, 623-629.

98. Bullitt, E., Rout, M.P., Kilmartin, J.V., and Akey, C.W. (1997). The yeast spindle pole body is assembled around a central crystal of Spc42p. Cell. *89*, 1077-1086.

99. Tanaka, K., Mukae, N., Dewar, H., van Breugel, M., James, E.K., Prescott, A.R., Antony, C., and Tanaka, T.U. (2005). Molecular mechanisms of kinetochore capture by spindle microtubules. Nature *434*, 987-994.

100. Rout, M.P., and Kilmartin, J.V. (1990). Components of the yeast spindle and spindle pole body. J Cell Biol. *111*, 1913-1927.

101. Byers, B., Shriver, K., and Goetsch, L. (1978). The role of spindle pole bodies and modified microtubule ends in the initiation of microtubule assembly in Saccharomyces cerevisiae. J Cell Sci *30*, 331-352.

102. Goshima, G., and Yanagida, M. (2000). Establishing Biorientation Occurs with Precocious Separation of the Sister Kinetochores, but Not the Arms, in the Early Spindle of Budding Yeast. Cell *100*, 619-633.

103. Pearson, C.G., Yeh, E., Gardner, M., Odde, D., Salmon, E.D., and Bloom, K. (2004). Stable Kinetochore-Microtubule Attachment Constrains Centromere Positioning in Metaphase. Current Biology *14*, 1962-1967.

104. Fowles, G.R. (1975). Introduction to Modern Optics, 117-120.

105. Dorn, J.F., Jaqaman, K., Rines, D.R., Jelson, G.S., Sorger, P.K., and Danuser, G. (2005). Yeast kinetochore microtubule dynamics analyzed by high-resolution three-dimensional microscopy. Biophys J. *89*, 2835-2854.

106. Civelekoglu-Scholey, G., Sharp, D.J., Mogilner, A., and Scholey, J.M. (2006). Model of chromosome motility in Drosophila embryos: Adaptation of a general mechanism for rapid mitosis. Biophys J *13*, 13.

107. Pinsky, B.A., and Biggins, S. (2005). The spindle checkpoint: tension versus attachment. Trends Cell Biol *15*, 486-493.

108. Pearson, C.G., Gardner, M.K., Paliulis, L.V., Salmon, E.D., Odde, D.J., and Bloom, K. (2006). Measuring Nanometer Scale Gradients in Spindle Microtubule Dynamics Using Model Convolution Microscopy. Mol Biol Cell *17*, 4069-4079.

109. Varga, V., Helenius, J., Tanaka, K., Hyman, A.A., Tanaka, T.U., and Howard, J. (2006). Yeast kinesin-8 depolymerizes microtubules in a length-dependent manner. Nat Cell Biol *8*, 957-962.

110. Gupta, M.L., Jr., Carvalho, P., Roof, D.M., and Pellman, D. (2006). Plus end-specific depolymerase activity of Kip3, a kinesin-8 protein, explains its role in positioning the yeast mitotic spindle. Nat Cell Biol *8*, 913-923.

111. Tao, L., Mogilner, A., Civelekoglu-Scholey, G., Wollman, R., Evans, J., Stahlberg, H., and Scholey, J.M. (2006). A homotetrameric kinesin-5, KLP61F, bundles microtubules and antagonizes Ncd in motility assays. Curr Biol *16*, 2293-2302.

112. Kapitein, L.C., Peterman, E.J., Kwok, B.H., Kim, J.H., Kapoor, T.M., and Schmidt, C.F. (2005). The bipolar mitotic kinesin Eg5 moves on both microtubules that it crosslinks. Nature *435*, 114-118.

113. Roof, D.M., Meluh, P.B., and Rose, M.D. (1992). Kinesin-related proteins required for assembly of the mitotic spindle. Journal of Cell Biology *118*, 95-108.

114. Saunders, W.S., and Hoyt, M.A. (1992). Kinesin-related proteins required for structural integrity of the mitotic spindle. Cell *70*, 451-458.

115. Gordon, D.M., and Roof, D.M. (1999). The kinesin-related protein Kip1p of Saccharomyces cerevisiae is bipolar. J Biol Chem *274*, 28779-28786.

116. Hoyt, M.A., He, L., Loo, K.K., and Saunders, W.S. (1992). Two Saccharomyces cerevisiae kinesin-related gene products required for mitotic spindle assembly. Journal of Cell Biology *118*, 109-120.

117. Desai, A., and Mitchison, T.J. (1997). Microtubule polymerization dynamics. Annu Rev Cell Dev Biol *13*, 83-117.

118. Tytell, J.D., and Sorger, P.K. (2006). Analysis of kinesin motor function at budding yeast kinetochores. J Cell Biol *172*, 861-874.

119. Gardner, M.K., Odde, D.J., and Bloom, K. (2007). Hypothesis testing via integrated computer modeling and digital fluorescence microscopy. Methods *41*, 232-237.

120. Hildebrandt, E.R., and Hoyt, M.A. (2000). Mitotic motors in Saccharomyces cerevisiae. Biochim Biophys Acta *1496*, 99-116.

121. Saunders, W., Lengyel, V., and Hoyt, M.A. (1997). Mitotic Spindle Function in Saccharomyces cerevisiae Requires a Balance between Different Types of Kinesin-related Motors. Molecular biology of the cell *8*, 1025-1033.

122. Bouck, D.C., and Bloom, K. (2007). Pericentric chromatin is an elastic component of the mitotic spindle. Curr Biol *17*, 741-748.

123. Gheber, L., Kuo, S.C., and Hoyt, M.A. (1999). Motile properties of the kinesin-related Cin8p spindle motor extracted from Saccharomyces cerevisiae cells. J Biol Chem *274*, 9564-9572.

124. Stumpff, J., von Dassow, G., Wagenbach, M., Asbury, C., and Wordeman, L. (2008). The kinesin-8 motor Kif18A suppresses kinetochore movements to control mitotic chromosome alignment. Dev Cell *14*, 252-262.

125. Gardner, M., Odde, D., and Bloom, K. (2008). Kinesin-8 molecular motors: putting the brakes on chromosome oscillations. Trends Cell Biol.

126. Mayr, M.I., Hummer, S., Bormann, J., Gruner, T., Adio, S., Woehlke, G., and Mayer, T.U. (2007). The human kinesin Kif18A is a motile microtubule depolymerase essential for chromosome congression. Curr Biol *17*, 488-498.

127. Straight, A.F., Sedat, J.W., and Murray, A.W. (1998). Time-lapse microscopy reveals unique roles for kinesins during anaphase in budding yeast. The Journal of Cell Biology *143*, 687.

128. Cottingham, F.R., and Hoyt, M.A. (1997). Mitotic spindle positioning in Saccharomyces cerevisiae is accomplished by antagonistically acting microtubule motor proteins. J Cell Biol *138*, 1041-1053.

129. Miller, R.K., Heller, K.K., and Rose, M.D. (1998). The Kinesin-related Proteins, Kip2p and Kip3p, Function Differently in Nuclear Migration in Yeast. Molecular Biology of the Cell *9*, 2051.

130. de Gramont, A., Barbour, L., Ross, K.E., and Cohen-Fix, O. (2007). The spindle midzone microtubule-associated proteins Ase1p and Cin8p affect the number and orientation of astral microtubules in Saccharomyces cerevisiae. Cell Cycle *6*, 1231-1241.

131. Geiser, J.R., Schott, E.J., Kingsbury, T.J., Cole, N.B., Totis, L.J., Bhattaacharyya, G., He, L., and Hoyt, M.A. (1997). Saccharomyces cerevisiae genes required in the absence of the CIN8-encoded spindle motor act in functionally diverse mitotic pathways. Molecular Biology of the Cell *8*, 1035-1050.

132. Hildebrandt, E.R., and Hoyt, M.A. (2001). Cell cycle-dependent degradation of the Saccharomyces cerevisiae spindle motor Cin8p requires APC(Cdh1) and a bipartite destruction sequence. Mol Biol Cell *12*, 3402-3416.

133. Valentine, M.T., Fordyce, P.M., Krzysiak, T.C., Gilbert, S.P., and Block, S.M. (2006). Individual dimers of the mitotic kinesin motor Eg5 step processively and support substantial loads in vitro. Nat Cell Biol *8*, 470-476.

134. Kashina, A.S., Baskin, R.J., Cole, D.G., Wedaman, K.P., Saxton, W.M., and Scholey, J.M. (1996). A bipolar kinesin. Nature *379*, 270-272.

135. Huang, B., and Huffaker, T.C. (2006). Dynamic microtubules are essential for efficient chromosome capture and biorientation in S. cerevisiae. J Cell Biol *175*, 17-23.

136. Cameron, L.A., Yang, G., Cimini, D., Canman, J.C., Kisurina-Evgenieva, O., Khodjakov, A., Danuser, G., and Salmon, E.D. (2006). Kinesin 5-independent poleward flux of kinetochore microtubules in PtK1 cells. J Cell Biol *173*, 173-179.

137. Kapoor, T.M., and Mitchison, T.J. (2001). Eg5 is static in bipolar spindles relative to tubulin: evidence for a static spindle matrix. J Cell Biol *154*, 1125-1133.

138. Helenius, J., Brouhard, G., Kalaidzidis, Y., Diez, S., and Howard, J. (2006). The depolymerizing kinesin MCAK uses lattice diffusion to rapidly target microtubule ends. Nature *441*, 115-119.

139. Howard, J., and Hyman, A.A. (2007). Microtubule polymerases and depolymerases. Curr Opin Cell Biol *19*, 31-35.

140. Wordeman, L., Wagenbach, M., and von Dassow, G. (2007). MCAK facilitates chromosome movement by promoting kinetochore microtubule turnover. J Cell Biol *179*, 869-879.

141. Sudakin, V., and Yen, T.J. (2007). Targeting mitosis for anti-cancer therapy. BioDrugs *21*, 225-233.

142. Joglekar, A.P., Bouck, D.C., Molk, J.N., Bloom, K.S., and Salmon, E.D. (2006). Molecular architecture of a kinetochore-microtubule attachment site. Nat Cell Biol *8*, 581-585.

143. O'Toole, E.T., Winey, M., McIntosh, J.R., and Mastronarde, D.N. (2002). Electron tomography of yeast cells. Methods Enzymol *351*, 81-95.

144. Kirschner, M., and Mitchison, T. (1986). Beyond self-assembly: from microtubules to morphogenesis. Cell *45*, 329-342.

145. Niethammer, P., Bastiaens, P., and Karsenti, E. (2004). Stathmin-tubulin interaction gradients in motile and mitotic cells. Science *303*, 1862-1866.

146. Vandecandelaere, A., Brune, M., Webb, M.R., Martin, S.R., and Bayley, P.M. (1999). Phosphate release during microtubule assembly: what stabilizes growing microtubules? Biochemistry *38*, 8179-8188.

147. Voter, W.A., O'Brien, E.T., and Erickson, H.P. (1991). Dilution-induced disassembly of microtubules: relation to dynamic instability and the GTP cap. Cell Motil Cytoskeleton *18*, 55-62.

148. Bayley, P.M., Schilstra, M.J., and Martin, S.R. (1990). Microtubule dynamic instability: numerical simulation of microtubule transition properties using a Lateral Cap model. J Cell Sci *95 (Pt 1)*, 33-48.

149. O'Brien, E.T., Salmon, E.D., Walker, R.A., and Erickson, H.P. (1990). Effects of magnesium on the dynamic instability of individual microtubules. Biochemistry *29*, 6648-6656.

150. O'Brien, E.T., Voter, W.A., and Erickson, H.P. (1987). GTP hydrolysis during microtubule assembly. Biochemistry *26*, 4148-4156.

151. Panda, D., Miller, H.P., and Wilson, L. (2002). Determination of the size and chemical nature of the stabilizing "cap" at microtubule ends using modulators of polymerization dynamics. Biochemistry *41*, 1609-1617.

152. Stewart, R.J., Farrell, K.W., and Wilson, L. (1990). Role of GTP hydrolysis in microtubule polymerization: evidence for a coupled hydrolysis mechanism. Biochemistry *29*, 6489-6498.

153. Kerssemakers, J.W., Munteanu, E.L., Laan, L., Noetzel, T.L., Janson, M.E., and Dogterom, M. (2006). Assembly dynamics of microtubules at molecular resolution. Nature *442*, 709-712.

154. Schek, H.T., 3rd, and Hunt, A.J. (2005). Micropatterned structures for studying the mechanics of biological polymers. Biomed Microdevices *7*, 41-46.

155. Brouhard, G.J., Schek, H.T., 3rd, and Hunt, A.J. (2003). Advanced optical tweezers for the study of cellular and molecular biomechanics. IEEE Trans Biomed Eng *50*, 121-125.

156. VanBuren, V., Cassimeris, L., and Odde, D.J. (2005). Mechanochemical model of microtubule structure and self-assembly kinetics. Biophys J *89*, 2911-2926.

157. Hyman, A.A., Chretien, D., Arnal, I., and Wade, R.H. (1995). Structural changes accompanying GTP hydrolysis in microtubules: information from a slowly hydrolyzable analogue guanylyl-(alpha,beta)-methylene-diphosphonate. J Cell Biol *128*, 117-125.

158. Melki, R., Carlier, M.F., Pantaloni, D., and Timasheff, S.N. (1989). Cold depolymerization of microtubules to double rings: geometric stabilization of assemblies. Biochemistry *28*, 9143-9152.

159. Simon, J.R., Parsons, S.F., and Salmon, E.D. (1992). Buffer conditions and non-tubulin factors critically affect the microtubule dynamic instability of sea urchin egg tubulin. Cell Motility & the Cytoskeleton *21*, 1-14.

160. Drechsel, D.N., and Kirschner, M.W. (1994). The minimum GTP cap required to stabilize microtubules. Curr Biol *4*, 1053-1061.

161. Nogales, E. (2000). Structural insights into microtubule function. Annu Rev Biochem *69*, 277-302.

162. Chen, Y.D., and Hill, T.L. (1985). Monte Carlo study of the GTP cap in a five-start helix model of a microtubule. Proc Natl Acad Sci U S A *82*, 1131-1135.

163. Flyvbjerg, H., Holy, T.E., and Leibler, S. (1996). Microtubule dynamics: Caps, catastrophes, and coupled hydrolysis. Phys Rev E Stat Phys Plasmas Fluids Relat Interdiscip Topics *54*, 5538-5560.

164. Flyvbjerg, H., Holy, T.E., and Leibler, S. (1994). Stochastic dynamics of microtubules: A model for caps and catastrophes. Phys Rev Lett *73*, 2372-2375.

165. Frigon, R.P., and Timasheff, S.N. (1975). Magnesium-induced self-association of calf brain tubulin. I. Stoichiometry. Biochemistry *14*, 4559-4566.

166. Frigon, R.P., and Timasheff, S.N. (1975). Magnesium-induced self-association of calf brain tubulin. II. Thermodynamics. Biochemistry *14*, 4567-4573.

167. Gildersleeve, R.F., Cross, A.R., Cullen, K.E., Fagen, A.P., and Williams, R.C., Jr. (1992). Microtubules grow and shorten at intrinsically variable rates. J Biol Chem *267*, 7995-8006.

168. Odde, D.J., Buettner, H.M., and Cassimeris, L. (1996). Spectral analysis of microtubule assembly dynamics. AIChE Journal *42*, 1434-1442.

169. Tran, P.T., Marsh, L., Doye, V., Inoue, S., and Chang, F. (2001). A mechanism for nuclear positioning in fission yeast based on microtubule pushing. J Cell Biol *153*, 397-411.

170. Derry, W.B., Wilson, L., and Jordan, M.A. (1995). Substoichiometric binding of taxol suppresses microtubule dynamics. Biochemistry *34*, 2203-2211.

171. Caplow, M., Shanks, J., and Ruhlen, R.L. (1988). Temperature-jump studies of microtubule dynamic instability. J Biol Chem *263*, 10344-10352.

172. Page, B.D., and Snyder, M. (1992). CIK1: a developmentally regulated spindle pole body-associated protein important for microtubule functions in Saccharomyces cerevisiae. Genes & Development *6*, 1414-1429.

173. Sproul, L.R., Anderson, D.J., Mackey, A.T., Saunders, W.S., and Gilbert, S.P. (2005). Cik1 targets the minus-end kinesin depolymerase kar3 to microtubule plus ends. Curr Biol *15*, 1420-1427.

174. Zeng, X., Kahana, J.A., Silver, P.A., Morphew, M.K., McIntosh, J.R., Fitch, I.T., Carbon, J., and Saunders, W.S. (1999). Slk19p is a centromere protein that functions to stabilize mitotic spindles. J Cell Biol *146*, 415-425.

175. Hoyt, M.A., He, L., Totis, L., and Saunders, W.S. (1993). Loss of function of Saccharomyces cerevisiae kinesin-related CIN8 and KIP1 is suppressed by KAR3 motor domain mutations. Genetics *135*, 35-44.

176. Janson, M.E., Loughlin, R., Loiodice, I., Fu, C., Brunner, D., Nedelec, F.J., and Tran, P.T. (2007). Crosslinkers and motors organize dynamic microtubules to form stable bipolar arrays in fission yeast. Cell *128*, 357-368.

177. Pellman, D., Bagget, M., Tu, H., and Fink, G.R. (1995). Two microtubule-associated proteins required for anaphase spindle movement in Saccharomyces cerevisiae. Journal of Cell Biology *130*, 1373-1385.

178. Schuyler, S.C., Liu, J.Y., and Pellman, D. (2003). The molecular function of Ase1p: evidence for a MAP-dependent midzone-specific spindle matrix. Microtubule-associated proteins. J Cell Biol *160*, 517-528.

179. Brock, J.A., and Bloom, K. (1994). A chromosome breakage assay to monitor mitotic forces in budding yeast. Journal of Cell Science *107*, 891-902.

180. Doheny, K.F., Sorger, P.K., Hyman, A.A., Tugendreich, S., Spencer, F., and Hieter, P. (1993). Identification of essential components of the S. cerevisiae kinetochore. Cell *73*, 761-774.

181. Mythreye, K., and Bloom, K.S. (2003). Differential kinetochore protein requirements for establishment versus propagation of centromere activity in Saccharomyces cerevisiae. J Cell Biol *160*, 833-843.

182. Hill, A., and Bloom, K. (1987). Genetic manipulation of centromere function. Molecular & Cellular Biology *7*, 2397-2405.

183. Hill, A., and Bloom, K. (1989). Acquisition and processing of a conditional dicentric chromosome in Saccharomyces cerevisiae. Molecular & Cellular Biology *9*, 1368-1370.

184. Straight, A.F., Marshall, W.F., and Murray, A.W. (1997). Mitosis in Living Budding Yeast: Anaphase A But No Metaphase Plate. Science *277*, 574.

185. Thrower, D.A., and Bloom, K. (2001). Dicentric chromosome stretching during anaphase reveals roles of Sir2/Ku in chromatin compaction in budding yeast. Mol Biol Cell *12*, 2800-2812.

186. Allingham, J.S., Sproul, L.R., Rayment, I., and Gilbert, S.P. (2007). Vik1 modulates microtubule-Kar3 interactions through a motor domain that lacks an active site. Cell *128*, 1161-1172.

187. Manning, B.D., Barrett, J.G., Wallace, J.A., Granok, H., and Snyder, M. (1999). Differential regulation of the Kar3p kinesin-related protein by two associated proteins, Cik1p and Vik1p. J Cell Biol *144*, 1219-1233.

188. Molk, J.N., Schuyler, S.C., Liu, J.Y., Evans, J.G., Salmon, E.D., Pellman, D., and Bloom, K. (2004). The Differential Roles of Budding Yeast Tem1p, Cdc15p, and Bub2p Protein Dynamics in Mitotic Exit. Mol Biol Cell.

189. Kremer, J.R., Mastronarde, D.N., and McIntosh, J.R. (1996). Computer visualization of three-dimensional image data using IMOD. J Struct Biol *116*, 71-76.

190. Mastronarde, D.N. (1997). Dual-axis tomography: an approach with alignment methods that preserve resolution. J Struct Biol *120*, 343-352.

191. Thompson, S.L., and Compton, D.A. (2008). Examining the link between chromosomal instability and aneuploidy in human cells. J Cell Biol *180*, 665-672.

192. Liu, J., Desai, A., Onuchic, J.N., and Hwa, T. (2007). A mechanobiochemical mechanism for monooriented chromosome oscillation in mitosis. Proc Natl Acad Sci U S A.

193. Franck, A.D., Powers, A.F., Gestaut, D.R., Gonen, T., Davis, T.N., and Asbury, C.L. (2007). Tension applied through the Dam1 complex promotes microtubule elongation providing a direct mechanism for length control in mitosis. Nat Cell Biol *9*, 832-837.

194. Cheerambathur, D.K., Civelekoglu-Scholey, G., Brust-Mascher, I., Sommi, P., Mogilner, A., and Scholey, J.M. (2007). Quantitative analysis of an anaphase B switch: predicted role for a microtubule catastrophe gradient. J Cell Biol *177*, 995-1004.

195. Bieling, P., Laan, L., Schek, H., Munteanu, E.L., Sandblad, L., Dogterom, M., Brunner, D., and Surrey, T. (2007). Reconstitution of a microtubule plus-end tracking system in vitro. Nature *450*, 1100-1105.

196. Vorobjev, I.A., Rodionov, V.I., Maly, I.V., and Borisy, G.G. (1999). Contribution of plus and minus end pathways to microtubule turnover. J Cell Sci *112 (Pt 14)*, 2277-2289.

197. Maly, I.V. (2002). Diffusion approximation of the stochastic process of microtubule assembly. Bull Math Biol *64*, 213-238.

198. Cassimeris, L., Pryer, N.K., and Salmon, E.D. (1988). Real-time observations of microtubule dynamic instability in living cells. J Cell Biol *107*, 2223-2231.

199. Dogterom, M., Felix, M.A., Guet, C.C., and Leibler, S. (1996). Influence of M-phase chromatin on the anisotropy of microtubule asters. J Cell Biol *133*, 125-140.

200. Howell, B., Odde, D.J., and Cassimeris, L. (1997). Kinase and phosphatase inhibitors cause rapid alterations in microtubule dynamic instability in living cells. Cell Motil Cytoskeleton *38*, 201-214.

201. Odde, D.J. (1997). Estimation of the diffusion-limited rate of microtubule assembly. Biophys J *73*, 88-96.

202. Adams, I.R., and Kilmartin, J.V. (1999). Localization of core spindle pole body (SPB) components during SPB duplication in Saccharomyces cerevisiae. J Cell Biol *145*, 809-823.

203. Shimogawa, M.M., Graczyk, B., Gardner, M.K., Francis, S.E., White, E.A., Ess, M., Molk, J.N., Ruse, C., Niessen, S., Yates, J.R., 3rd, Muller, E.G., Bloom, K., Odde, D.J., and Davis, T.N. (2006). Mps1 phosphorylation of dam1 couples kinetochores to microtubule plus ends at metaphase. Curr Biol *16*, 1489-1501.

204. King, J.M., and Nicklas, R.B. (2000). Tension on chromosomes increases the number of kinetochore microtubules but only within limits. J Cell Sci *113 Pt 21*, 3815-3823.

205. Bloom, K., Beach, D.L., Maddox, P., Shaw, S.L., Yeh, E., and Salmon, E.D. (1998). Using Green Fluorescent Protein Fusion Proteins to Quantitate Microtubule and Spindle Dynamics in Budding Yeast. In Methods in Cell Biology, Volume 61. (San Diego: Academic Press), pp. 369-383.

206. Hunt, A.J., and Howard, J. (1993). Kinesin swivels to permit microtubule movement in any direction. Proc Natl Acad Sci U S A *90*, 11653-11657.

207. Kuo, S.C., Gelles, J., Steuer, E., and Sheetz, M.P. (1991). A model for kinesin movement from nanometer-level movements of kinesin and cytoplasmic dynein and force measurements. Journal of Cell Science - Supplement *14*, 135-138.

208. Hancock, W.O., and Howard, J. (1998). Processivity of the motor protein kinesin requires two heads. J Cell Biol *140*, 1395-1405.

209. Odde, D.J., and Hawkins, S.S. (1997). Computer-Assisted Motion Analysis of Fluorescent Tubulin Dynamics in the Nerve Growth Cone. Journal of Computer-Assisted Microscopy *9*, 143-151.

210. Korneev, M.J., Lakamper, S., and Schmidt, C.F. (2007). Load-dependent release limits the processive stepping of the tetrameric Eg5 motor. Eur Biophys J *36*, 675-681.

211. Lee, G., Abdi, K., Jiang, Y., Michaely, P., Bennett, V., and Marszalek, P.E. (2006). Nanospring behaviour of ankyrin repeats. Nature *440*, 246-249.

212. Bell, G.I. (1978). Models for the specific adhesion of cells to cells. Science *200*, 618-627.

213. Evans, E.A., and Calderwood, D.A. (2007). Forces and bond dynamics in cell adhesion. Science *316*, 1148-1153.

214. Kawaguchi, K., and Ishiwata, S. (2001). Nucleotide-dependent single- to double-headed binding of kinesin. Science *291*, 667-669.

215. Northrup, S.H., and Erickson, H.P. (1992). Kinetics of protein-protein association explained by Brownian dynamics computer simulation. Proc Natl Acad Sci U S A *89*, 3338-3342.

216. Gardner, M.K., Haase, J., Mythreye, K., Molk, J.N., Anderson, M., Joglekar, A.P., O'Toole, E.T., Winey, M., Salmon, E.D., Odde, D.J., and Bloom, K. (2008). The microtubule-based motor Kar3 and plus end-binding protein Bim1 provide structural support for the anaphase spindle. J Cell Biol *180*, 91-100.

217. Ashkin, A. (1998). Forces of a single-beam gradient laser trap on a dielectric sphere in the ray optics regime. Methods Cell Biol *55*, 1-27.

218. Block, S.M. (1992). Making light work with optical tweezers. Nature *360*, 493-495.

219. Bayley, P., Schilstra, M., and Martin, S. (1989). A lateral cap model of microtubule dynamic instability. FEBS Lett *259*, 181-184.

220. Gittes, F., Mickey, B., Nettleton, J., and Howard, J. (1993). Flexural rigidity of microtubules and actin filaments measured from thermal fluctuations in shape. J Cell Biol *120*, 923-934.

221. Brock, J.A., and Bloom, K. (1994). A chromosome breakage assay to monitor mitotic forces in budding yeast. J Cell Sci *107 (Pt 4)*, 891-902.

222. Bi, E., and Pringle, J.R. (1996). ZDS1 and ZDS2, genes whose products may regulate Cdc42p in Saccharomyces cerevisiae. Molecular & Cellular Biology *16*, 5264-5275.

223. Meluh, P.B., and Rose, M.D. (1990). KAR3, a kinesin-related gene required for yeast nuclear fusion. Cell *60*, 1029-1041.

224. Straight, A.F., Marshall, W.F., Sedat, J.W., and Murray, A.W. (1997). Mitosis in living budding yeast: anaphase A but no metaphase plate. Science *277*, 574-578.

225. Hill, A., and Bloom, K. (1987). Genetic manipulation of centromere function. Mol Cell Biol *7*, 2397-2405.